

CLAS-ANALYSIS 2015-XXX

**Deeply Virtual Production
of the ρ^+ Meson
on the proton
Analysis of the e1-dvcs data**

A. Fradi, M. Guidal and S. Niccolai

IPN Orsay, France
(fradi@ipno.in2p3.fr)

March 4, 2015

Contents

1	Introduction	3
2	Data analysis	5
2.1	Dataset selection	6
2.2	Selection of the $ep \rightarrow e'n\rho^+ \hookrightarrow \pi^+\pi^0 \hookrightarrow \gamma\gamma$ events	7
2.2.1	Identification of the particles	7
2.2.2	Momentum corrections	20
2.2.3	Identification of the exclusive reaction $ep \rightarrow e'n\rho^+ \hookrightarrow \pi^+\pi^0$	23
2.3	Normalisation of the experimental data for the reaction $ep \rightarrow e'n\pi^+\pi^0$	41
2.3.1	Binning of the kinematical phase space	41
2.3.2	Cross sections	43
2.3.3	Acceptance of the CLAS detector	46
2.3.4	Radiative correction	63
2.3.5	Efficiency of the selection cuts of electrons in the Čerenkov counters and the electromagnetic calorimeters of CLAS	65
2.3.6	Bin volume correction	70
2.3.7	Total cross section of the reaction $\gamma^*p \rightarrow n\pi^+\pi^0$	73
2.4	Extraction of the cross sections of the reaction $\gamma^*p \rightarrow n\rho^+$	73
2.4.1	Background subtraction	73
2.4.2	Total cross section $\sigma_{\gamma^*p \rightarrow n\rho^+}$	82
2.4.3	Differential cross section $d\sigma/dt$ ($\gamma^*p \rightarrow n\rho^+$)	82
2.4.4	Differential cross sections in Φ and test of SCHC	84
2.4.5	Extraction of the longitudinal cross sections $\gamma_L^*p \rightarrow n\rho_L^+$	86
2.4.6	Estimation of systematic errors	95
A	Acceptance hole factor for each (Q^2, x_B, t) bin	111
B	Acceptance hole factor for each (Q^2, x_B, Φ) bin	114
C	Acceptance hole factor for each (Q^2, x_B, ϕ_{HS}) bin	117
D	Acceptance hole factor for each $(Q^2, x_B, \cos \theta_{HS})$ bin	120

E Background subtraction for each (Q^2, x_B, t) bin	123
F Background subtraction for each (Q^2, x_B, Φ) bin	126
G Background subtraction for each (Q^2, x_B, ϕ_{HS}) bin	129
H Background subtraction for each $(Q^2, x_B, \cos \theta_{HS})$ bin	132
I Background subtraction for each (Q^2, x_B) fixing the skewdness parameter	135
J Background subtraction for each (Q^2, x_B) varing the exclusivity cuts	137

Chapter 1

Introduction

The process that we study is the exclusive electroproduction of the ρ^+ on the proton:

$$e + p \rightarrow e' + n + \rho^+ \quad (1.1)$$

The interaction between the electron and the nucleon goes mainly through the exchange of one virtual photon γ^* and can be rewritten as:

$$\gamma^* + p \rightarrow n + \rho^+ \quad (1.2)$$

We aim at measuring the cross section of this process, which has never been done up to now.

If the ρ^+ is considered as stable, this process is described (if the masses of the particles in the final state are all known) by 5 independent kinematic variables : the 4 components of the 4-vectors \times the 3 particles in the final state minus the 3 known masses minus the 4 equations of energy-momentum conservation. In the case in which the target is not polarised, there is a global azimuthal symmetry and the azimuthal angle of the scattered electron contains no physics and can be ignored. It therefore remains only 4 independent kinematic variables, which we choose as follows:

- The virtuality of the photon: $Q^2 = -q^2 = 4EE' \sin^2(\frac{\theta}{2})$ where θ is the polar scattering angle of the electron, E and E' are the energies of the incident and scattered electron respectively and q is the 4-momentum of the virtual photon.
- The square of the 4-vector of the energy-momentum transfer between the target nucleon (of 4-momentum p) and the recoil nucleon (of 4-momentum p'): $t = (p' - p)^2$.
- The variable x_B defined by: $x_B = \frac{Q^2}{2pq}$. x_B is inversely proportionnal to W , the energy of the center-of-mass of the γ^*p system: $W^2 = (p + q)^2 = m_p^2 + Q^2(\frac{1-x_B}{x_B})$. In this analysis, we will use either x_B or W , according to the framework.
- The angle Φ between the leptonic plane (the scattering plane of the electron) and the hadronic plane (the meson production plane).

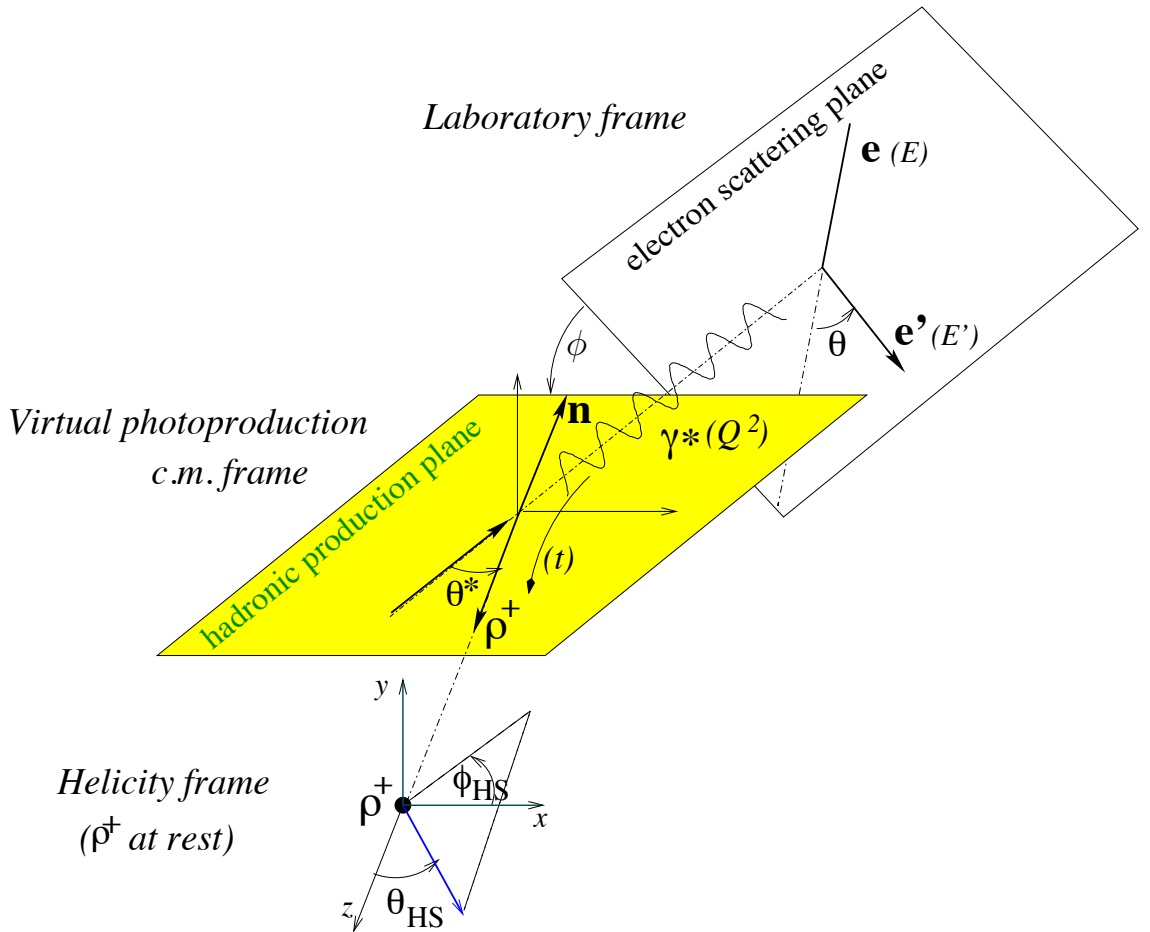


Figure 1.1: Illustration of the kinematic variables of the exclusive ρ^+ electroproduction process on the nucleon. There are three planes entering into play: the leptonic plane, the hadronic plane and the ρ^+ decay plane (in the so-called ρ^+ “helicity frame”).

When one takes into account the meson decay (the ρ^+ decays mainly into $\pi^+\pi^0$, which is the channel that we are going to analyse), there are 3 more variables (if the masses of the decay particles are known). For the ρ^+ , we choose:

- $M_{\pi^+\pi^0} = \sqrt{(p_{\pi^+} + p_{\pi^0})^2}$: the invariant mass of the two pions,
- θ_{HS}, ϕ_{HS} : the decay angles of the π^+ in the rest frame of the ρ^+ .

Figure 1.1 shows these 7 independent kinematic variables.

Chapter 2

Data analysis

The data that we have analyzed come from the "e1-dvcs" run. This experiment was mainly dedicated to the analysis of the DVCS reaction $ep \rightarrow ep\gamma$. We recall that, for this run, CLAS was supplemented by the Inner calorimeter (IC) aimed at detecting the final state photon. Since our channel contains several photons in the final state (through the π^0 decay), this run was actually also particularly well adapted for our analysis. The data taking period of the "e1-dvcs" run took place from March 11th up to May 27th 2005, using a 5.776 GeV electron beam. The effective beam time was about 36 days. The luminosity was $1.6 \times 10^{34} \text{ cm}^{-2} \text{ s}^{-1}$. Figure 2.1 shows the evolution of the accumulated charge with time. The red curve represents the accumulated charge that would have been obtained with a luminosity of $2 \times 10^{34} \text{ cm}^{-2} \text{ s}^{-1}$ which was originally planned.

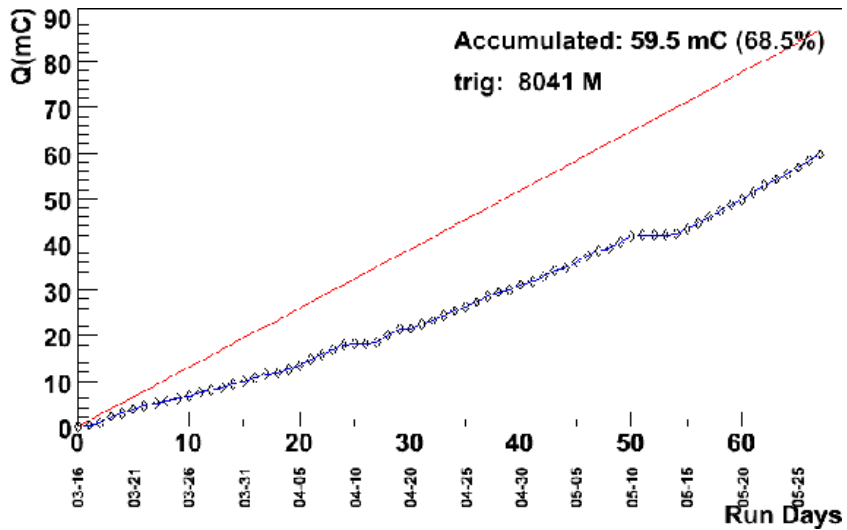


Figure 2.1: Accumulated charge as a function of time for the e1-dvcs run.

The e1-dvcs data used for this analysis correspond to version 4 of PASS 1, resulting

from the recooking that was performed in 2011, using an improved version of the tracking and reconstruction software.

2.1 Dataset selection

For the e1-dvcs experiment, a total of 445 runs were collected but a large portion was not used in the analysis. During the first part of the experiment, the quality of the data was affected by various issues. One major issue was the drift chambers from region 1 not working for quite a long time. Figure 2.2 shows the ratio of the number of $ep \rightarrow epX$ events to the livetime-gated charge measured by the Faraday cup ("a livetime-gate" means that the data acquisition deadtime is taken into account) as a function of "equal-charge slices" of events (corresponding to the time interval between subsequent Faraday cup scaler recordings), for the whole e1-dvcs dataset (from run 46586 to run 47455). That ratio, which is supposed to be constant, was quite unstable during the first part of the experiment. Therefore we decided to exclude all the runs preceding run 47000 (indicated by a red line on the Figure) from the analysis.

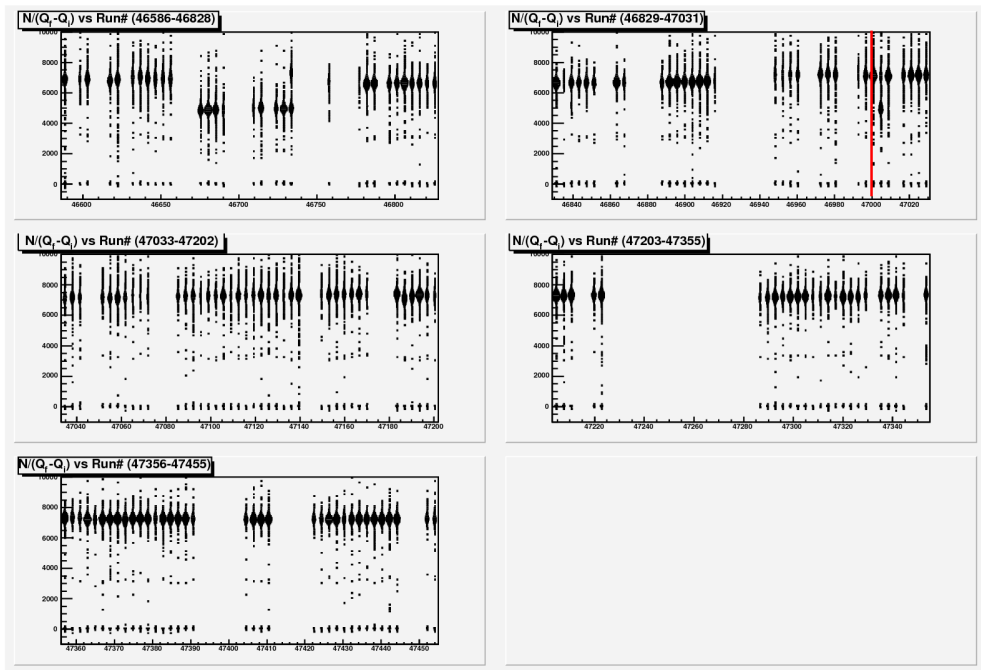


Figure 2.2: Ratio of number of $ep \rightarrow epX$ events to the measured livetime-gated charge as a function of "equal-charge slices" of events, for the whole e1-dvcs dataset (from run 46586 to run 47455). The red line indicates run 47000. All the runs preceding run 47000 were excluded from this analysis.

2.2 Selection of the $ep \rightarrow e'n\rho^+ \hookrightarrow \pi^+\pi^0 \hookrightarrow \gamma\gamma$ events

To identify the reaction $ep \rightarrow e'n\rho^+ \hookrightarrow \pi^+\pi^0 \hookrightarrow \gamma\gamma$, we have chosen to detect the electron, the π^+ and the two photons γ which originate from the decay of the π^0 . Given the small efficiency of neutron detection in CLAS (< 50%), we do not require the detection of the neutron in this analysis in order to have a better statistics.

In a first stage, by calculating the invariant mass of the two photons, we will select a π^0 . In a second stage, by calculating the missing mass of the final state $e\pi^+\pi^0X$, we will select a "missing" neutron so as to identify the exclusive reaction. Finally, we will calculate the invariant mass $\pi^+\pi^0$ in order to identify a ρ^+ .

We begin by the description of the identification of each individual particle.

2.2.1 Identification of the particles

Identification of the electrons

An electron is defined in the reconstruction program of CLAS as a particle of negative charge (i.e. deflected in the forward direction by the magnetic field of CLAS) and having interacted both with the Čerenkov counters and the electromagnetic calorimeters. We begin by applying a series of cuts to get rid of accidental tracks and to define the fiducial zones of detection. Then, we will show how we separate the electrons signal from the pions signal, which contaminates it.

Cut on the vertex position Z_{vertex}

In order to reject electrons which originate from the scattering on the windows of the target, we cut on the vertex position along the z -axis. The hydrogen target (2.5 cm long) is centered around $z = -66.3$ cm. Figure 2.3 shows, for each CLAS sector, the vertex position reconstructed from the trajectories of the electrons detected in the drift chambers. One observes, for each sector, a central peak which corresponds to the target and two small peaks which correspond to interactions with the exit windows of the target chamber. In order to eliminate the secondary peaks, we cut, for each sector, at 2.5 cm left and right from the central peak (whose position slightly varies from sector to sector because of the bad centering of the beam with respect to CLAS).

Fiducial cuts for the electromagnetic calorimeters

The electron detection efficiency decreases on the edges of the electromagnetic calorimeters. Indeed, on the edges, the electromagnetic showers created by an electron is not fully contained in the detector, and the measured energy doesn't reflect the "true" energy of the incident particle. It is estimated that the impact point of particles must be at least 10 cm inside the calorimeter edge in order to trust the energy measurement. In the local coordinate system of the calorimeters (U, V, W), this means the following cuts: 40 cm

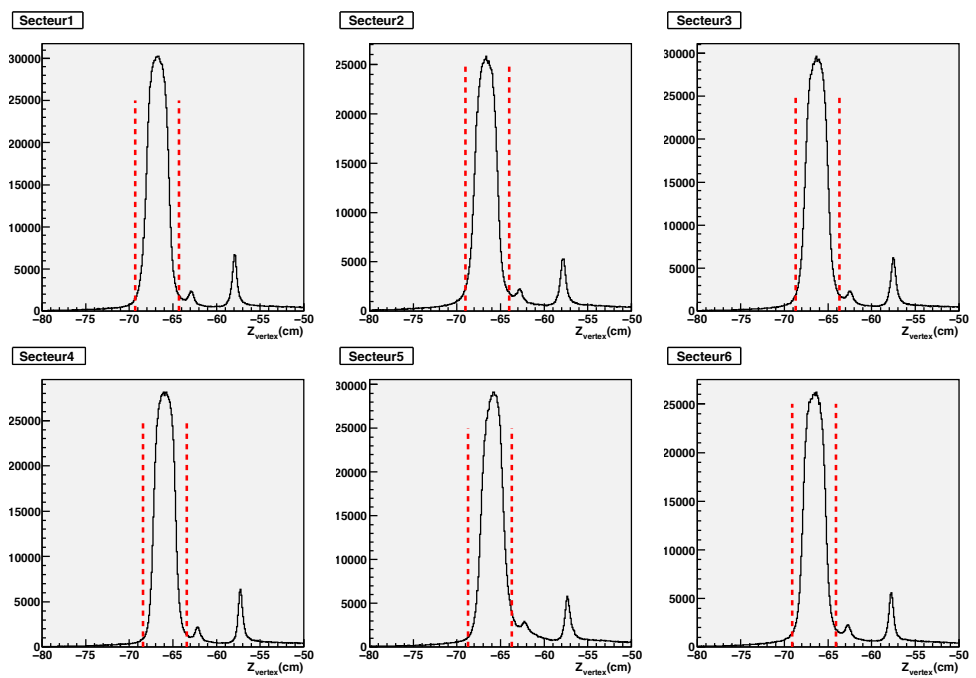


Figure 2.3: Distribution of the vertex positions for the particles identified as electrons, for the six sectors of CLAS. The red lines show the cuts that have been applied in order to eliminate the secondary peaks.

$< U < 400$ cm, $V < 360$ cm and $W < 390$ cm. The U , V and W distributions of the particles identified as electrons, and the associated fiducial cuts are shown in figure 2.4. In this same figure (lower right plot), one sees the Y distribution as a function of X (global coordinates) for these same particles, before (in black) and after (in color) these fiducial cuts.

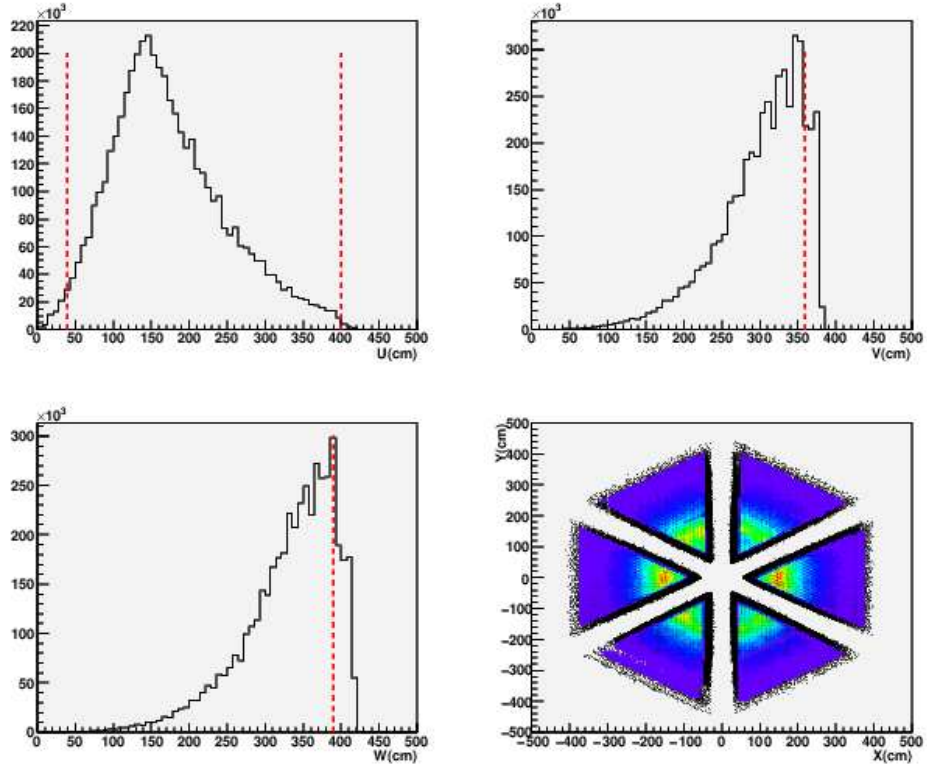


Figure 2.4: Distribution U , V and W of the particles identified as electrons. The red lines show the fiducial cuts. Lower right plot: distribution Y as a function of X before (in black) and after (in color) the fiducial cuts.

Fiducial cuts for the Čerenkov counters

The Čerenkov light collection efficiency decreases on the edges of the mirrors, which corresponds to particles touching the limits of the sectors. To eliminate the signals of these particles, we apply fiducial cuts. These cuts depend on the polar (θ) and azimuthal (ϕ) angles of the detected particles as well as their momentum (p). These cuts are parametrised as follows (common to all e1-dvcs analysis):

$$\theta \geq \theta_{cut} \quad (2.1)$$

$$|\phi_S - \phi_0| \leq \phi_{cut}(p, \theta) \quad (2.2)$$

where ϕ_S is the azimuthal angle relative to the sector ($0^\circ \leq \phi_S \leq 60^\circ$). The angles $\theta_{cut}(p), \phi_0(p), \phi_{cut}$ (in degrees), are defined as follows:

$$\theta_{cut}(p) = 16.8 + \frac{0.93}{p - 0.52} \quad (2.3)$$

$$\phi_0(p) = 1.012 + \frac{6.632}{p} \quad (2.4)$$

$$\phi_{cut}(\theta, \phi) = 27 \times (\sin[\theta - \theta_{cut}(p)])^{0.195} \quad (2.5)$$

Figure 2.5 shows the distribution ϕ as a function of θ for the particles identified as electrons, before and after the fiducial cuts for the Čerenkov counters. One observes in particular the detection inefficiencies at small θ angles in sectors 5 and 6 (ϕ between -150° and -30°). These inefficiencies are due to the shape of the IC-shielding. At large θ angles in sector 5, the inefficiencies are mostly due to the time-of-flight counters.

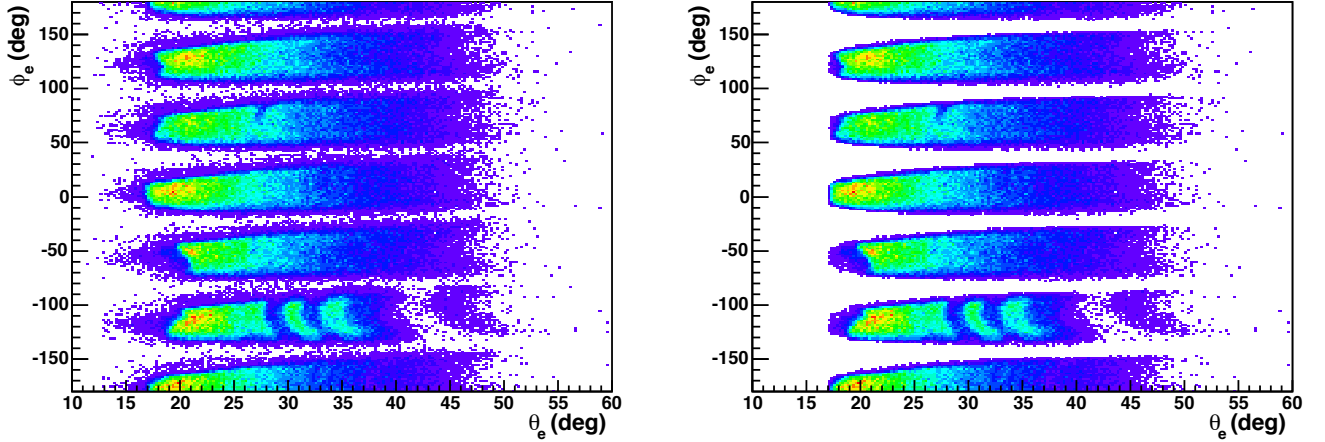


Figure 2.5: Distributions ϕ as a function of θ of the particles identified as electrons, before (left) and after (right) the fiducial cuts for the Čerenkov counters.

Contamination of the electron signal by pions

Like electrons, negatively charged pions (π^-) can interact both in the Čerenkov counters (for momenta ≥ 2.5 GeV/c) and in the electromagnetic calorimeters. Then, by mistake, one can identify a pion like an electron. In order to get rid of this contamination, we apply additional requirements for the electron identification.

In the electromagnetic calorimeters, electrons and pions interact differently: electrons produce an electromagnetic shower and the deposited energy in the calorimeter is proportional to their momentum. Pions are MIPs (Minimum Ionisation Particles) and deposit

in EC the same quantity of energy by unit of thickness of the material which is traversed, independently of their momentum. This deposited energy is roughly 2 MeV/cm (Particle Data Group (PDG) [39]). The part of the calorimeters which collects the deposited energy by a particle is made of 39 layers of scintillators, each being 10 mm thick. One therefore expects that the total energy deposited by pions be:

$$E_{tot} = 39 \times 10 \text{ mm} \times 2 \text{ MeV/cm} = 78 \text{ MeV} \quad (2.6)$$

We are going to use the longitudinal profile of the deposited energy in the calorimeters in order to distinguish electrons from pions. We recall that in each CLAS calorimeter, the 39 layers of scintillators are grouped into 2 sets which provide each their own signal. The 15 first layers define the "inner" part and the 24 following layers define the "outer" part. We call E_{in} and E_{out} the deposited energy in the "inner" part and the "outer" part, respectively. Figure 2.6 shows the distribution E_{out} as a function of E_{in} . One observes very clearly two signals. The signal at the right of the red line corresponds to electrons while the signal at the left correspond to pions misidentified as electrons. Indeed, for electrons, one expects that E_{in} be larger than E_{out} since they lose most of their energy in the inner part through the process of the electromagnetic shower. For pions, they lose the same amount of energy per unit of length, so that the relation between E_{in} et E_{out} is:

$$\frac{E_{in}}{15} = \frac{E_{out}}{24} = \frac{E_{tot}}{39} = \frac{78}{39}$$

donc $E_{in} = \frac{15}{39} \times 78 = 30 \text{ MeV}$ and $E_{out} = \frac{24}{39} \times 78 = 48 \text{ MeV}$ (2.7)

In order to reject pions, we therefore cut on the energy E_{in} :

$$E_{in} > 60 \text{ MeV} \quad (2.8)$$

In order to further refine the identification of electrons and diminish the pion contamination, we are going to use the feature that the energy deposited by electrons in the electromagnetic calorimeters is proportional to their momentum.

This is illustrated by figure 2.7 which shows the distribution E_{tot} (total deposited energy) as a function of the momentum p of the particles identified as electrons. In this figure, the contamination of electrons by pions is not so clear (E_{tot} for pions should be independent of p). We will therefore rather use the distribution E_{tot}/p as a function of p for the particles identified as electrons as shown in figure 2.8. We will apply cuts on this latter distribution. For several intervals in momentum, we project the bidimensionnal distribution $(E_{tot}/p, p)$ on the E_{tot}/p variable and we fit the resulting spectra by a gaussian. We determin then for each momentum p , the mean μ and the width σ of the distribution E_{tot}/p . The distributions $\mu(p)$ and $\sigma(p)$ are then fitted by the following formulaes:

$$\begin{aligned} \mu(p) &= 0.214 + 0.0454p - 0.007987p^2 + 0.000435934p^3 \\ \sigma(p) &= \sqrt{(0.01705)^2 + \left(\frac{0.02668}{\sqrt{p}}\right)^2} \end{aligned} \quad (2.9)$$

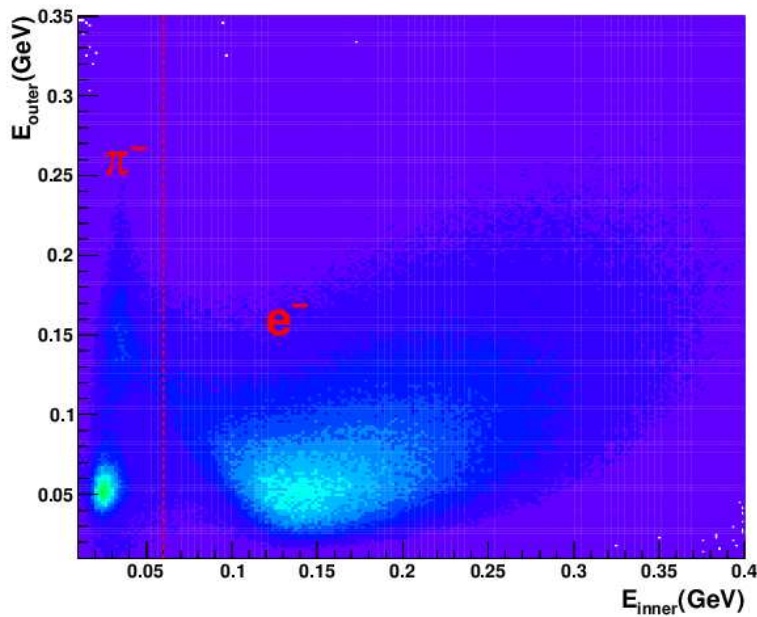


Figure 2.6: Distribution E_{out} as a function of E_{in} . The cut at 60 MeV is represented as the red dashed line.

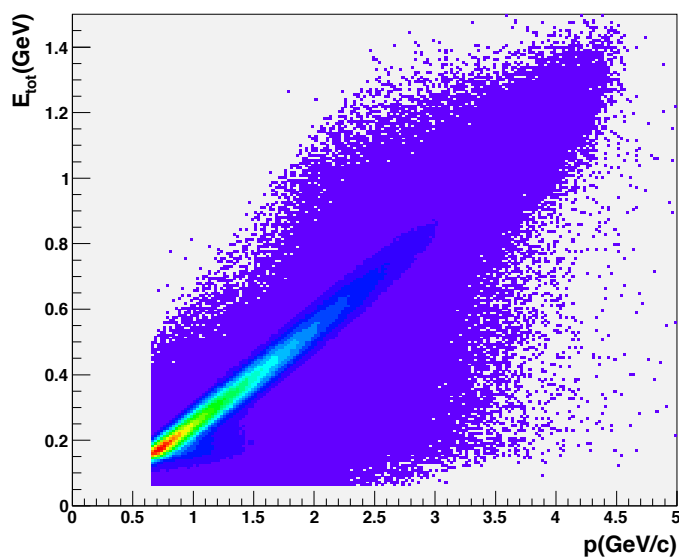


Figure 2.7: Total energy E_{tot} deposited in the electromagnetic calorimeters as a function of the momentum p as measured by the drift chambers.

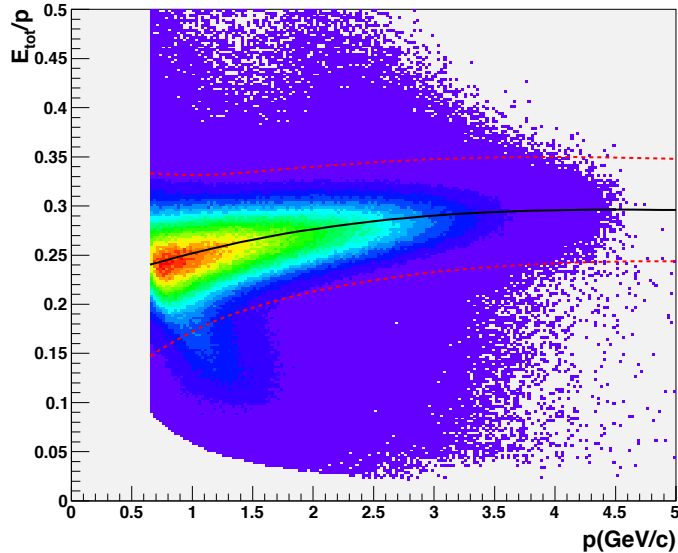


Figure 2.8: Distribution E_{tot}/p as a function of p . The black curve represents the mean $\mu(p)$ and the two red curves represent the cuts for the selection of electrons, at $2.5\sigma(p)$ from $\mu(p)$.

For the selection of electrons, we apply the following requirement:

$$|E_{tot}/p - \mu(p)| < 2.5\sigma(p) \quad (2.10)$$

A last cut that we apply is based on the signal of the Čerenkov counters. It will further improve the electron/pion discrimination.

Pions are in general not energetic enough to produce directly Čerenkov light (the threshold is at 2.5 GeV/c momentum). However, they can interact with the gas of the detector and give rise to "δ-electrons", these latter having enough momentum (> 9 MeV) to create Čerenkov light. It is expected that this light will be in general weak (corresponding to 1 or 2 photo-electrons in the photomultipliers).

Figure 2.9 shows the number of photo-electrons ($Nphe \times 10$) for particles identified as electrons, after the application of all the cuts previously mentioned. On the left, the peak induced by pions appears, which corresponds to a small number of photo-electrons ($Nphe \times 10 \simeq 20$). On the right, the continuum corresponds to the spectrum of electrons ($Nphe \times 10 \simeq 100$). In order to reject the π^- , we apply the following cut:

$$Nphe > 2.5 \quad (2.11)$$

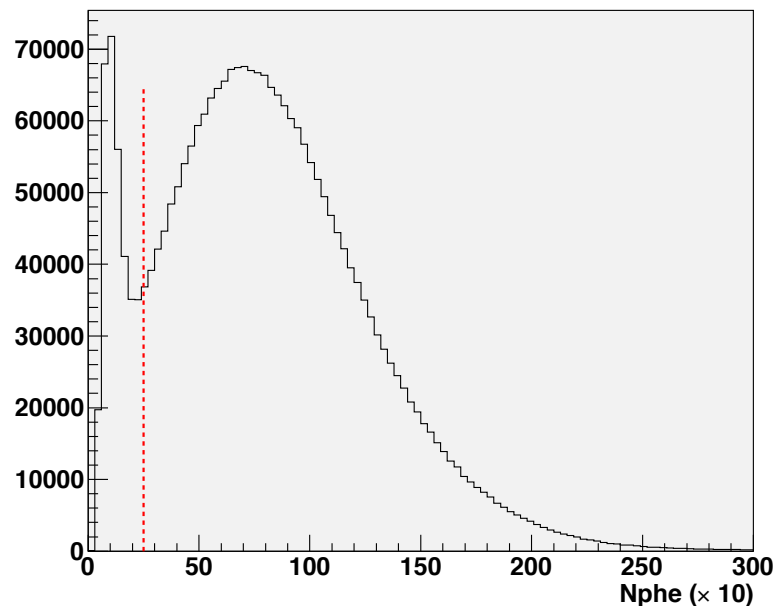


Figure 2.9: Spectrum of the number of photo-electrons ($\times 10$) of the Čerenkov counters, produced by particles identified as electrons, having passed all the cuts previously mentionned. The red dashed line shows the cut $Nphe \times 10 > 25$.

Identification of the π^+ meson

The π^+ is identified by the reconstruction program as a particle of charge +1 which interacts in the drift chambers. This "gross" identification has to be completed by additionnal cuts, which we now detail.

Cut on Z_{vertex}

Figure 2.10 shows the distribution of the vertex position of particles of charge +1. One observes only one peak corresponding to the hydrogen target. One doesn't observe the secondary peaks since they have already been cut off at the electron identification stage. However, we still apply some cuts on the distributions' tails which extend beyond the target's dimensions: $-69 < Z_{vertex} < -63$.

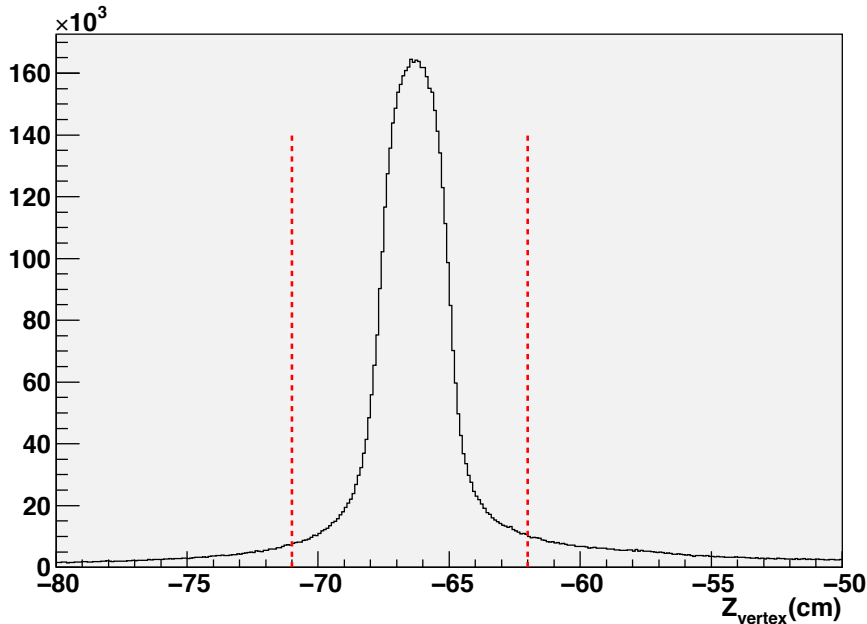


Figure 2.10: Distribution of Z_{vertex} for particles of charge +1. The cuts are represented by the red dashed lines.

Cut on $\Delta\beta$

The identification of charged hadrons is done by correlating the time-of-flight measurement (t_{TOF}) (given by the scintillators) and the momentum measurement (derived from the tracking of the drift chambers). The track reconstruction in the drift chambers yields also the distance d followed by the particle from the vertex up to the scintillators. Knowing the time at the vertex t_0 which is the accelerator Radio-Frequency time, one can

derive the velocity (β) of the particles:

$$\beta = \frac{d}{(t_{TOF} - t_0)c} \quad (2.12)$$

The velocity β is related to the momentum p and to the mass M of a particle through the following relation:

$$\beta = \frac{p}{\sqrt{p^2 + M^2}} \quad (2.13)$$

In figure 2.11, one sees the distributions β as a function of p for particles of positive charge. One can distinguish the various bands corresponding to the various particles. One notes a contamination of the π^+ by positrons e^+ for momenta $p \geq 0.3$ GeV/c, a contamination by K^+ mesons at higher momenta ($p \geq 2$ GeV/c) and finally another contamination by protons for $p \geq 3$ GeV.

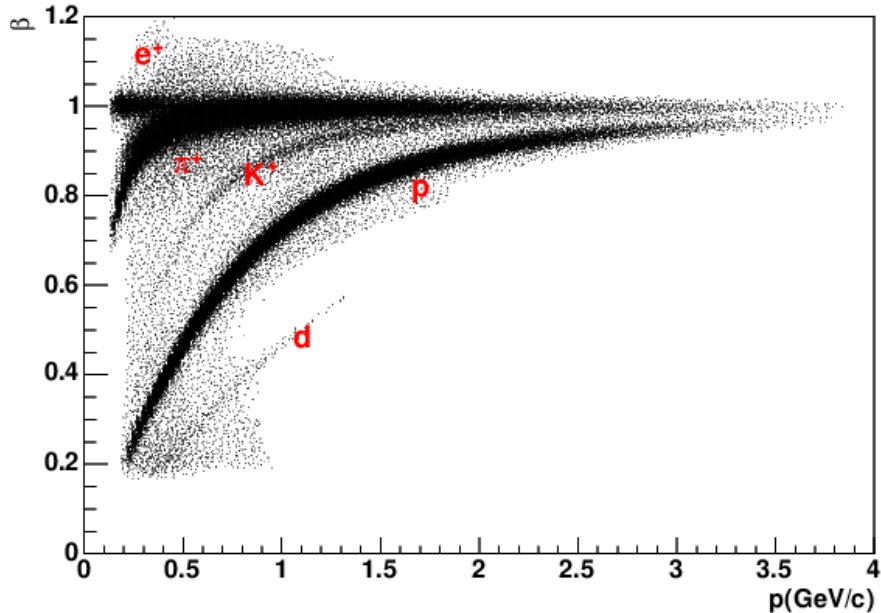


Figure 2.11: β as a function of momentum p for particles positively charged.

In order to select the π^+ 's, we calculate $\Delta\beta$ defined by:

$$\Delta\beta = \beta_{Meas} - \beta_{Calc} \quad (2.14)$$

where β_{Meas} is defined by the relation 2.12 and β_{Calc} by the relation 2.13 with the mass of a π^+ for M .

Figure 2.12 shows $\Delta\beta$ as a function of momentum p . One sees in the figure the cut on $\Delta\beta$ to select the π^+ 's. This cut is obtained by projecting $\Delta\beta$ for several intervals in p and by fitting these projections by gaussians. The means $\mu(p)$ and the widths $\sigma(p)$ are then fitted by a 6th degree polynomial and a 3rd degree polynomial, respectively:

$$\mu(p) = 0.001251 - 0.002539 p + 0.000829 p^2 + 0.000737 p^3 - 0.000609 p^4 + 0.000159 p^5 - 0.000014 p^6 \quad (2.15)$$

$$\sigma(p) = 0.016159 - 0.011720 p + 0.003617 p^2 - 0.000368 p^3 \quad (2.16)$$

In order to select the π^+ 's, we have applied the cut: $|\Delta\beta - \mu(p)| < 4.5 \sigma(p)$.

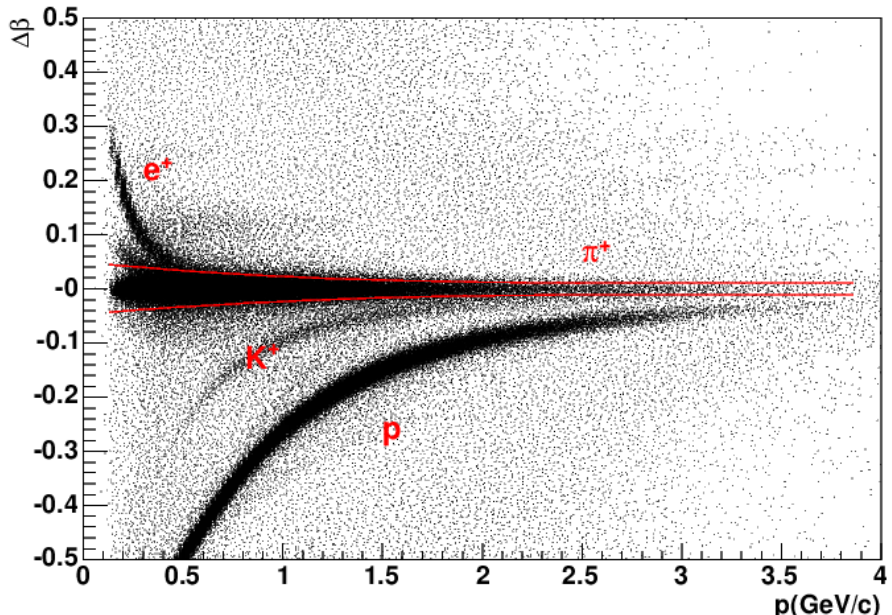


Figure 2.12: $\Delta\beta$ as a function of momentum p for particles positively charged. The two red lines represent the selection cuts of the π^+ 's, at $4.5\sigma(p)$ from $\mu(p)$.

Identification of the photons

For our analysis, we require to detect the two photons which originate from the decay of the π^0 . The detection of the photons is done by the electromagnetic calorimeters, EC and IC. In both cases, one requests 150 MeV as minimum/threshold energy for the photons.

In the case of EC, a particle is defined as a photon if it hasn't interacted in the drift chambers (neutral particle). In order to distinguish photons from neutrons, one applies,

in addition to the minimum energy threshold, a cut on the quantity $\beta = \frac{d}{t_{EC}}$ (where t_{EC} is the time measurement provided by the calorimeters EC and d the distance between the target and the impact point on the calorimeters). The cuts are thus:

$$E_\gamma \geq 0.150 \text{ GeV} \quad (2.17)$$

$$\beta \geq 0.92 \quad (2.18)$$

Figure 2.13 shows the β distribution for neutral particles with the cut at $\beta = 0.92$ (red dashed line).

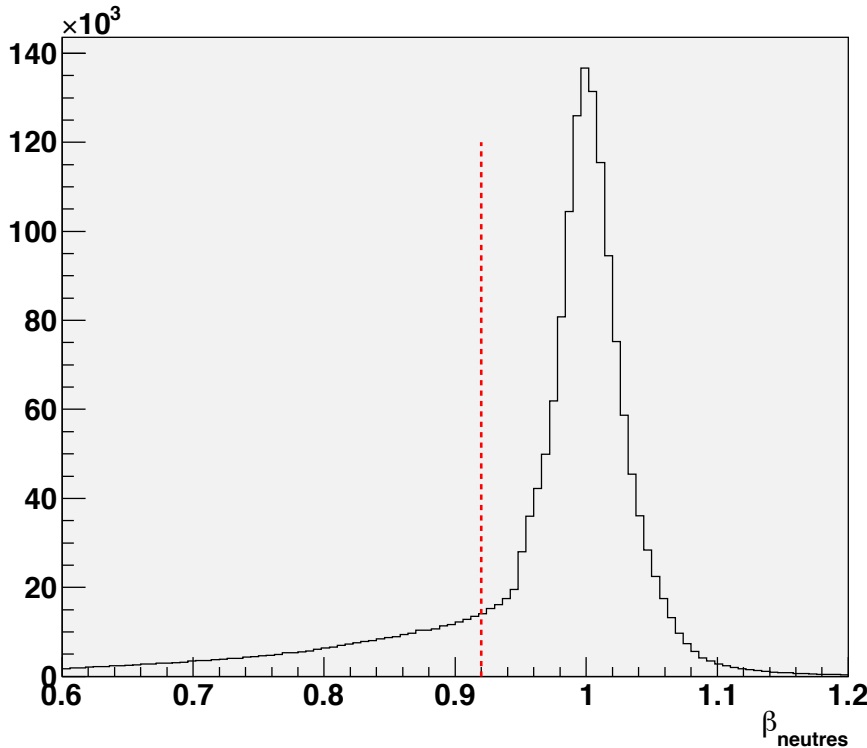


Figure 2.13: Distribution $\beta = v/c$ for neutral particles. The cut at 0.92 is represented by the red dashed line.

In order to avoid the edges of the calorimeter EC, we have applied the same fiducial cuts than those applied for the electrons' identification: $40 \text{ cm} < U < 400 \text{ cm}$, $V < 360 \text{ cm}$ et $W < 390 \text{ cm}$. Figure 2.14 shows the U , V and W distribution of the neutral particules and the associated fiducial cuts. In the lower right plot, one sees the distribution of Y as a function of X before (in black) and after (in color) the fiducial cuts.

Concerning the IC calorimeter, one considers that all the showers which are reconstructed originate from a photon. If electrons (originating from Møller scattering or other electroproduction processes) traverse IC, they will therefore be considered/misidentified

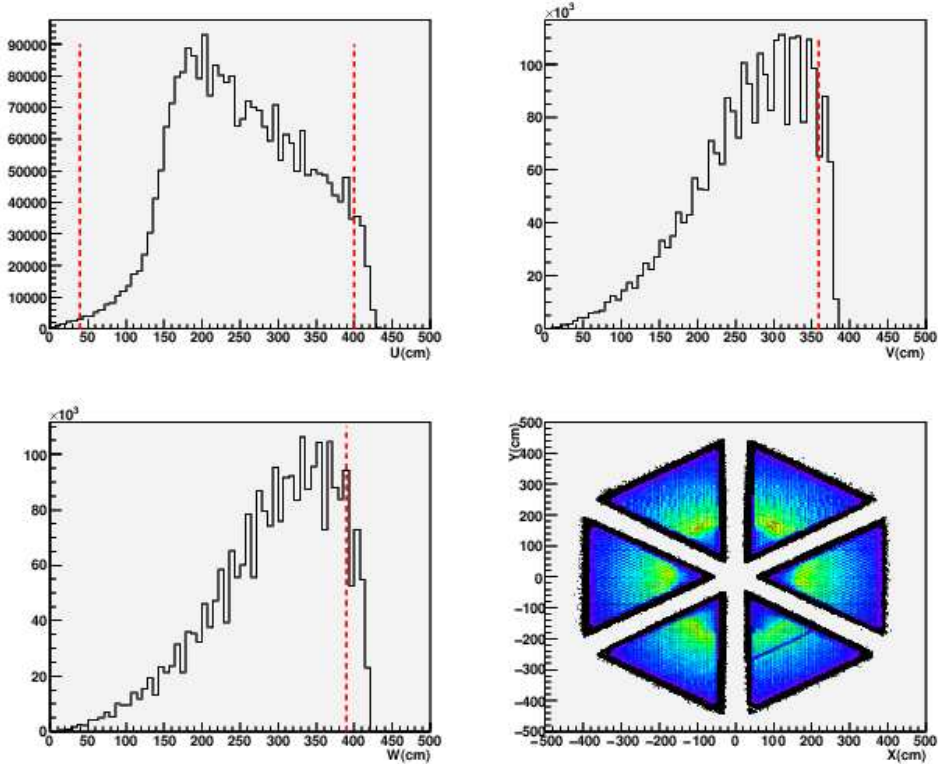


Figure 2.14: Distributions U, V and W of neutral particles. The red lines show the fiducial cuts. Lower right plot: distribution of Y as a function of X before (in black) and after (in color) the fiducial cuts.

as photons. However, a final state with two electrons is quite unlikely given that we already request that an electron be detected in EC (required for the triggering of the data acquisition) and also given the "exclusivity" cuts that we will apply later on to select our reaction $ep \rightarrow e'n\rho^+ \rightarrow \pi^+\pi^0$.

Fiducial cuts on IC are applied so as to avoid the edges of the calorimeter and so as to obtain a better reconstruction on the position and the energy of the detected particles. Figures 2.15 and 2.16 show respectively the distribution of particles in the XY plane of the calorimeter IC, before and after the fiducial cuts. Even after applying these fiducial cuts, one notices in figure 2.16 a large number of events (red zone) around the centre of IC which correspond to electrons: they can be Møller's, low angle scattered electrons, electrons from the beam ... In order to get rid of these electrons which will then be considered as photons, we apply a cut on a combination of the energy E_γ and polar angle θ , of the photon candidates:

$$E_\gamma(\text{GeV}) \times 12 + \theta_\gamma(\text{deg}) > 9. \quad (2.19)$$

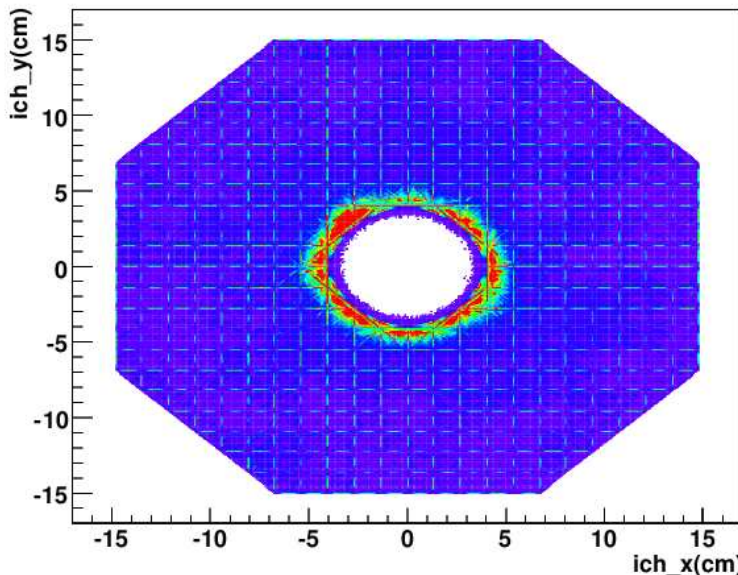


Figure 2.15: Distribution, in the XY plane of IC, of the particles identified as photons, before the fiducial cuts.

Figure 2.17 shows the distribution of ϕ as a function of θ for the photons detected in IC and EC, before (left) and after (right) the fiducial cuts.

2.2.2 Momentum corrections

- Charged particles:

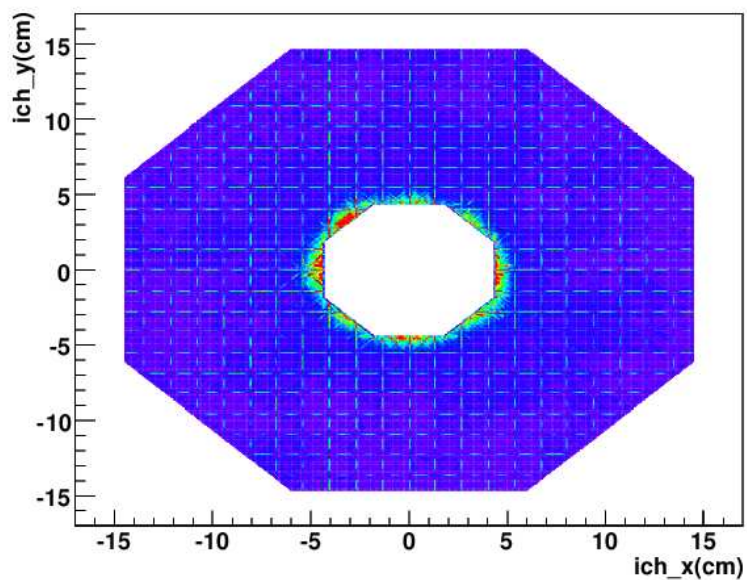


Figure 2.16: Distribution, in the XY plane of IC, of particles identified as photons, after the fiducial cuts.

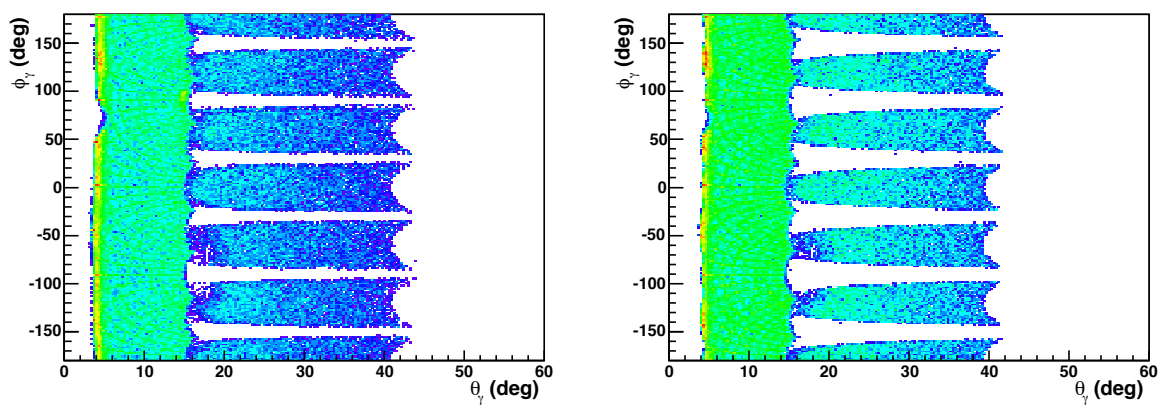


Figure 2.17: Distribution of ϕ as a function of θ for the photons before (left) and after (right) the fiducial cuts.

It is necessary to apply some corrections to the momenta and angles of the charged particles because, in particular, of the azimuthal offset induced by the presence of the solenoidal magnetic field, which is not taken into account precisely enough in the reconstruction code.

We quote here the results of the studies [40] carried out with GEANT simulations concerning the reconstruction of the momentum and angles of charged particles in the solenoidal magnetic field along with the field of the standard CLAS coils. In this study, the corrections have been established by comparing the generated and reconstructed kinematics.

The most important corrections are those for the π^+ , which are:

$$p \text{ (GeV/c)} \rightarrow p + 0.0015p + 0.00031 \quad (2.20)$$

$$\theta \text{ (rad)} \rightarrow \theta + \frac{0,0005 + 0,0011\theta}{p^{1,8\theta}} - 0,0008 \quad (2.21)$$

$$\phi \text{ (rad)} \rightarrow \phi + \frac{0,0011\sqrt{\theta}}{p^{1+1.29\theta}} + 0,0014^\theta \quad (2.22)$$

- Photons :

For the inner calorimeter (IC), two corrections were performed: a correction to the reconstructed energy and a correction to the Z -coordinate of the reconstructed cluster.

- Correction to the reconstructed energy:

Due to leakage, not all the energy is deposited in the crystals of the calorimeter. The average reconstructed energy is about 92%. The correction was done by comparing the generated and the reconstructed energies of photons and π^0 s. Simulations showed that the reconstructed energy does not have any ϕ dependence. So the correction factor depends only on θ (for numerical details, see [41] and [42]).

- Correction to the Z -coordinate of the reconstructed cluster :

The reconstruction code assumes that the average value of the shower position starts at the Z -coordinate corresponding to the position of the front plane of the calorimeter. The reconstructed shower depth in the z -direction was calculated using the generated angle θ_{gen}^γ , the reconstructed cluster coordinates X_{clust} and Y_{clust} . The target-calorimeter distance being known ($D = 46\text{cm}$), the correction is determined by:

$$\Delta D = \frac{\sqrt{X_{clust}^2 + Y_{clust}^2}}{\tan(\theta_{gen}^\gamma)} - D \quad (2.23)$$

For numerical values see [42].

For the EC electromagnetic calorimeters, a correction procedure has been established using real data [43]. Only about a quarter of the deposited energy by a particle in the

calorimeters is reconstructed. The total energy of the particle corresponds then to $E = E_{\text{measured}}/0,273$.

By selecting events containing two photons detected and by calculating the invariant mass of these two photons in the following way:

$$m_{\pi^0 \text{measured}} = 2\sqrt{E_1}\sqrt{E_2} \sin \frac{\theta_{\gamma_1 \gamma_2}}{2} \quad (2.24)$$

where $\theta_{\gamma_1 \gamma_2}$ is the angle between the two photons, the correction to be applied to the energy of the photons is determined by requesting a match between this invariant mass and the mass of the π^0 :

$$m_{\pi^0} = 2\sqrt{\frac{E_1}{\text{corr}(E_1)}}\sqrt{\frac{E_2}{\text{corr}(E_2)}} \sin \frac{\theta_{\gamma_1 \gamma_2}}{2} = 0,135 \text{ GeV} \quad (2.25)$$

Then:

$$\frac{m_{\pi^0 \text{measured}}}{m_{\pi^0}} = \sqrt{\text{corr}(E_1)\text{corr}(E_2)} \quad (2.26)$$

The correction is then calculated for different values of the energy E and the fit yields:

$$\text{corr}(E) = 1,01034 - \frac{0,0272506}{E} - \frac{0,00147336}{E^2} \quad (2.27)$$

2.2.3 Identification of the exclusive reaction $ep \rightarrow e'n\rho^+ \hookrightarrow \pi^+\pi^0$

To recap, in our analysis, we request the detection of at least one electron, at least one π^0 (i.e., at least two photons) and at least one π^+ . These (loose) conditions allow us to analyse the maximum of events.

In order to select a π^0 , we calculate the invariant mass of two photons. We analyse the experimental data event by event. For each event, one identifies the detected photons. Three configurations are possible: 1/ the two photons are detected in IC, 2/ the two photons are detected in EC and 3/ one of the photons is detected in IC and the other one in EC. If, in one event, one has more than two photons, our analysis algorithm makes all the possible combinations of two photons and selects the configuration which corresponds to the invariant mass $IM(\gamma\gamma)$ the closest to the mass of a π^0 (~ 134 MeV). Figures 2.18, 2.19 and 2.20 show the distributions de invariant mass $IM(\gamma\gamma)$ for the three cases IC-IC, IC-EC and EC-EC respectively, integrated over the whole statistics of the experimental data of our experiment. One can notice from the total number total of events ("entries") that the IC-IC and IC-EC configurations correspond, each, to $\sim 45\%$ of the total number of events and that the EC-EC configuration corresponds to only 10%. This shows that the majority of the photons originating from the decay of a π^0 is emitted at the forward angles (corresponding to the angular coverage of IC).

In order to refine the selection of the π^0 and so as to take into account a possible dependence of the $IM(\gamma\gamma)$ distribution on the kinematics, we have analysed the invariant

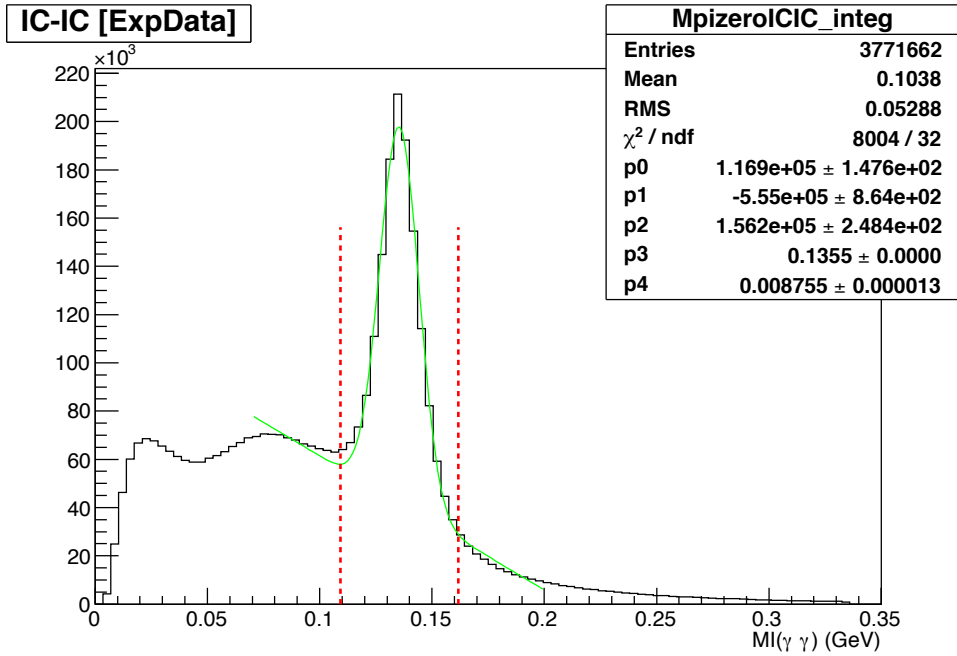


Figure 2.18: Distribution of the $IM(\gamma\gamma)$ integrated over all the statistics, configuration IC-IC. The selection cuts are represented by the red dashed lines. The mean and the width of the Gaussian are given by the parameters p_3 and p_4 , respectively.

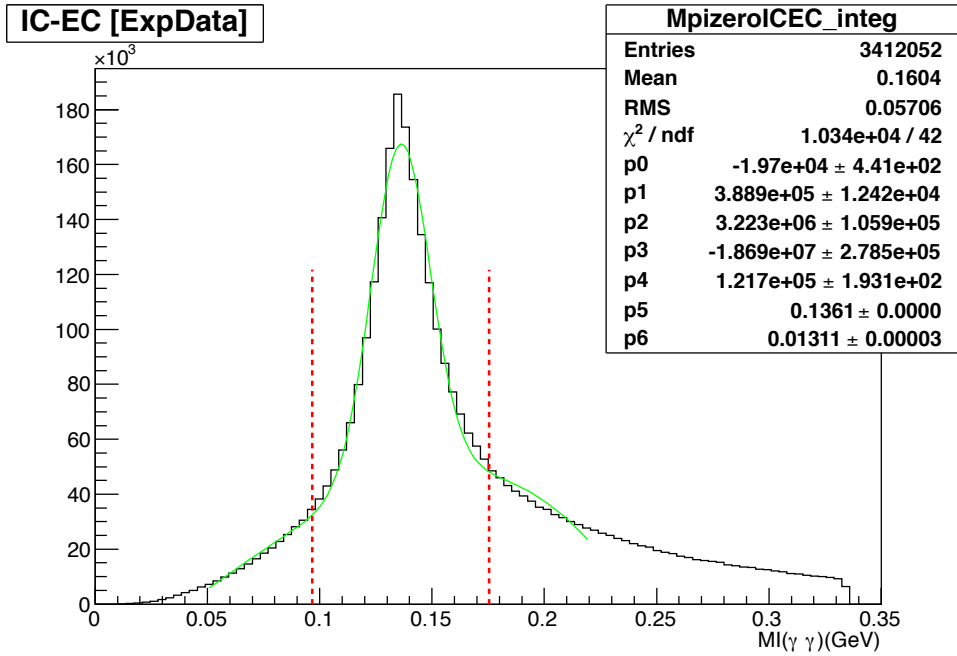


Figure 2.19: Distribution of the $IM(\gamma\gamma)$ integrated over all the statistics, configuration IC-EC. The selection cuts are represented by the red dashed lines. The mean and the width of the Gaussian are given by the parameters p_5 and p_6 , respectively.

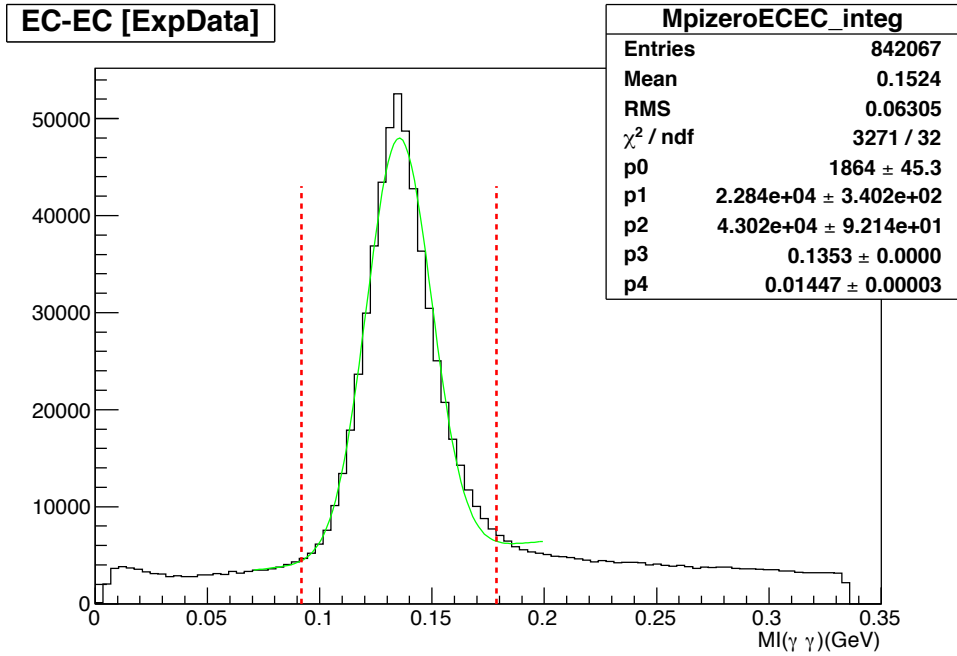


Figure 2.20: Distribution of the $IM(\gamma\gamma)$ integrated over all the statistics, configuration EC-EC. The selection cuts are represented by the red dashed lines. The mean and the width of the Gaussian are given by the parameters p_3 and p_4 , respectively.

mass of the two photons for each interval (Q^2, x_B) (the choice of our binning and the limits of these intervals will be detailed in the next section). To select a π^0 , we fit, for each configuration and each bin, these spectra by a Gaussian centered around the mass of the π^0 and we apply a cut at 3σ on each side of the centroid. Figures 2.21, 2.22 and 2.23 show, for all our (Q^2, x_B) bins, the spectra of invariant masses $IM(\gamma\gamma)$ for each configuration: IC-IC, IC-EC and EC-EC. One sees that the shape of the background varies according to the configuration. Indeed, we observe in the IC-IC configuration that there is a larger background under and on the left of the π^0 peak. Close to the π^0 peak, the background is roughly linear (fitted by a straight line) over all the kinematical bins (Q^2, x_B) .

For the IC-EC case, the background is different from the IC-IC case: it is not symmetric on both sides of the π^0 peak and is therefore not really linear. We therefore fitted it by a 3rd degree polynomial.

The last case $EC - EC$ is the configuration for which there is the least background and where this latter is relatively symmetric on both sides of the π^0 peak and linear.

Although the background is not linear in some cases, we have applied the "side band" subtraction method. This method consists in removing the events which are in the two bands of width 3σ at a distance of 3σ on both sides of the centroid of the Gaussian (of

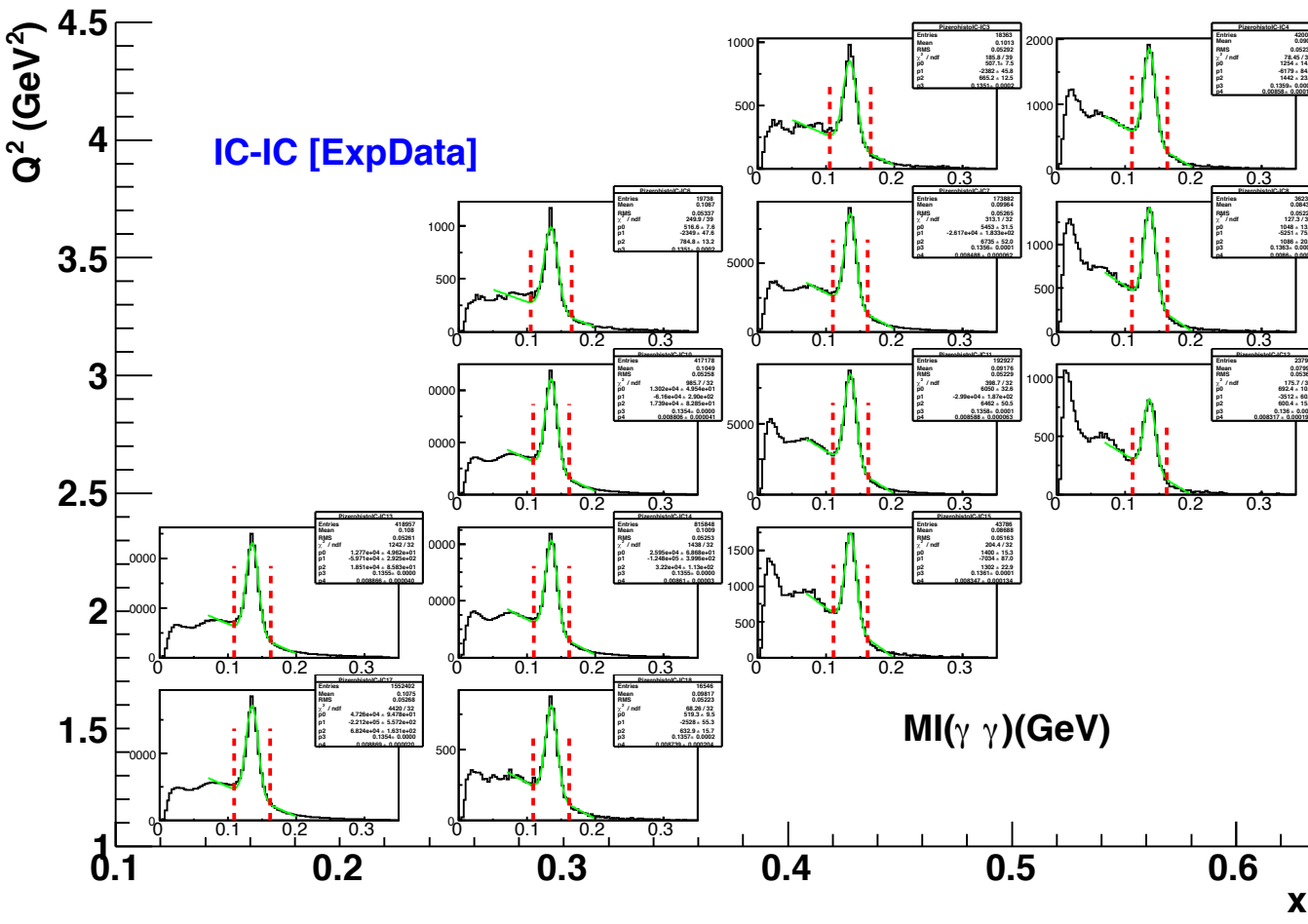


Figure 2.21: $IM(\gamma\gamma)$ for each bin (Q^2, x_B) , case IC-IC. The selection cuts are represented by the red dashed lines.

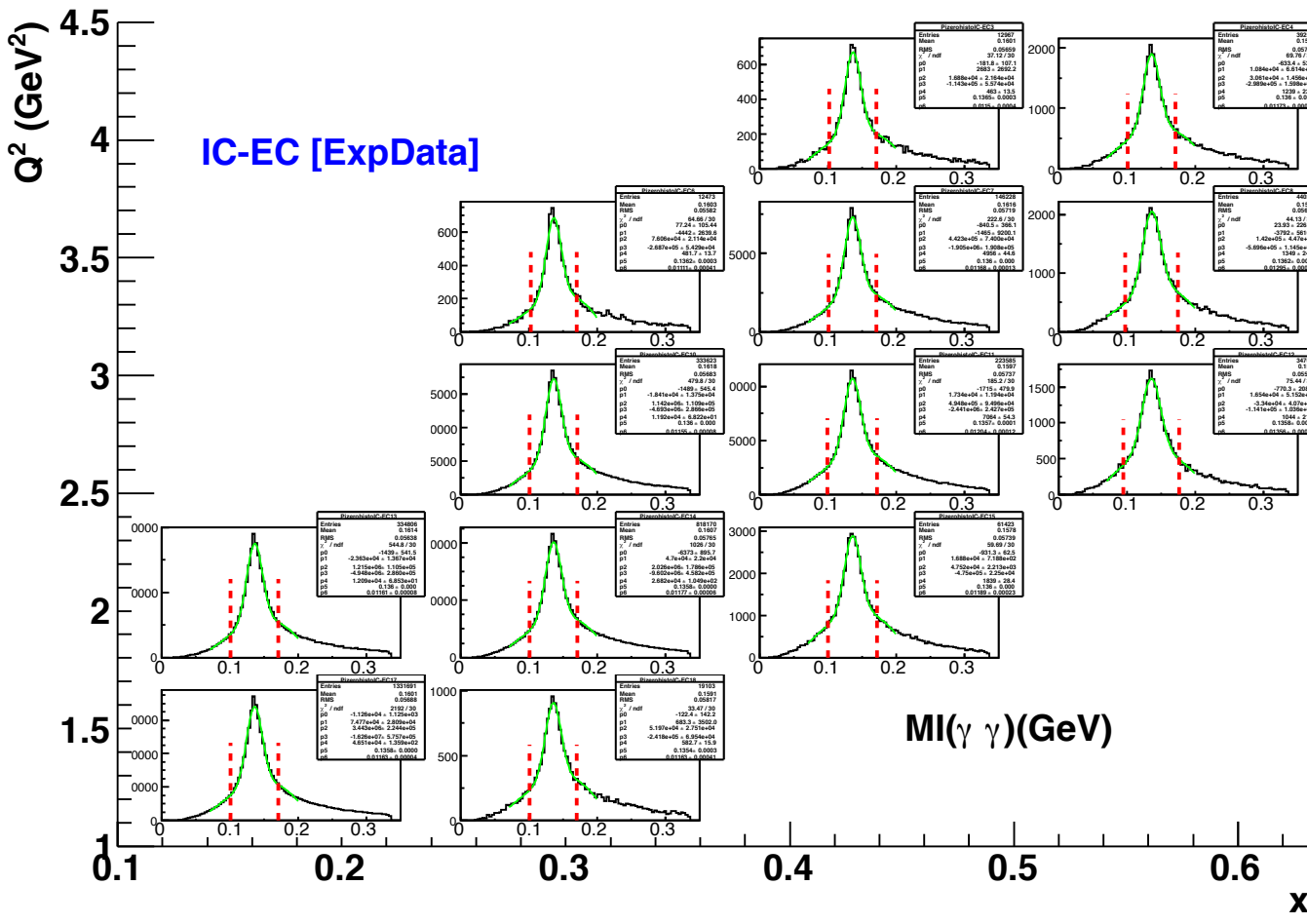


Figure 2.22: $IM(\gamma\gamma)$ for each bin (Q^2, x_B) , case IC-EC. The selection cuts are represented by the red dashed lines.

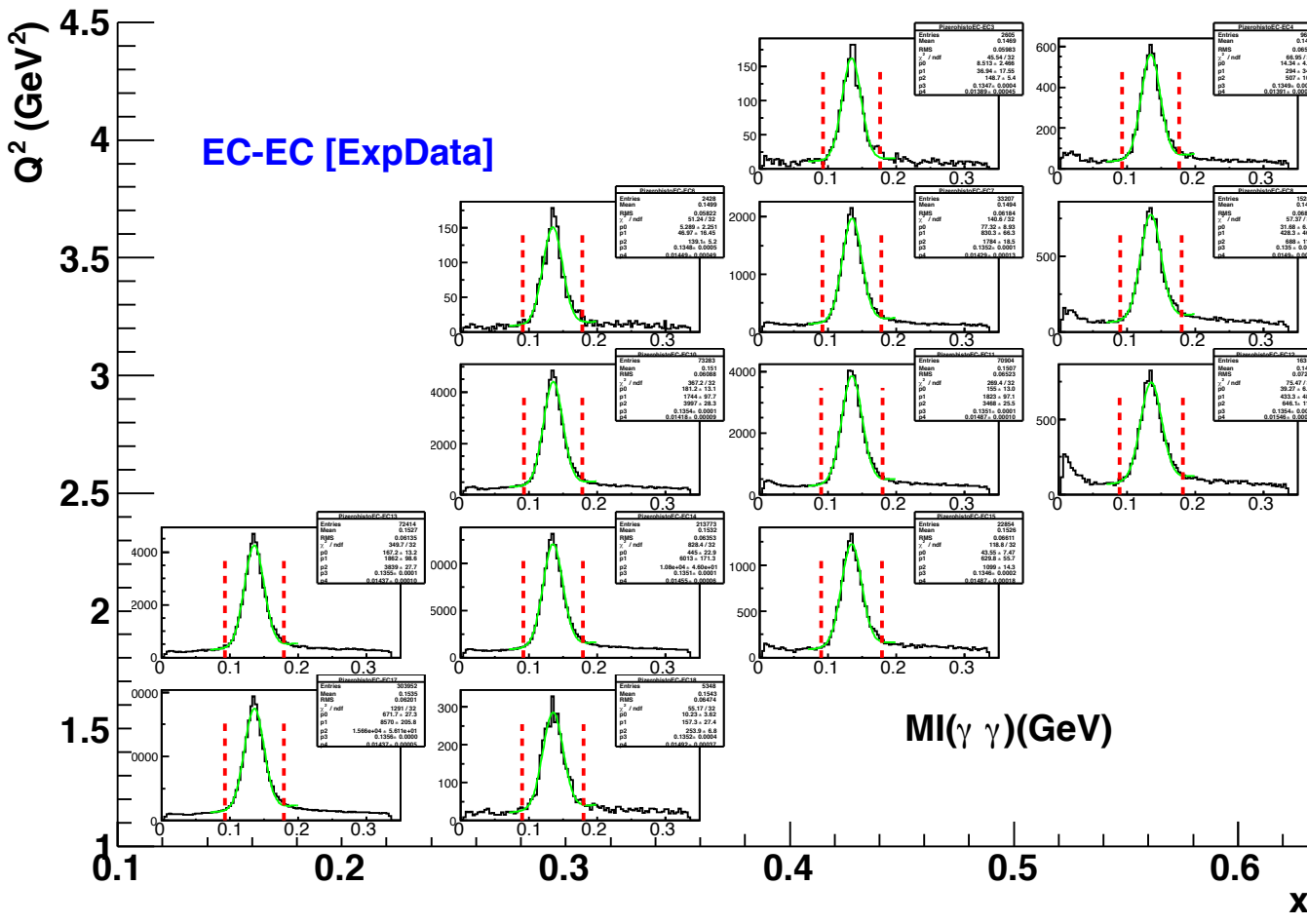


Figure 2.23: $IM(\gamma\gamma)$ for each bin (Q^2, x_B) , case EC-EC. The selection cuts are represented by the red dashed lines.

width σ). In the limit of a linear background, the number of events in those two bands is equal to the number of events under the π^0 peak that one wants to subtract. In this method, one makes the assumption that the events in the two bands have the same kinematic behavior than those of the background under the π^0 peak. The application of this method will be justified a posteriori as we will see shortly. In addition to the differences in the shape and the amount of background, the 3 configurations show differences in the width of the π^0 peak. For the IC-IC configuration, the average width of the π^0 peak is of the order of 8 MeV. For the IC-EC configuration, the average width is of the order of 12 MeV. Finally, for the EC-EC configuration, the average width is of the order of 14.5 MeV. This difference in the widths originates mainly from the difference in the resolution between IC and EC, the resolution of IC being clearly better. In all cases, the centroids and the widths do not vary by large amount as a function of the (Q^2, x_B) bins.

Once the electron, the π^+ and the π^0 are identified, the selection of the neutron is done by cutting on the missing mass of the process $ep \rightarrow e'\pi^+\pi^0X$, which is defined by:

$$MM_{ep \rightarrow e'\pi^+\pi^0X}^2 = (p_e + p_p - (p_{e'} + p_{\pi^+} + p_{\pi^0}))^2 \quad (2.28)$$

This cut ensures the exclusivity of the reaction.

As can be seen in figures 2.24, 2.25 and 2.26, after this exclusivity cut on the missing mass of the neutron (that we will detail shortly), the invariant mass spectra $IM(\gamma\gamma)$ show that the π^0 peaks are relatively "clean" and, in cases where there is still some background, this latter is basically linear. This justifies then the use of the "side band" method, given that all the selection cuts are applied simultaneously.

Figures 2.27, 2.28 and 2.29 show the spectra of the missing mass $MM(e'\pi^+\pi^0X)$ for the three configurations of identification of the π^0 .

In all cases, the neutron peak is well distinguishable. To select this neutron, we fit these spectra by a Gaussian centered around the neutron mass (the background under the peak of the neutron is fitted by a straight line) and we apply a cut at 3σ on each side of the centroid. One observes in most cases an important background on the right of the neutron peak which, in some instances, makes the identification of the neutron difficult, mainly for the IC-EC configuration. This background is not symmetric with respect to the neutron peak in the vast majority of the cases and therefore it is preferable not to apply the "side band" method to subtract it.

In order to understand the origin of this background, we have carried out simulations with 3-pion electroproduction channels (non resonant $ep \rightarrow en(p)\pi^+\pi^0(\pi^-)\pi^0$) and 4-pion electroproduction channels ($ep \rightarrow en(p)\pi^+\pi^0(\pi^-)\pi^0\pi^0$), based on phase space distributions. We have generated and simulated through GSIM the distribution of the missing mass $MM(e\pi^+\pi^0X)$ corresponding to each of these reactions. We have then fitted the experimental distributions $MM(e\pi^+\pi^0X)$ with those simulated spectra. The only fitting parameters are the normalization (not the shape) of the 3-pion and 4-pion distributions. Figures 2.30, 2.31 and 2.32 show the results of these fits for the integrated distributions.

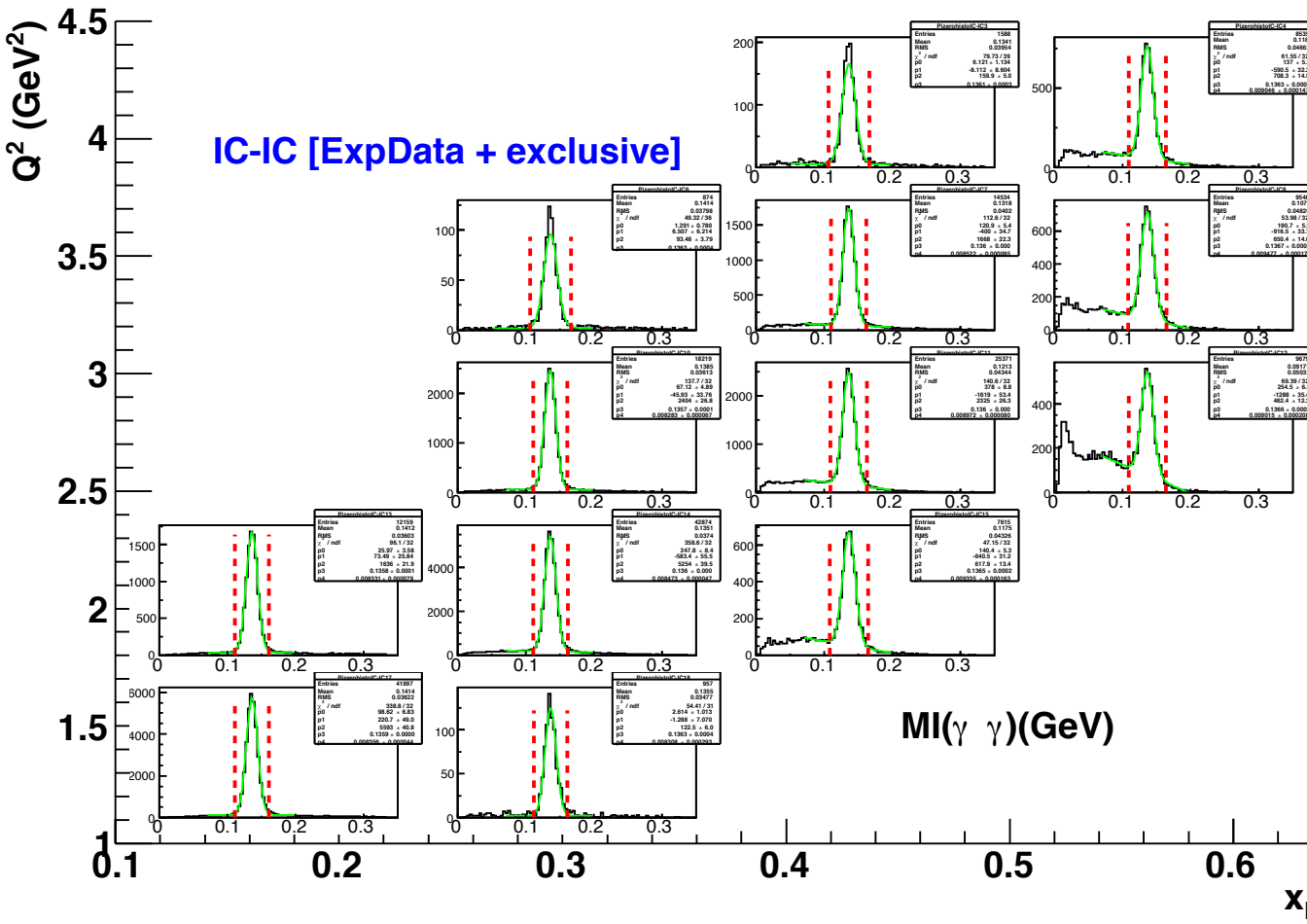


Figure 2.24: $IM(\gamma\gamma)$ for each bin (Q^2, x_B) , after selection of a missing neutron, case IC-IC.

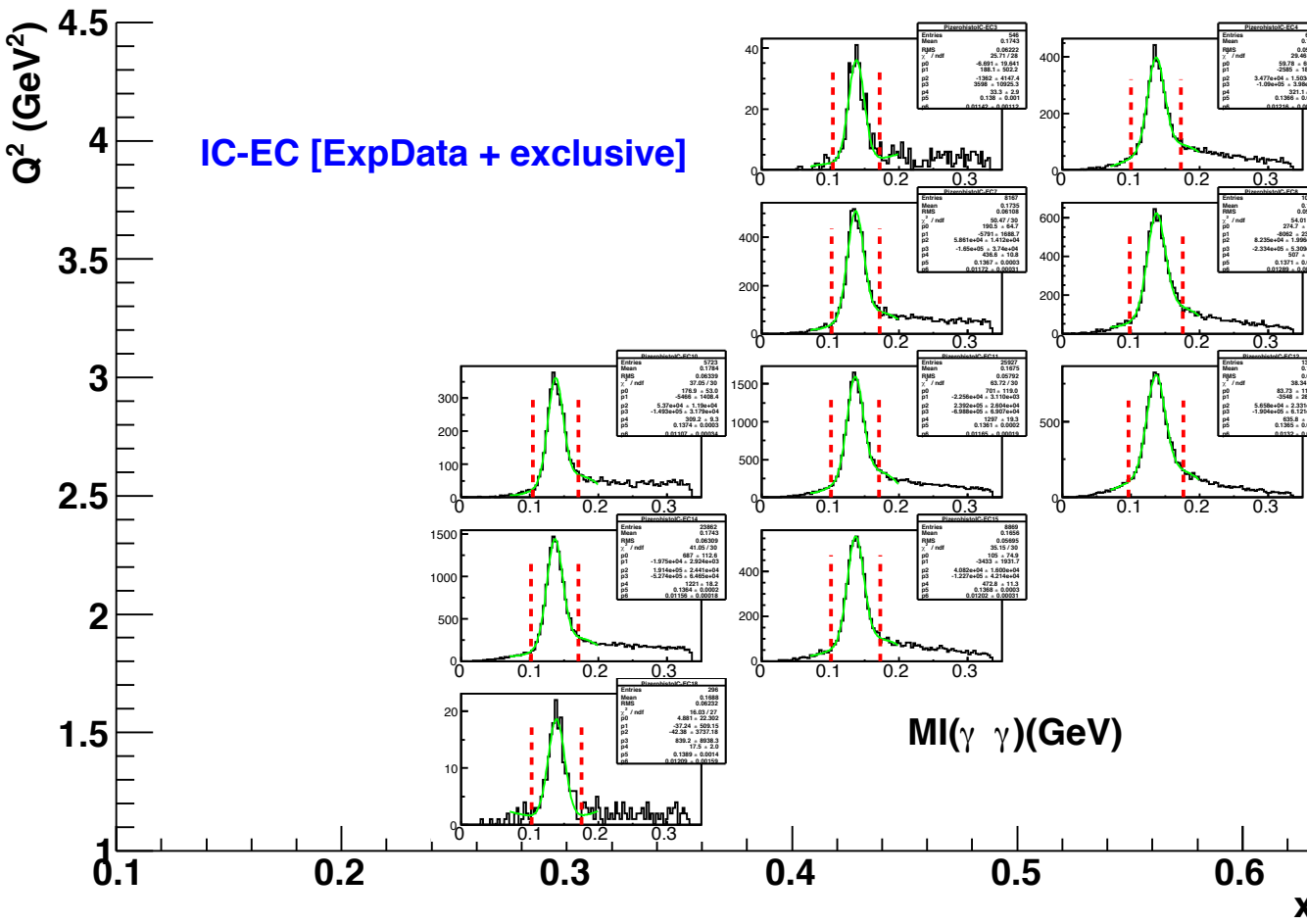


Figure 2.25: $IM(\gamma\gamma)$ for each bin (Q^2, x_B) , after selection of a missing neutron, case IC-EC. The selection cuts are represented by the red dashed lines.

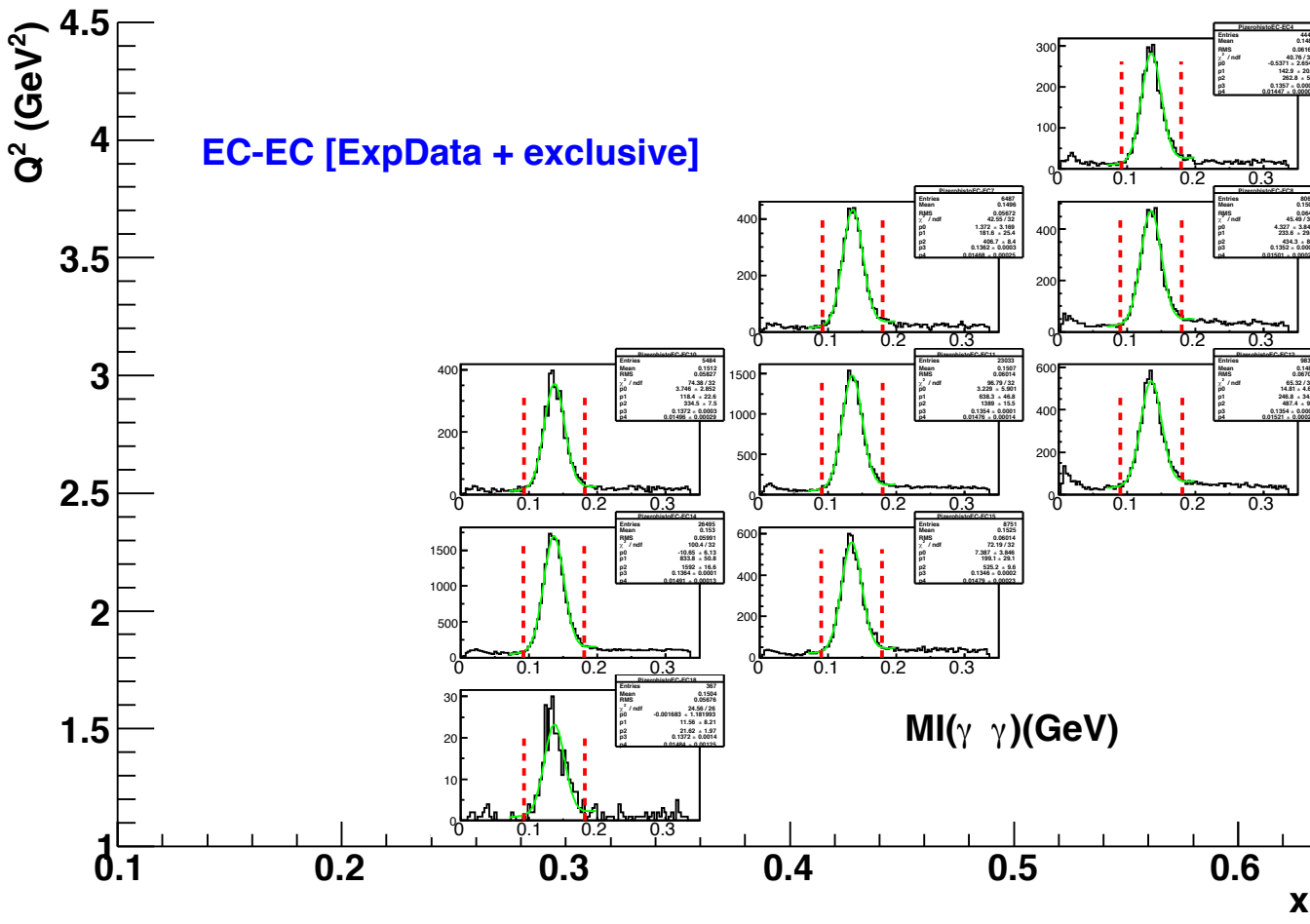


Figure 2.26: $IM(\gamma\gamma)$ for each bin (Q^2, x_B) , after selection of a missing neutron, case EC-EC. The selection cuts are represented by the red dashed lines.

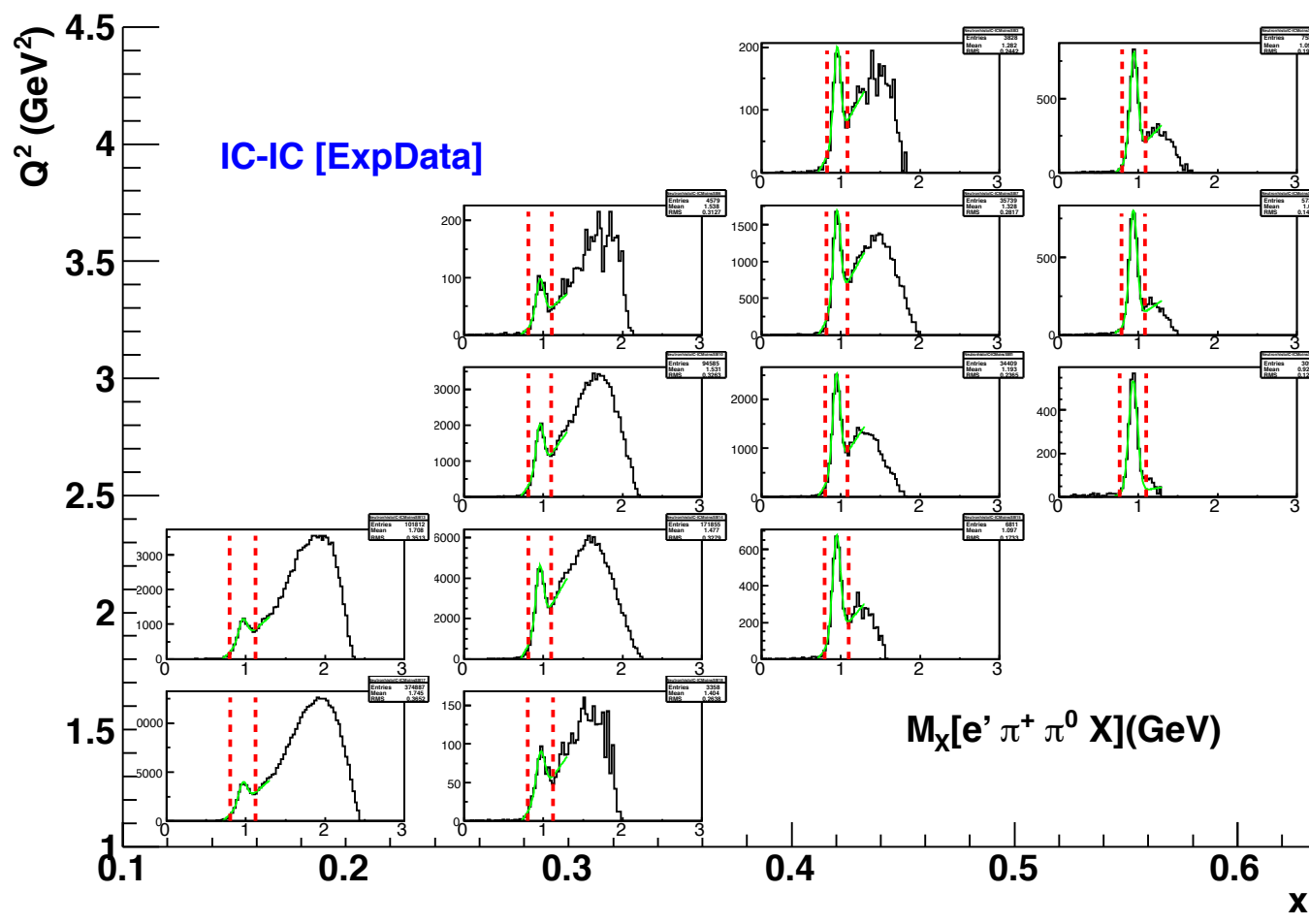


Figure 2.27: $MM(e'\pi^+\pi^0X)$ for each bin (Q^2, x_B) , case IC-IC. The selection cuts are represented by the red dashed lines.

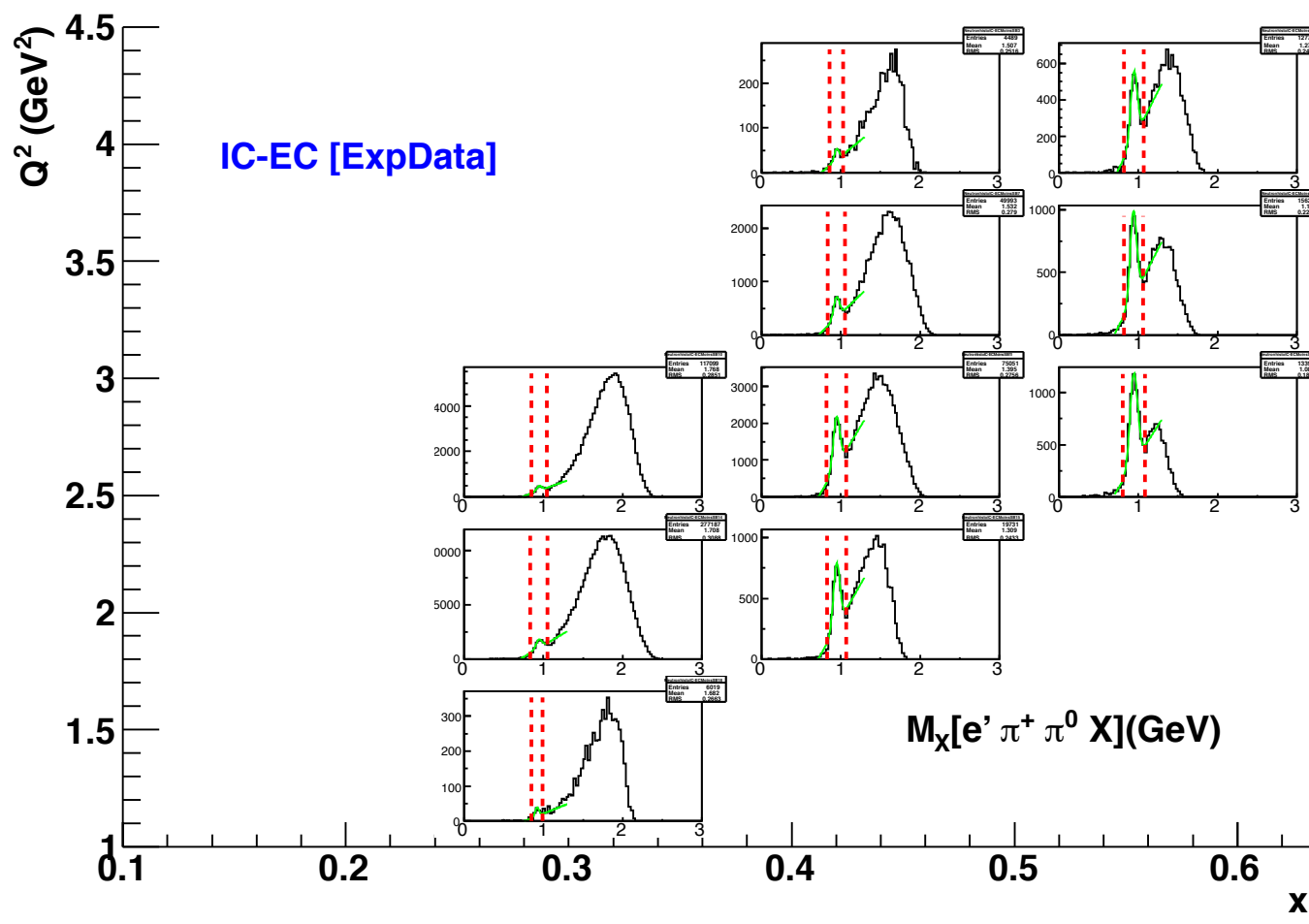


Figure 2.28: $MM(e'\pi^+\pi^0X)$ for each bin (Q^2, x_B) , case IC-EC. The selection cuts are represented by the red dashed lines.

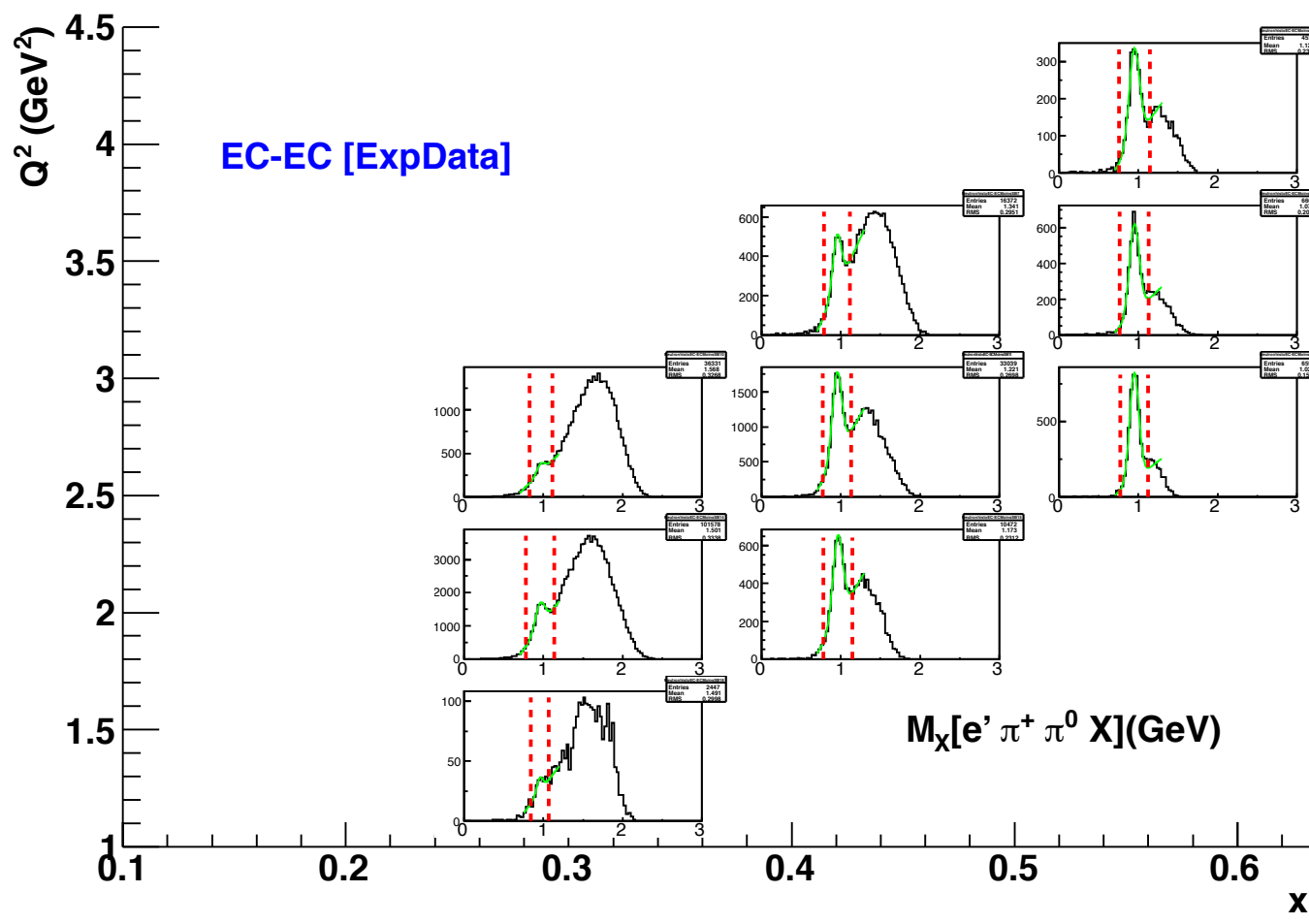


Figure 2.29: $MM(e'\pi^+\pi^0X)$ for each bin (Q^2, x_B) , case EC-EC. The selection cuts are represented by the red dashed lines.

We consider that we obtain a very reasonable description of the $MM(e\pi^+\pi^0X)$ missing mass distributions. The red spectrum shows the contribution of the non-resonant 4-pion electroproduction channels. As shown in the figures listed above, within the 3σ cut around the neutron mass, the contamination of the 4-pion channels to the neutron peak is negligible. The blue spectrum shows the contribution of the non-resonant 3-pion electroproduction channels. The contamination of these channels to the neutron peak is $\sim 9\%$ for the IC-IC case, $\sim 6\%$ for IC-EC and $\sim 15\%$ for EC-EC. At this stage, we do not subtract this background under the neutron peak. We rather consider that this $\sim 10\%$ 3-pion background will contribute to and be absorbed in the background of the subsequent $MM(\pi^+\pi^0)$ distributions, which will have to be subtracted in turn. We recall that our ultimate goal is to extract the ρ^+ cross section from the $MM(\pi^+\pi^0)$ distributions, not so much the $n\pi^+\pi^0$ cross section, and that therefore another background subtraction will be necessary.

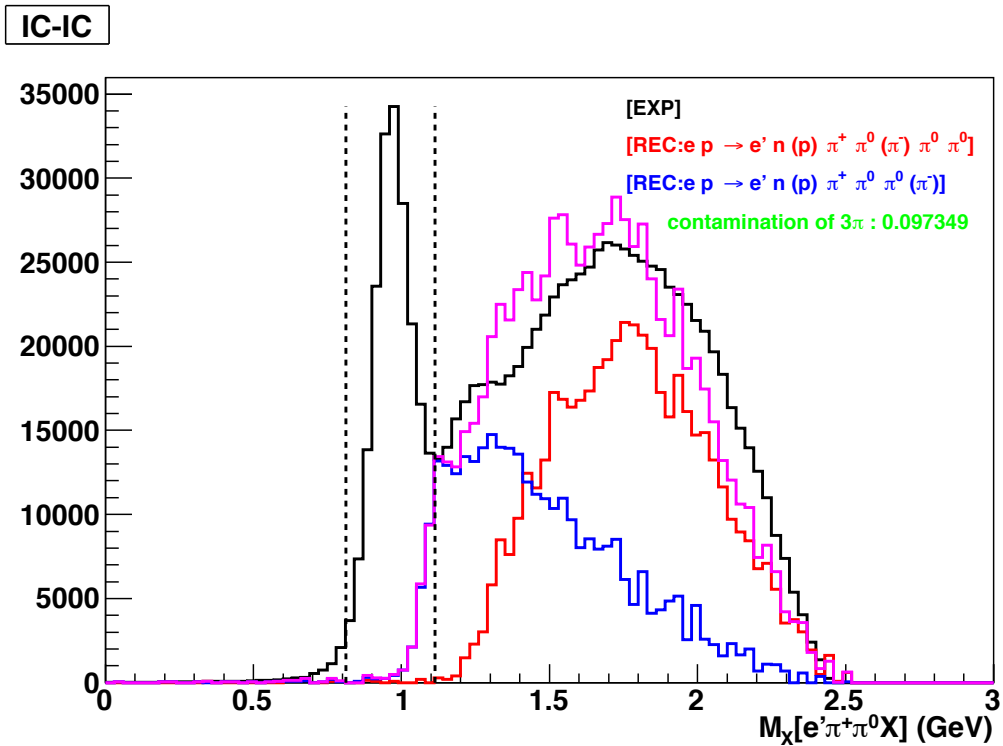


Figure 2.30: Distribution of $MM(e'\pi^+\pi^0X)$ for the $IC - IC$ configuration integrated over all our (Q^2, x_B) bins. In black, the experimental data. In blue, simulated data of the non-resonant 3-pion electroproduction channel. In red, simulated data of the non-resonant 4-pion electroproduction channel. The purple spectrum is the sum of the 3-pion and 4-pion electroproduction channels contributions.

Having selected all the particles of the final state (n, π^+, π^0), one can now construct the invariant mass of the $\pi^+\pi^0$ system. Figure 2.33 shows this $\pi^+\pi^0$ invariant mass spectrum,

IC-EC

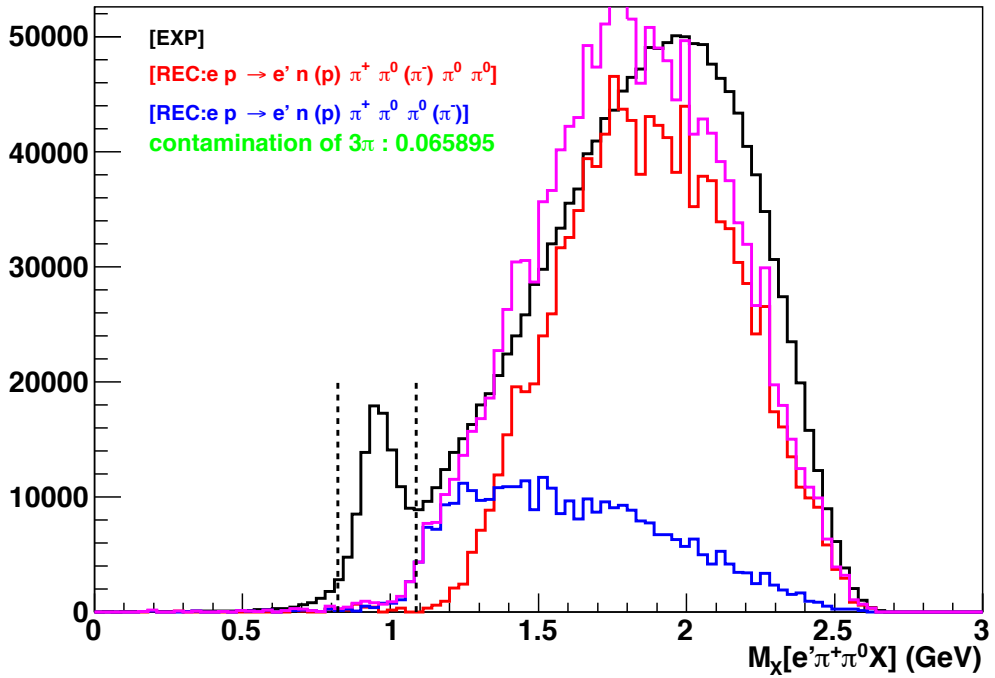


Figure 2.31: Distribution of $MM(e'\pi^+\pi^0X)$ for the $IC - EC$ configuration integrated over all our (Q^2, x_B) bins. In black, the experimental data. In blue, simulated data of the non-resonant 3-pion electroproduction channel. In red, simulated data of the non-resonant 4-pion electroproduction channel. The purple spectrum is the sum of the 3-pion and 4-pion electroproduction channels contributions.

integrated over all our statistics. One sees clearly a peak for the ρ^+ around 775 MeV. We show on figure 2.34 the $M(\pi^+\pi^0)$ spectra for each bin (Q^2, x_B) , integrated over the three configurations of the π^0 identification. These ρ^+ peaks are always well visible but are however sitting over a non-negligible non resonant 2-pion background which will have to be subtracted. In order to do this subtraction, and more generally to normalize our data, we now have to correct these spectra by the CLAS efficiency and acceptance. These studies are presented in the next section.

EC-EC

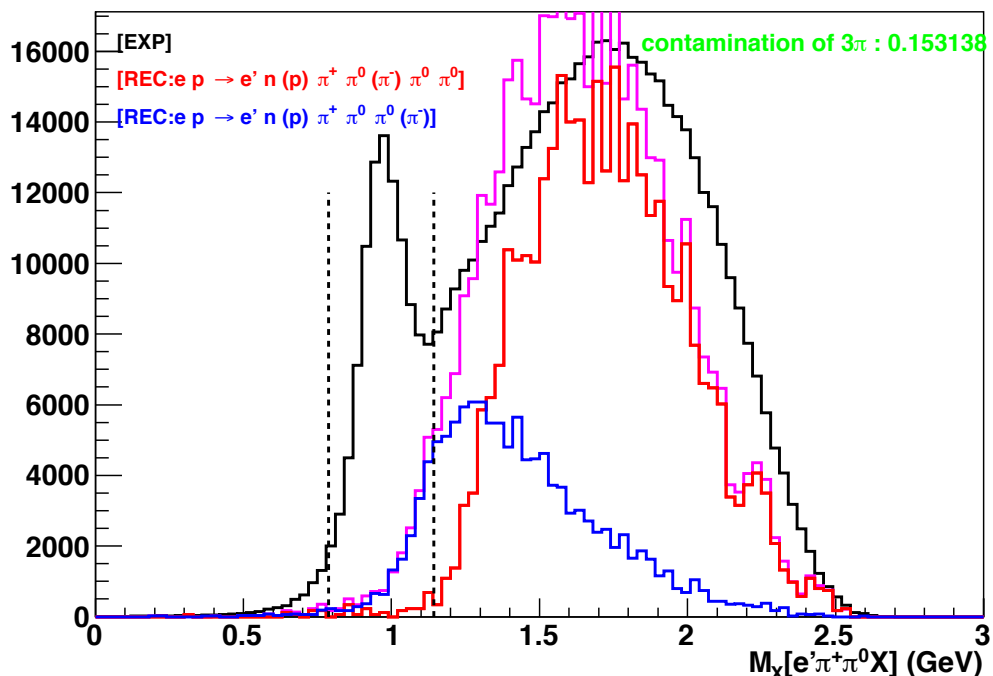


Figure 2.32: Distribution of $MM(e'\pi^+\pi^0X)$ for the $EC - EC$ configuration integrated over all our (Q^2, x_B) bins. In black, the experimental data. In blue, simulated data of the non-resonant 3-pion electroproduction channel. In red, simulated data of the non-resonant 4-pion electroproduction channel. The purple spectrum is the sum of the 3-pion and 4-pion electroproduction channels contributions.

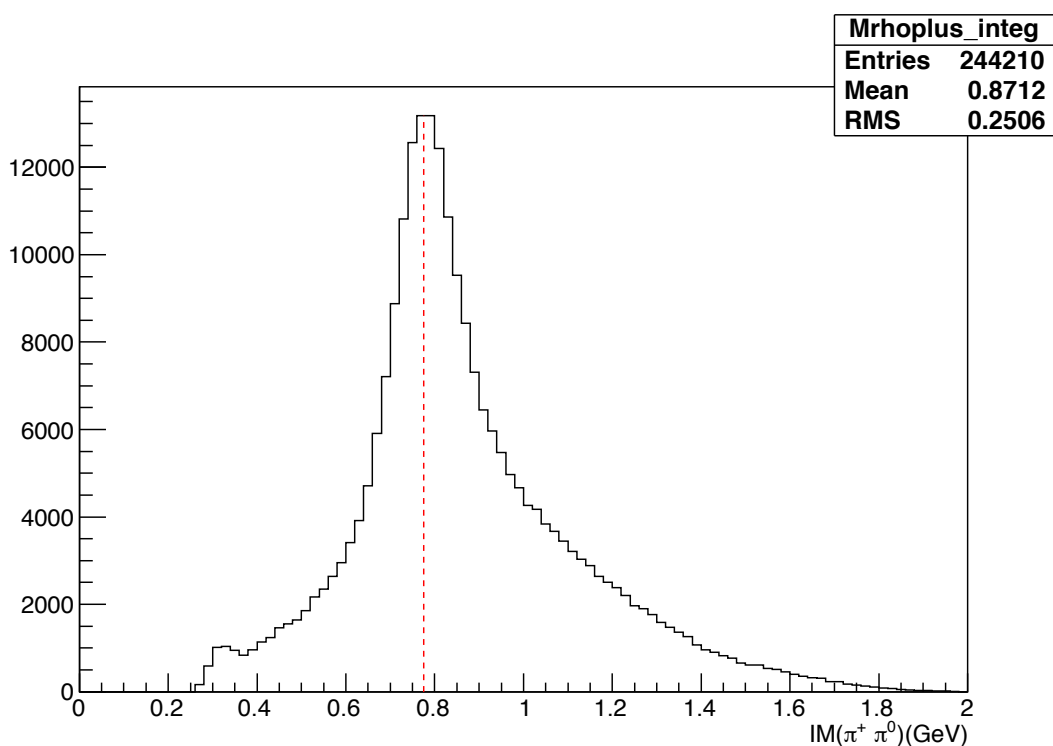


Figure 2.33: $MI(\pi^+\pi^0)$ integrated over all our data statistics. The red line shows the ρ^+ mass according to the PDG[39].

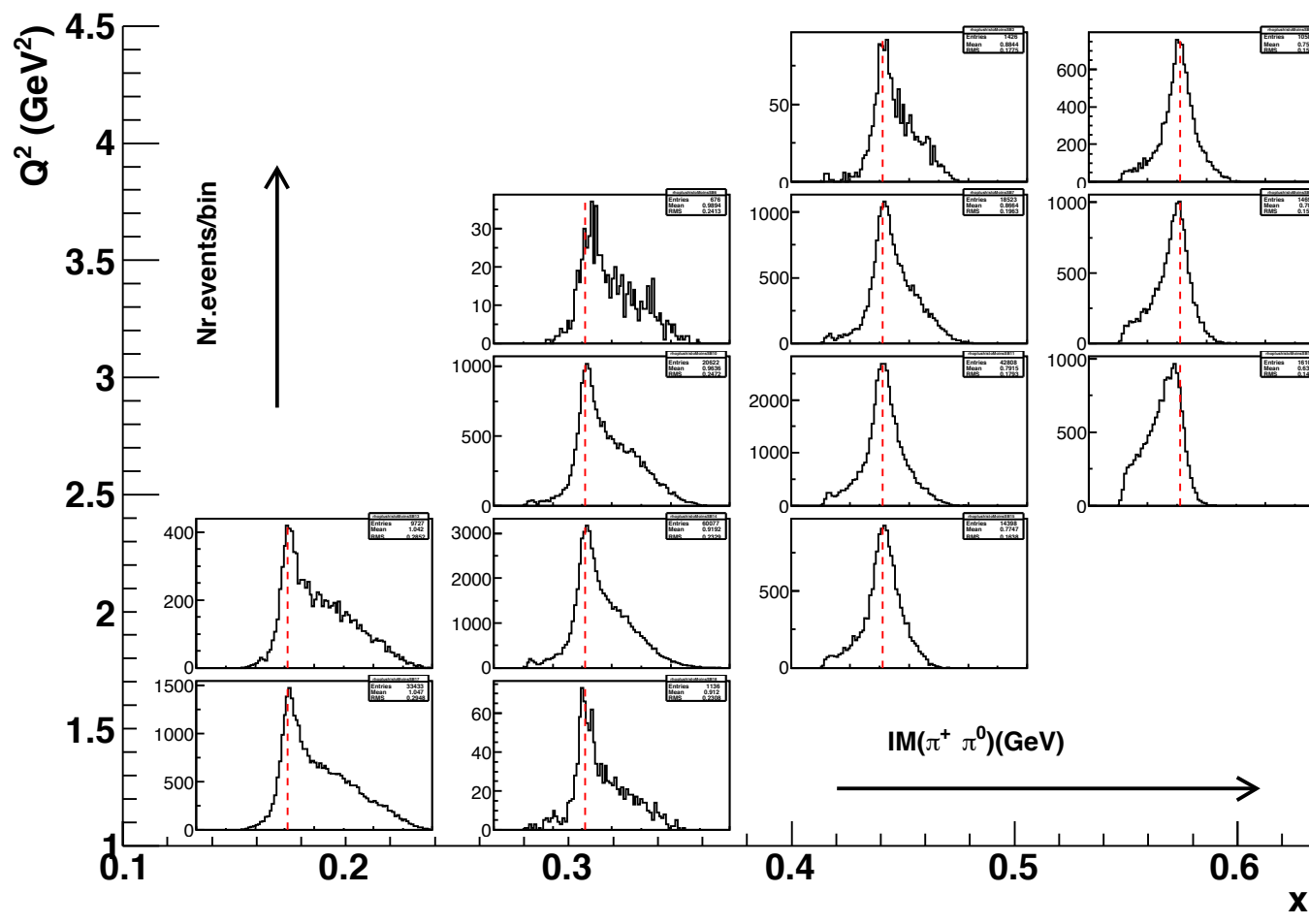
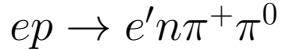


Figure 2.34: $MI(\pi^+\pi^0)$ for each bin (Q^2, x_B). The red line shows the ρ^+ mass according to the PDG[39].

2.3 Normalisation of the experimental data for the reaction



In this section, we present the different steps required to extract the total and differential cross sections of the reaction $ep \rightarrow e'n\pi^+\pi^0$. We start by presenting the kinematic domain covered by the experimental data and the adopted binning. Then, we describe the different steps of the data normalisation. We devote a separate section for each factor involved in the normalisation.

2.3.1 Binning of the kinematical phase space

As we have already seen in the first chapter, the reaction $ep \rightarrow e'n\pi^+\pi^0$ is completely described by 7 kinematical variables that we choose to be as following: Q^2 , x_B (or W), $-t$, $M_{\pi^+\pi^0}$, Φ , θ_{HS} and ϕ_{HS} . These variables are reconstructed as follows:

- The 4-momentum of the virtual photon is defined as $q = (p_e - p_{e'})$ where p_e and $p_{e'}$ are the 4-momenta of the incident and of the scattered electron respectively. $p_e = (E, 0, 0, E)$ (we neglect the electron mass) where $E = 5.776$ GeV is the electron beam energy. The Q^2 variable is then defined as $Q^2 = -q^2$.
- x_B is given by the formula: $x_B = Q^2/2m_p\nu$, where m_p is the proton mass and ν is the energy of the virtual photon in the lab, reconstructed as the difference between the energy of the scattered electron and the energy of the incident one. We can use in an equivalent way the γ^*p center of mass energy given by $W^2 = m_p^2 + Q^2(\frac{1-x_B}{x_B})$.
- t is reconstructed from the detection of the π^+ and of the π^0 (in addition to the scattered electron): $t = [(p_{\pi^+} + p_{\pi^0}) - q]^2$, where p_{π^+} et p_{π^0} are the 4-momenta of the π^+ and of the π^0 respectively.
- The leptonic plane is defined by the 3-momenta of the incident electron \vec{p}_e and the scattered one $\vec{p}_{e'}$. We reconstruct an orthogonal vector to this plane $\vec{p}_{lept} = \vec{p}_e \wedge \vec{p}_{e'}$. The hadronic plane is defined by the 3-momentum of the virtual photon \vec{q} and the one of the system ($\pi^+\pi^0$): $\vec{p}_{\pi^+\pi^0} = \vec{p}_{\pi^+} + \vec{p}_{\pi^0}$. We define an orthogonal vector to this plane $\vec{p}_{hadr} = \vec{p}_{\pi^+\pi^0} \wedge \vec{q}$. The angle Φ between the leptonic plane and the hadronic plane is then the angle between \vec{p}_{lept} and \vec{p}_{hadr} .
- To define the decaying angles of the ρ^+ , we choose the helicity frame of the ρ^+ . In this frame, where the ρ^+ is at rest, the quantization axis is chosen to be along the 3-momentum of the ρ^+ (more precisely $\vec{p}_{\pi^+} + \vec{p}_{\pi^0}$) in the center of masse frame of the γ^*p system. The decaying angles θ_{HS} and ϕ_{HS} are respectively the polar and the azimuthal angles of the π^+ in this helicity frame.

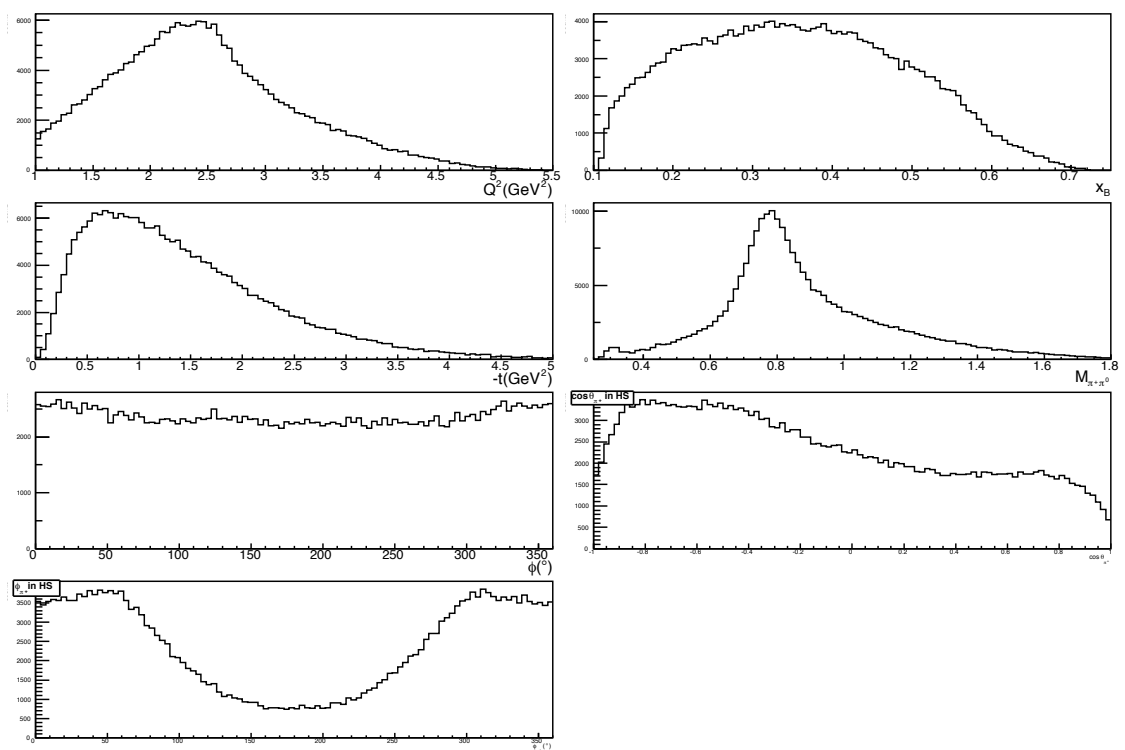


Figure 2.35: Distribution of the kinematic variables describing the reaction $ep \rightarrow e'n\pi^+\pi^0$ (experimental data).

Variable	$Q^2(GeV^2)$	x_B	$-t(GeV^2)$	$M_{\pi^+\pi^0}(GeV)$	$\Phi(deg)$	$\cos \theta_{HS}$	$\phi_{HS}(deg)$
No. of bins	5	4	4	10	5	5	5
Range	$1. \rightarrow 4.5$	$0.1 \rightarrow 0.64$	$0. \rightarrow 3.5$	$0.4 \rightarrow 1.4$	$0. \rightarrow 360.$	$-1 \rightarrow 1.$	$0. \rightarrow 360.$

Table 2.1: Binning in the 7 independent variables describing the reaction $ep \rightarrow e'n\rho^+$.

In this analysis, we will make the cut $Q^2 > 1. \text{ GeV}^2$. Figure 2.35 shows the distributions of the kinematic variables for our experimental data.

The binning in the 7 independent variables which we choose is defined in table 2.1. The choice of this binning is essentially motivated by the statistics of the experimental data. Also, the bin sizes should not be smaller than the resolution of the CLAS detector. We have estimated this resolution for the different kinematic variables, using simulation (which will be described later in this chapter). Figure 2.36 shows these resolutions (difference between reconstructed variables and generated ones) as a function of the value of the reconstructed variable. The red lines indicate the bin size of the considered variable. We notice that the size of the bins is much larger than the resolution for all the variables except for $M_{\pi^+\pi^0}$ where the size of the bins is close to the resolution of that variable. The large number of bins chosen for the variable $M_{\pi^+\pi^0}$ (compared to the other variables) is motivated (as we will see later) by the fact that we will need to make fits on the distributions of $M_{\pi^+\pi^0}$ to extract the ρ^+ signal from the $en\pi^+\pi^0$ final state. In order to have reliable fits, a large number of bins is preferable.

Figure 2.37 illustrates the kinematic phase space (Q^2, x_B) , (Q^2, t) and (x_B, t) covered by our experiment (for the final state $ep \rightarrow e'n\pi^+\pi^0$). The grid represents the binning for the considered variables. We can see on this figure that bins at the limit of the phase space are not completely filled by events. At the stage of the data normalisation, this effect will be taken into account by correction factors. If these correction factors are too big, the corresponding bins will be rejected from the analysis. Also, we did not consider parts of the phase space which have very low statistics.

2.3.2 Cross sections

The reduced cross section for the process $\gamma^*p \rightarrow n\pi^+\pi^0$ (or $\gamma^*p \rightarrow n\rho^+$) is related to the (measured) $ep \rightarrow e'n\pi^+\pi^0$ (or $ep \rightarrow e'n\rho^+$) cross section through the virtual photon flux factor Γ_V :

$$\sigma^{\gamma^*p}(Q^2, x_B) = \frac{1}{\Gamma_V(Q^2, x_B)} \frac{d^2\sigma^{ep}}{dQ^2 dx_B} \quad (2.29)$$

where Γ_V is defined by: [44]

$$\Gamma_V(Q^2, x_B) = \frac{\alpha}{8\pi} \frac{Q^2}{m_p^2 E^2} \frac{1-x_B}{x_B^3} \frac{1}{1-\epsilon} \quad (2.30)$$

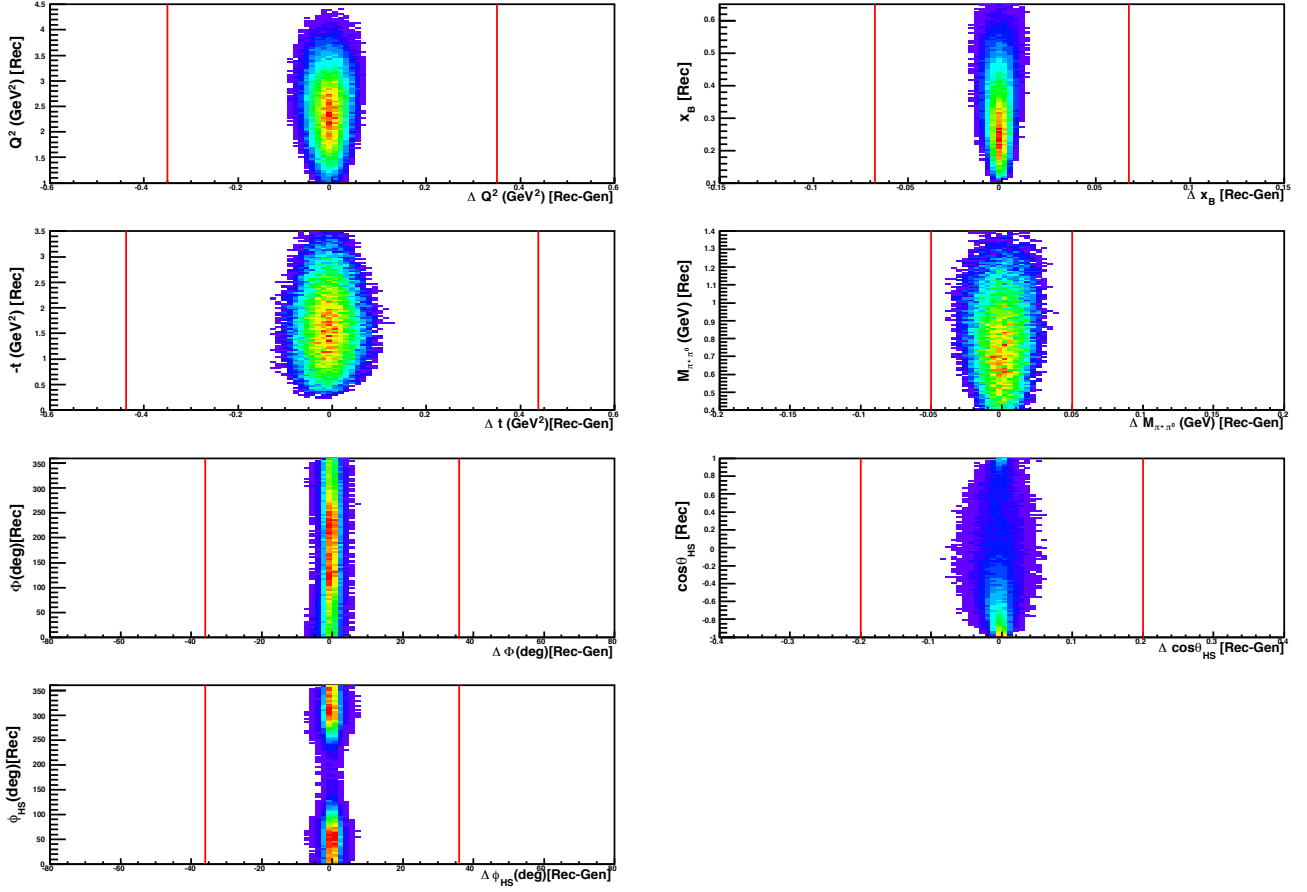


Figure 2.36: Resolution of the kinematic variables describing the reaction $ep \rightarrow e'n\pi^+\pi^0$ as a function of the reconstructed variables. The red lines indicate the bin size of the considered variable.

with ϵ the polarization parameter of the virtual photon:

$$\epsilon = \frac{1}{[1 + 2\frac{Q^2 + \nu^2}{4EE' - Q^2}]}. \quad (2.31)$$

$$(2.32)$$

α is the electromagnetic coupling constant.

For each 3-dimensional bin (Q^2, x_B, τ) (where τ designates one of the variables: $-t, M_{\pi^+\pi^0}, \Phi, \theta_{HS}, \phi_{HS}$), the differential cross section for the reaction $\gamma^* p \rightarrow n\pi^+\pi^0$ is then calculated with this formula:

$$\frac{d\sigma_{\gamma^* p \rightarrow n\pi^+\pi^0}}{d\tau} = \frac{N_{ep \rightarrow e'n\pi^+\pi^0}}{\Gamma_V(Q^2, x_B) L_{int} Acc F_h Eff_{EC} Eff_{CC} \Delta Q^2 \Delta x_B \Delta \tau F_{CorrVol} F_n} F_{rad} \quad (2.33)$$

where:

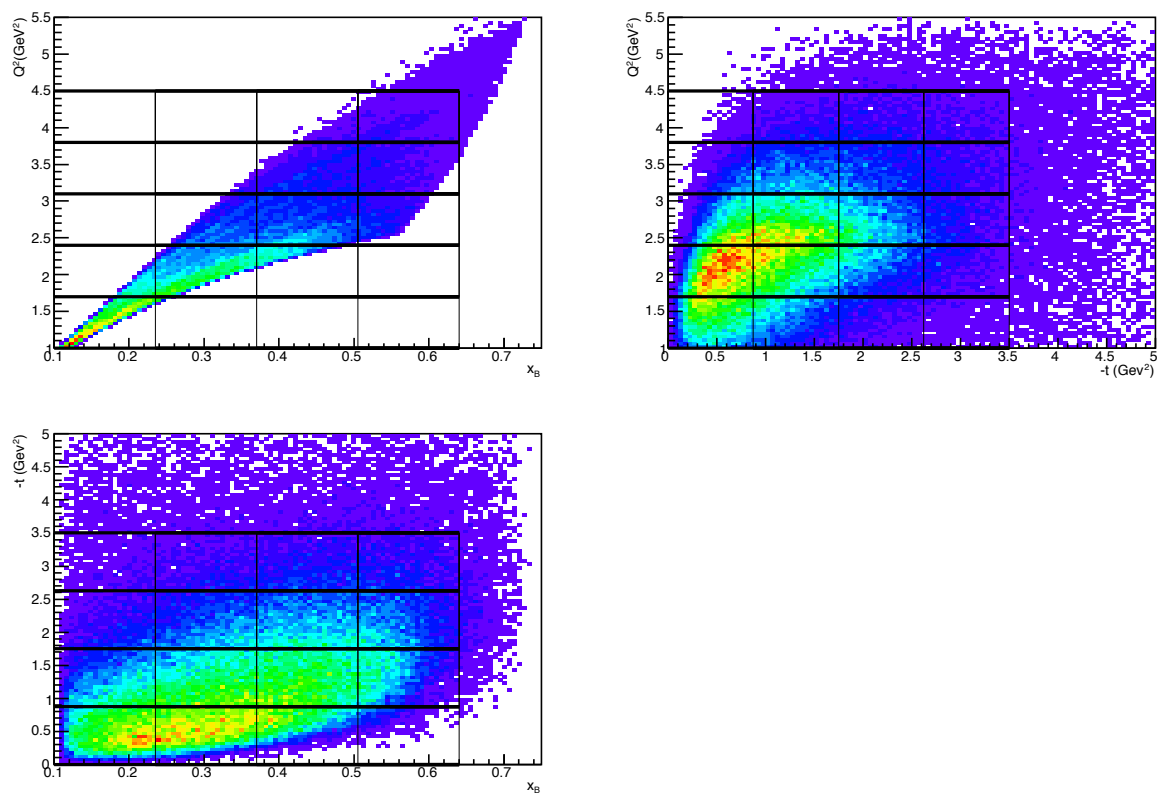


Figure 2.37: Phase spaces (Q^2, x_B) , (Q^2, t) and (x_B, t) for the experimental data corresponding to the final state $e' n \pi^+ \pi^0$.

- $N_{ep \rightarrow e'n\pi^+\pi^0}$ is the number of $e'n\pi^+\pi^0$ events detected in CLAS,
- Acc is the acceptance of the CLAS detector calculated with Monte Carlo simulation (see section 2.3.3),
- F_h is the correction factor due to "holes" in the acceptance (see section 2.3.3),
- Eff_{EC} and Eff_{CC} are, respectively, the efficiencies of the selection cuts of electrons in the electromagnetic calorimeter EC and in the Čerenkov counters. These quantities are determined from experimental data (see section 2.3.5),
- $\Delta Q^2 \Delta x_B \Delta \tau$ represents the 3-dimensional (Q^2, x_B, τ) bin volume,
- $F_{CorrVol}$ is the bin volume correction factor (see section 2.3.6),
- F_n is a correction factor for a global normalization (see section 2.3.6),
- F_{rad} is the radiative correction factor (see section 2.3.4),
- L_{int} is the integrated luminosity defined by:

$$L_{int} = \frac{l_{cible} \times \rho_{cible} \times N_A}{M_H} \times \frac{Q_{int}}{q_e} = 2.1495 \times 10^{40} cm^{-2} = 2.1495 \times 10^{10} \mu b^{-1} \quad (2.34)$$

where:

- l_{target} is the target length: $l_{target} = 2.5 \text{ cm}$,
- ρ_{target} the hydrogen density: $\rho_{target} = 0.0708 \text{ g.cm}^{-3}$,
- N_A the Avogadro constant: $N_A = 6.022 \times 10^{23} mol^{-1}$,
- M_H the molar density of hydrogen: $M_H = 1 \text{ g.mol}^{-1}$,
- Q_{int} the integrated charge during the duration of the acquisition: $Q_{int} = 32502.160156 \times 10^{-6} C$,
- and q_e the electron charge: $q_e = 1.602 \times 10^{-19} C$.

In the following sections, we will detail the various factors involved in the formula 2.33.

2.3.3 Acceptance of the CLAS detector

In order to calculate the acceptance¹, we will use a method based on Monte Carlo simulation. Firstly, we are going to describe the event generator that we used and we will show the comparison of the simulated data to the experimental ones. Then, we will detail the method we used to calculate the acceptance.

¹Here, acceptance means the pure geometrical acceptance of the detector as well as the efficiency for the detection of particles and the reconstruction of events.

The event generator and the simulations

Monte Carlo events were generated with the event generator "genev" from the Genoa group [45]. This event generator allows to generate several exclusive electroproduction reactions of mesons (including their decay for instable mesons) on the nucleon. Cross section tables for these processes are used, based on photoproduction data. In our case, there are a few data for the reactions $\gamma p \rightarrow n\pi^+\pi^0$ and $\gamma p \rightarrow n\rho^+$ [46]. In order to extrapolate to the case of electroproduction, the code multiplies the photoproduction cross sections by the virtual photon flux Γ_V and introduces ad-hoc electromagnetic form factors to obtain a reasonable Q^2 dependence for the cross sections. This code allows also to generate radiative effects calculated according to Mo and Tsai [47] (elastic approximation $ep \rightarrow ep$).

To reproduce our particular channel, we generated two reactions: $\gamma^*p \rightarrow n\rho^+$ and $\gamma^*p \rightarrow n\pi^+\pi^0$. We neglected other channels such as the production of the Δ^+ resonance: $\gamma^*p \rightarrow \pi^0\Delta^+ \hookrightarrow n\pi^+$ and the production of the Δ^0 : $\gamma^*p \rightarrow \pi^+\Delta^0 \hookrightarrow n\pi^0$. Indeed, we do not observe any prominent Δ or N^* resonances in the kinematical domain covered by our experimental data (see section 2.4.1 on the background subtraction and in particular the figures 2.57 and 2.58). Also, the method we are going to use to calculate the acceptance is relatively independent, in the limit of the bins' sizes, of the model chosen to generate events.

Monte-Carlo events were generated in a kinematical domain slightly larger than the one chosen for the binning to take into account the imprecision of the reconstruction and the "bin migration" effect (i.e when an event is generated in a certain bin and reconstructed in a slightly different one due to multiple scattering effects for example). Also, in order to save computing time, we remain close to the geometrical acceptance of the CLAS detector. To be more specific, events were generated in the kinematic domain defined by the following cuts:

- beam energy: 5.776 GeV,
- $1. \leq Q^2(\text{GeV})^2 \leq 5.4$,
- $1.4 \leq W(\text{GeV}) \leq 3.2$,
- $0.1 \leq \nu/5.776 \leq 0.95$ (the goal of these cuts is to minimise the radiative corrections),
- $12.5^\circ \leq \theta_e \leq 55^\circ$.

Once the $n\pi^+\pi^0$ events are generated, they pass through GSIM [48] which contains all geometrical and physical characteristics of all CLAS subsystems. This stage of simulation by GEANT takes a lot of time because the trajectories of the particles of the final state $e'n\pi^+\pi^0$ and their interactions with the subsystems of CLAS are simulated step by step. We processed through GSIM more than 1.2 billion events using computers farms at JLab. The simulated data were then "cooked" with the same reconstruction program as for the experimental data.

The same particle identification cuts were applied on MC data and on real data, except for the cuts related to the energy in the electromagnetic calorimeter (i.e the cuts on E_{inner} and E_{tot}/p) and on the number of photo-electrons detected in the Čerenkov counter ($Nphe$). Indeed, the simulation of electromagnetic showers in the calorimeter was truncated with a threshold of 20 MeV for all secondaries because the complete simulation of these showers would take too much computing time. Regarding the Čerenkov counters, the complex mirror geometry is not appropriately described in GSIM. We will detail in the section 2.3.5 how we determine the correction factors related to the efficiency of the cuts on EC and CC from the experimental data.

Finally, all the exclusivity cuts for the reaction $ep \rightarrow e'n\pi^+\pi^0$ were applied to the simulated data. These cuts are the cut on the $IM(\gamma\gamma)$ to select a π^0 and the cut on $M_X[e'\pi^+\pi^0X]$ to select a missing neutron. Figures 2.38, 2.39 and 2.40 show the invariant mass $IM(\gamma\gamma)$ for MC data and for real data for each (Q^2, x_B) bin, for the three topologies of the detection of photons (IC-IC, IC-EC and EC-EC). We can see that the MC data (in red) reproduce quite well the experimental data (in black) regarding the position of the π^0 peak as well as its width. The mean and the width of the π^0 peak for each (Q^2, x_B) bin for MC and experimental data are given in tables 2.2, 2.3 and 2.4

Bin Q^2	Bin x_B	$\mu[\text{Exp}](\text{GeV})$	$\mu[\text{MC}](\text{GeV})$	$\sigma[\text{Exp}](\text{GeV})$	$\sigma[\text{MC}](\text{GeV})$
1	1	0.135399	0.136089	0.008869	0.006920
2	1	0.135502	0.136157	0.008866	0.006959
1	2	0.135671	0.135994	0.008739	0.006562
2	2	0.135506	0.135972	0.008610	0.006769
3	2	0.135449	0.136078	0.008806	0.006843
4	2	0.135056	0.135989	0.010000	0.006888
2	3	0.136063	0.135877	0.008347	0.006668
3	3	0.135754	0.135885	0.008588	0.006658
4	3	0.135638	0.136005	0.008488	0.006713
5	3	0.135133	0.136172	0.010000	0.006736
3	4	0.135990	0.135776	0.008317	0.006811
4	4	0.136294	0.135811	0.008600	0.006692
5	4	0.135904	0.135938	0.008580	0.006641

Table 2.2: Mean (μ) and width (σ) of the π^0 peak for each (Q^2, x_B) bin for the experimental and MC data (IC-IC configuration).

Figures 2.41, 2.42 and 2.43 show the missing mass $M_X[e'\pi^+\pi^0X]$ for each (Q^2, x_B) bin. We can see that the MC data (in red) reproduce quite well the experimental data (in black) regarding the position of the neutron peak as well as its width. The background continuum comes essentially from the 3π and 4π production channels, as we have already seen in the particle identification section. The mean and the width of the neutron peak for each (Q^2, x_B) bin for MC and experimental data are given in tables 2.5, 2.6 and 2.7

After applying the exclusivity cuts, we can reconstruct the kinematic variables which describe the reaction $ep \rightarrow e'n\pi^+\pi^0$. Figure 2.44 shows the distribution of the kinematic

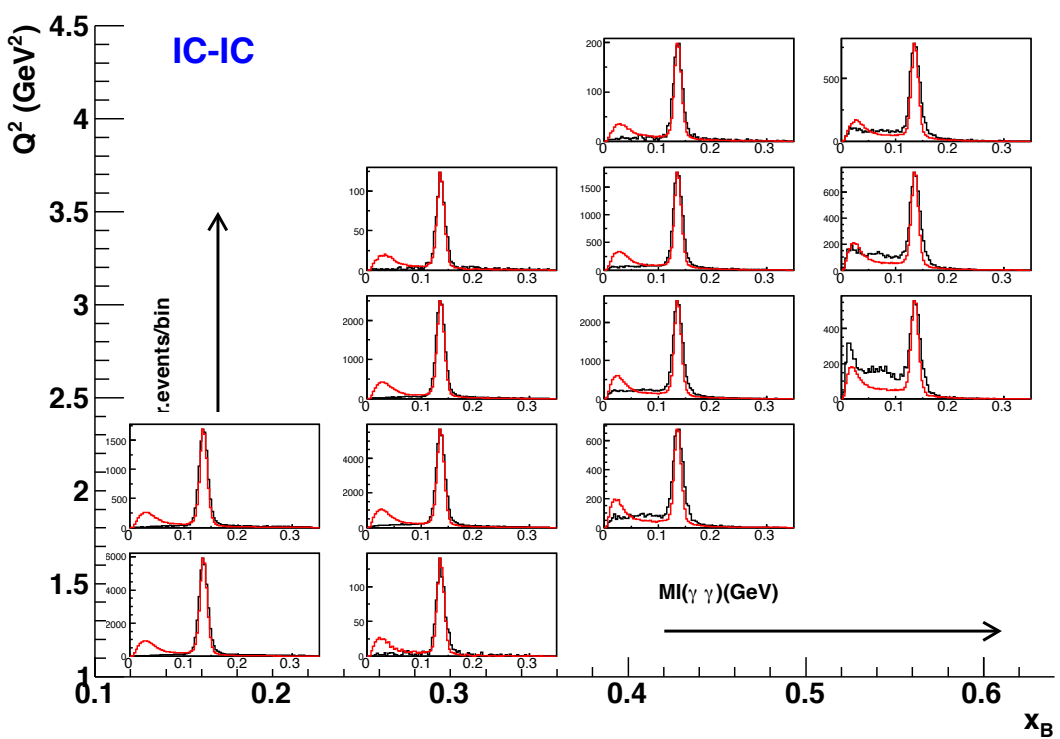


Figure 2.38: $IM(\gamma\gamma)$ for each (Q^2, x_B) bin, case IC-IC. Comparison between MC data (in red) and experimental data (in black). The simulated data have been normalised to the experimental data for comparison.

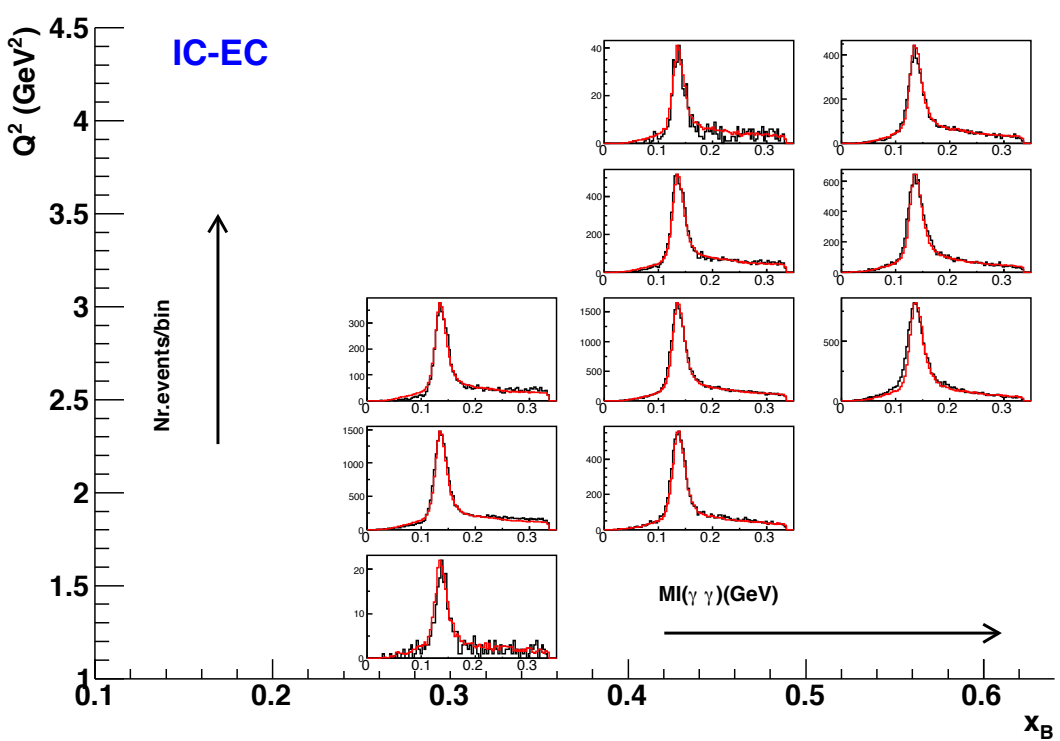


Figure 2.39: $IM(\gamma\gamma)$ for each (Q^2, x_B) bin, case IC-EC. Comparison between MC data (in red) and experimental data (in black). The simulated data have been normalised to the experimental data for comparison.

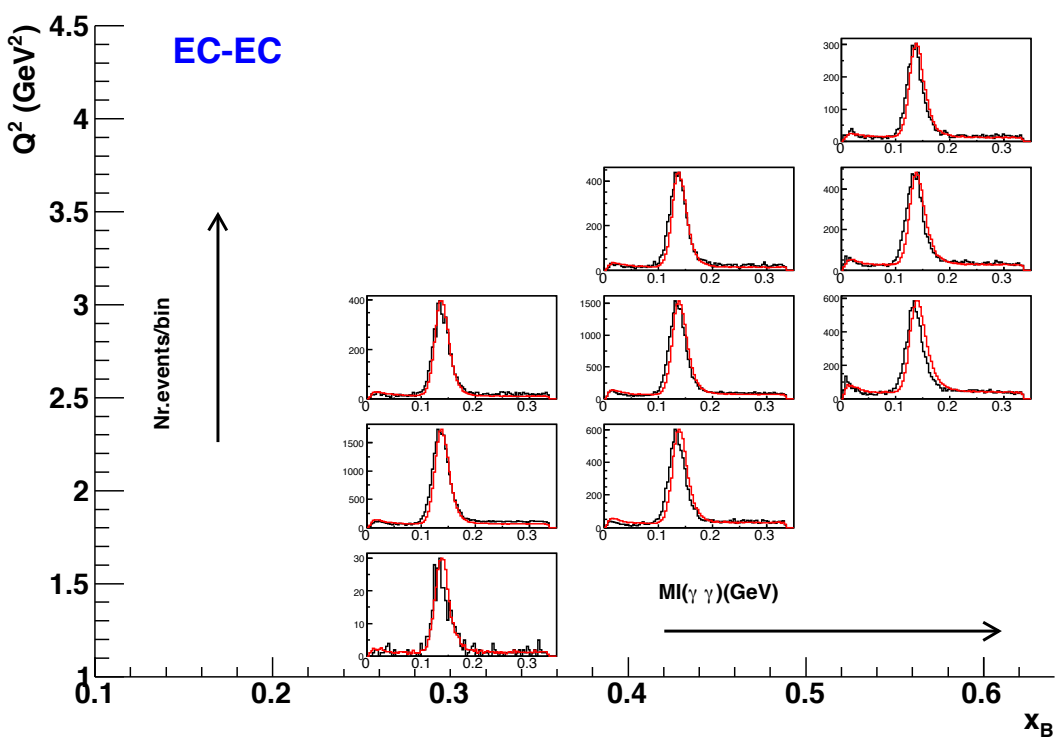


Figure 2.40: $IM(\gamma\gamma)$ for each (Q^2, x_B) bin, case EC-EC. Comparison between MC data (in red) and experimental data (in black). The simulated data have been normalised to the experimental data for comparison.

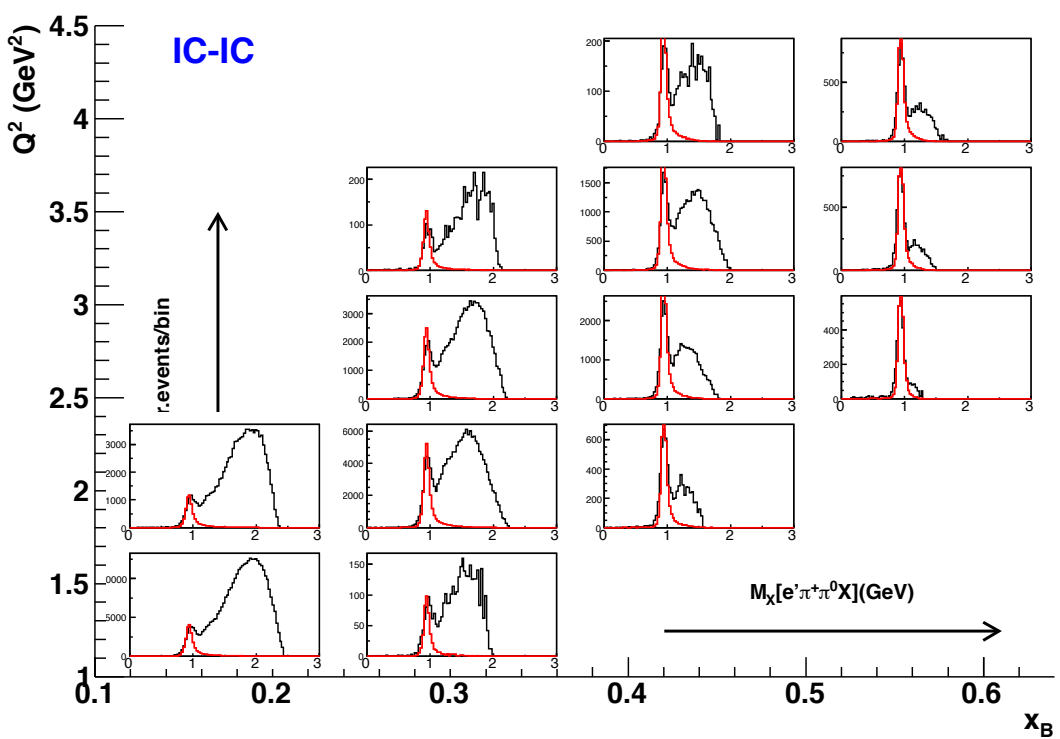


Figure 2.41: $M_X[e'\pi^+\pi^0X]$ for each (Q^2, x_B) bin, case IC-IC. Comparison between MC data (in red) and experimental data (in black). The simulated data have been normalised to the experimental data for comparison.

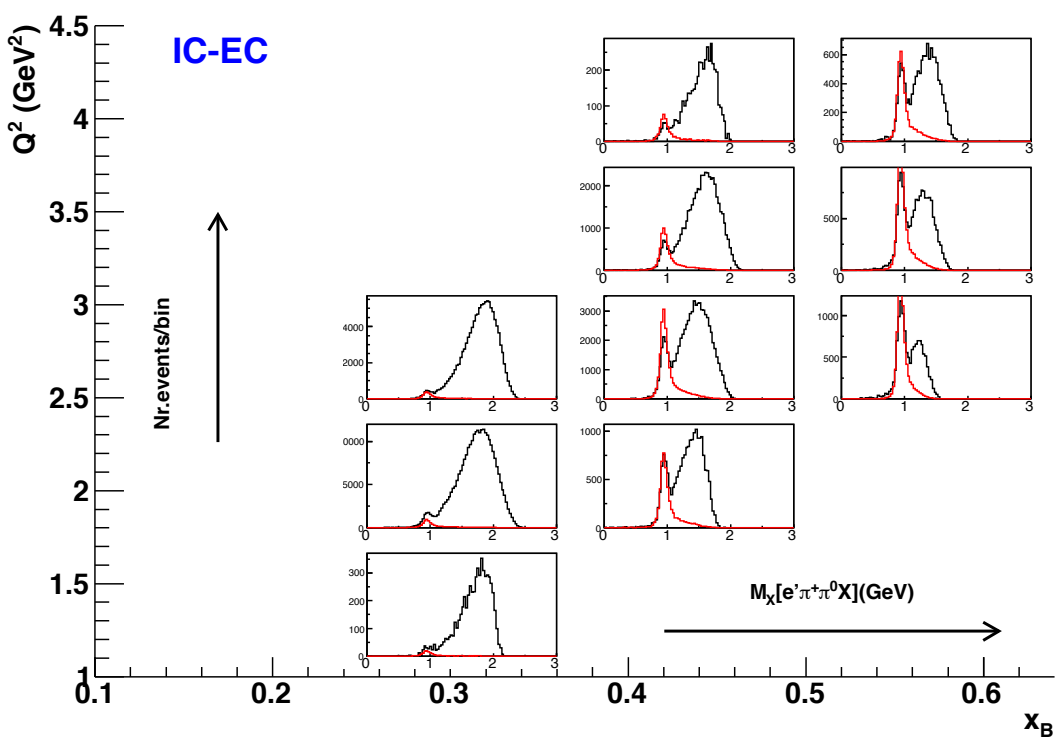


Figure 2.42: $M_X[e'\pi^+\pi^0X]$ for each (Q^2, x_B) bin, case IC-EC. Comparison between MC data (in red) and experimental data (in black). The simulated data have been normalised to the experimental data for comparison.

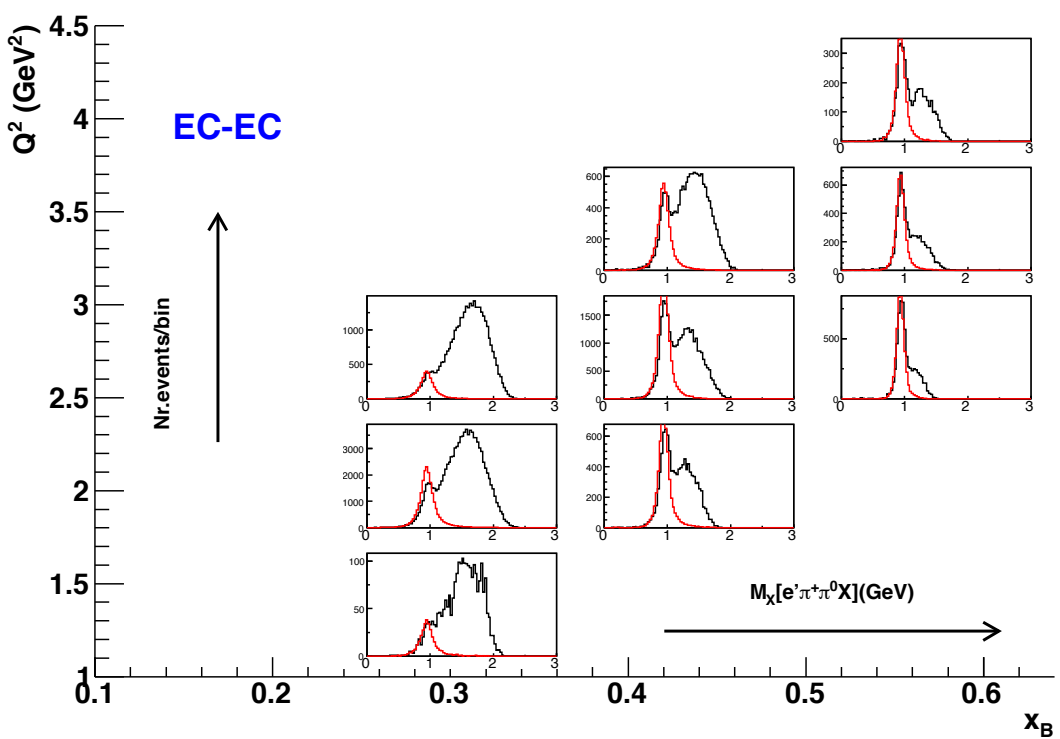


Figure 2.43: $M_X[e'\pi^+\pi^0X]$ for each (Q^2, x_B) bin, case EC-EC. Comparison between MC data (in red) and experimental data (in black). The simulated data have been normalised to the experimental data for comparison.

Bin Q^2	Bin x_B	$\mu[\text{Exp}](\text{GeV})$	$\mu[\text{MC}](\text{GeV})$	$\sigma[\text{Exp}](\text{GeV})$	$\sigma[\text{MC}](\text{GeV})$
1	1	0.135790	0.136608	0.011627	0.011666
2	1	0.136000	0.136658	0.011609	0.011413
1	2	0.135444	0.136797	0.011627	0.012041
2	2	0.135821	0.136986	0.011767	0.011537
3	2	0.136001	0.136940	0.011555	0.011441
4	2	0.136161	0.136712	0.011108	0.011150
2	3	0.136028	0.138331	0.011891	0.012187
3	3	0.135705	0.137906	0.012044	0.011789
4	3	0.136010	0.137368	0.011676	0.011425
5	3	0.136487	0.137382	0.011503	0.011388
3	4	0.135811	0.139609	0.013563	0.012861
4	4	0.136180	0.138569	0.012952	0.012302
5	4	0.136036	0.138121	0.011726	0.012112

Table 2.3: Mean (μ) and width (σ) of the π^0 peak for each (Q^2, x_B) bin for the experimental and MC data (IC-EC configuration).

variables for MC data compared to the real data. By adjusting the weight of the two channels that we considered ($n\rho^+$ et $n\pi^+\pi^0$), we manage to reproduce in a reasonable way the distributions of the real data except for the $-t$ variable where the MC data does not have exactly the same slope as the experimental data.

The physical processes leading to the final state $e'n\pi^+\pi^0$ are numerous, diverse, and interfere with each other. There is no model to this date which describes in details this final state in our kinematic regime and we should not expect to reproduce our experimental data with our simple event generator which just sums two contributions ($n\rho^+$ and $n\pi^+\pi^0$ phase space) with the relative weight adjusted "by hand".

As we are going to calculate the acceptance of the CLAS detector using a "bin by bin" method, the agreement between real data and MC data is not crucial in principle. In this method, we calculate for each 7-dimensional bin the ratio between the number of reconstructed events and generated ones. In the limit of very small bins, the acceptance calculated in this way is independent of the particular model used in the event generator. Nevertheless, in practice, it is difficult to have bins as small as we would wish because the number of generated events (and thus reconstructed) is limited because of the huge computing time needed for the simulation by GEANT. As we are going to extract 3- or 4-fold differential cross sections, it will be necessary to make an integration over certain variables (there are 7 independent ones). This integration leads then to a certain dependence on the model. We are looking here for a compromise: although our method of acceptance correction is model-independent to a great extent in principle, it is advisable in practice, to have an event generator which reproduces the general trends of the real data in order to minimize some systematic errors.

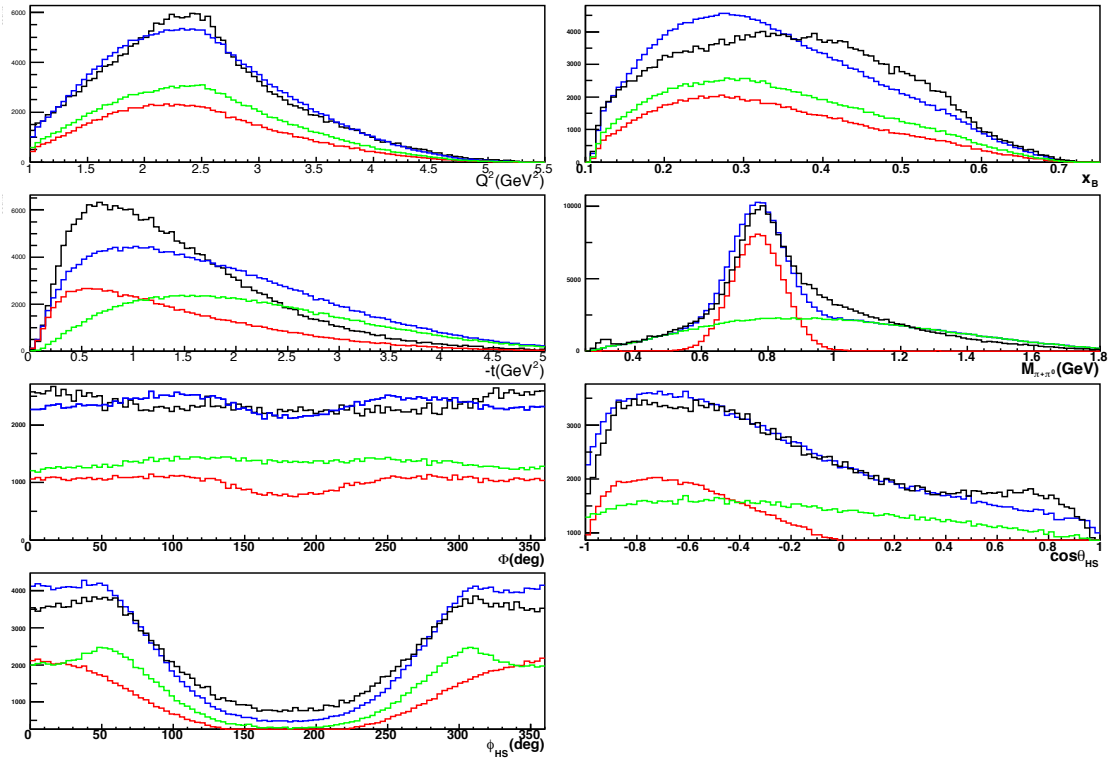


Figure 2.44: Distributions of the kinematical variables. The experimental data are shown in black. The simulated data (reconstructed) are shown in blue. The individual contributions of the $n\rho^+$ channel are in red and of the phase space $n\pi^+\pi^0$ in green. The simulated data have been normalised to the real data for comparison.

Bin Q^2	Bin x_B	$\mu[\text{Exp}](\text{GeV})$	$\mu[\text{MC}](\text{GeV})$	$\sigma[\text{Exp}](\text{GeV})$	$\sigma[\text{MC}](\text{GeV})$
1	1	0.135573	0.138424	0.014368	0.012891
2	1	0.135507	0.138409	0.014371	0.013059
1	2	0.135195	0.138897	0.014925	0.012879
2	2	0.135138	0.139179	0.014547	0.013200
3	2	0.135434	0.138952	0.014184	0.013143
4	2	0.134804	0.139107	0.014485	0.013194
2	3	0.134612	0.140421	0.014872	0.013560
3	3	0.135110	0.140204	0.014873	0.013529
4	3	0.135189	0.139538	0.014288	0.013266
5	3	0.134660	0.139396	0.013888	0.013221
3	4	0.135438	0.142342	0.015462	0.014419
4	4	0.134975	0.141024	0.014902	0.013895
5	4	0.134903	0.140415	0.013912	0.013572

Table 2.4: Mean (μ) and width (σ) of the π^0 peak for each (Q^2, x_B) bin for the experimental and MC data (EC-EC configuration).

Acceptance calculation

For each seven-dimensional bin $(Q^2, x_B, -t, M_{\pi^+\pi^0}, \Phi, \theta_{HS}, \phi_{HS})$ the CLAS acceptance is calculated as:

$$Acc(Q^2, x_B, -t, M_{\pi^+\pi^0}, \Phi, \theta_{HS}, \phi_{HS}) = \frac{Rec(Q^2, x_B, -t, M_{\pi^+\pi^0}, \Phi, \theta_{HS}, \phi_{HS})}{Gen(Q^2, x_B, -t, M_{\pi^+\pi^0}, \Phi, \theta_{HS}, \phi_{HS})} \quad (2.35)$$

where $Rec(Q^2, x_B, -t, M_{\pi^+\pi^0}, \Phi, \theta_{HS}, \phi_{HS})$ is the number of reconstructed events in this bin and $Gen(Q^2, x_B, -t, M_{\pi^+\pi^0}, \Phi, \theta_{HS}, \phi_{HS})$ is the number of generated events. The corresponding statistical error is:

$$\Delta(Acc) = \frac{\Delta(Rec)}{Gen} = \sqrt{\frac{Acc(1 - Acc)}{Gen}} \quad (2.36)$$

The acceptances are of the order of a few percents. The integrated acceptances (not the ones used in the cross section extraction, since we do the correction bin by bin) are shown in figure 2.45.

Cut on the acceptance

Figure 2.46 shows the distribution of the relative error $\Delta(Acc)/Acc$ for all the 7-D bins (of course for which $Acc \neq 0$). A cut of 30% (red dashed line) was made in order to avoid bins with high statistical errors on the acceptance. Indeed, an elementary bin with a very small number of accepted events will yield a very high weight, which may lead to anomalies in resulting distributions.

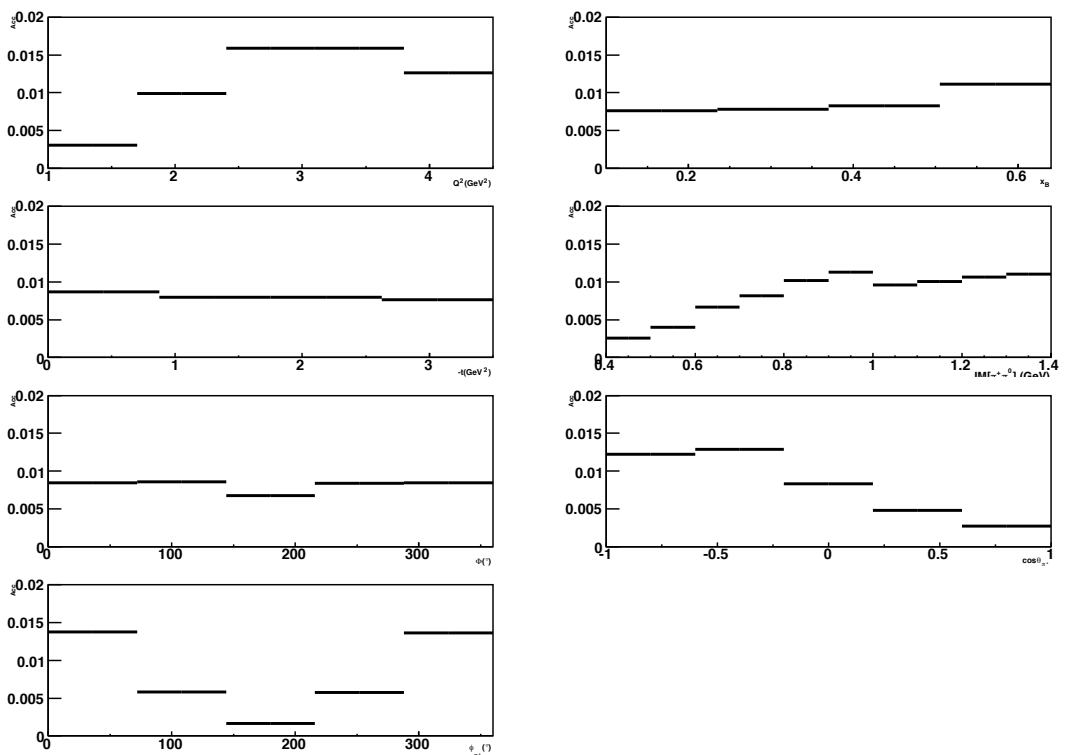


Figure 2.45: Acceptances as a function of each of the 7 kinematic variable, each one integrated over the other 6 variables.

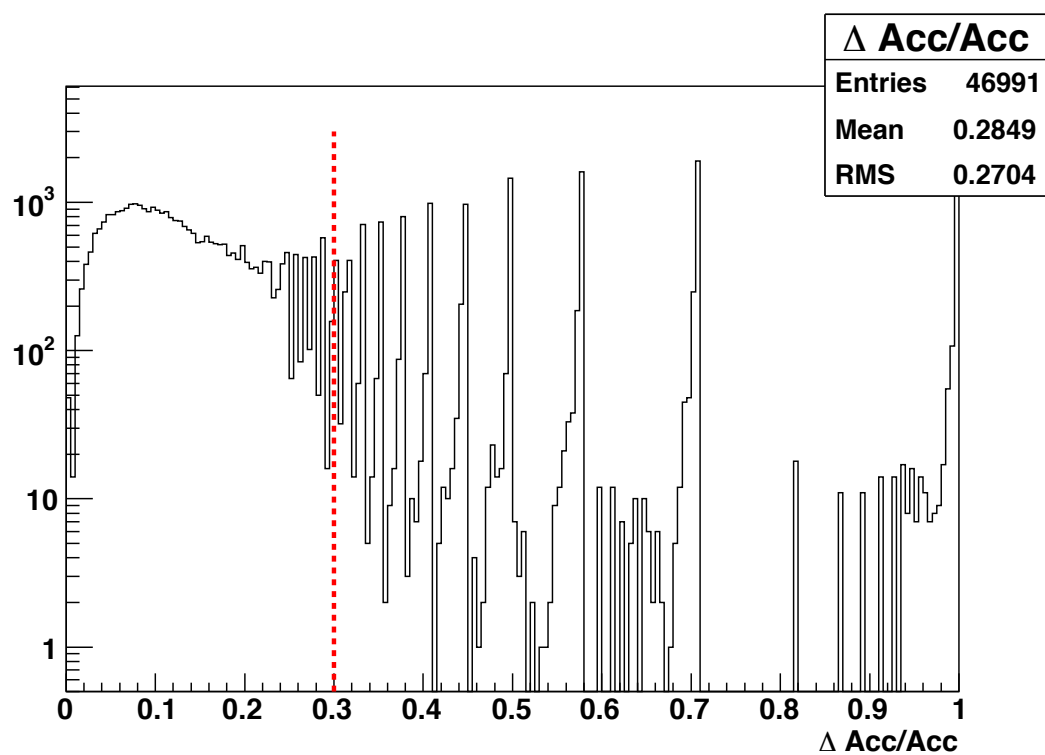


Figure 2.46: Distribution of the relative error $\Delta(\text{Acc})/\text{Acc}$ for the 7-D bins. The dashed-red line shows the cut applied on $\Delta(\text{Acc})/\text{Acc}$

Bin Q^2	Bin x_B	$\mu[\text{Exp}](\text{GeV})$	$\mu[\text{MC}](\text{GeV})$	$\sigma[\text{Exp}](\text{GeV})$	$\sigma[\text{MC}](\text{GeV})$
1	1	0.961318	0.941411	0.053709	0.056515
2	1	0.960241	0.940291	0.054161	0.055143
1	2	0.964065	0.946405	0.053161	0.048783
2	2	0.953257	0.945046	0.047419	0.048789
3	2	0.955814	0.943022	0.047605	0.049567
4	2	0.958402	0.941879	0.049436	0.050781
2	3	0.946456	0.948429	0.049723	0.042436
3	3	0.944631	0.947044	0.045951	0.043161
4	3	0.950475	0.945150	0.044472	0.044834
5	3	0.952777	0.943188	0.043057	0.043441
3	4	0.935179	0.945266	0.055574	0.042405
4	4	0.937090	0.947010	0.048402	0.042289
5	4	0.944495	0.945774	0.048037	0.042980

Table 2.5: Mean (μ) and width (σ) of the neutron peak for each (Q^2, x_B) bin for the experimental and MC data (IC-IC configuration).

"Hole factor"

In principle, by weighting the number of reconstructed events with the inverse of the acceptance in a bin X of dimension n :

$$\text{Corr}(X) = \int \frac{\text{Rec}(X, y, z \dots)}{\text{Acc}(X, y, z, \dots)} dy dz d\dots \quad (2.37)$$

where $\text{Corr}(X)$ is the number of weighted events in the bin X and y, z, \dots are the kinematic variables which are integrated over, one should recover the initially generated distributions. However, when one performs this sum, some kinematic bins have zero acceptance ("hole") and therefore $\text{Rec}(X, y, z \dots) = 0$. Consequently, these bins are not taken into account in the integral. Hence, there is a difference with the number of generated events in the same bin X given by:

$$\text{Gen}(X) = \int \text{Gen}(X, y, z \dots) dy dz d\dots \quad (2.38)$$

In general, these "holes" in the acceptance are either due to the limited statistics of the simulations or to the small acceptance in certain kinematic regions. The cut that we make on the error on the acceptance actually increases the number of such holes.

To solve this problem of "holes", we correct the acceptance by a factor which we name "hole factor", F_h , defined as:

$$F_h(X) = \frac{\text{Corr}(X)}{\text{Gen}(X)} \quad (2.39)$$

where $\text{Corr}(X)$ and $\text{Gen}(X)$ are defined with the equations 2.37 and 2.38 respectively.

Bin Q^2	Bin x_B	$\mu[\text{Exp}](\text{GeV})$	$\mu[\text{MC}](\text{GeV})$	$\sigma[\text{Exp}](\text{GeV})$	$\sigma[\text{MC}](\text{GeV})$
1	1	-	0.954355	-	0.072523
2	1	-	0.954809	-	0.073137
1	2	0.920049	0.952779	0.023168	0.070707
2	2	0.943783	0.951799	0.036858	0.064511
3	2	0.945338	0.952770	0.032648	0.065725
4	2	-	0.950556	-	0.067993
2	3	0.946798	0.948306	0.040139	0.060004
3	3	0.945464	0.948519	0.041080	0.058376
4	3	0.945151	0.950889	0.036401	0.061384
5	3	0.946023	0.948386	0.028420	0.062911
3	4	0.943888	0.943773	0.047562	0.054880
4	4	0.938667	0.946149	0.040548	0.055666
5	4	0.945633	0.947612	0.040828	0.055798

Table 2.6: Mean (μ) and width (σ) of the neutron peak for each (Q^2, x_B) bin for the experimental and MC data (IC-EC configuration).

To summarize, our "bin by bin" method to calculate the acceptance is an "hybrid" method. On the one hand, we normalize event by event the experimental data with a 7-dimensional acceptance. On the other hand, as we do not calculate 7-times differential cross sections but rather 2-, 3- or 4-times differential cross sections (we integrate over the remaining kinematical variables), we correct with a 2-, 3- or 4-dimensional hole factor F_h . This integration is sensitive to the holes in the 7-dimensional acceptance which we have to correct for with the hole factor.

Figure 2.47 shows the hole factor as a function of the invariant mass $M_{\pi^+\pi^0}$ for each (Q^2, x_B) bin. We can notice that the hole factor is in general constant for the central values of the $M_{\pi^+\pi^0}$ (around the ρ^+ peak). In this region, it is in general of the order of 80% which means that the bin-by-bin correction method reconstructs the generated events at the level of $\sim 80\%$. The hole factor decreases at the edges of the $M_{\pi^+\pi^0}$ spectra, which is due to the fact that we are at the limit of the kinematical phase space of the bin (and therefore the statistics of the simulated events is lower than elsewhere).

The figures illustrating the 4-dimensional hole factors $F_h(M_{\pi^+\pi^0}, Q^2, x_B, t)$, $F_h(M_{\pi^+\pi^0}, Q^2, x_B, \Phi)$, $F_h(M_{\pi^+\pi^0}, Q^2, x_B, \phi_{HS})$ and $F_h(M_{\pi^+\pi^0}, Q^2, x_B, \cos \theta_{HS})$ are presented, respectively, in the appendices A, B, C and D.

Acceptance weighting of experimental data

The experimental data are analysed event by event. Each event (which belongs to a 7-dimensional bin k) is weighted with the corresponding 7-dimensional acceptance Acc_k . If N_k is the number of events contained in a bin k , NC_k , the weighted number of events in

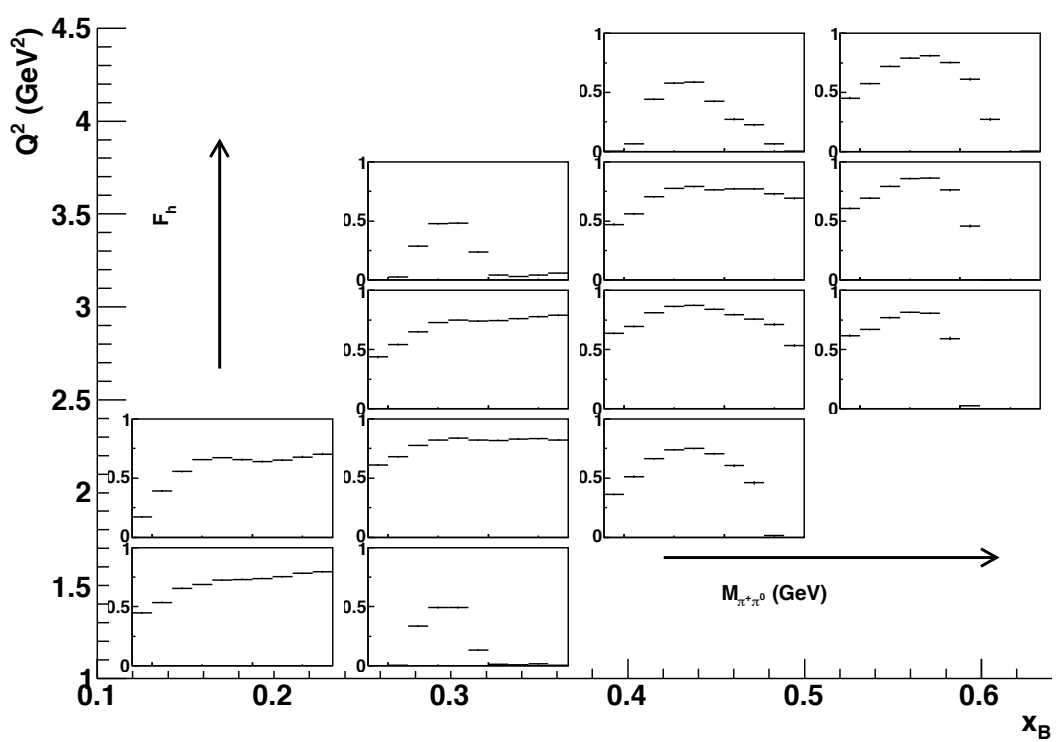


Figure 2.47: The hole factor as a function of $M_{\pi^+\pi^0}$ for each (Q^2, x_B) bin.

Bin Q^2	Bin x_B	$\mu[\text{Exp}](\text{GeV})$	$\mu[\text{MC}](\text{GeV})$	$\sigma[\text{Exp}](\text{GeV})$	$\sigma[\text{MC}](\text{GeV})$
1	1	-	0.951286	-	0.098758
2	1	-	0.951084	-	0.099910
1	2	0.954856	0.944541	0.037957	0.090566
2	2	0.958375	0.946823	0.059600	0.090040
3	2	0.966670	0.947731	0.048048	0.092124
4	2	-	0.946010	-	0.091303
2	3	0.962928	0.940934	0.061900	0.074299
3	3	0.951880	0.942694	0.059563	0.077054
4	3	0.951523	0.943050	0.053415	0.083527
5	3	-	0.941179	-	0.082015
3	4	0.949782	0.934662	0.058078	0.062893
4	4	0.949946	0.938056	0.061668	0.067870
5	4	0.949506	0.939075	0.064870	0.072085

Table 2.7: Mean (μ) and width (σ) of the neutron peak for each (Q^2, x_B) bin for the experimental and MC data (EC-EC configuration).

the same bin k will be:

$$NC_k = \frac{N_k}{Acc_k}. \quad (2.40)$$

The statistical error for NC_k is given by:

$$\Delta^2(NC_k) = \frac{\Delta^2(N_k)}{Acc_k^2} + N_k^2 \frac{\Delta^2(Acc_k)}{Acc_k^4} \quad (2.41)$$

with $\Delta(N_k) = \sqrt{N_k}$, the statistical error associated to N_k and $\Delta(Acc_k)$ is defined by the formula 2.36.

We call N_i the weighted number of events contained in a bin i of dimension < 7 . N_i is then given by:

$$N_i = \sum_k NC_k \quad (2.42)$$

where the sum is over all the 7-dimensional bins contained in the bin i .

The statistical error for N_i is then given by:

$$\Delta^2(N_i) = \sum_k \Delta^2(NC_k) \quad (2.43)$$

2.3.4 Radiative correction

Because of their small masses, electrons can radiate photons. These photons, most of them of low energy, are not detected ("soft photons") but carry a fraction of the momentum and

the energy of the initial electron. Our experimental data contain such kind of soft photons and so the effective reaction we are analysing contains some $ep \rightarrow e'n\pi^+\pi^0\gamma$ events. The effect of these photons shows up when we calculate the missing mass $M_X[e'\pi^+\pi^0X]$ as a tail at the right of the neutron peak.

This radiative effect was introduced in our event generator using the formula of Mo and Tsai [47]. We can see the radiative tail in figure 2.48. In this figure, we can see the

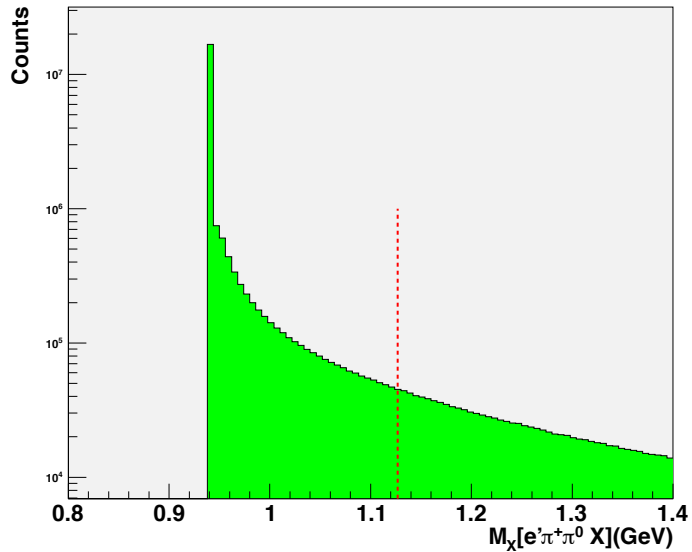


Figure 2.48: Missing mass $M_X[e'\pi^+\pi^0X]$ corresponding to generated events. We observe the radiative tail at the right of the neutron peak. The red line separates the "soft" photons (at the left) from the "hard" photons (at the right).

red line which we choose in order to distinguish soft photons from hard photons (i.e when the photon is detected). This cut is located at 3σ from the neutron peak, where σ is the experimental width of the neutron determined from the distributions shown in figure 2.27 (in average, $\sigma \approx 60$ MeV).

The acceptance we have calculated corresponds to events containing soft photons. As our goal is to extract the cross section of the reaction $ep \rightarrow e'n\pi^+\pi^0$ (without soft photons), we have to introduce a correction factor F_{rad} to take into account the radiative effects. Our event generator offers the possibility to generate events with and without radiative effects. The correction factor F_{rad} is then defined as:

$$F_{rad} = \frac{gen_{nonrad}}{gen_{radsoft}}. \quad (2.44)$$

We have calculated F_{rad} for each (Q^2, x_B) bin. Figure 2.49 shows F_{rad} as a function of

x_B for fixed Q^2 . We can notice that F_{rad} increases the cross sections by a factor varying from 10% to 20% according to the kinematic bins.

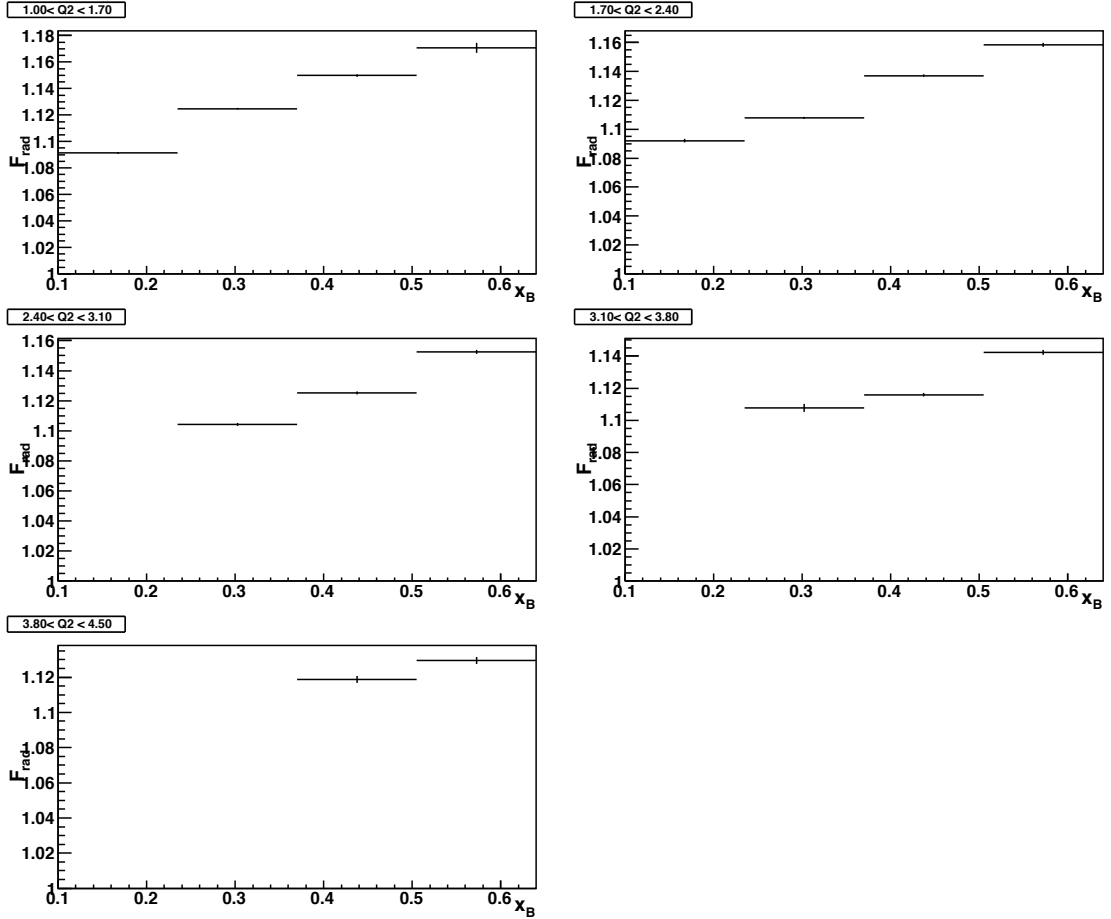


Figure 2.49: Radiative correction factor as a function of x_B for fixed Q^2 .

2.3.5 Efficiency of the selection cuts of electrons in the Čerenkov counters and the electromagnetic calorimeters of CLAS

In order to discriminate electrons from pions, we have applied cuts on the signals of the Čerenkov counters and of the electromagnetic calorimeter. These cuts were applied only to experimental data as we have already mentioned, since simulations are not reliable for these cases. Because of these cuts, we reject a certain number of good events (good electrons) that we have to estimate.

Determination of the efficiency cuts on CC

The cut applied on the number of photo-electrons detected in the Čerenkov counters is: $Nphe \times 10 > 25$. To estimate the number of good events lost due to this cut, we adjust the distribution of $Nphe$ with a generalized Poisson function given by the formula:

$$y\left(\frac{x}{p}\right) = k \frac{L^{\frac{x}{p}} e^{-L}}{\Gamma\left(\frac{x}{p} + 1\right)} \quad (2.45)$$

where k, L and p are the parameters we have to fit. By extrapolating the Poisson distribution to $Nphe = 0$, we can estimate the total number of good electrons. The efficiency of the cut on the $Nphe$ detected in CC is then given by:

$$Eff_{CC} = \frac{\int_{25}^{200} y(Nphe \times 10)}{\int_0^{200} y(Nphe \times 10)}. \quad (2.46)$$

The fit of the $Nphe \times 10$ distribution was done for each (Q^2, x_B) bin. Figure 2.50 shows an example of this fit for a particular (Q^2, x_B) bin.

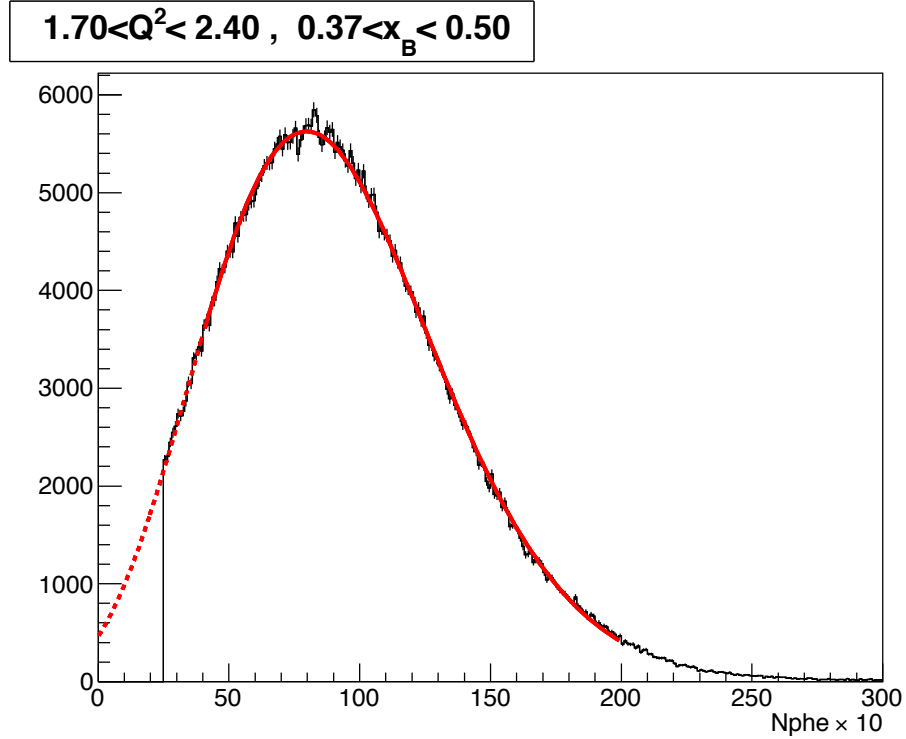


Figure 2.50: Distribution of $Nphe \times 10$ for a particular (Q^2, x_B) bin, with the cut $Nphe > 25$. The fit with the generalized Poisson function is presented with the red curve.

The efficiency of the cut on CC calculated for each (Q^2, x_B) bin is presented in figure 2.51. It is of the order of $\sim 95\%$.

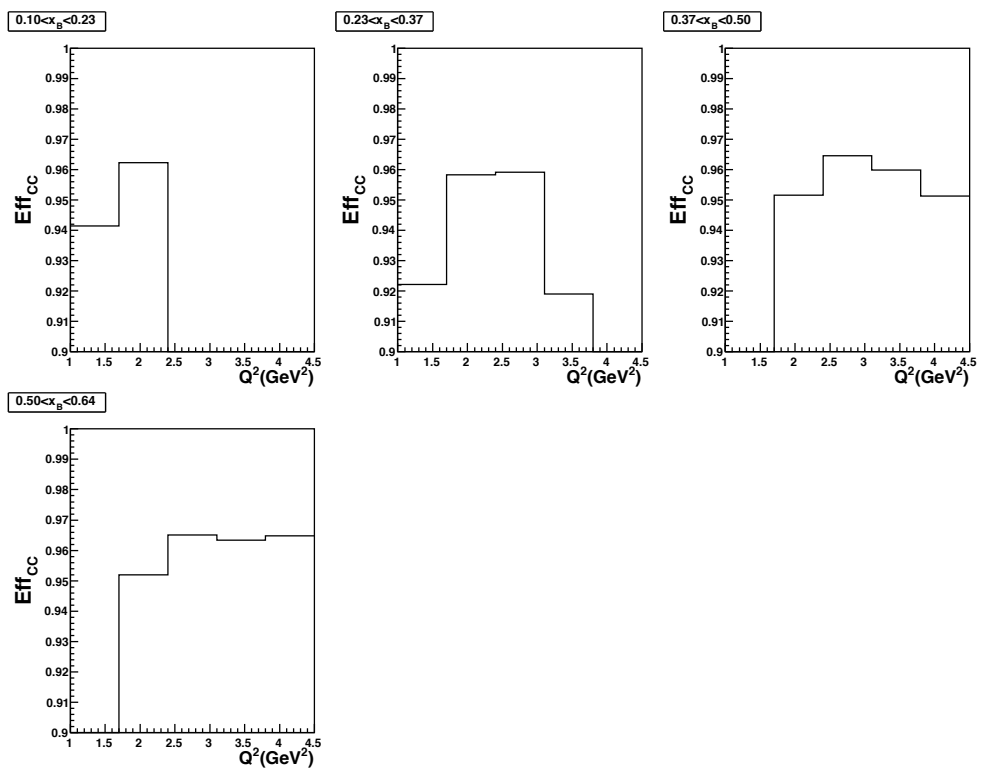


Figure 2.51: Efficiency of the cut on CC to select electrons, as a function of Q^2 for fixed x_B .

Determination of the efficiency cuts on EC

In order to select electrons, we have applied cuts on the energy detected in the electromagnetic calorimeter (E_{inner} and E_{tot}/p). To estimate the efficiency of these cuts, we use the $Nphe \times 10$ distributions. We consider that the cut $Nphe \times 10 > 80$ selects unambiguously good electrons. The efficiency of the cuts on EC is then calculated as follows:

$$Eff_{EC} = \frac{\int_{80}^{200} Nphe \times 10 \text{ (with the cuts on EC)}}{\int_{80}^{200} Nphe \times 10 \text{ (without the cuts on EC)}}. \quad (2.47)$$

Eff_{EC} was calculated for each (Q^2, x_B) bin. Figure 2.52 shows, for a particular bin, an example of $Nphe \times 10$ with and without cuts on the energy in the electromagnetic calorimeter. The efficiencies Eff_{EC} are presented in figure 2.53 as a function of Q^2 for

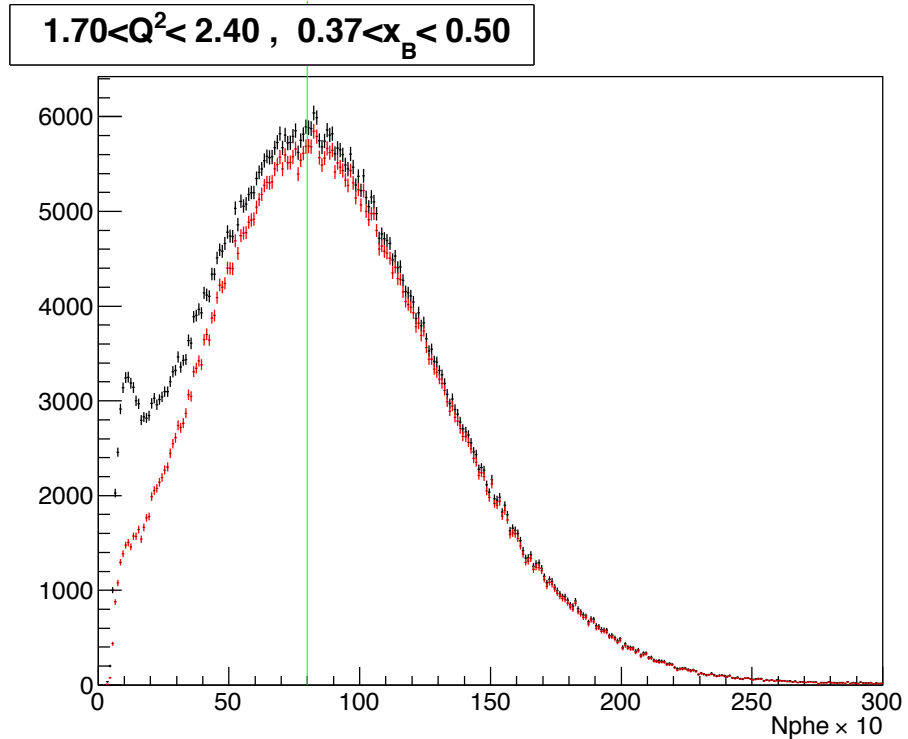


Figure 2.52: $Nphe \times 10$ distributions for electrons with (in red) and without (in black) cuts on the energy in the electromagnetic calorimeter, for a particular (Q^2, x_B) bin. The efficiency Eff_{EC} is defined as the ratio of the integrals of the two distributions beyond the green line ($Nphe \times 10 > 80$).

fixed x_B . The average efficiency is of the order of $\sim 95\%$.

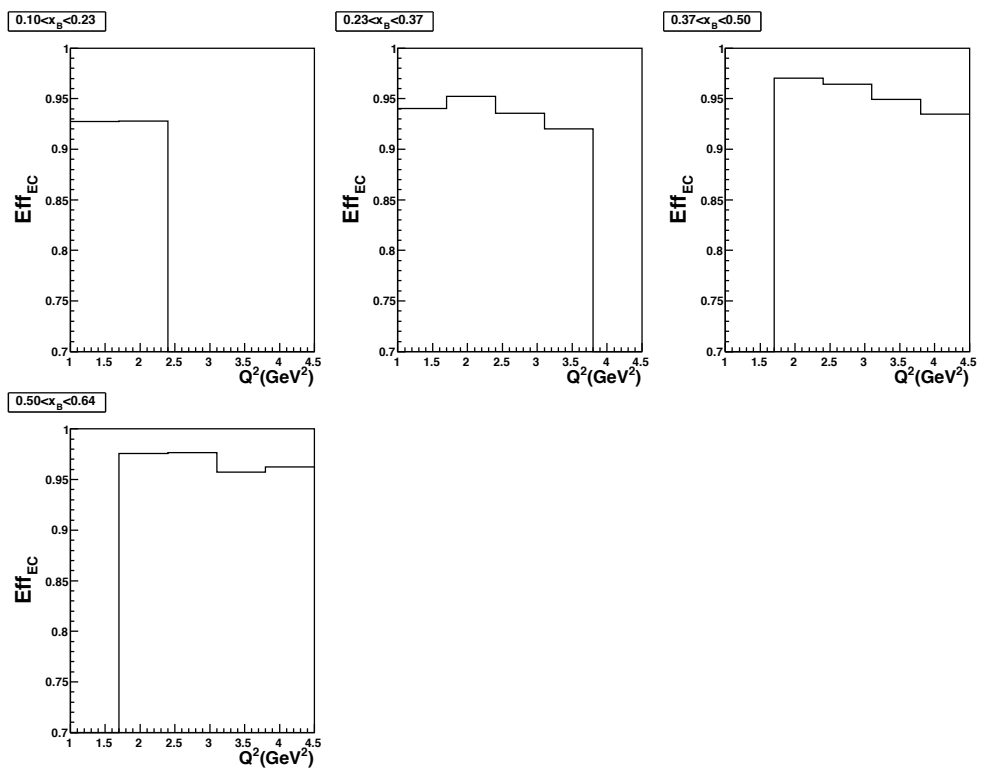


Figure 2.53: Efficiency of the selection cuts of electrons in EC as a function of Q^2 for fixed x_B .

2.3.6 Bin volume correction

In the equation of the cross section (equation 2.33), we see that we divide by the width of the kinematic bins. However, because of the kinematic cuts and because of the edges of the phase space of our reaction, the kinematic bins are not all filled everywhere with events. We deal with partially filled bins which we call reduced bins. The variables which are the most concerned with this effect are Q^2 , x_B and t (see figure 2.37).

To calculate the cross sections, we have to divide by the width of the reduced bin and not of the full one. To do so, we correct the bin volume (product of the bins widths) with the "volume correction factor" defined as:

$$F_{CorrVol} = \frac{V'}{V} \quad (2.48)$$

where V and V' are, respectively, the volume of the full bin and of the reduced one ($V' < V$).

When we calculate the total cross section $\sigma(Q^2, x_B)$, the "volume" is reduced to a "surface" in the (Q^2, x_B) plane.

Here is the algorithm we adopted to calculate the volume correction factor:

- We divide each bin of the variables Q^2 , x_B and t into 100 sub-bins, which means that we obtain $100 \times 100 \times 100$ elementary volumes for each 3-dimensional bins (Q^2, x_B, t) .
- We parametrize then all the cuts that we use and the kinematical limits (for instance t_{min} and t_{max}) as a function of the variables Q^2 , x_B and t . The sub-bins which pass these cuts make up the reduced bins.
- We calculate for each 3-dimensional bin (Q^2, x_B, t) , the number of elementary volumes in the reduced bins,
- The volume correction factor is then obtained by calculating, for each (Q^2, x_B, t) bin, the ratio between the number of elementary volumes within the reduced bins and the total number of elementary volumes (i.e. 10^6).

With this algorithm, we have reconstructed the phase space (Q^2, x_B, t) . Figure 2.54 shows the reconstructed (Q^2, x_B) phase space for the different bins in t . We do observe totally filled bins in the center of the phase space and partially filled bins at the edges. Figure 2.55 shows the phase space (t, x_B) for the different bins in Q^2 . We can see the limits t_{min} and t_{max} varying as a function of (Q^2, x_B) . We have discarded from the analysis the bins where the volume (or surface) correction factor is less than 0.1 (which corresponds to quasi-empty bins).

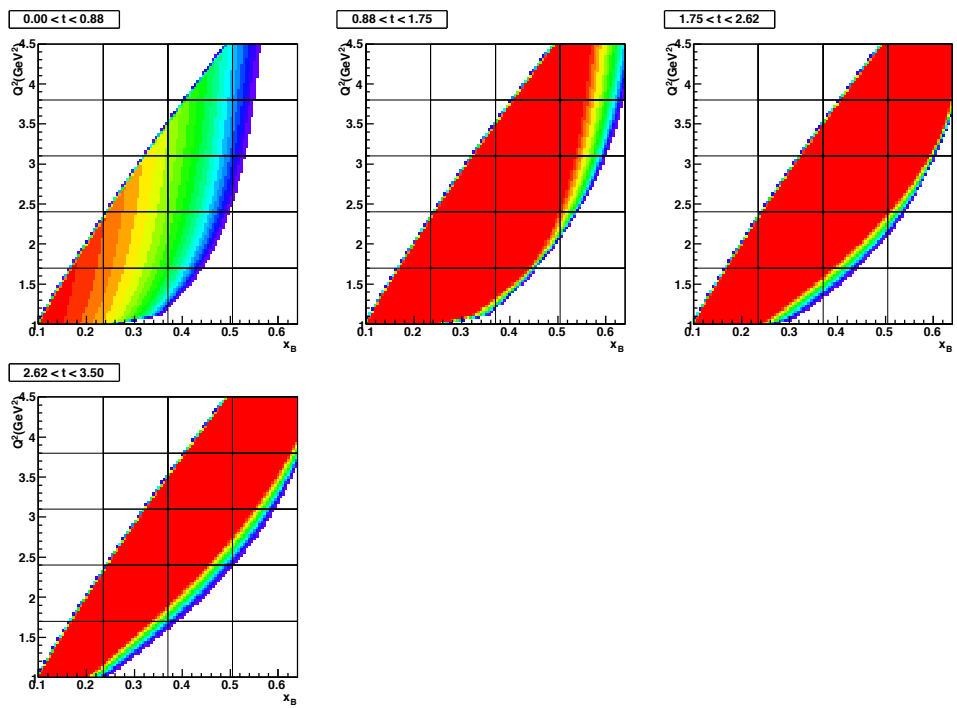


Figure 2.54: Phase space (Q^2, x_B) for different bins in t as reconstructed by the algorithm which calculates the volume correction factor. The binning is represented with the grid.

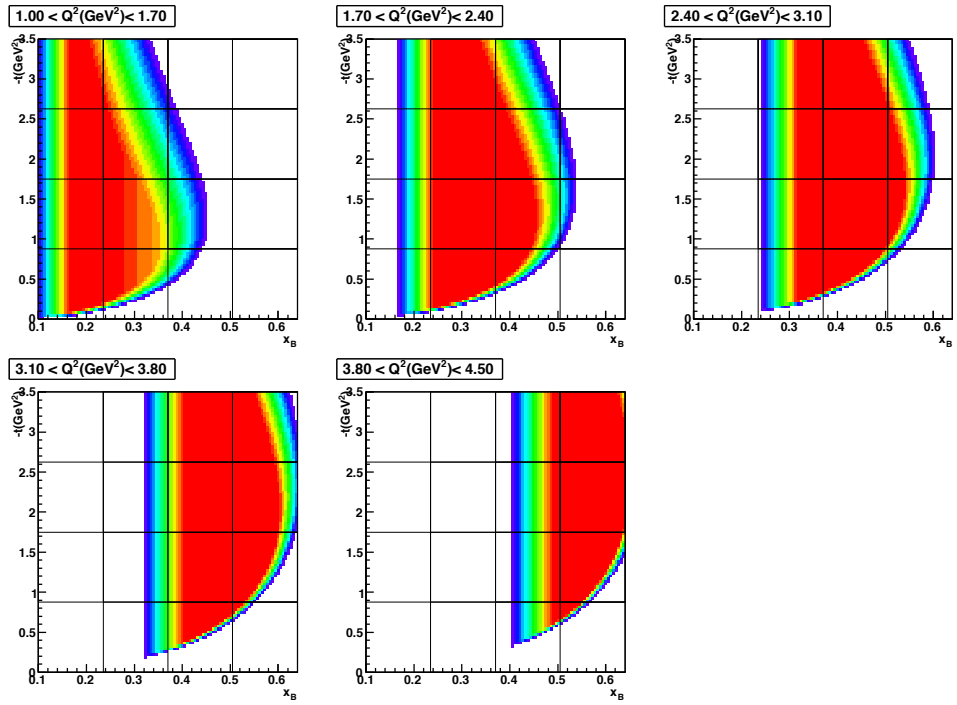


Figure 2.55: Phase space $(-t, x_B)$ for different bins in Q^2 as reconstructed by the algorithm which calculates the volume correction factor. The binning is represented by the grid.

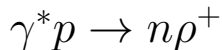
Global normalisation factor

The e1-dvcs collaboration analysed the cross section of the elastic reaction $ep \rightarrow e'p'$. This cross section is well-known and established. For the e1-dvcs run, in spite of a lot of efforts made during many months, the group has found the elastic cross section to be 12.34% off. We therefore apply a global normalisation factor $F_n = 0.8766$ to our cross sections. This factor corrects for SC inefficiency, not implemented in GSIM, and reconstruction inefficiency caused either by holes in the DC or SC, that are not (or badly) reproduced by GPP (seen [70] and [71] for more details). The systematic uncertainty associated with this normalization factor is estimated to be 5%.

2.3.7 Total cross section of the reaction $\gamma^* p \rightarrow n\pi^+\pi^0$

Having studied and calculated in the previous sections all the elements needed to extract the cross sections, we present in figure 2.56 the total cross section of the reaction $\gamma^* p \rightarrow n\pi^+\pi^0$ as a function of Q^2 for each x_B bin. This is the world's first-ever measurement of the cross section of this reaction. We observe the expected behaviour of the cross section which decreases with Q^2 . The cross section is of the order of the μb , which is similar to the other cross sections of exclusive 2-pion electroproduction in this range of energy (see reference [24]). Our error bars (statistical at this stage) are less than 15%. As this cross section is not our ultimate goal, we do not discuss at this stage the systematic errors. We recall that our goal is to extract the cross sections of ρ^+ exclusive electroproduction. To reach this goal, it remains an important step which is the subtraction of the non resonant 2-pion background under the ρ^+ peak .

2.4 Extraction of the cross sections of the reaction



2.4.1 Background subtraction

In order to determine the cross sections of the reaction $\gamma^* p \rightarrow n\rho^+$, we have to extract the ρ^+ signal from the distribution of the $\pi^+\pi^0$ invariant mass. Among the channels which have the final state $n\pi^+\pi^0$ and thus represent a background to the ρ^+ signal, there is a priori, the process of the non resonant 2-pion production $n\pi^+\pi^0$ (which we will simulate with a phase space distribution), the channel of the Δ^+ production associated to a π^0 ($\gamma^* p \rightarrow \pi^0\Delta^+ \leftrightarrow n\pi^+$), the channel of the Δ^0 production associated to a π^+ ($\gamma^* p \rightarrow \pi^+\Delta^0 \leftrightarrow n\pi^0$) and possibly other N^* decaying into $n\pi^0$ and $n\pi^+$, associated to a pion.

Figures 2.57 and 2.58 show the distributions of the invariant masses $n\pi^+$ and $n\pi^0$ corresponding to our experimental data (in black). In red, are the same distributions but for the MC reconstructed data (ρ^+ and phase space channels). Concerning the distributions of the invariant mass $n\pi^+$, we do not clearly see any prominent structures (resonances)

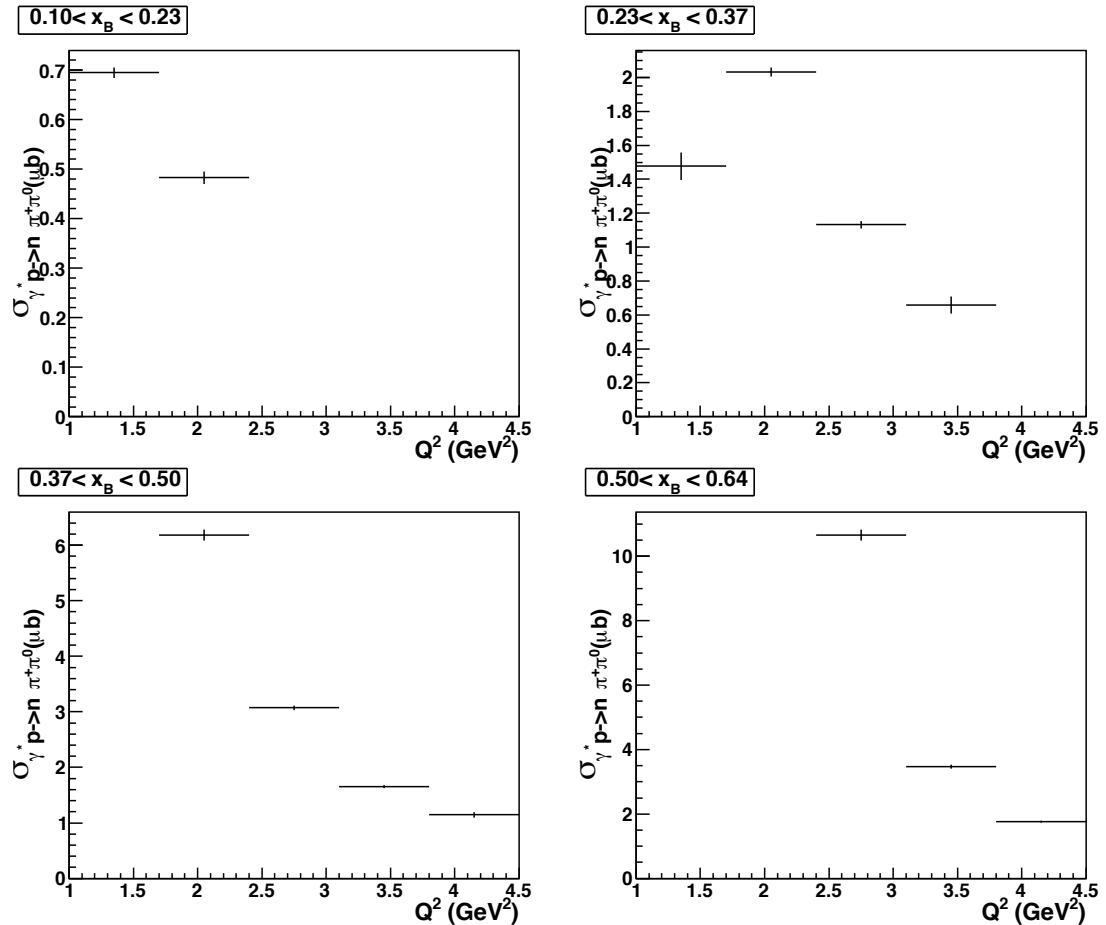


Figure 2.56: Total cross section as a function of Q^2 for fixed bins in x_B for the reaction $\gamma^* p \rightarrow n\pi^+\pi^0$. The presented error bars are pure statistical.

in any of our (Q^2, x_B) bins. The agreement between the data and our MC is reasonable. Regarding the distributions of the invariant mass $n\pi^0$, we can distinguish some structures which correspond to the resonance Δ^0 at 1232 MeV. However, these structures are not that prominent and they are also not present in all our (Q^2, x_B) bins. They are localised only at large x_B (near the resonance region). Our MC reproduces the general shape of the invariant mass $n\pi^0$ but not the baryonic resonances of course as they are not taken into account in the simulation. We deem that it is reasonable, in order to model the background under the ρ^+ peak, to take into account only the non resonant continuum (phase space) $\gamma^* p \rightarrow n\pi^+\pi^0$ contribution. This is further supported by the observation that the $M_{\pi^+\pi^0}$ projected shapes of the Δ^0 and Δ^+ channels is very similar to the phase space one. One can therefore consider that the phase space contribution can thus, in an effective way, "absorb" and "mimick" the Δ resonances contributions (see figures 2.59 and 2.60).

We show in figure 2.61 the fits (carried out with the least-square minimization method and MINUIT [50]) of the $M_{\pi^+\pi^0}$ distribution for all our (Q^2, x_B) bins. We have used 2 contributions to fit these spectra: a (skewed) Breit-Wigner distribution, described by an analytical function, in order to model the resonant structure of the ρ^+ and an histogram which is the $M_{\pi^+\pi^0}$ projection of the $\gamma^* p \rightarrow n\pi^+\pi^0$ phase space (which is given by the *genev* event generator), in order to model the non-resonant 2-pion background.

For the ρ^+ contribution, we have used a "skewed" Breit-Wigner as an effective way to take into account distortions due to interferences between the ρ^+ (which is broad) and the $\pi^+\pi^0$ continuum. The approach is inspired of what is usually done for the ρ^0 channel for which a lot of data is available and which has been studied in many details. The elements entering our B-W formula are the following:

- Introduction of an energy dependent width (to take into account that the ρ^+ is an unstable spin-1 particle which decays into 2 spin-0 particles; one talks about a "p-wave" Breit-Wigner [51]). The modified Breit-Wigner reads then:

$$\frac{dN}{dM_{\pi^+\pi^0}} = BW(M_{\pi^+\pi^0}) = \frac{M_{\rho^+}\Gamma(M_{\pi^+\pi^0})}{(M_{\rho^+}^2 - M_{\pi^+\pi^0}^2)^2 + M_{\rho^+}^2\Gamma^2(M_{\pi^+\pi^0})} \quad (2.49)$$

with the energy dependent width:

$$\Gamma(M_{\pi^+\pi^0}) = \Gamma_{\rho^+} \left(\frac{q}{q_0}\right)^{2l+1} \frac{M_{\rho^+}}{M_{\pi^+\pi^0}} \quad (2.50)$$

where $l = 1$ for a p-wave Breit-Wigner, q is the momentum of the decay pion in the ρ^+ center of mass frame and q_0 is equal to q for $M_{\rho^+} = M_{\pi^+\pi^0}$, i.e.:

$$q = \frac{\sqrt{M_{\pi^+\pi^0}^2 - 4M_\pi^2}}{2}, q_0 = \frac{\sqrt{M_{\rho^+}^2 - 4M_\pi^2}}{2}. \quad (2.51)$$

- Ross and Stodolsky [52] have shown that interferences between the broad ρ^+ peak and the background underneath leads to a "skewing"/distortion of the Breit-Wigner.

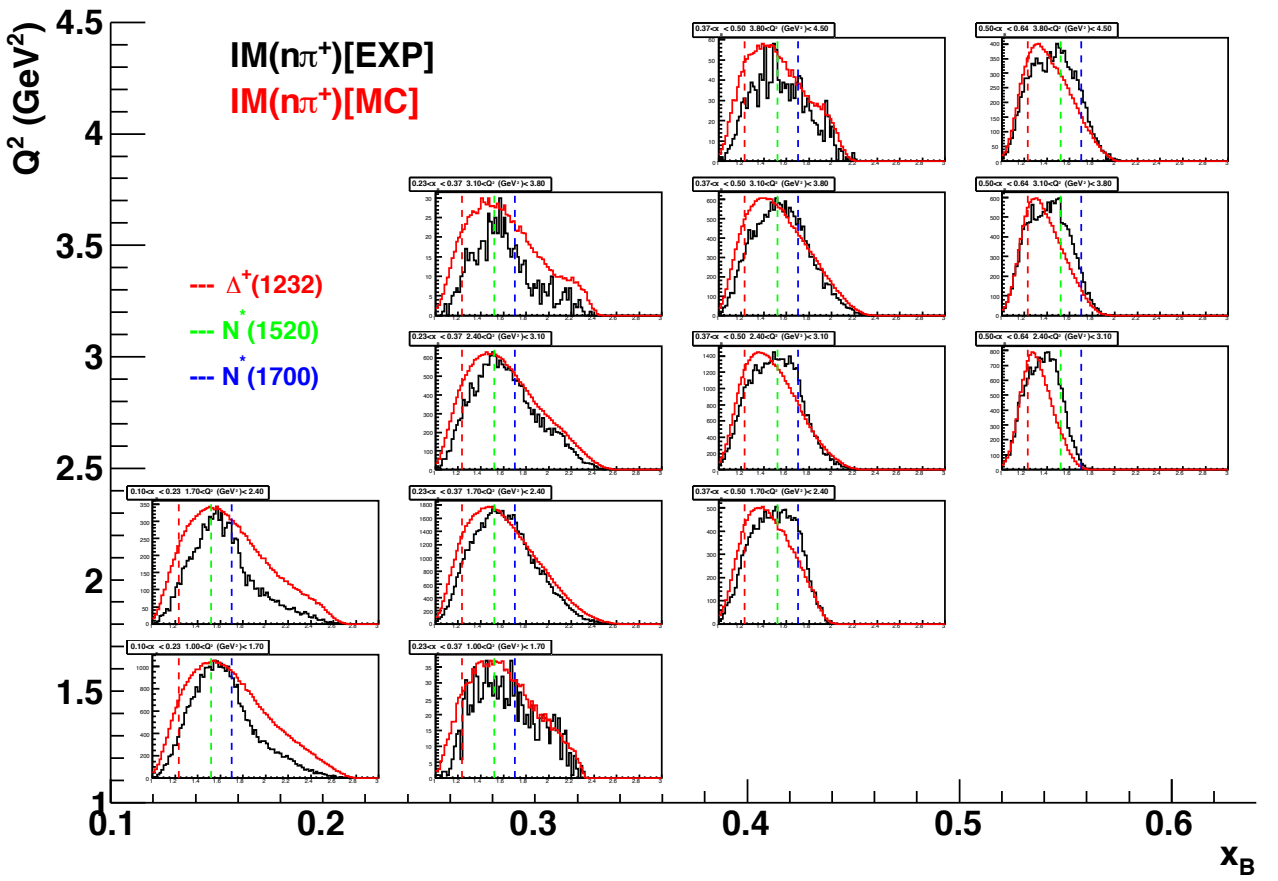


Figure 2.57: Invariant mass $n\pi^+$ for each (Q^2, x_B) bin (experimental data). In red, are the same distributions for the MC reconstructed data. The green line, the blue one and the red one indicate the well-known nucleonic resonance masses decaying into $n\pi^+$ [39]: respectively, $\Delta^+(1232)$, $N^*(1520)$ and $N^*(1700)$.

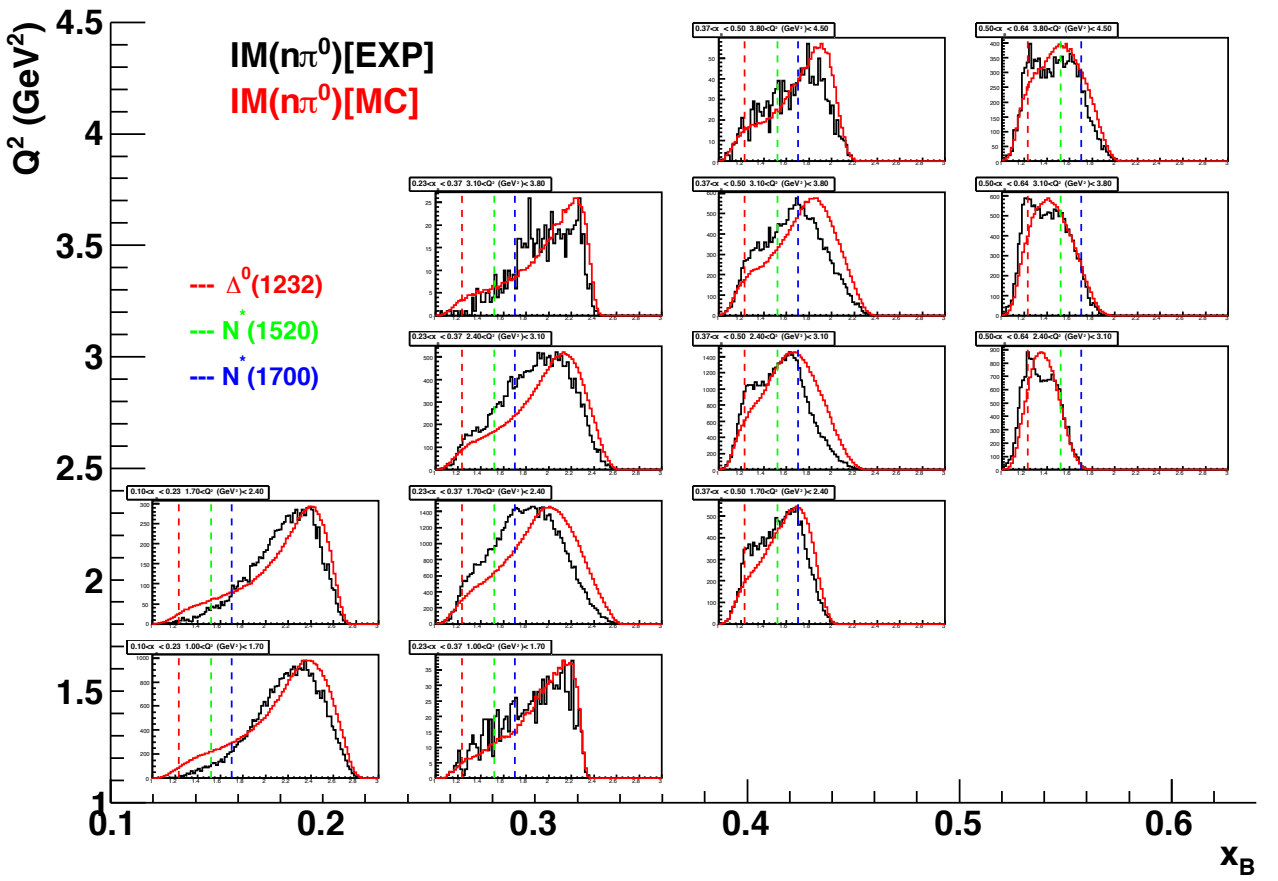


Figure 2.58: Invariant mass $n\pi^0$ for each (Q^2, x_B) bin (experimental data). In red, are the same distributions for the MC reconstructed data. The green line, the blue one and the red one indicate the well-known nucleonic resonance masses decaying into $n\pi^0$ [39]: respectively, $\Delta^0(1232)$, $N^*(1520)$ and $N^*(1700)$.

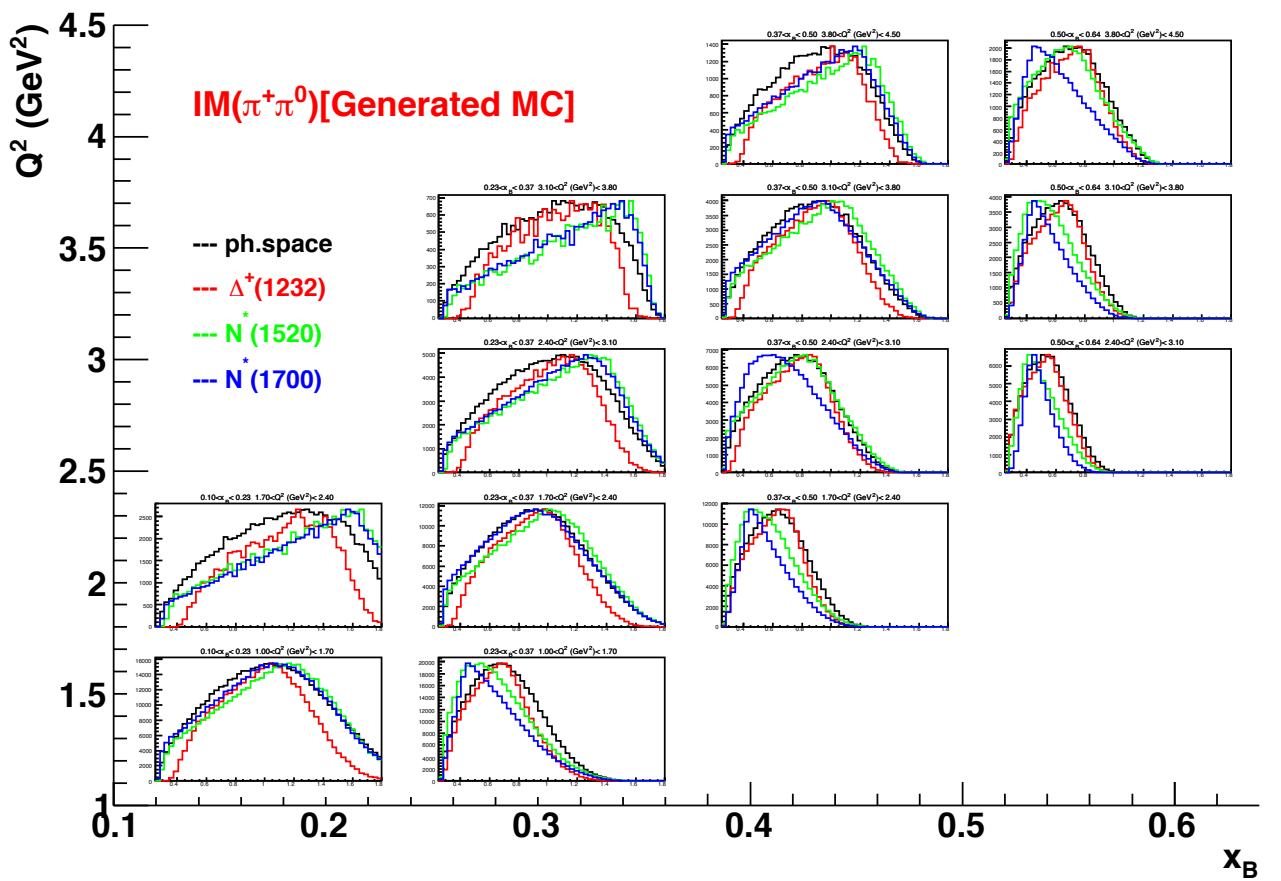


Figure 2.59: Comparison of the $IM(\pi^+\pi^0)$ distributions corresponding to the phase space and Δ^+ channels (generated distributions).

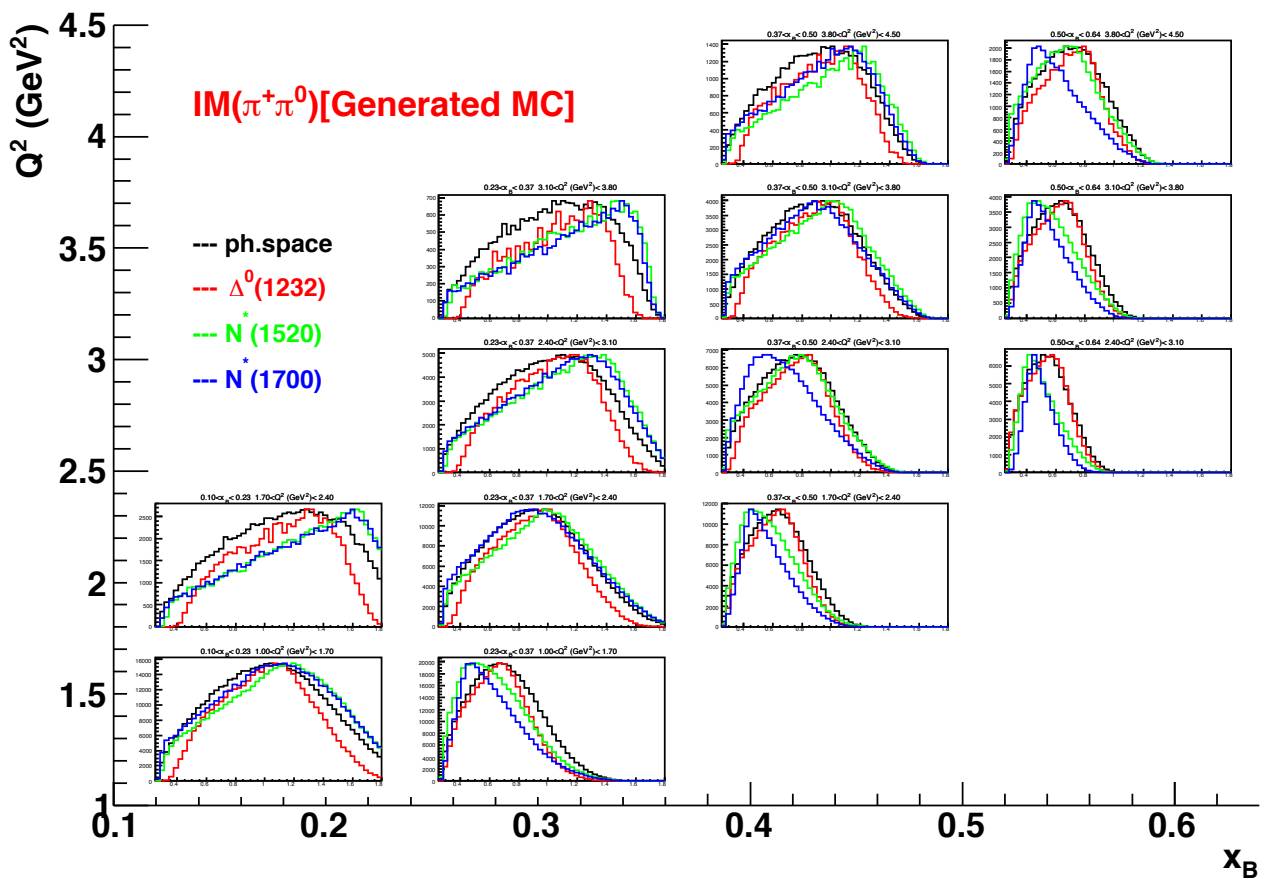


Figure 2.60: Comparison of the $IM(\pi^+\pi^0)$ distributions corresponding to the phase space and Δ^0 channels (generated distributions).

One way to take into account this effect is to introduce a correction term which consists in multiplying the Breit-Wigner by an empirical factor which shifts the centroid of the distribution.

$$\frac{dN}{dM_{\pi^+\pi^0}} = BW(M_{\pi^+\pi^0}) \left(\frac{M_{\rho^+}}{M_{\pi^+\pi^0}} \right)^{n_{skew}} \quad (2.52)$$

where n_{skew} is a distortion ("skewing") parameter. Although Ross and Stodolsky have predicted n_{skew} to be equal to 4 [52], it is usually considered as a parameter to be fitted to the data because it can depend on the different kinematic variables, as not much is known concerning the interference between the ρ^+ channel and the $\pi^+\pi^0$ continuum.

In principle, the only free parameter to vary, besides the overall normalization, in the formula 2.52 is n_{skew} . However we have also allowed to vary, in a relatively limited range, the central mass (from 750 to 790 MeV) and the width (from 140 to 170 MeV) of the ρ^+ . The motivation for this is that, besides the largely unknown interference effects between the ρ^+ meson and the $\pi^+\pi^0$ continuum already mentioned, several other (hardly controllable) effects can shift or distort the meson shape: radiative corrections, acceptance correction, resolution, etc... which do not control perfectly.

To summarize, all in all, the $M_{\pi^+\pi^0}$ spectra were fitted (for each (Q^2, x_B) bin) by 5 parameters which are:

1. the weight (normalization) of the Breit-Wigner,
2. the central mass of the Breit-Wigner,
3. the width of the Breit-Wigner,
4. the distortion parameter n_{skew} ,
5. the weight (normalization) of the non-resonant continuum $\gamma^* p \rightarrow n\pi^+\pi^0$ process.

This background subtraction procedure is not perfect. The continuum phase space represents the sum of several processes leading to the same final state $n\pi^+\pi^0$ ($\gamma^* p \rightarrow \pi N^*$ for example, as mentioned before) which probably have $M_{\pi^+\pi^0}$ distributions slightly different from those of a pure phase space. Also, we sum the $\pi^+\pi^0$ continuum and the Breit-Wigner of the ρ^+ at the level of cross sections while these processes interfere, in principle, at the level of amplitudes (although, this interference effect is somewhat modeled, in an effective way, by the n_{skew} parameter). Our simplified fit procedure comes from our lack of knowledge of the details of all the interfering mechanisms leading to the final state $n\pi^+\pi^0$. There is currently no theoretical model on the market which can be applied in our energy range. Even though our method is not perfect, it has the merit of being simple, efficient, stable and with only a few free parameters (taking into account differential cross sections, we will have several hundreds of spectra to fit).

In figure 2.61, one can observe that the shape of the background varies with the kinematic bins. In particular, the background is relatively important for high x_B (corresponding to small W) where one can think that the phase space continuum contains contributions coming from the $\Delta^0\pi^+$ channel for example. In general, we deem that the fits describe reasonably well the data.

One can note that the χ^2 values of the fit are relatively large (although, "by eye", the fits look relatively reasonable). This is due to the error bars of the data which are rather small (chi^2 is proportional to the inverse of the squared error bars). We recall that, at this stage, the error bars are purely statistical so that they are underestimated (see section 2.4.6 for the estimation of the systematic error bars). One can therefore consider that the chi^2 values are "artificially" large; we nevertheless choose to leave them on the plots.

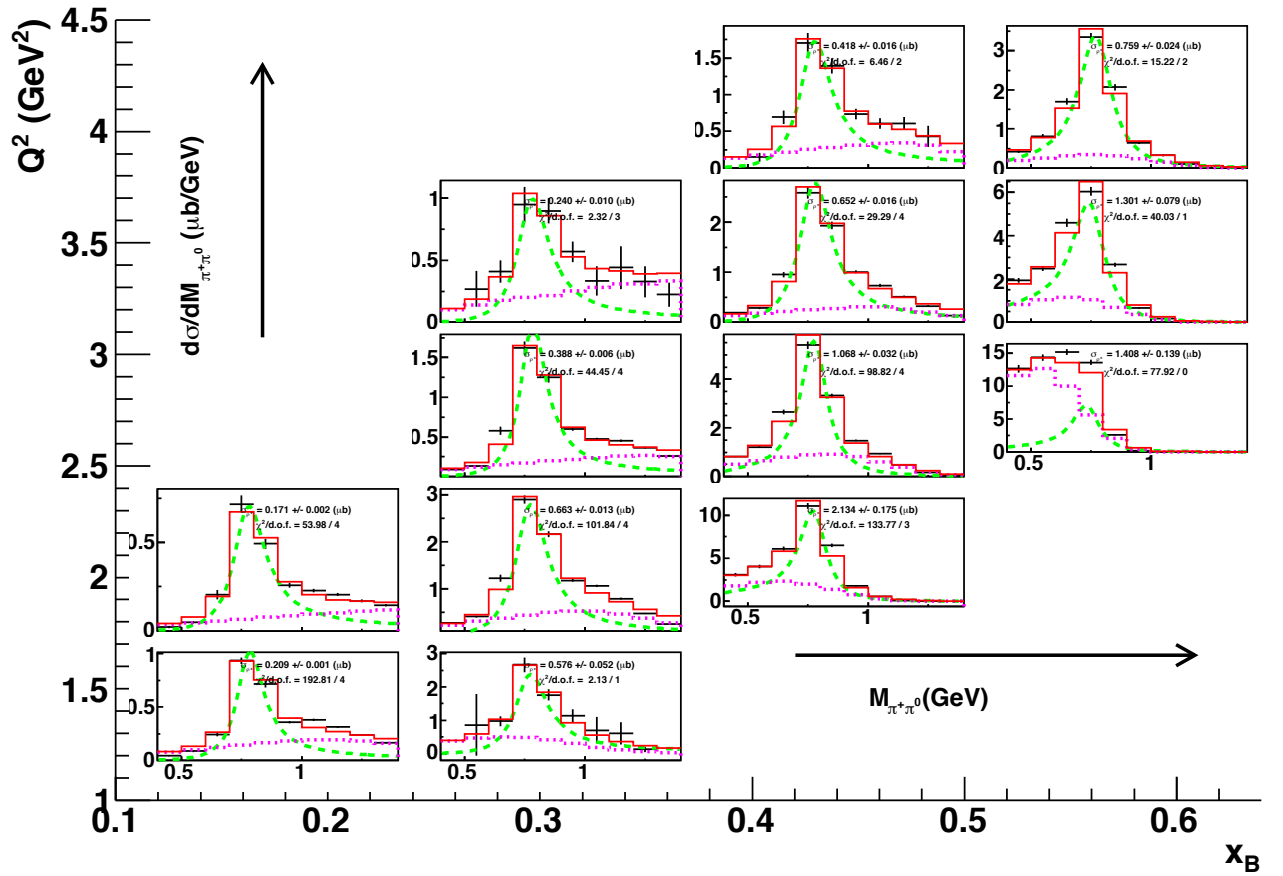


Figure 2.61: $M_{\pi^+\pi^0}$ acceptance-corrected distributions, showing fits for the background subtraction. In black: experimental data; In green: Breit-Wigner of ρ^+ ; in purple: $M_{\pi^+\pi^0}$ projection of the non-resonant continuum $\gamma^*p \rightarrow n\pi^+\pi^0$ reaction; in red: total fit result.

2.4.2 Total cross section $\sigma_{\gamma^* p \rightarrow n\rho^+}$

In order to extract the total cross section of the reaction $\gamma^* p \rightarrow n\rho^+$, we calculate for each (Q^2, x_B) bin the area of the Breit-Wigner (green curve in figure 2.61). We recall that the distributions are already normalized and corrected by the acceptance according to the procedure of the section 2.3. The total cross sections of the electroproduction of ρ^+ thus extracted are presented in figure 2.62 as a function of Q^2 for fixed x_B . The cross sections are of the order of a few μb and, as expected, decrease with Q^2 . The presented errors correspond purely statistical errors.

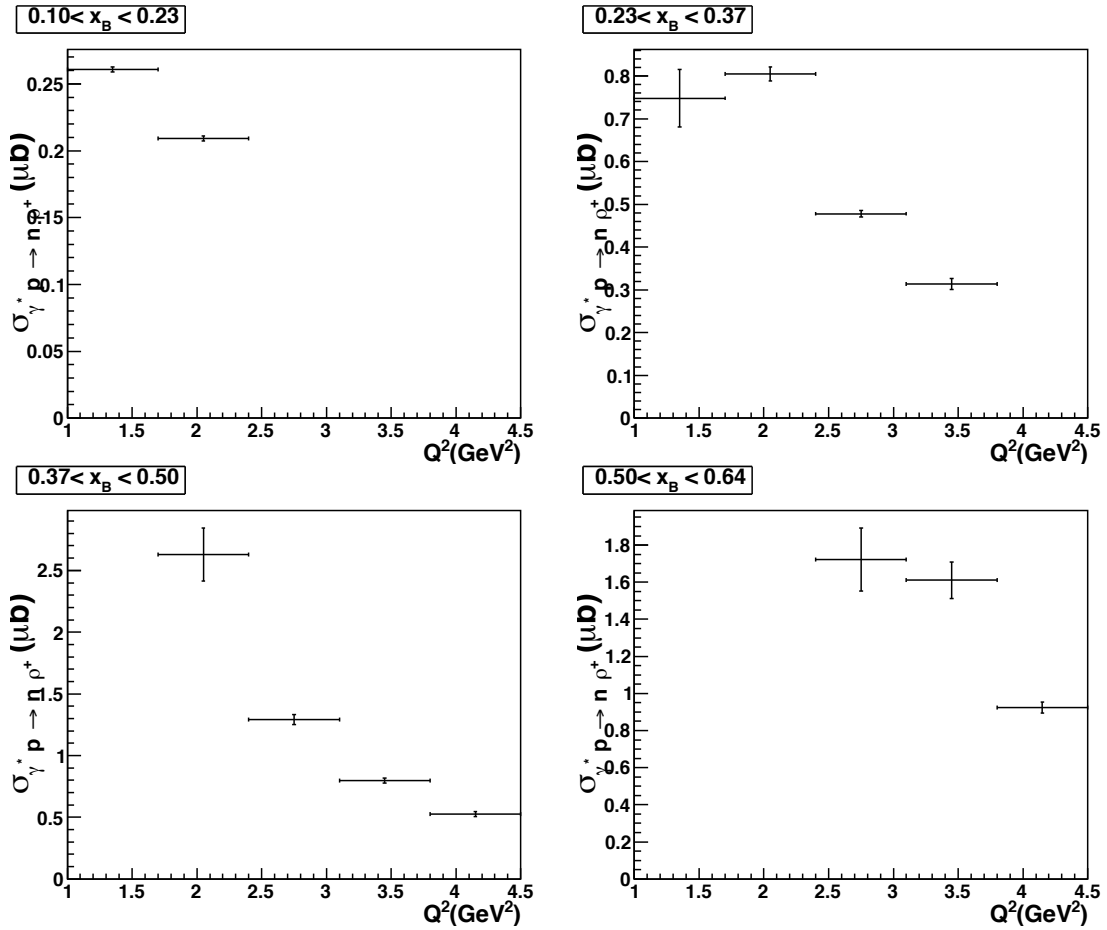


Figure 2.62: Total cross section as function of Q^2 at fixed x_B for the reaction $\gamma^* p \rightarrow n\rho^+$.

2.4.3 Differential cross section $d\sigma/dt$ ($\gamma^* p \rightarrow n\rho^+$)

The procedure of fitting the invariant mass ($M_{\pi^+\pi^0}$) spectra is the same for the differential cross sections as for total cross section, but it is performed for each (Q^2, x_B, t) bin instead of each (Q^2, x_B) bin (about 40 spectra to fit). Figures E.1 to E.4 in the appendix E

show the results of the fits for each (Q^2, x_B, t) bin. By calculating the area of the Breit-Wigner which fits the ρ^+ peak, we extract the differential cross section $d\sigma/dt$ for the reaction $\gamma^* p \rightarrow n\rho^+$. Figure 2.63 shows the t dependence of these cross section for each (Q^2, x_B) bin. The general feature of these distributions is that they are of a diffractive

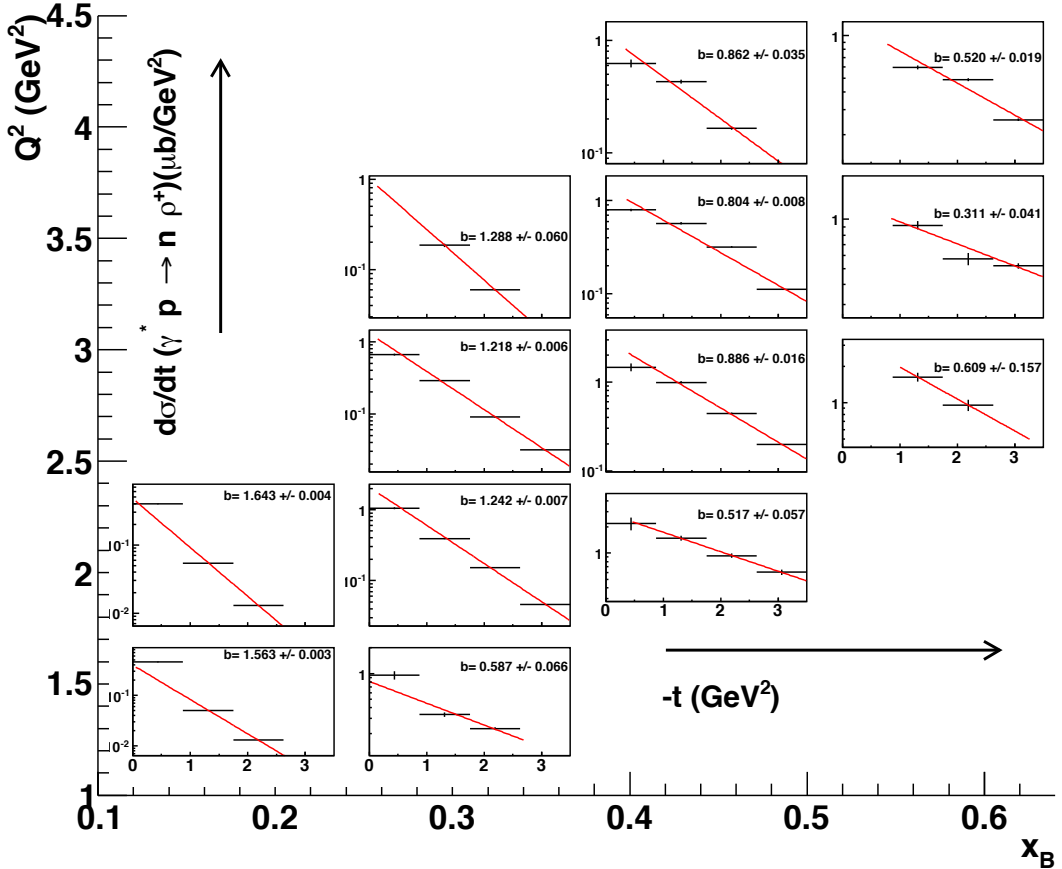


Figure 2.63: Differential cross section $d\sigma/dt$ as function of t for each (Q^2, x_B) bin for the reaction $\gamma^* p \rightarrow n\rho^+$. The red curve represents the fit with the formula 2.53. The extracted slope b of $d\sigma/dt$ is shown for each bin.

type ($\propto e^{-bt}$). The distributions are then fitted with the following formula:

$$\frac{d\sigma}{dt} = Ae^{-bt} \quad (2.53)$$

where A and b are the free parameters of the fit.

In figure 2.64, the slope b is plotted as a function of the center of mass energy W . One can observe that b increases with W varying between 0.3 and 1.6 GeV^{-2} . This behaviour was observed for other mesons like for example the electroproduction of ρ^0 (see ref. [24]).

Intuitively, b represents the transverse size of the $\rho - N$ system. The observation that it increases with W (i.e. as x_B gets smaller) hints that the transverse size of the nucleon increases with W (i.e. as one probes more and more sea quarks, i.e. small x_B values). Figure 2.65 shows the same extracted t -slope b but as a function of x_B for the different Q^2 values. The slope b is increasing with x_B decreasing.

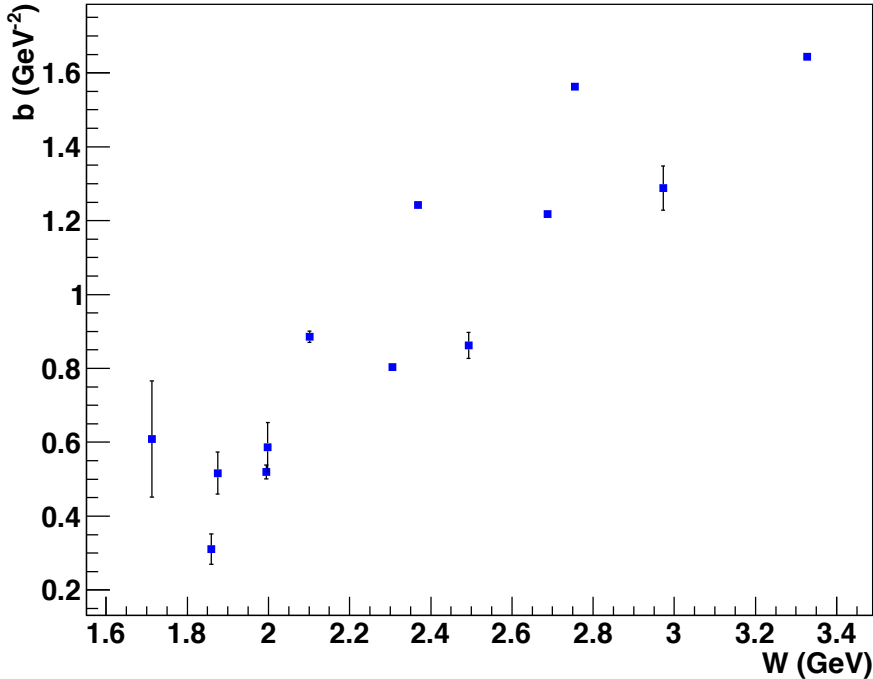


Figure 2.64: Slope b of $d\sigma/dt$ (defined by eq. 2.53) as a function of the center of mass energy W for the reaction $\gamma^* p \rightarrow n \rho^+$. Relatively large error bars come mainly from fits of $d\sigma/dt$ with only two bins.

2.4.4 Differential cross sections in Φ and test of SCHC

We proceed in the same way to extract $d\sigma/d\Phi$. In figures F.1 to F.5 of the appendix F are shown the results of the $M_{\pi^+\pi^0}$ fits for all our (Q^2, x_B, Φ) bins. The extracted cross sections $d\sigma/d\Phi$ for all our (Q^2, x_B) bins are presented in figure 2.66.

These distributions were fitted with the standard Φ dependence (expected from 1- γ exchange):

$$\frac{d\sigma}{d\Phi} = \frac{1}{2\pi} (\sigma_T + \epsilon \sigma_L + \epsilon \cos 2\Phi \sigma_{TT} + \sqrt{2\epsilon(1+\epsilon)} \cos \Phi \sigma_{TL}) \quad (2.54)$$

where σ_L , σ_T , σ_{TT} and σ_{TL} are, respectively, the standard "longitudinal", "transverse", "transverse-transverse" and "transverse-longitudinal" response functions ("transverse"

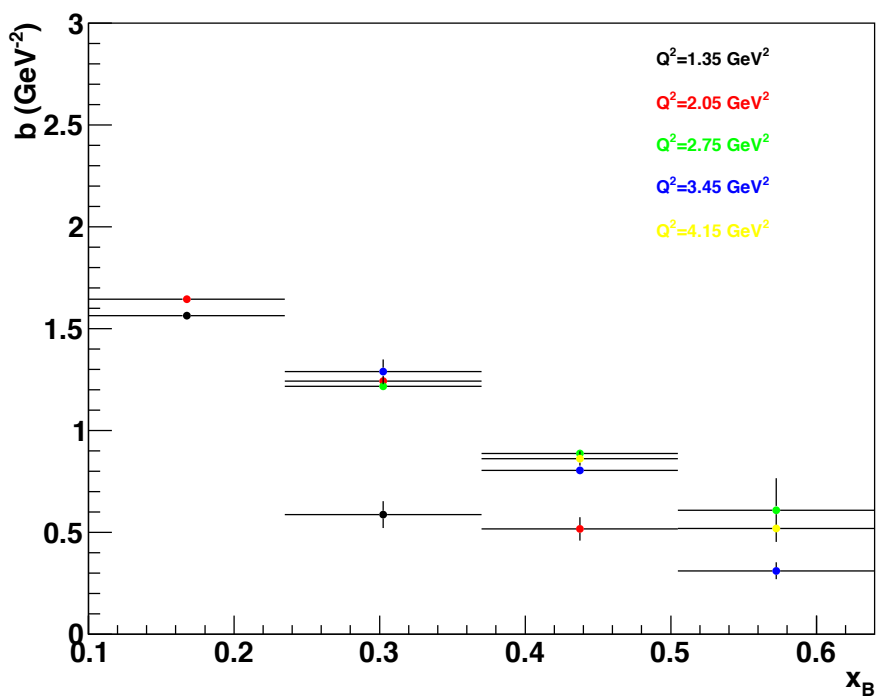


Figure 2.65: Slope b of $d\sigma/dt$ as a function of x_B for the reaction $\gamma^*p \rightarrow n\rho^+$. Relatively large error bars come mainly from fits of $d\sigma/dt$ with only two bins.

and "longitudinal" refer to the polarization of the virtual photon).

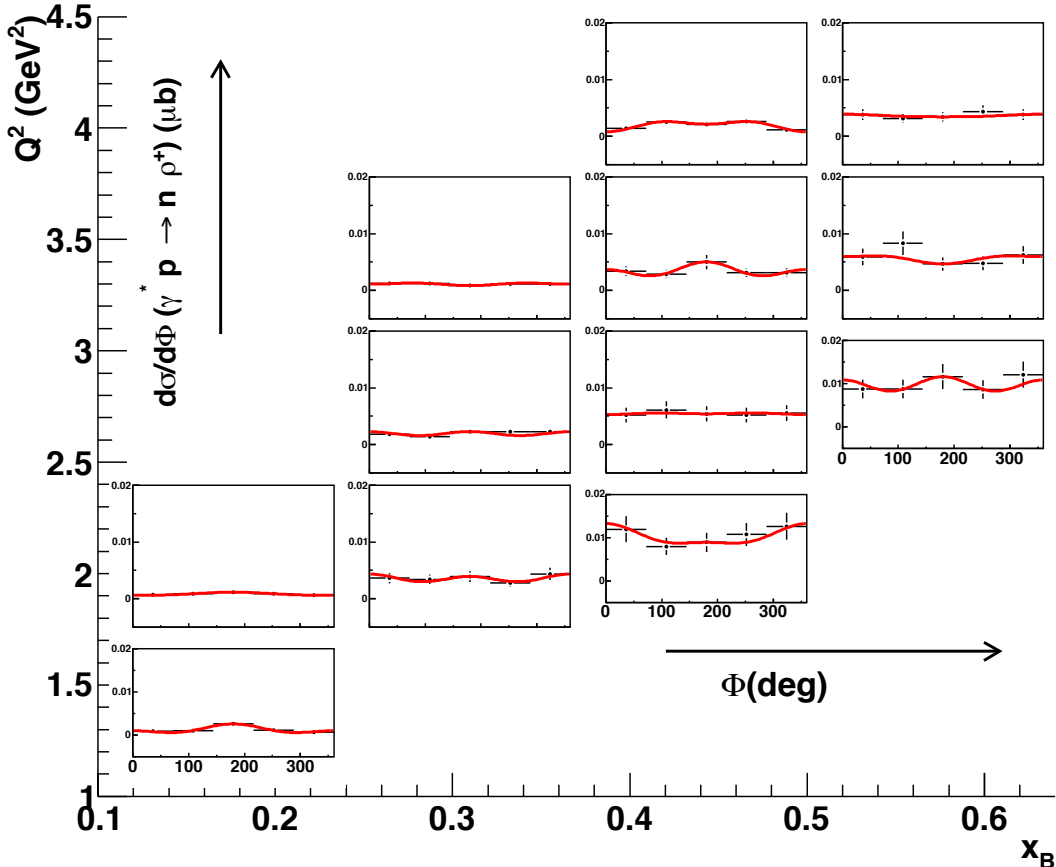


Figure 2.66: $d\sigma/d\Phi$ as a function of Φ for each (Q^2, x_B) bin for the reaction $\gamma^* p \rightarrow n \rho^+$. The red curve shows the fit of the data to the function of eq. 2.54.

From this fit, one can extract the cross sections $\sigma_T + \epsilon\sigma_L$ and the interference terms σ_{TT} and σ_{TL} . Figure 2.67 shows these three observables as a function of Q^2 for fixed bins in x_B . If there is s-channel helicity conservation (SCHC) between the initial virtual photon and the final ρ^+ , σ_{TT} and σ_{TL} should vanish. We see from the figure 2.67 that most of σ_{TT} 's and σ_{TL} 's are compatible with 0 (within our error bars) and, in any case, quite smaller than $\sigma_T + \epsilon\sigma_L$. This is a (first) sign of confidence that SCHC holds for our process. We will see in the next subsection that the advantage of having SCHC.

2.4.5 Extraction of the longitudinal cross sections $\gamma_L^* p \rightarrow n \rho_L^+$

One of the physics motivations of this analysis is the study of GPDs and a comparison to GPD models. The factorization of the handbag diagram for the electroproduction of mesons is valid only for longitudinal virtual photons. In order to compare our results

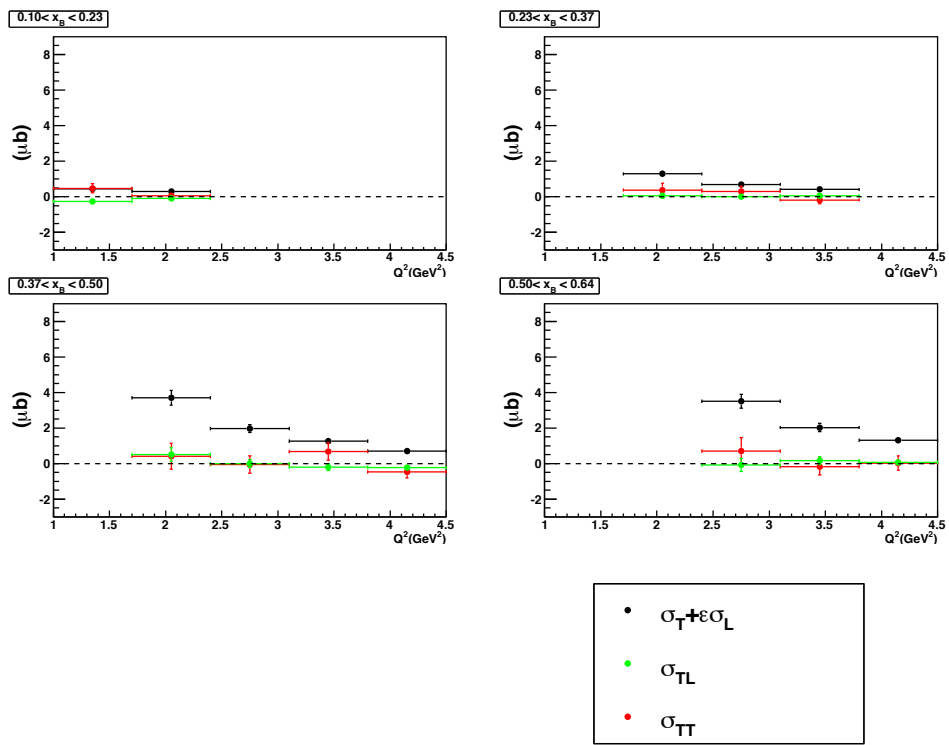


Figure 2.67: $\sigma_T + \epsilon\sigma_L$ (in black), σ_{TL} (in green) and σ_{TT} (in red) as a function of Q^2 for different bins in x_B for the reaction $\gamma^* p \rightarrow n\rho^+$.

with models based on GPDs, it is necessary to separate longitudinal cross sections from transverse ones. The total cross section can be written as:

$$\sigma = \sigma_T + \epsilon \sigma_L \quad (2.55)$$

In general, to separate σ_L and σ_T , one makes a "Rosenbluth" separation: one measures the total cross section for two different beam energies in order to let ϵ vary while Q^2 and x_B remain constant. However, for the electroproduction of vector mesons, this delicate procedure can be avoided. Indeed, one can access the polarization of the vector meson, in a model independent way, by analyzing the angular distributions of its decay products. Then, if one can establish that SCHC holds, one can relate the polarization of the vector meson to the polarization of the virtual photon; to be precise, the polarization of the vector meson and the virtual photon are the same. The conservation of the helicity between the ρ^+ and γ^* is motivated originally by the fact that a vector meson has the same quantum numbers as the photon ($J^P = 1^-$ where J is the spin and P is the parity). SCHC has been shown to be valid to a large extent for the ρ^0 channel for which a lot of data are available. As seen in the previous section with our data, it also seems to be valid for our ρ^+ channel.

In order to access the polarization of the ρ^+ , we analyse the θ_{HS} and ϕ_{HS} angular distributions of its decay products. These distributions should follow the following general and model-independent formula of the decay of a spin 1 particle into 2 spin 0 particles [55]:

$$W(\Phi, \cos \theta_{HS}, \phi_{HS}) = \frac{3}{4\pi} \left[\frac{1}{2}(1 - r_{00}^{04}) + \frac{1}{2}(3r_{00}^{04} - 1) \cos^2 \theta_{HS} \right. \\ - \sqrt{2} \operatorname{Re}(r_{10}^{04}) \sin 2\theta_{HS} \cos \phi_{HS} - r_{1-1}^{04} \sin^2 \theta_{HS} \cos 2\phi_{HS} \\ - \epsilon \cos 2\Phi(r_{11}^1 \sin^2 \theta_{HS} + r_{00}^1 \cos^2 \theta_{HS}) \\ - \sqrt{2} \operatorname{Re}(r_{10}^1) \sin 2\theta_{HS} \cos \phi_{HS} - r_{1-1}^1 \sin^2 \theta_{HS} \cos 2\phi_{HS} \\ - \epsilon \sin 2\Phi(\sqrt{2} \operatorname{Im}(r_{10}^2) \sin 2\theta_{HS} \sin \phi_{HS} + \operatorname{Im}(r_{1-1}^2) \sin^2 \theta_{HS} \sin 2\phi_{HS}) \\ + \sqrt{2\epsilon(1+\epsilon)} \cos \Phi(r_{11}^5 \sin^2 \theta_{HS} + r_{00}^5 \cos^2 \theta_{HS}) \\ - \sqrt{2} \operatorname{Re}(r_{10}^5) \sin 2\theta_{HS} \cos \phi_{HS} - r_{1-1}^5 \sin^2 \theta_{HS} \cos 2\phi_{HS} \\ + \sqrt{2\epsilon(1+\epsilon)} \sin \Phi(\sqrt{2} \operatorname{Im}(r_{10}^6) \sin 2\theta_{HS} \sin \phi_{HS} \\ \left. + \operatorname{Im}(r_{1-1}^6) \sin^2 \theta_{HS} \sin 2\phi_{HS} \right] \quad (2.56)$$

where the parameters r_{ij}^α are related to the "Spin Density Matrix Elements" (SDMEs) ρ_{ij}^α as follows:

$$r_{ij}^{04} = \frac{\rho_{ij}^0 + \epsilon R \rho_{ij}^4}{1 + \epsilon R} \\ r_{ij}^\alpha = \frac{\rho_{ij}^\alpha}{1 + \epsilon R} \quad \alpha = 1, 2 \quad (2.57) \\ r_{ij}^\alpha = \sqrt{R} \frac{\rho_{ij}^\alpha}{1 + \epsilon R} \quad \alpha = 5, 6$$

with R the ratio σ_L/σ_T .

The SDMEs ρ_{ij}^α are bilinear combinations of the helicity amplitudes that describe the $\gamma^* p \rightarrow n \rho^+$ transition. They come from a decomposition of the 3×3 spin density matrix of the ρ^+ in a basis of 9 Hermitian matrices which represent the different polarization states of the virtual photon. The superscript α refers to the virtual photon polarization: $\alpha = 0 - 2$ for transverse photons, $\alpha = 4$ for longitudinal photons, and $\alpha = 5 - 6$ for the interference between transverse and longitudinal states. The subscripts refer to the vector meson polarization: $i, j = 0$ refer to a longitudinal polarization state and $i, j = 1, -1$ to a transverse polarization state. For example ρ_{00}^0 describes the probability of the transition between a transverse photon ($\alpha = 0$) and a longitudinal vector meson ($i, j = 0$) and ρ_{10}^0 is an interference term between the transverse ($i = 1$) and longitudinal ($j = 0$) meson helicity states produced by a transverse virtual photon ($\alpha = 0$).

If SCHC applies, then $\rho_{00}^0 = 0$ and $\rho_{00}^4 = 1$, i.e. if the virtual photon is longitudinal, the produced vector meson is also longitudinal (there is no longitudinal to transverse transition between the photon and the ρ^+). Then eq. 2.57 leads to a direct relation between the measured r_{00}^{04} (ratio between the longitudinal and the transverse polarization state of the meson that can be measured from the experimental distributions of $\cos \theta_{HS}$) and the ratio $R = \frac{\sigma_L}{\sigma_T}$. This relation is:

$$r_{00}^{04} = \frac{\epsilon R}{1 + \epsilon R}. \quad (2.58)$$

it is to be noted that this relation remains relatively stable in the case of small violation of SCHC (see the reference [56]).

We have seen in the previous section when we studied the $d\sigma/d\Phi$ distributions that our data are already compatible with SCHC. SCHC can be further tested by studying the integrated distributions $W(\phi_{HS})$. Integrating $W(\Phi, \cos \theta_{HS}, \phi_{HS})$ over $\cos \theta_{HS}$ and Φ yields:

$$W(\phi_{HS}) = \frac{1}{2\pi} [1 - 2r_{1-1}^{04} \cos 2\phi_{HS}] \quad (2.59)$$

which isolates r_{1-1}^{04} . This SDME contains the matrix element ρ_{1-1}^4 which violates SCHC. If SCHC applies, r_{1-1}^{04} should be 0 and the ϕ_{HS} distribution should be flat.

We extracted $d\sigma/d\phi_{HS}$ for each (Q^2, x_B) bin, after applying the same background subtraction procedure previously mentioned, for each (Q^2, x_B, ϕ_{HS}) bin (see the appendix G). By fitting the $d\sigma/d\phi_{HS}$ distributions (see figure 2.68) with the formula 2.59, we extracted r_{1-1}^{04} . This SDME is plotted in figure 2.69 as a function of Q^2 for fixed bins in x_B . It is clear that r_{1-1}^{04} is small compared to 1 and even, in almost all cases, compatible with 0.

We therefore think that it is reasonable to apply the formula 2.58 in order to extract $R = \frac{\sigma_L}{\sigma_T}$. Firstly, to extract r_{00}^{04} , we integrate $W(\Phi, \cos \theta_{HS}, \phi_{HS})$ (eq. 2.56) over the angles Φ and ϕ_{HS} , which yields:

$$W(\cos \theta_{HS}) = \frac{3}{4} [1 - r_{00}^{04} + (3r_{00}^{04} - 1) \cos^2 \theta_{HS}] \quad (2.60)$$

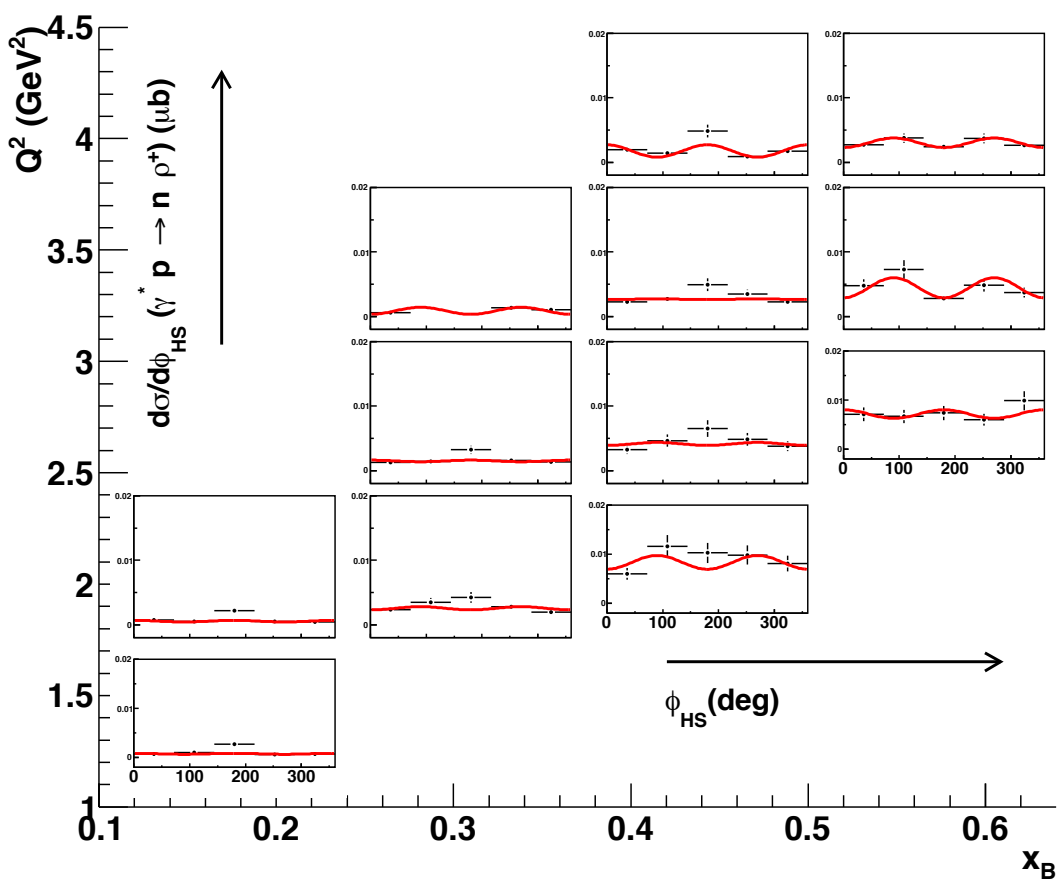


Figure 2.68: $d\sigma/d\phi_{HS}$ as a function of ϕ_{HS} for each (Q^2, x_B) bin for the reaction $\gamma^* p \rightarrow n \rho^+$. The red curve shows the fit of the data to the function 2.59.

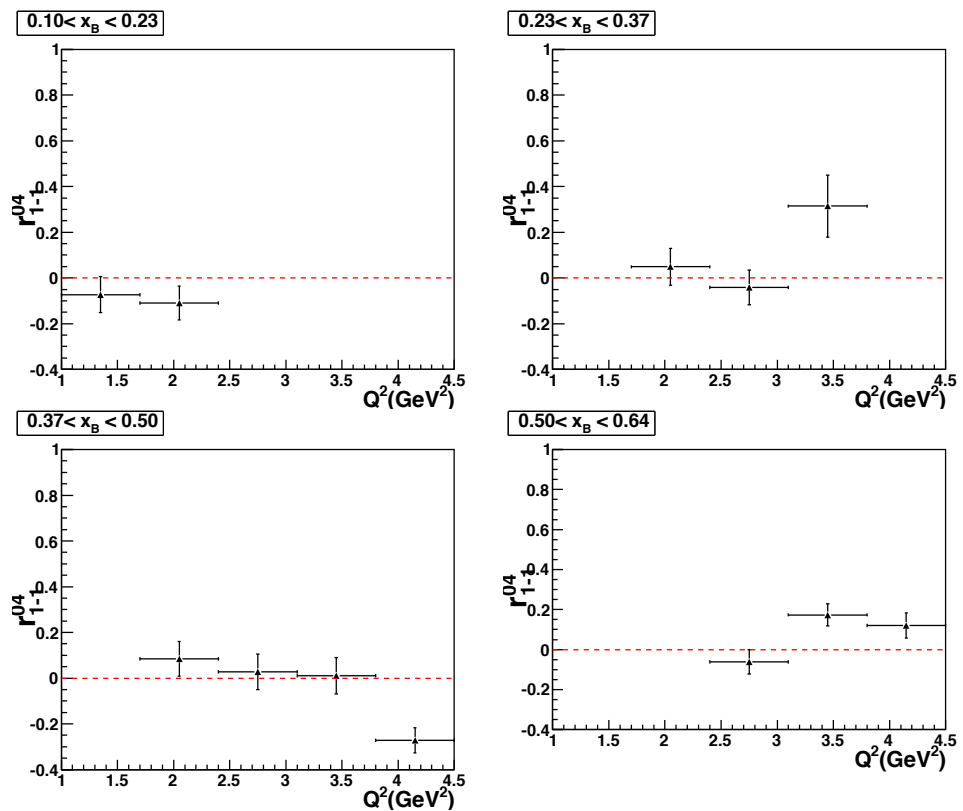


Figure 2.69: r_{1-1}^{04} as a function of Q^2 for fixed x_B bins, for the reaction $\gamma^* p \rightarrow n\rho^+$.

For statistical reasons, we did the extraction of r_{00}^{04} for only 4 (Q^2, x_B) bins (i.e. a reduced binning compared to the acceptance calculation). The fits on the invariant mass $M_{\pi^+\pi^0}$ for the non-resonant 2-pion subtraction are presented in the appendix H.

The extracted cross sections $d\sigma/d\cos\theta_{HS}$ are shown in figure 2.70. In figure 2.71,

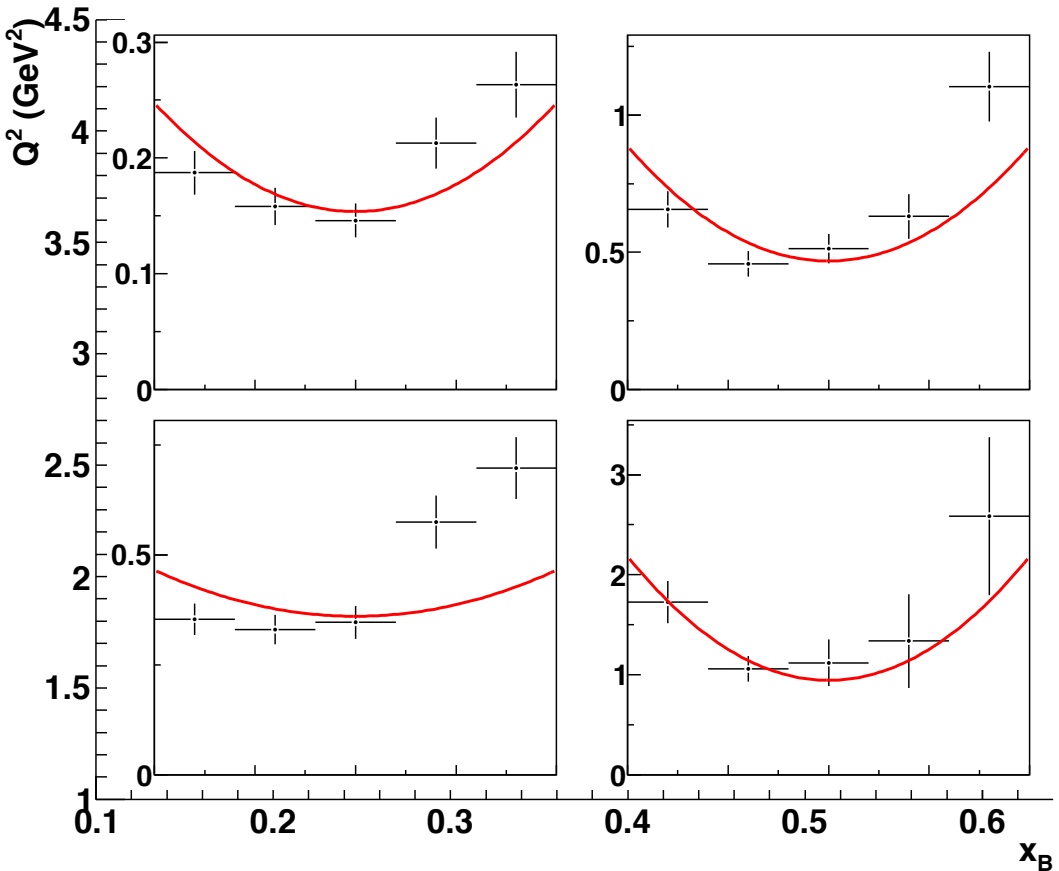


Figure 2.70: $d\sigma/d\cos\theta_{HS}$ as a function of $\cos\theta_{HS}$ for our 4 (Q^2, x_B) bins, for the reaction $\gamma^* p \rightarrow n\rho^+$. The red curve shows the fit to the data of the function of eq.2.60.

we compare the distributions of $\cos\theta_{HS}$ before and after the background subtraction. We note that the unsubtracted distribution is highly asymmetrical. After the background subtraction, the distributions $\cos\theta_{HS}$ should be totally symmetrical in $\cos\theta_{HS}$ according to the formula 2.60. But, as we can observe on the figure 2.70, it remains some asymmetry in the $\cos\theta_{HS}$ distribution, for some (Q^2, x_B) bins. These asymmetries show that our method of background subtraction did not manage (in some bins) to perfectly isolate the ρ^+ signal. In absence of a detailed theoretical description and understanding of the channels contributing to the $n\pi^+\pi^0$ final state, we think that it is difficult to do better than what we did.

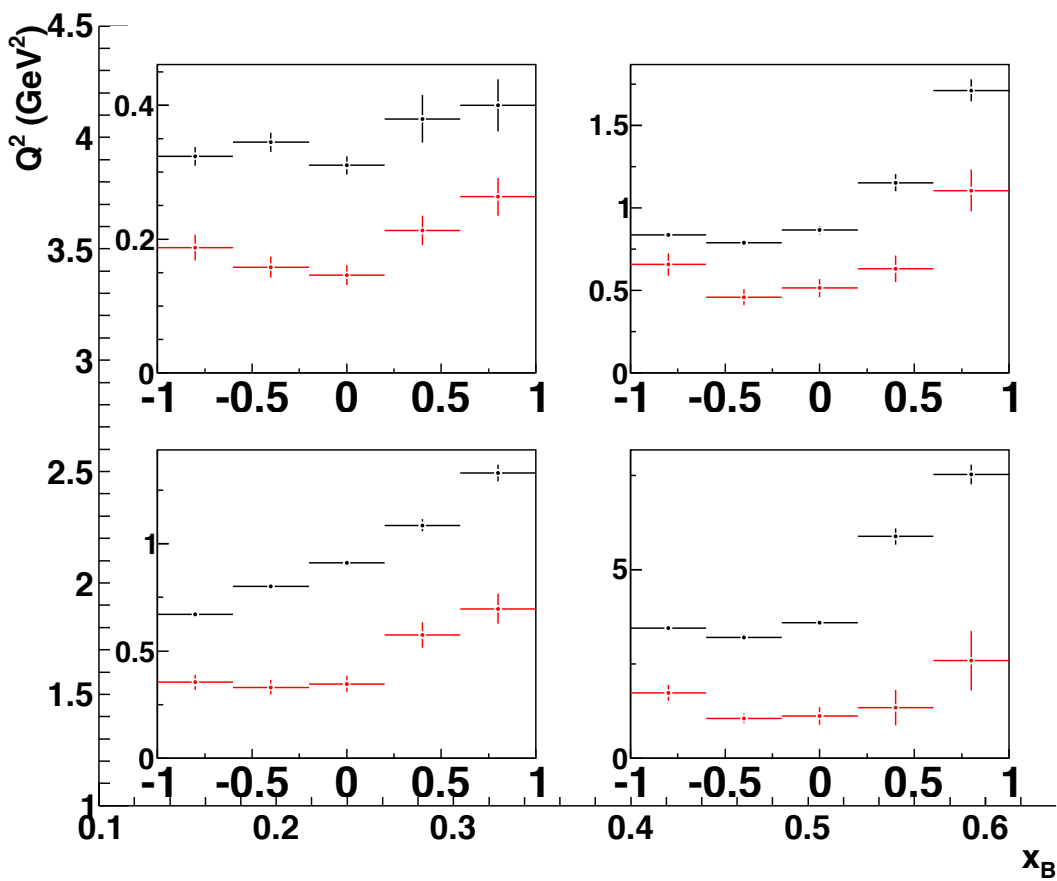


Figure 2.71: Distribution of $d\sigma/d \cos \theta_{HS}$ for the 4 (Q^2, x_B) bins, before (in black) and after (in red) the subtraction of the non-resonant 2 pions background. The error bars are purely statistics.

By fitting $d\sigma/d \cos \theta_{HS}$ with the formula 2.60, we then extract r_{00}^{04} . Figure 2.72 shows r_{00}^{04} as a function of Q^2 for fixed bins in x_B .

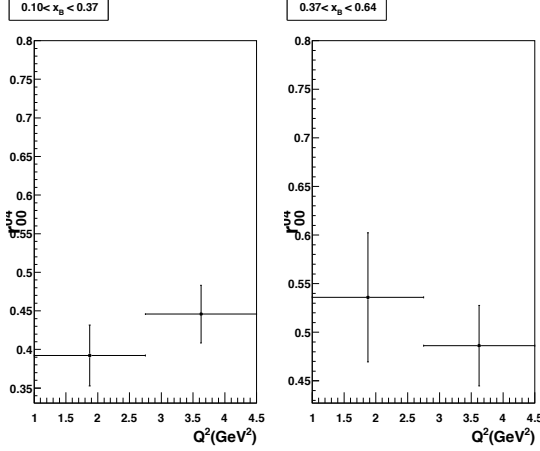


Figure 2.72: r_{00}^{04} as function of Q^2 for each x_B bin, for our reaction $\gamma^* p \rightarrow n\rho^+$.

Under the assumption of SCHC, the ratio R can then be extracted as:

$$R = \frac{\sigma_L}{\sigma_T} = \frac{1}{\epsilon} \frac{r_{00}^{04}}{1 - r_{00}^{04}}. \quad (2.61)$$

Figure 2.73 shows the extracted ratio R as a function of Q^2 for our 2 x_B bins. Although error bars are quite large, one can infer that $R > 1$ and has a trend to increase with Q^2 (a linear rise is a prediction of pQCD).

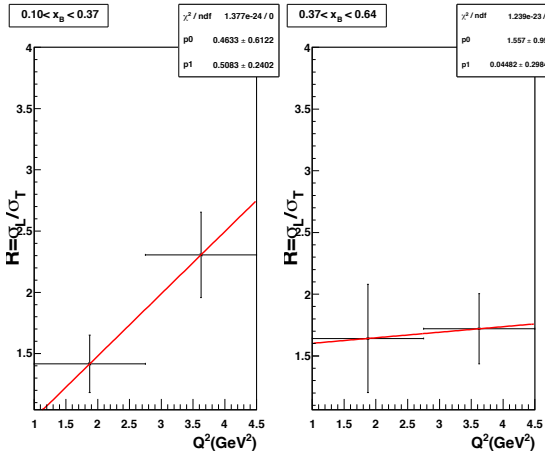


Figure 2.73: The ratio $R = \frac{\sigma_L}{\sigma_T}$ as function of Q^2 for each x_B bin, for the reaction $\gamma^* p \rightarrow n\rho^+$.

We parametrize the Q^2 dependence of R by making a linear fit. Then, we extract σ_L and σ_T from:

$$\sigma_L = \frac{R}{1 + \epsilon R} \sigma. \quad (2.62)$$

$$\sigma_T = \frac{1}{1 + \epsilon R} \sigma. \quad (2.63)$$

The resulting values for σ , σ_L and σ_T for the $\gamma^* p \rightarrow n \rho^+$ reaction are shown in figure 2.74.

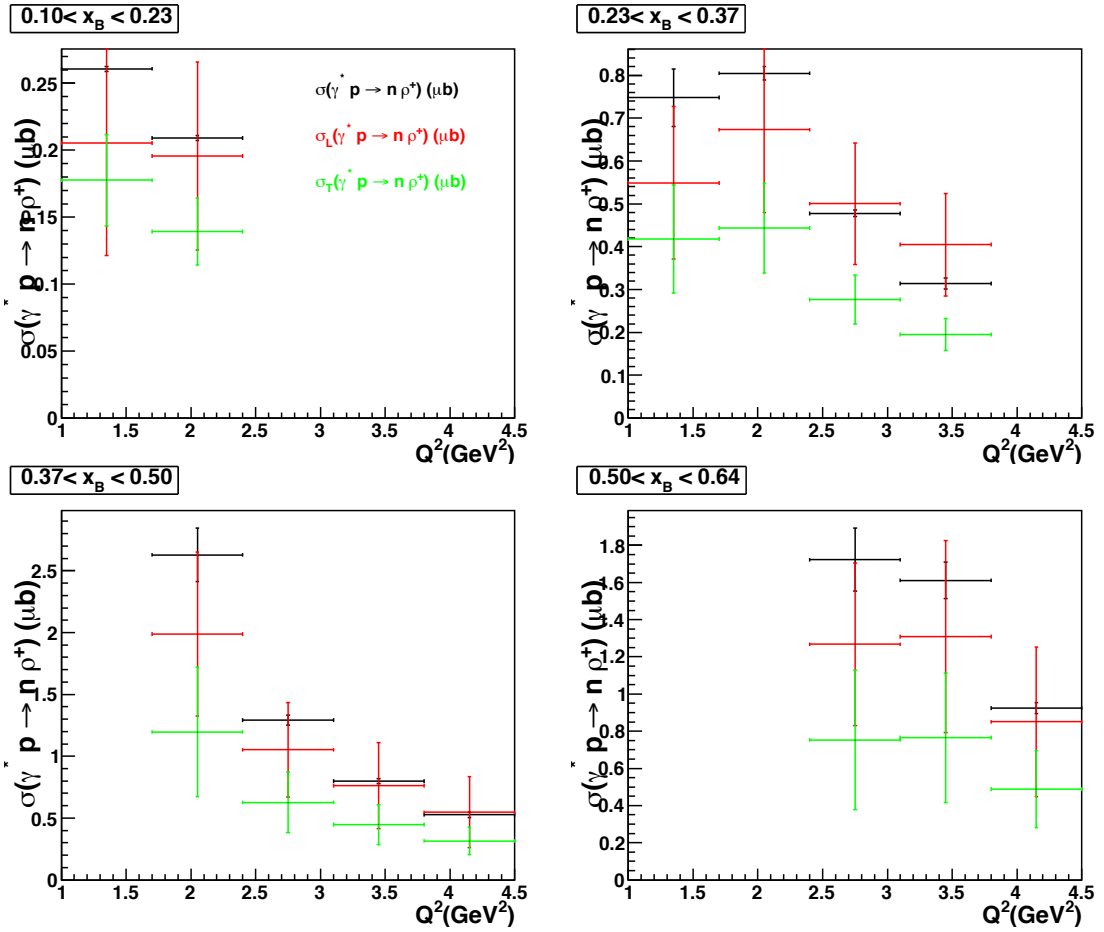


Figure 2.74: Reduced cross sections σ_L (in red), σ_T (in green) and σ (in black) for the reaction $\gamma^* p \rightarrow n \rho^+$, as a function of Q^2 for each bin in x_B .

2.4.6 Estimation of systematic errors

We detail in this section the systematic errors which are proper to our analysis. There are general sources of systematic errors which are common to all CLAS runs: the efficiency of

the Čerenkov detectors and of the EC electromagnetic calorimeters, the corrections due to the density and the width of the target, the integrated charge of the beam,... However, these latter are of the order of the percent (see for example ref. [24]) and are smaller than the ones which we are going to present.

Global normalization factor

The systematic uncertainty resulting from the global normalization factor F_n from section 2.3.6 was estimated at 5%.

Exclusivity cuts

As presented in section 2.4.4, in order to select the neutron and the π^0 of the final state of the reaction $ep \rightarrow en\rho^+ \rightarrow en\pi^+\pi^0$, we applied two exclusivity cuts. The first one is a 3σ cut on the invariant mass of the two decaying photons $IM(\gamma\gamma)$ around the π^0 mass. The second one is a 3σ cut on the missing mass $M_X(eX\pi^+\pi^0)$ around the neutron mass. We extracted and estimated the variations of the $\gamma^*p \rightarrow n\rho^+$ cross sections caused by the change of the exclusivity cuts and used these variations as systematic errors. We varied the 3σ cut to 2σ and 4σ cuts. We thus ended up with eight different configurations that we compared with the "standard" one (3σ cut on $IM(\gamma\gamma)$ and $M_X(eX\pi^+\pi^0)$). The configurations that we studied are thus the following (see the appendix J for the results of the fits for each case):

- 3 σ cut on $IM(\gamma\gamma)$ and 2 σ cut on $M_X(eX\pi^+\pi^0)$
- 3 σ cut on $IM(\gamma\gamma)$ and 4 σ cut on $M_X(eX\pi^+\pi^0)$
- 2 σ cut on $IM(\gamma\gamma)$ and 3 σ cut on $M_X(eX\pi^+\pi^0)$
- 4 σ cut on $IM(\gamma\gamma)$ and 3 σ cut on $M_X(eX\pi^+\pi^0)$
- 2 σ cut on $IM(\gamma\gamma)$ and 2 σ cut on $M_X(eX\pi^+\pi^0)$
- 2 σ cut on $IM(\gamma\gamma)$ and 4 σ cut on $M_X(eX\pi^+\pi^0)$
- 4 σ cut on $IM(\gamma\gamma)$ and 2 σ cut on $M_X(eX\pi^+\pi^0)$
- 4 σ cut on $IM(\gamma\gamma)$ and 4 σ cut on $M_X(eX\pi^+\pi^0)$

Figure 2.75 shows the comparison between the corresponding eight $\gamma^*p \rightarrow n\rho^+$ cross sections compared with the "standard" one (in black). We define the relative systematic error for each (Q^2, xB) bin as the difference between the configuration i and the standard one divided by the standard one:

$$\delta_i^{sys} = \frac{|\sigma_0 - \sigma_i|}{\sigma_0}. \quad (2.64)$$

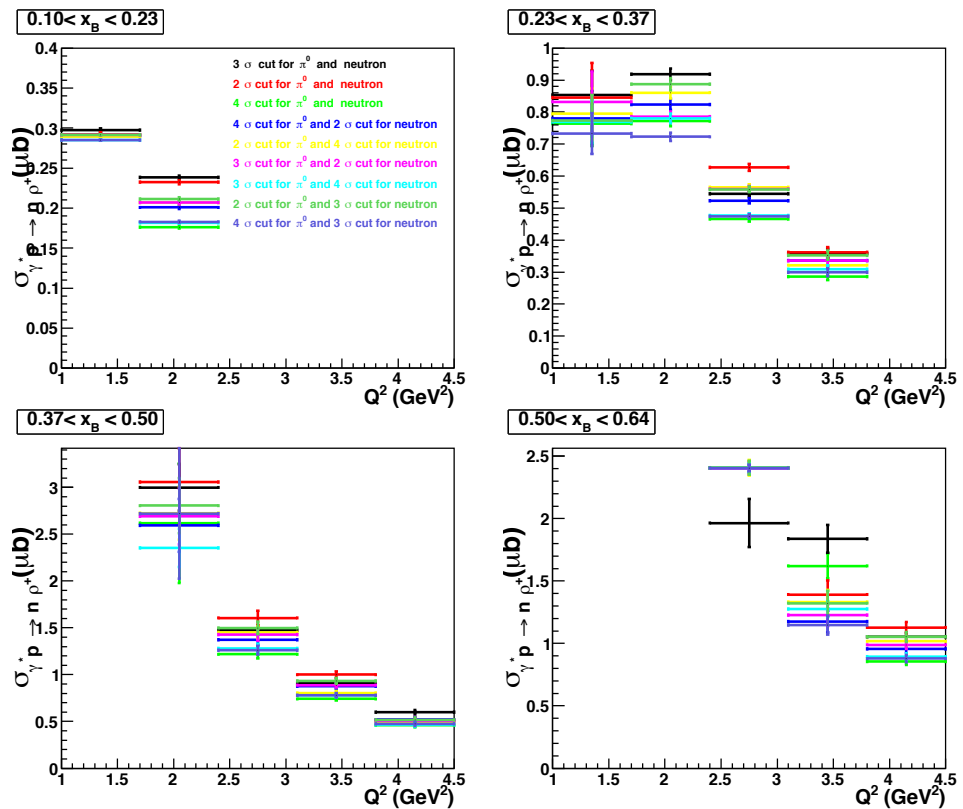


Figure 2.75: Comparison between the standard cross sections $\gamma^* p \rightarrow n\rho^+$ and those calculated with the eight other exclusivity cuts configurations.

We define the resulting systematic error in the (Q^2, x_B) bin as the "quadratic average" of all the δ_i^{sys} . We denote it as δ_{source}^{exclu} .

$$(\delta_{exclu}^{sys})^2 = \frac{\sum_i (\delta_i^{sys})^2}{n}. \quad (2.65)$$

where n is the number of configurations (in this study $n = 8$).

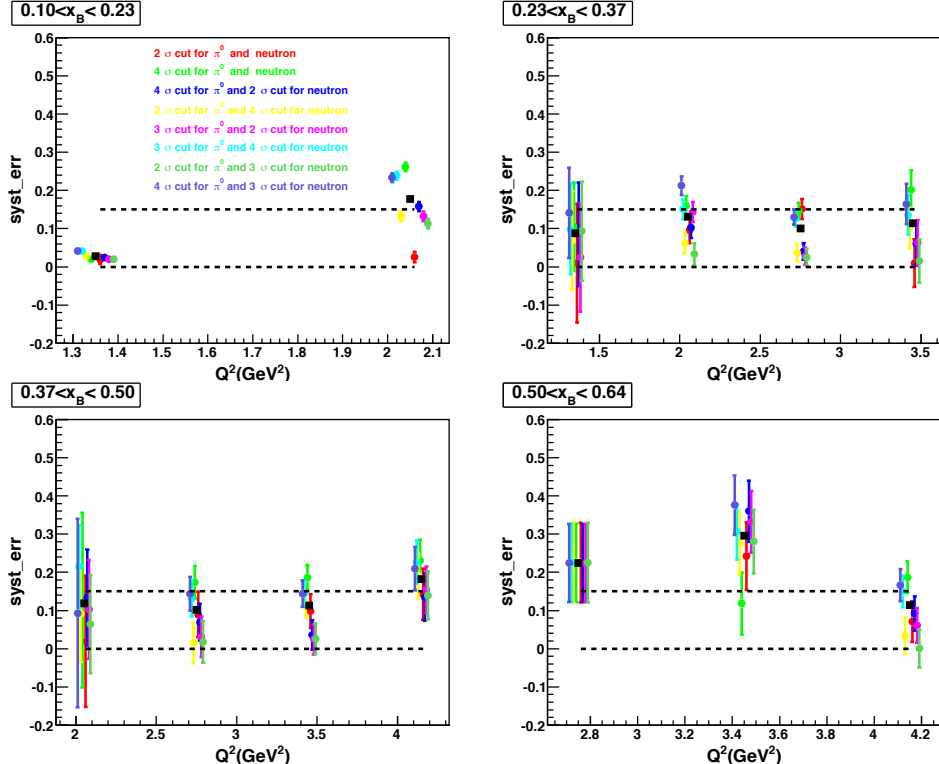


Figure 2.76: Systematic errors due the variation of the exclusivity cuts. Each color corresponds to a different configuration. The solid black square is the total systematic error for each (Q^2, x_B) bin.

Figure 2.76 shows the extracted systematics errors for each (Q^2, x_B) bin. The black solid square corresponds to δ_{exclu}^{sys} for each bin.

Model dependance of acceptances

The determination of the CLAS acceptance for our process is another source of systematic error. Indeed, because of the finite bin width, our acceptance will differ slightly according to the model used in the event generator. We studied this effect by calculating the acceptance with 3 different models. In the first model (the "standard" one), we mix 700 millions generated events of the ρ^+ channel ($\approx 60\%$) with 500 millions generated events of the phase space channel ($\approx 40\%$). In the second model, we mix 250 millions generated

events of the ρ^+ channel ($\approx 33\%$) with 500 millions of generated events of the phase space channel ($\approx 67\%$). The third model, we mix 500 millions generated events of the ρ^+ channel ($\approx 67\%$) with 250 millions of generated events of the phase space channel ($\approx 33\%$).

We calculated the total cross section $\gamma^* p \rightarrow n\pi^+\pi^0$ with the results of the four acceptances. Ideally, in the limit of large statistics and very small 7-D bin size, one would find the same acceptances and so the same cross sections. In practice, we find differences of the order of 10% in average. Figure 2.77 shows the comparison between the "standard" cross section produced with the first model acceptance (in black) and the cross section produced with the two other model acceptances (in color). The systematic errors due to this model dependence for the acceptance are computed with the same method used in the previous section (see eqs.2.64 and 2.65). Figure 2.78 shows the extracted systematics errors for each (Q^2, x_B) bin. The black solid square corresponds to the total δ_{acc}^{sys} for each bin.

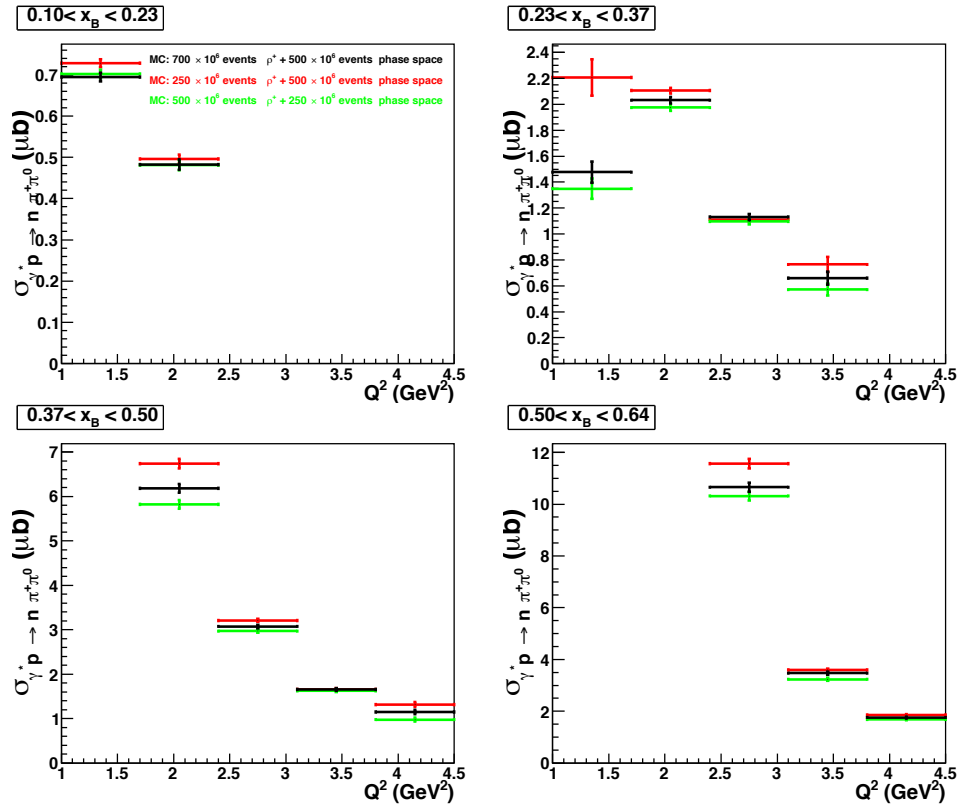


Figure 2.77: Comparison between cross sections $\gamma^* p \rightarrow n\pi^+\pi^0$ calculated with 3 different models for the acceptance. The error bars are purely statisticcs.

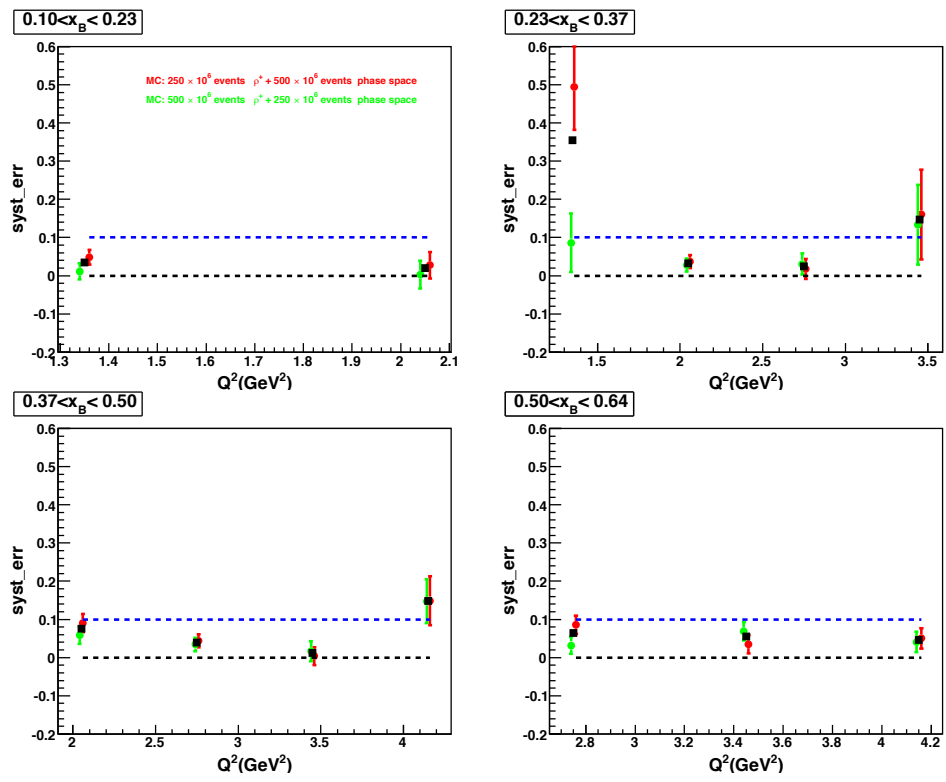


Figure 2.78: Systematic error estimated from the comparison between the standard $\gamma^* p \rightarrow n\pi^+\pi^0$ cross section and those calculated with 2 other models for the acceptance.

Acceptance table binning dependance

In order to estimate the dependance of the acceptance and thus of the cross sections on the binning of the acceptance table, we extracted the cross sections $\gamma^* p \rightarrow n\pi^+\pi^0$ for 3 different binnings. These binnings are described in the table 2.8 below. The first row is the "standard" binning which we have used so far. The Q^2 and x_B binnings were kept constant in order to ease the comparison between the different tables.

Variable	$Q^2(GeV^2)$	x_B	$-t(GeV^2)$	$M_{\pi^+\pi^0}(GeV)$	$\Phi(deg)$	$\cos \theta_{HS}$	$\phi_{HS}(deg)$	Total
Range	1. → 4.5	0.1 → 0.64	0. → 3.5	0.4 → 1.4	0. → 360.	-1 → 1.	0. → 360.	
Table 1	5	4	4	10	5	5	5	1
Table 2	5	4	3	8	4	4	4	
Table 3	5	4	5	12	6	6	6	

Table 2.8: Binnings for the 3 acceptance tables

Figure 2.79 shows the $\gamma^* p \rightarrow n\pi^+\pi^0$ cross sections as a function of Q^2 for each x_B extracted with the 3 acceptance table binnings. The standard cross sections are in black and the two others are in color. Figure 2.80 shows the extracted systematics errors for each (Q^2, x_B) bin. The black solid square corresponds the δ_{bin}^{sys} for each bin. We find δ_{bin}^{sys} of the order of 5% in average.

Background subtraction

Another important source of systematic error in our analysis comes from the subtraction of the non-resonant 2-pion background under the ρ^+ peak. As mentioned before, this procedure is very simplified and model dependent: we sum at the level of cross sections a simple phase space $n\pi^+\pi^0$ and a skewed Breit-Wigner. This approach takes into account only in an approximative and phenomenological way the interference (that are currently impossible to control precisely) between the $n\rho^+$ channel and the other channels leading to the same final state $n\pi^+\pi^0$. It is not easy to estimate the systematic error associated to this procedure. As a start, we fix the skewness parameter of the Breit-Wigner function to $n_{skew} = 2$ and $n_{skew} = 3$ and compare the extracted ρ^+ cross sections with the standard case where we let the n_{skew} parameter vary ($0 \leq n_{skew} \leq 5$).

Figure 2.81 shows the extracted $\gamma^* p \rightarrow n\rho^+$ cross sections corresponding to the 3 topologies described above (the $M_{\pi^+\pi^0}$ fits are in figures I.1 and I.2 in appendix I). A systematic error was then extracted according to formulae 2.64 and 2.65. Figure 2.82 shows the extracted systematic errors. δ_{back1}^{sys} is of the order of 20%.

Another study we carried out was to vary the composition of the background under the ρ^+ peak. In addition to the phase space continuum $\pi^+\pi^0$ that we used so far to extract our cross sections, we now add the $\pi^+\pi^0$ projection from the Δ^+ and the Δ^0 channels. Thus, three configurations are studied:

- Only phase space non-resonant $\pi^+\pi^0$ continuum: see the $M_{\pi^+\pi^0}$ fits in figure 2.61.

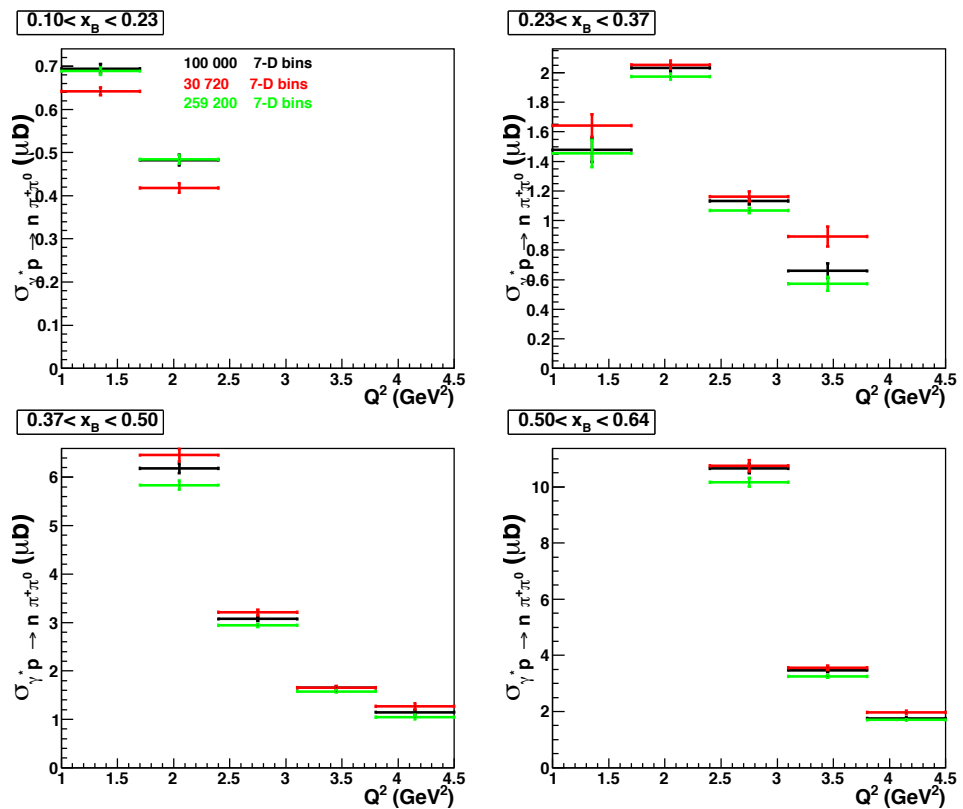


Figure 2.79: Comparison between the $\gamma^* p \rightarrow n\pi^+\pi^0$ cross sections calculated using 3 different acceptance table binnings.

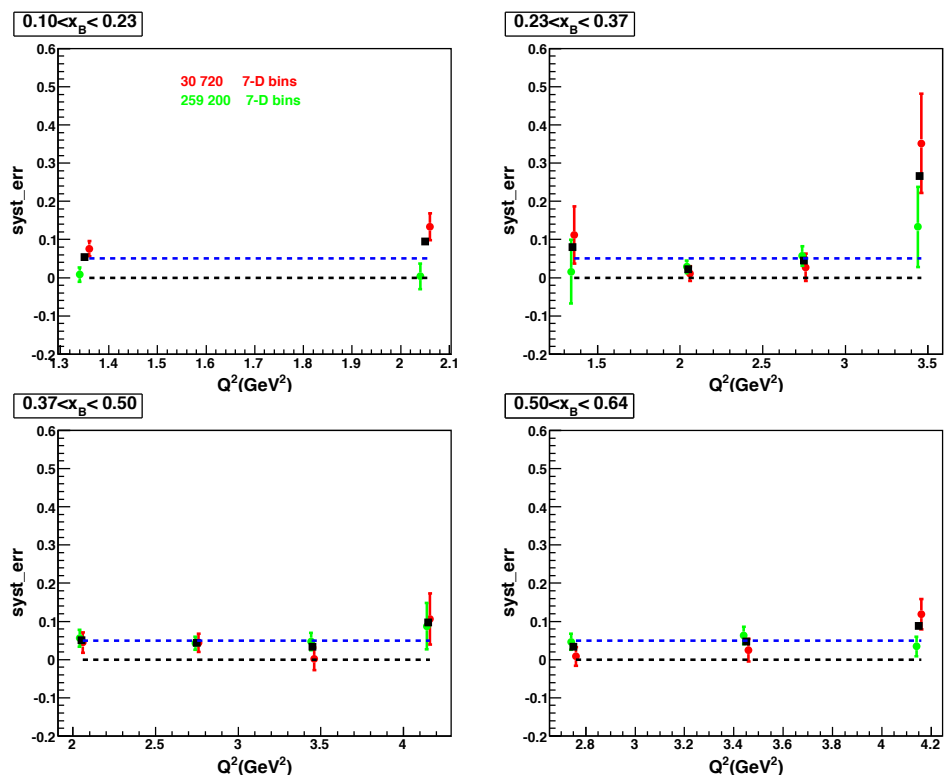


Figure 2.80: Systematic error estimated from the comparison between the $\gamma^* p \rightarrow n\pi^+\pi^0$ cross sections using 3 different acceptance table binnings.

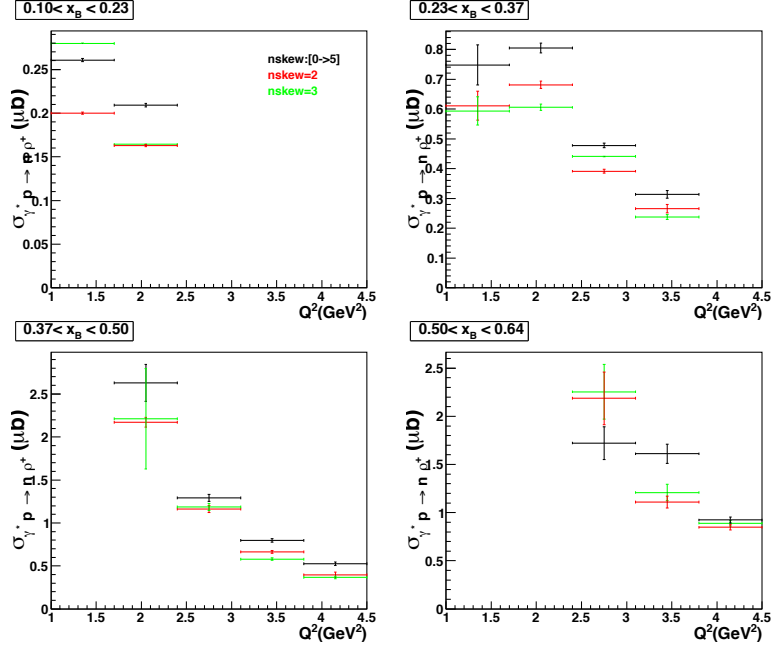


Figure 2.81: Comparison between the $\gamma^* p \rightarrow n\rho^+$ cross sections extracted by fitting the ρ^+ peak with a Breit-Wigner function corresponding to 3 different conditions on n_{skew} : $0 \leq n_{skew} \leq 5$ (in black), $n_{skew} = 2$ (in red) and $n_{skew} = 3$ (in green).

- Phase space non-resonant $\pi^+\pi^0$ continuum + $(\Delta^+ + \Delta^0)$ contributions: see $M_{\pi^+\pi^0}$ fits in figure 2.83.
- Phase space non-resonant $\pi^+\pi^0$ continuum + Δ^0 contribution: see $M_{\pi^+\pi^0}$ fits in figure 2.84.

The $\gamma^* p \rightarrow n\rho^+$ cross sections were extracted for each of the 3 configurations listed above. Figure 2.85 shows the comparison between the standard cross sections (background fitted with only the phase space non-resonant $\pi^+\pi^0$ continuum) and the two other configurations. The systematic error was then extracted according to the formulae 2.64 and 2.65. Figure 2.86 shows the extracted systematic errors. δ_{back2}^{sys} is in general less than 10%.

We decide to take for our total systematic error associated to the background non-resonant 2-pion subtraction the quadratic average of δ_{back1}^{sys} and δ_{back2}^{sys} .

Total systematic uncertainties and summary

The total systematic uncertainty δ_{tot}^{sys} for our $\gamma^* p \rightarrow n\rho^+$ cross sections was extracted for each of our (Q^2, x_B) bin as the quadratic sum of all the systematics uncertainties δ_{source}^{sys} . Figure 2.87 shows our $\gamma^* p \rightarrow n\rho^+$ final cross sections with their statistical uncertainties (black points and error bars), as a function of Q^2 for each x_B bin. The systematic

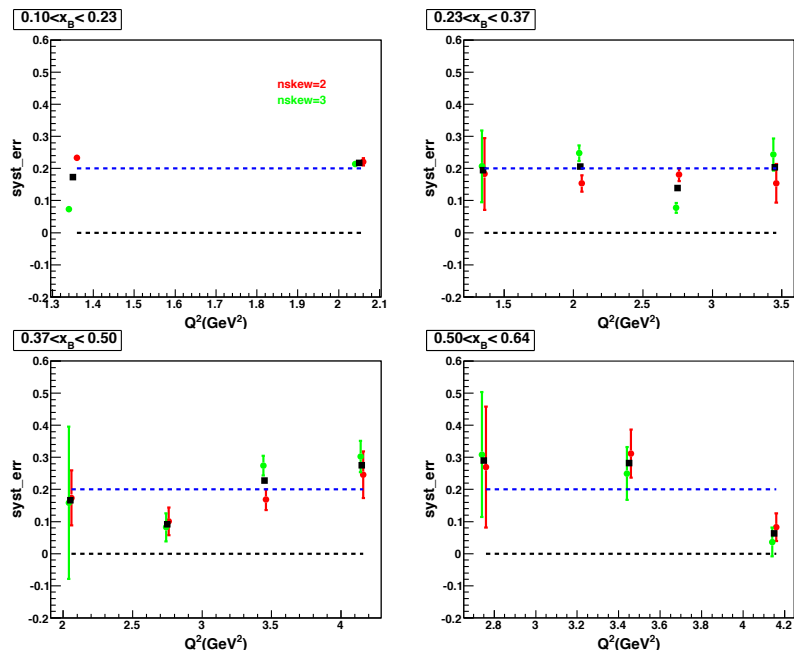


Figure 2.82: Systematic error estimated from the comparison between the cross sections $\gamma^* p \rightarrow n\rho^+$ extracted by fitting the ρ^+ peak with a skewed Breit-Wigner function (n_{skew} left to vary within $0 \leq n_{skew} \leq 5$) and two other cases where: $n_{skew} = 2$ (in red) and $n_{skew} = 3$ (in green).

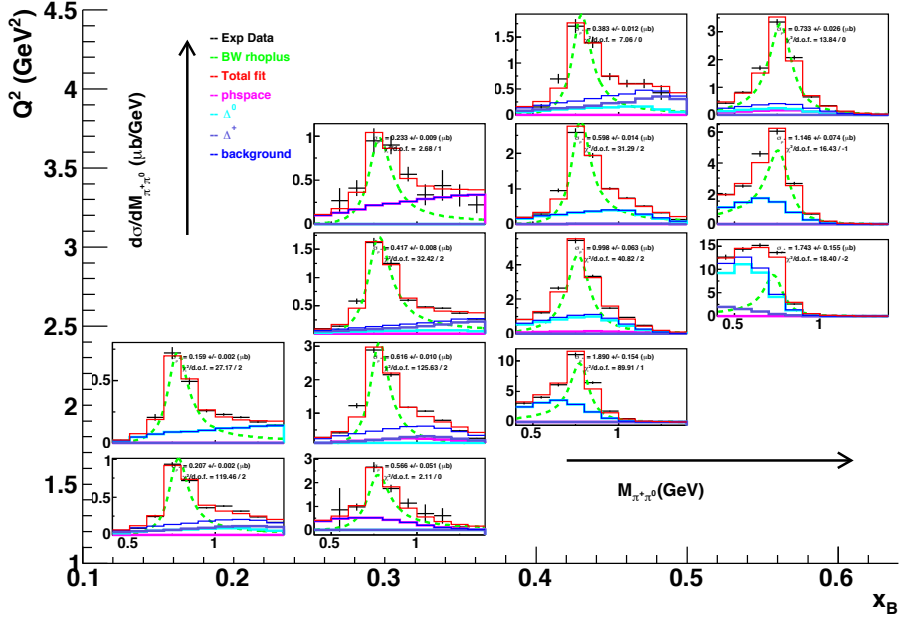


Figure 2.83: Fits to the $IM(\pi^+\pi^0)$ for each (Q^2, x_B) bin. The ρ^+ peak is fitted with a skewed Breit-Wigner function and the background is fitted with 3 components: phase space + Δ^+ + Δ^0 .

uncertainties computed for the various sources are shown with colored bands in the bottom part of the plots. The black lowest band is the total systematic uncertainty.

For the 3-fold differential cross sections, we will assign to all points the systematic error of the (Q^2, x_B) point.

Table 2.9 lists all the systematic uncertainties that we evaluated with their values averaged over all the bins.

Source of systematic error	Estimated error (in %)
Global normalization factor	5%
Exclusivity cuts	13.7%
Acceptance models	8%
Acceptance table binning	7%
Background subtraction	15%
Total(quadratic sum)	25.8%

Table 2.9: Summary of all systematic uncertainties (in %) averaged over all the Q^2, x_B bins.

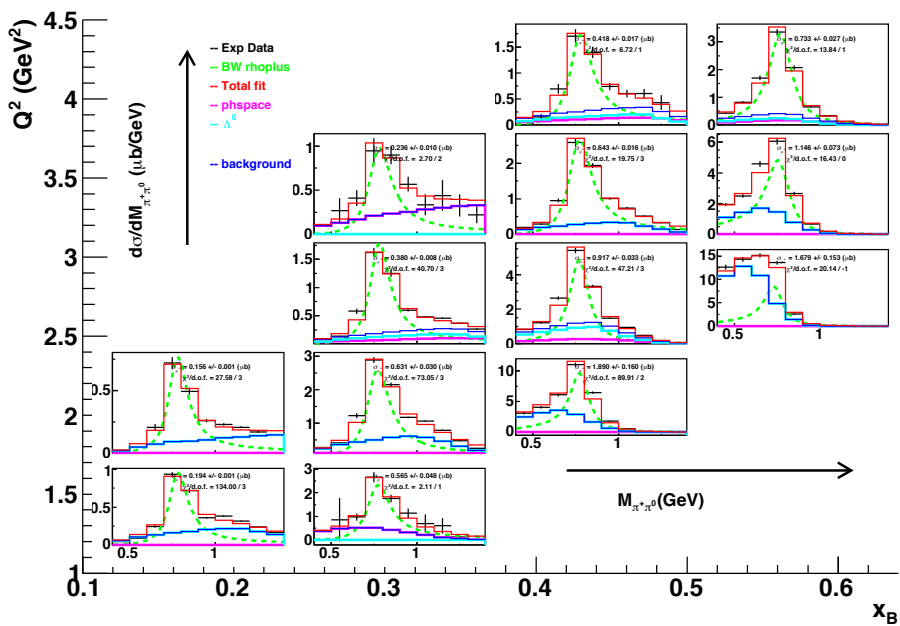


Figure 2.84: Fits to the $IM(\pi^+\pi^0)$ for each (Q^2, x_B) bin. The ρ^+ peak is fitted with a skewed Breit-Wigner function and the background is fitted with 2 components: phase space + Δ^0 .

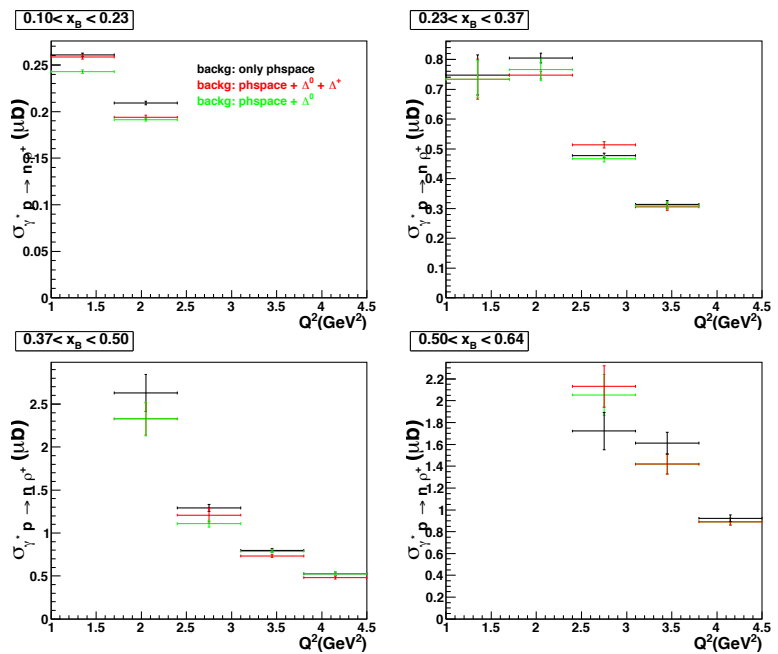


Figure 2.85: Comparison between the $\gamma^* p \rightarrow n \rho^+$ cross sections extracted by fitting the ρ^+ background with only a phase space contribution and two other cases: phase space + $(\Delta^+ + \Delta^0)$ contributions (in red) and phase space + Δ^0 contribution (in green).

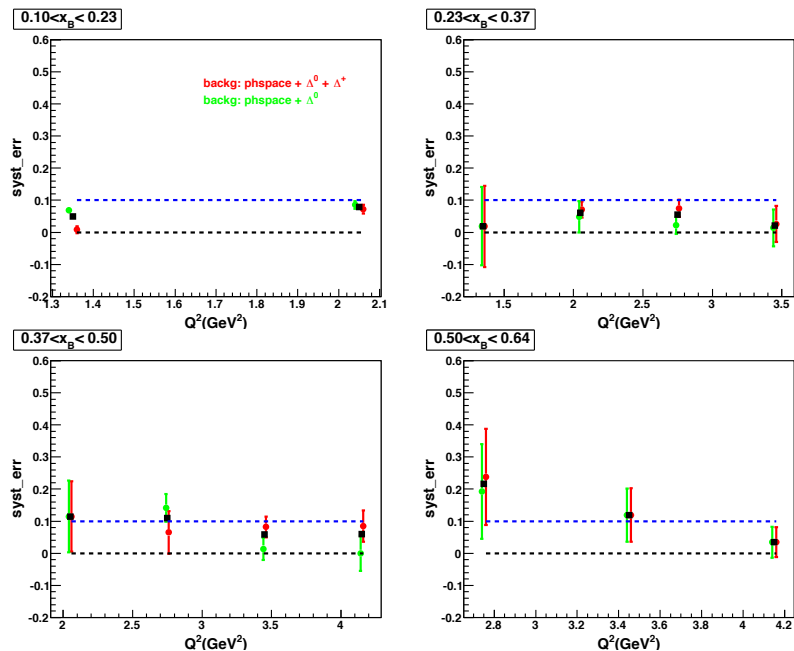


Figure 2.86: Systematic error estimated from the comparison between the $\gamma^* p \rightarrow n\rho^+$ cross sections extracted by fitting the ρ^+ background with only a phase space and two other cases: phase space + ($\Delta^+ + \Delta^0$) contributions (in red) and phase space + Δ^0 contribution (in green). The solid square is the total systematic error for each (Q^2, x_B) bin.

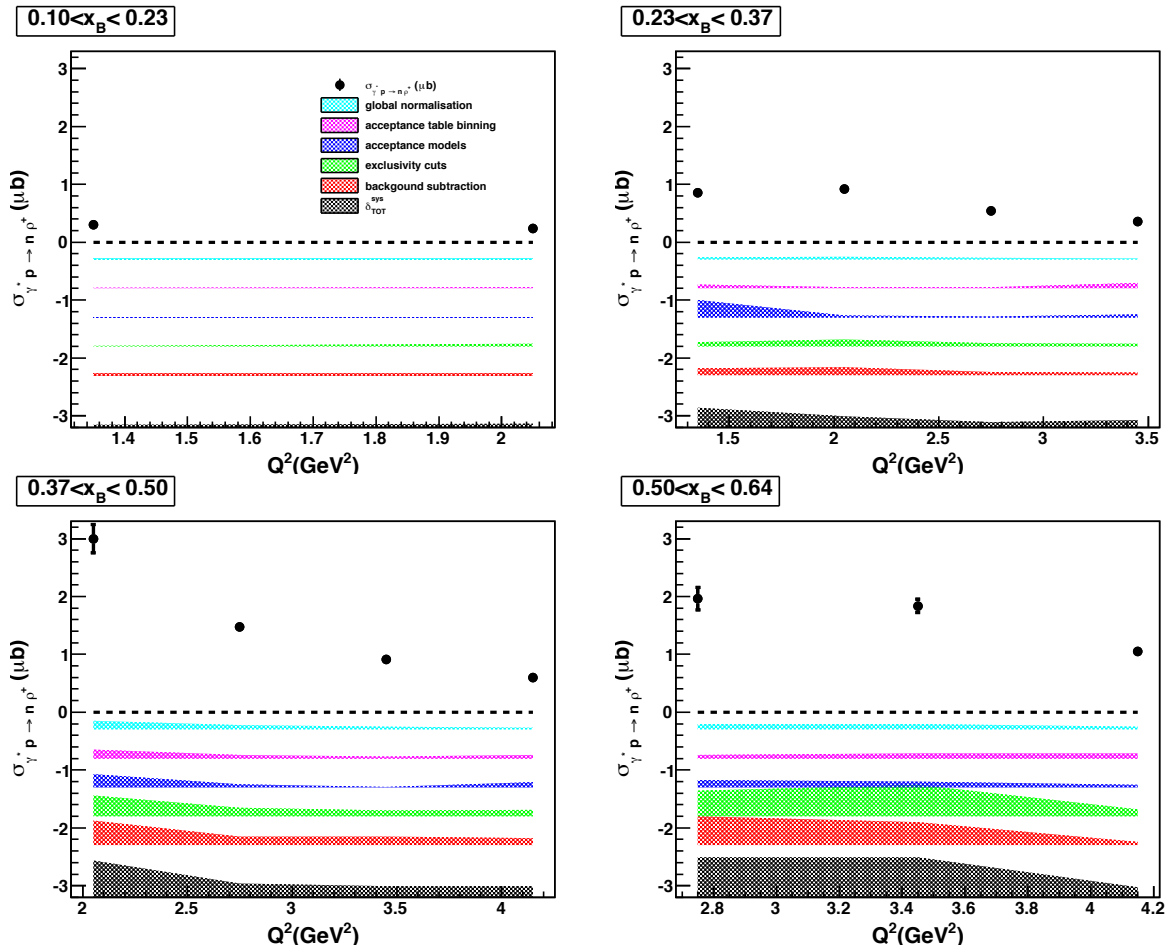


Figure 2.87: Total $\gamma^* p \rightarrow n p^+$ cross sections as a function of Q^2 for each x_B bin. The systematic uncertainties computed for the various sources are shown with colored bands in the bottom. The lowest black band is the total systematic uncertainty.

Appendix A

Acceptance hole factor for each (Q^2, x_B, t) bin

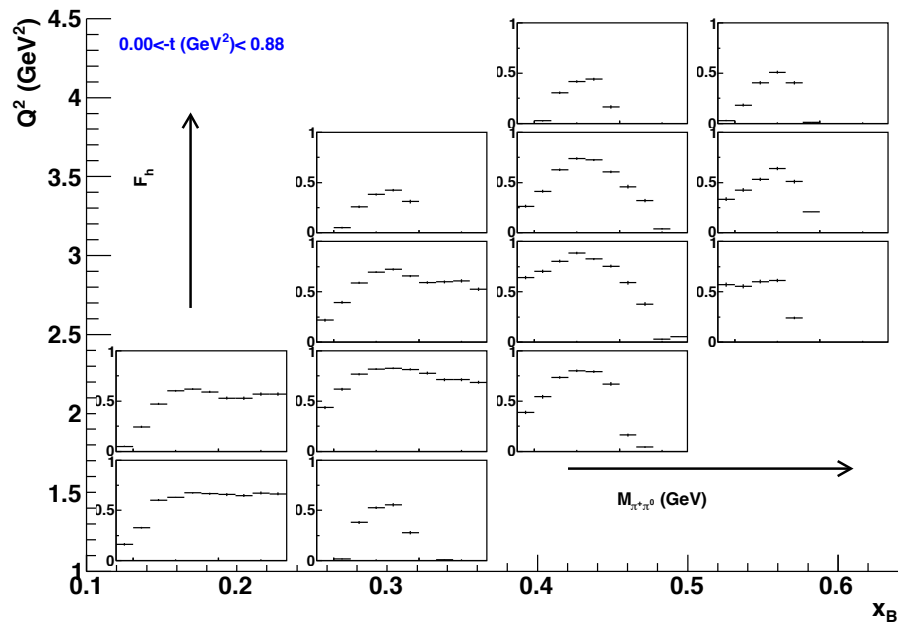


Figure A.1: The hole factor as a function of $M_{\pi^+\pi^0}$ for each (Q^2, x_B) bin and fixed t .

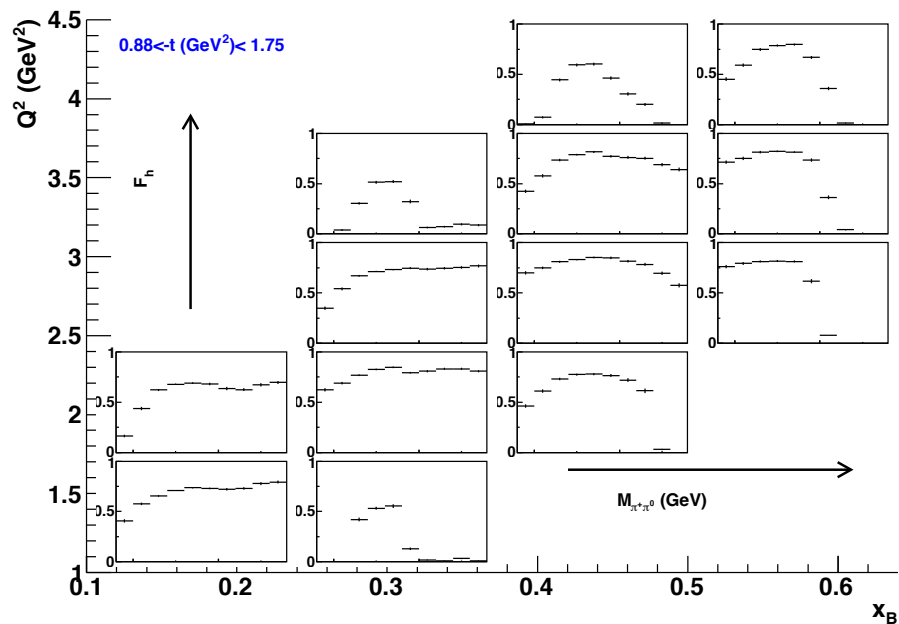


Figure A.2: The hole factor as a function of $M_{\pi^+\pi^0}$ for each (Q^2, x_B) bin and fixed t .

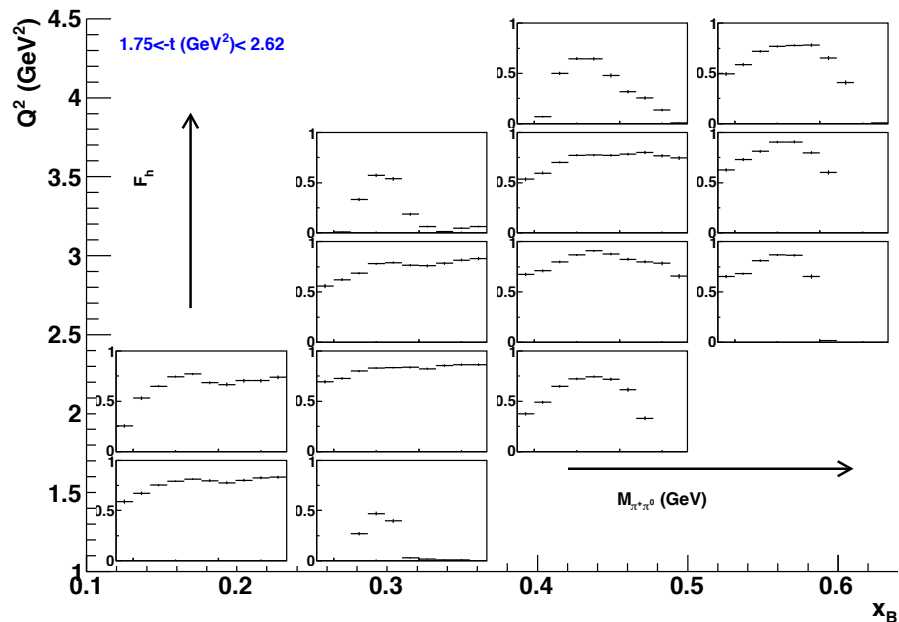


Figure A.3: The hole factor as a function of $M_{\pi^+\pi^0}$ for each (Q^2, x_B) bin and fixed t .

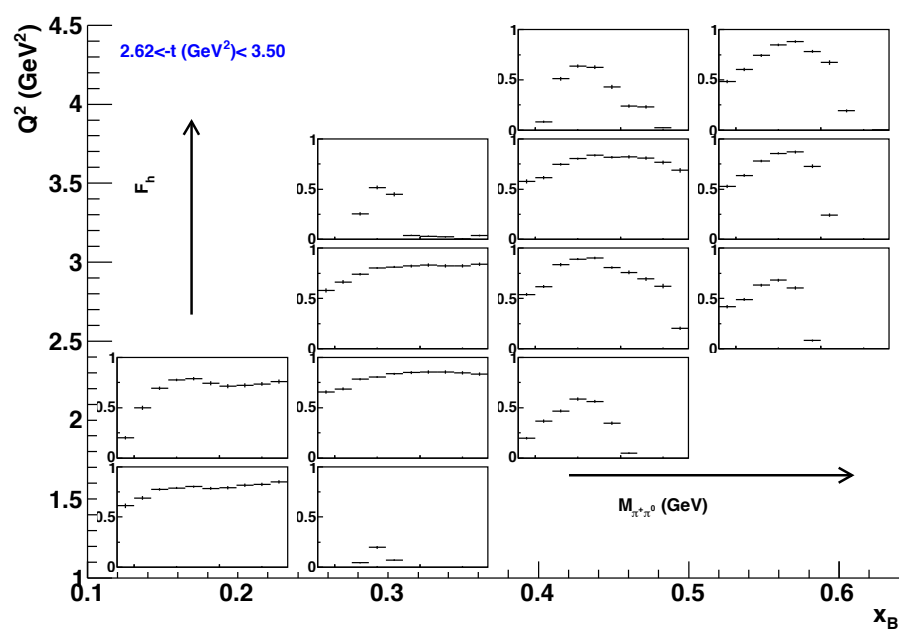


Figure A.4: The hole factor as a function of $M_{\pi^+\pi^0}$ for each (Q^2, x_B) bin and fixed t .

Appendix B

Acceptance hole factor for each (Q^2, x_B, Φ) bin

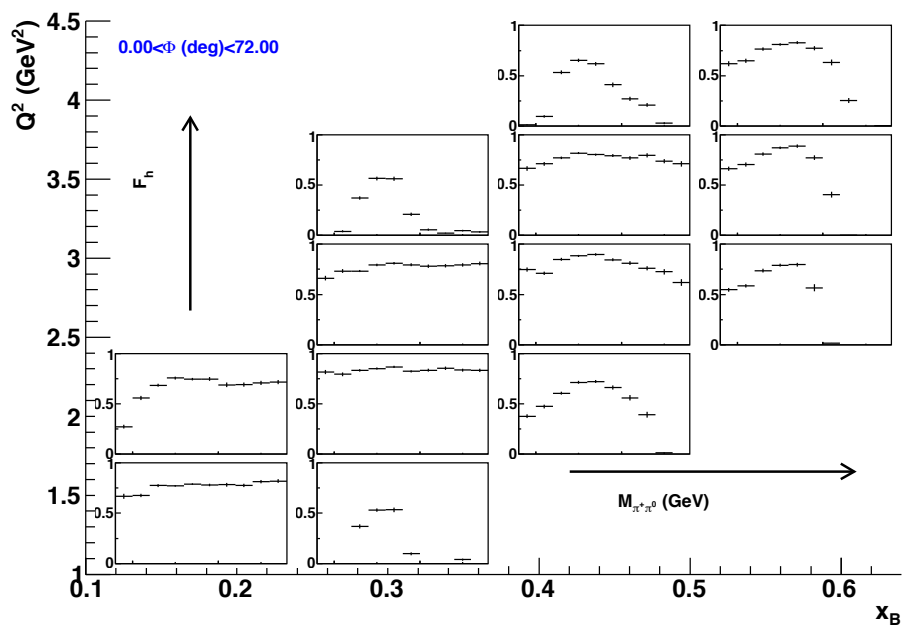


Figure B.1: The hole factor as a function of $M_{\pi^+\pi^0}$ for each (Q^2, x_B) bin and fixed Φ .

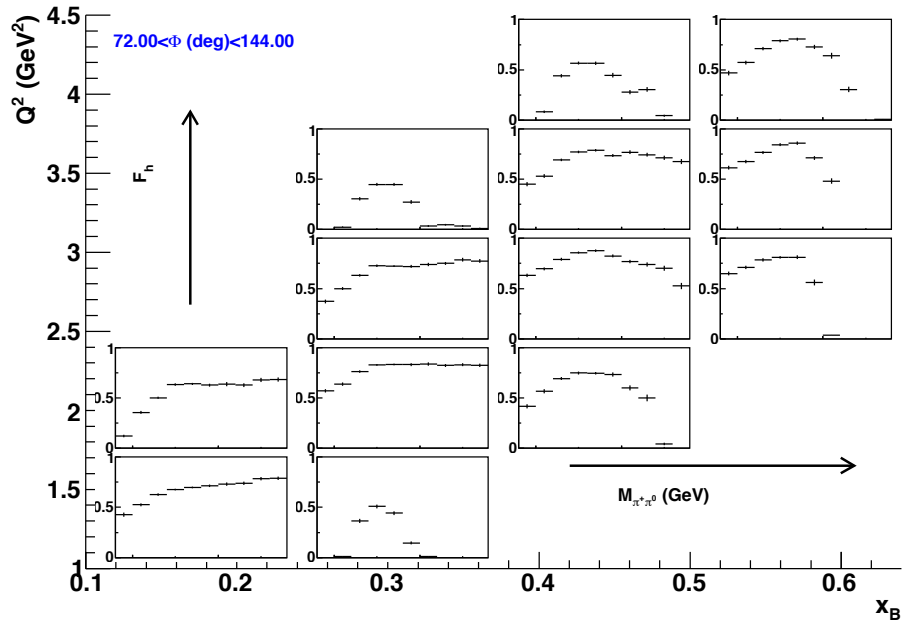


Figure B.2: The hole factor as a function of $M_{\pi^+\pi^0}$ for each (Q^2, x_B) bin and fixed Φ .

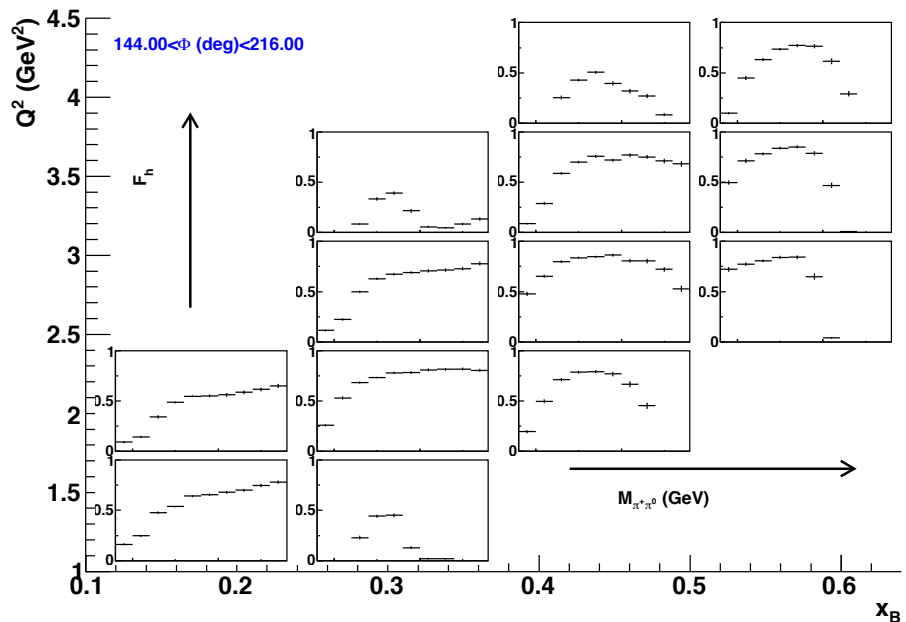


Figure B.3: The hole factor as a function of $M_{\pi^+\pi^0}$ for each (Q^2, x_B) bin and fixed Φ .

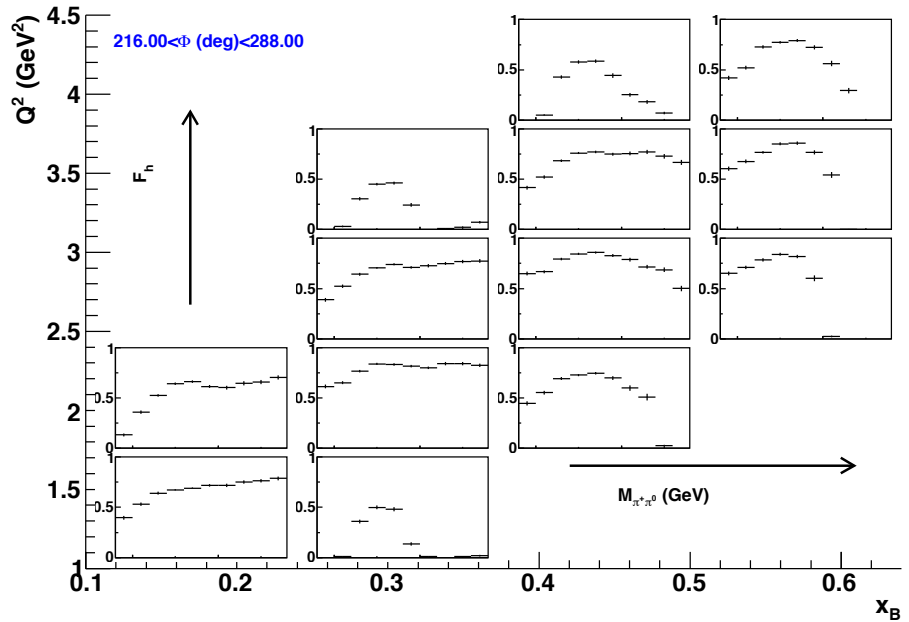


Figure B.4: The hole factor as a function of $M_{\pi^+\pi^0}$ for each (Q^2, x_B) bin and fixed Φ .

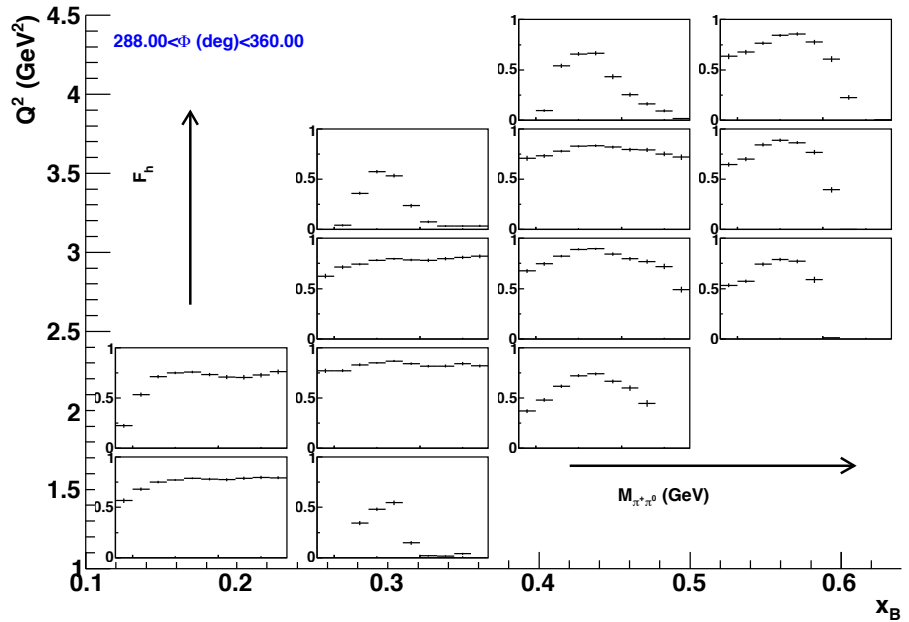


Figure B.5: The hole factor as a function of $M_{\pi^+\pi^0}$ for each (Q^2, x_B) bin and fixed Φ .

Appendix C

Acceptance hole factor for each (Q^2, x_B, ϕ_{HS}) bin

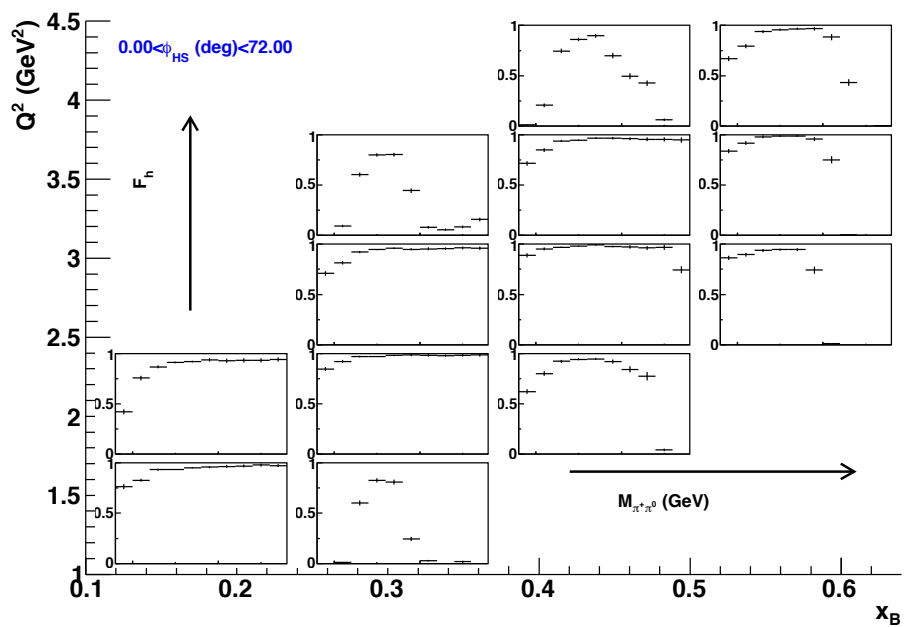


Figure C.1: The hole factor as a function of $M_{\pi^+\pi^0}$ for each (Q^2, x_B) bin and fixed ϕ_{HS} .

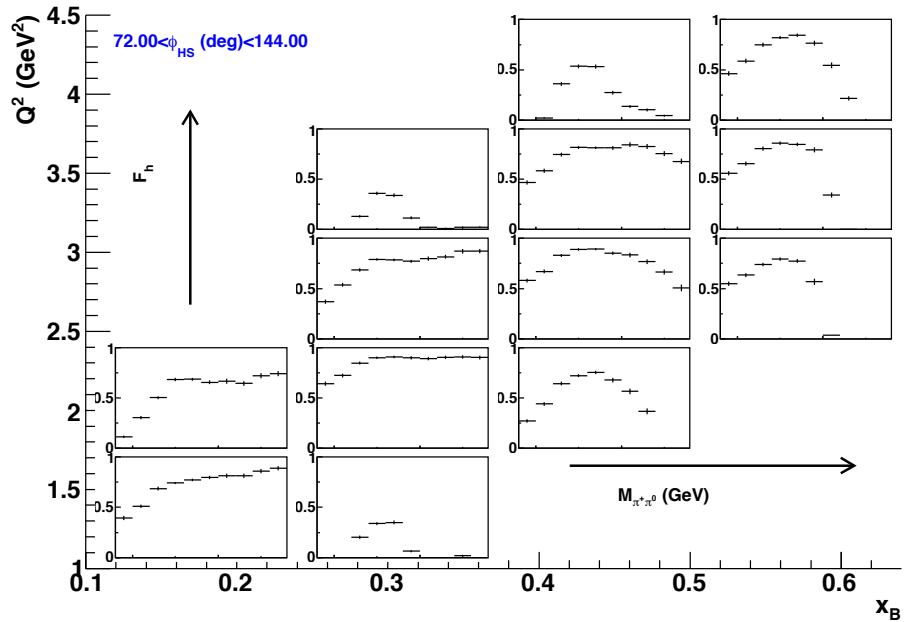


Figure C.2: The hole factor as a function of $M_{\pi^+\pi^0}$ for each (Q^2, x_B) bin and fixed ϕ_{HS} .

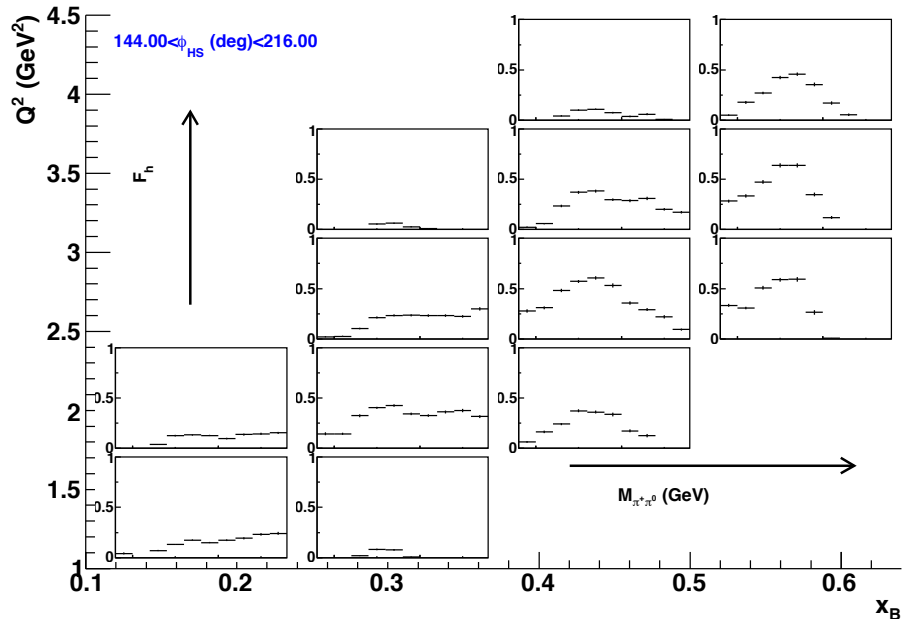


Figure C.3: The hole factor as a function of $M_{\pi^+\pi^0}$ for each (Q^2, x_B) bin and fixed ϕ_{HS} .

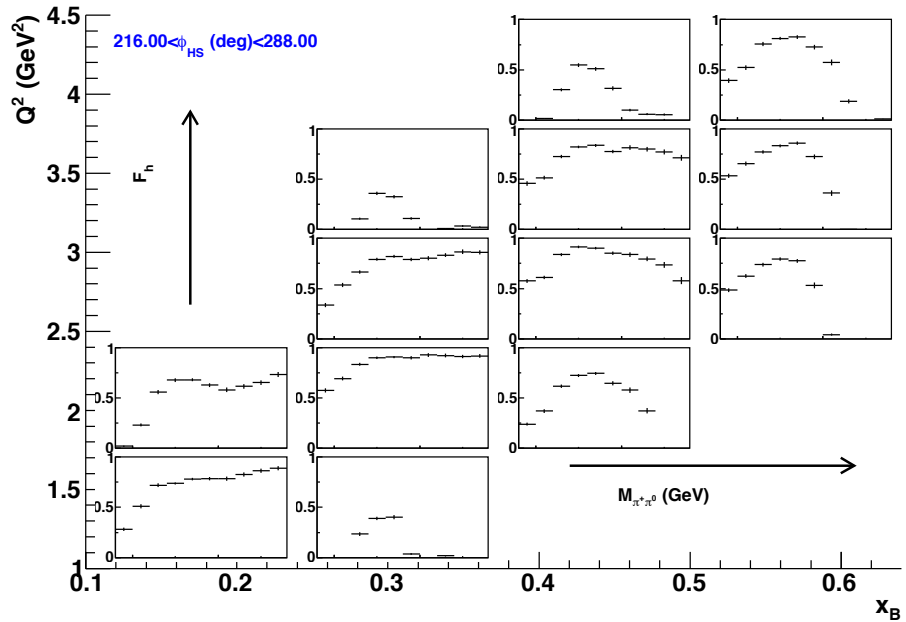


Figure C.4: The hole factor as a function of $M_{\pi^+\pi^0}$ for each (Q^2, x_B) bin and fixed ϕ_{HS} .

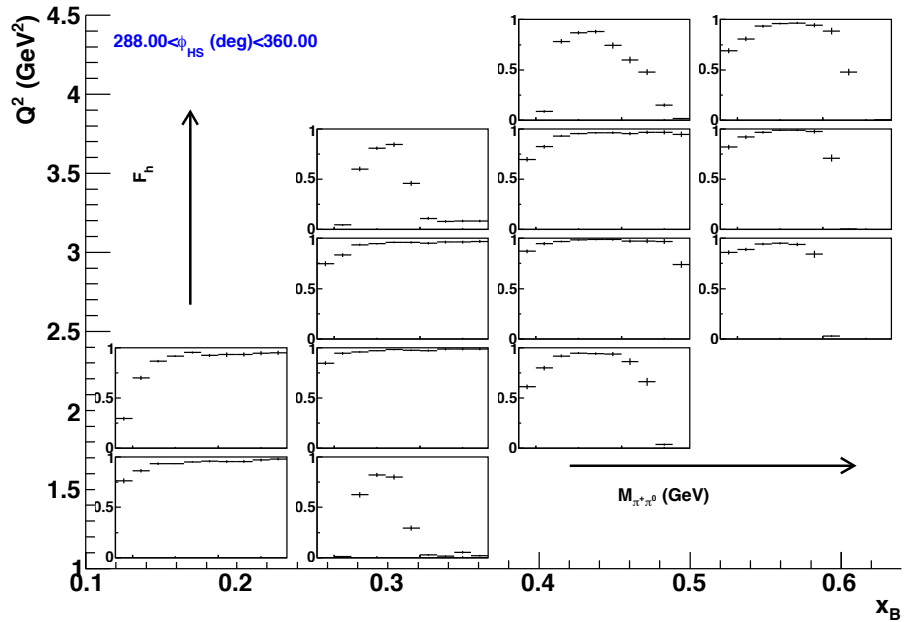


Figure C.5: The hole factor as a function of $M_{\pi^+\pi^0}$ for each (Q^2, x_B) bin and fixed ϕ_{HS} .

Appendix D

Acceptance hole factor for each $(Q^2, x_B, \cos \theta_{HS})$ bin

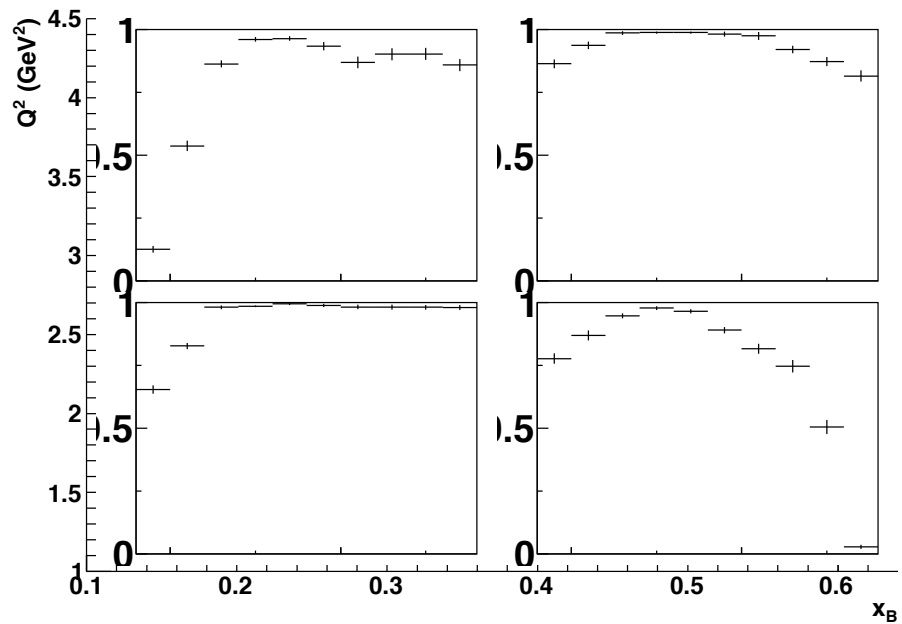


Figure D.1: The hole factor as a function of $M_{\pi^+\pi^0}$ for each (Q^2, x_B) bin and $-1. < \cos \theta_{HS} < -0.6$.

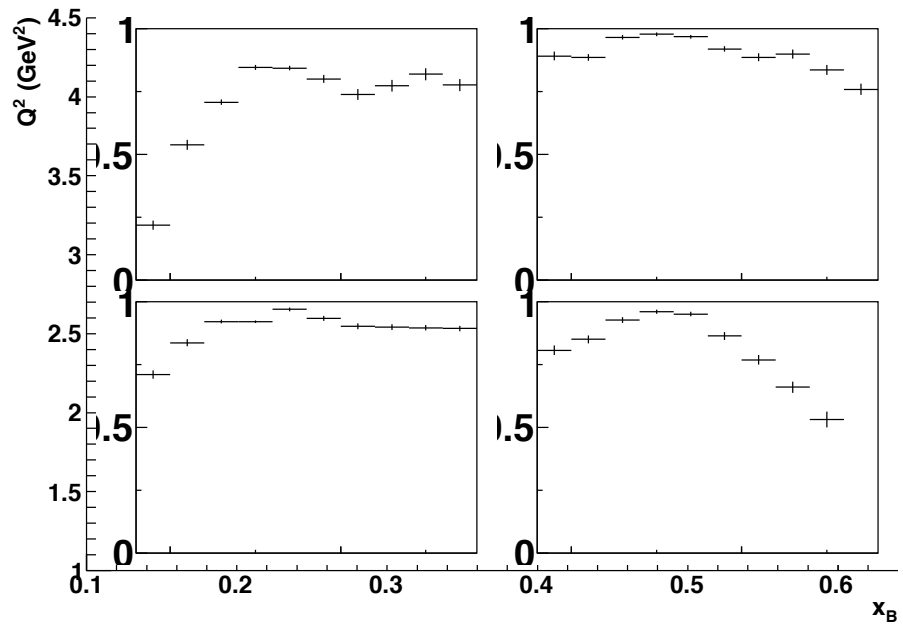


Figure D.2: The hole factor as a function of $M_{\pi^+\pi^0}$ for each (Q^2, x_B) bin and $-0.6 < \cos \theta_{HS} < -0.2$.

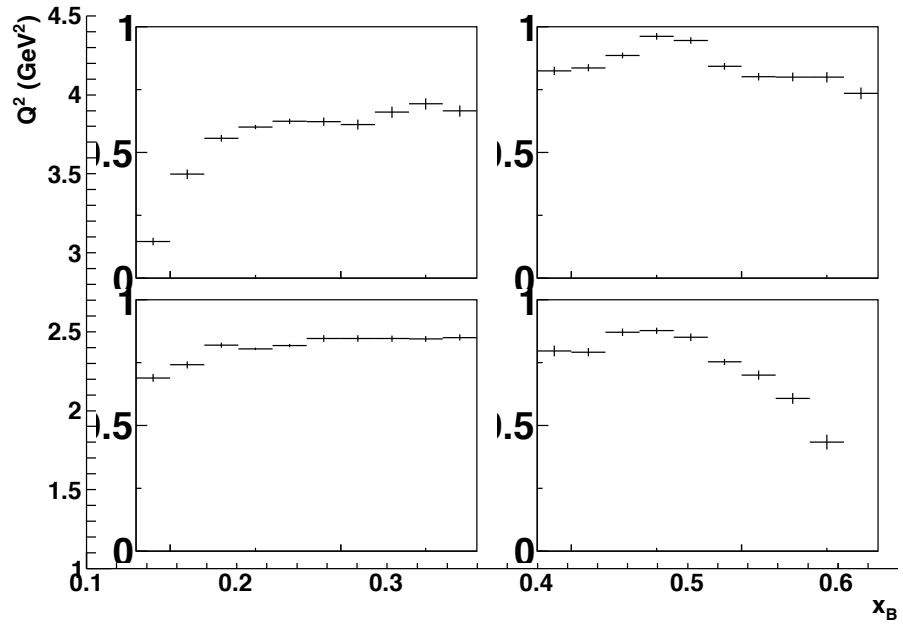


Figure D.3: The hole factor as a function of $M_{\pi^+\pi^0}$ for each (Q^2, x_B) bin and $-0.2 < \cos \theta_{HS} < 0.2$.

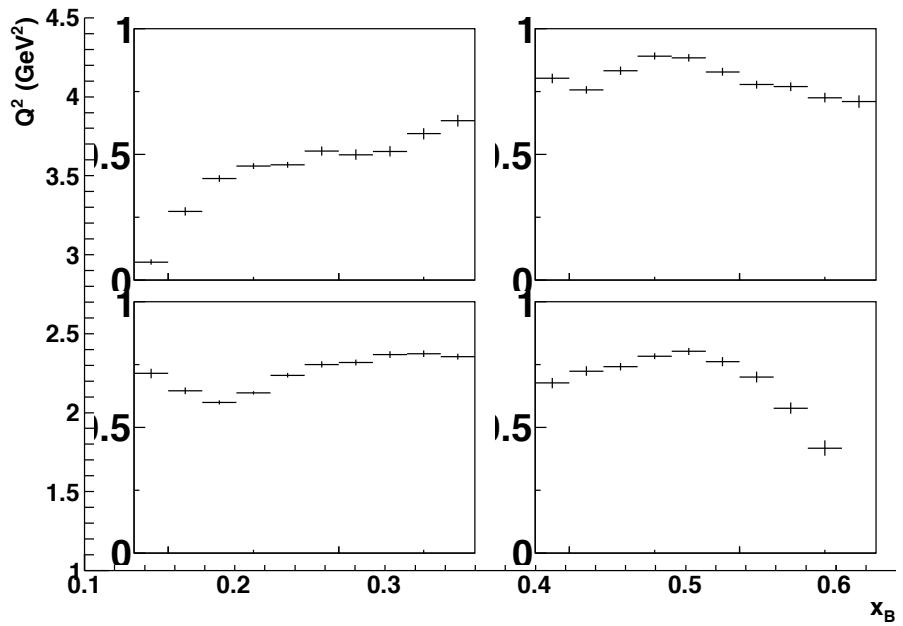


Figure D.4: The hole factor as a function of $M_{\pi^+\pi^0}$ for each (Q^2, x_B) bin and $0.2 < \cos \theta_{HS} < 0.6$.

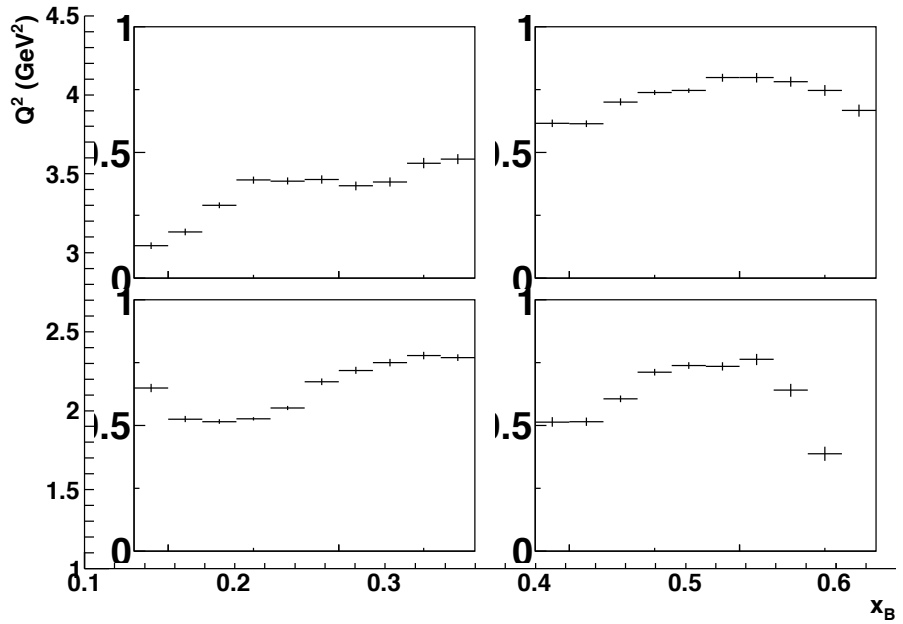


Figure D.5: The hole factor as a function of $M_{\pi^+\pi^0}$ for each (Q^2, x_B) bin and $0.6 < \cos \theta_{HS} < 1..$

Appendix E

Background subtraction for each (Q^2, x_B, t) bin

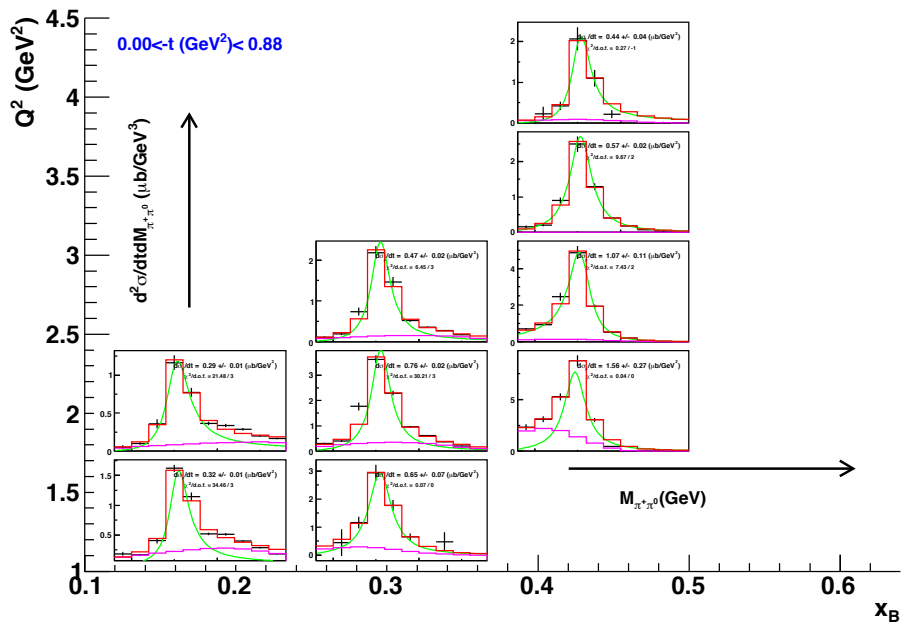


Figure E.1: $M_{\pi^+\pi^0}$ acceptance-corrected distributions, showing fits for the background subtraction for each (Q^2, x_B) and $0. < -t(\text{GeV}^2) < 0.88$.

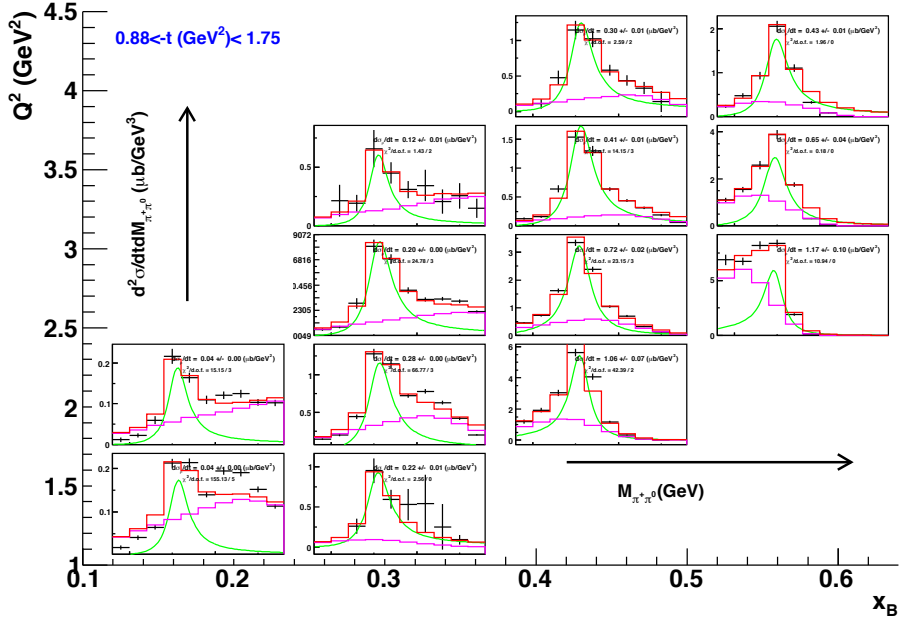


Figure E.2: $M_{\pi^+\pi^0}$ acceptance-corrected distributions, showing fits for the background subtraction for each (Q^2, x_B) and $0.88 < -t(\text{GeV}^2) < 1.75$.

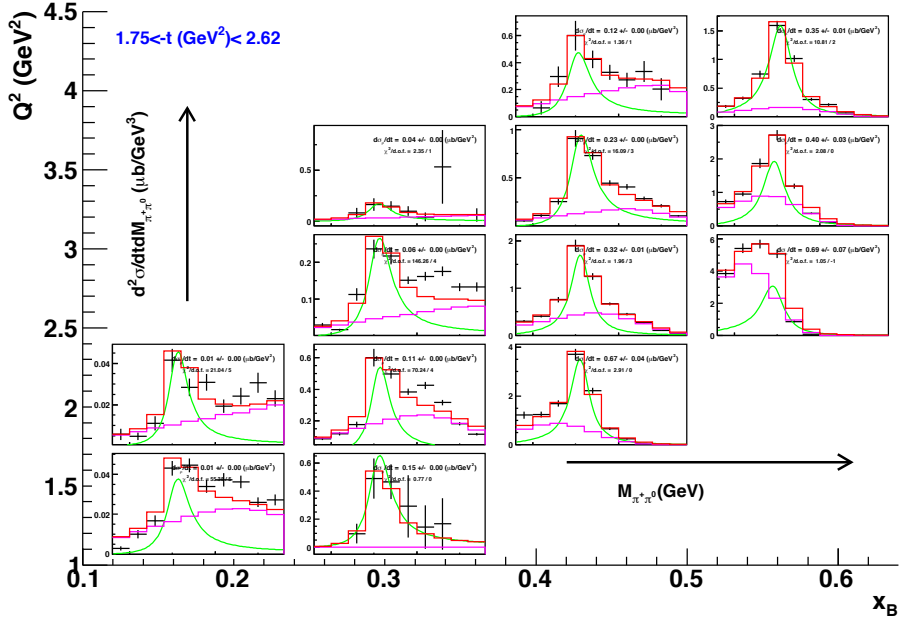


Figure E.3: $M_{\pi^+\pi^0}$ acceptance-corrected distributions, showing fits for the background subtraction for each (Q^2, x_B) and $1.75 < -t(\text{GeV}^2) < 2.62$.

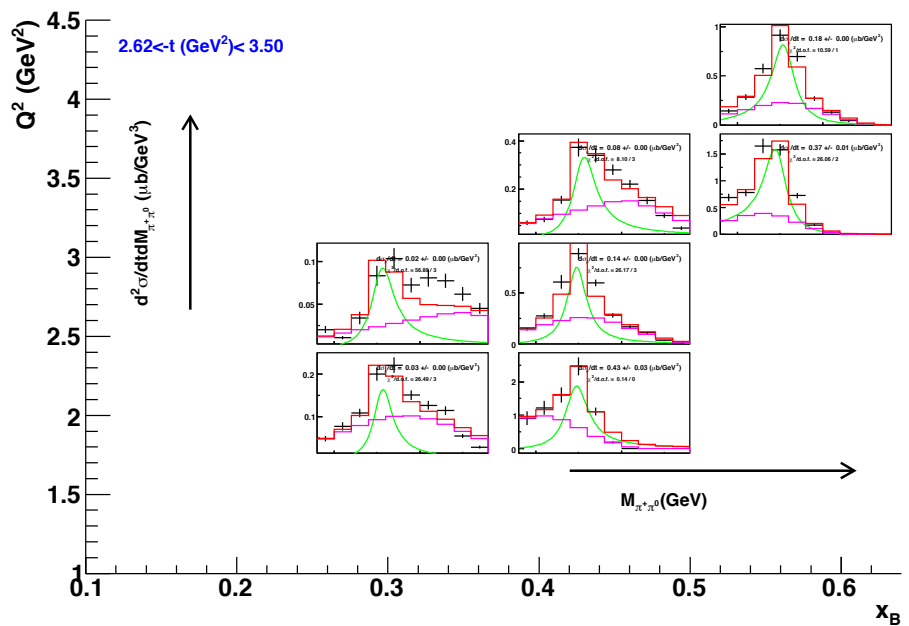


Figure E.4: $M_{\pi^+\pi^0}$ acceptance-corrected distributions, showing fits for the background subtraction for each (Q^2, x_B) and $2.62 < -t(\text{GeV}^2) < 3.5$.

Appendix F

Background subtraction for each (Q^2, x_B, Φ) bin

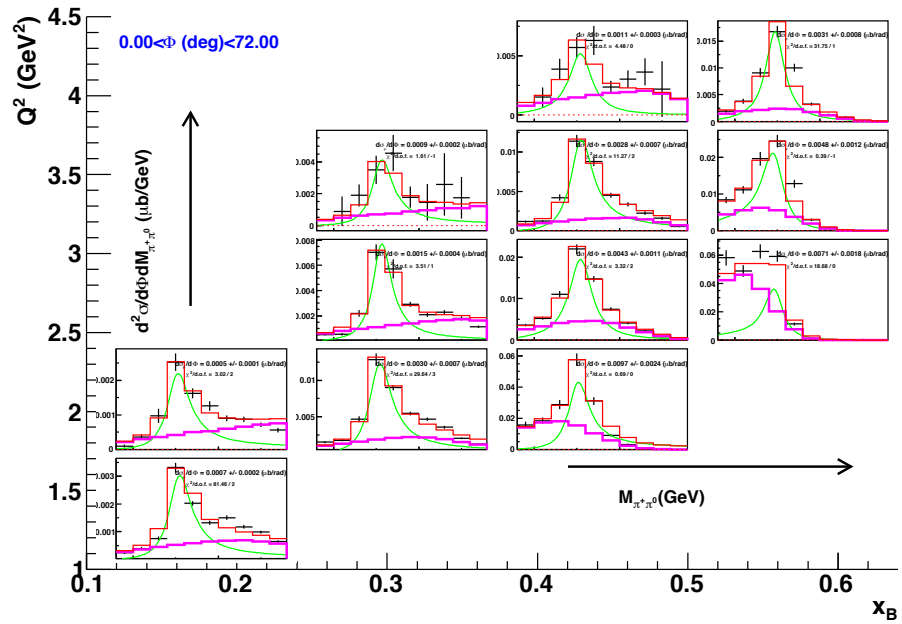


Figure F.1: $M_{\pi^+\pi^0}$ acceptance-corrected distributions, showing fits for the background subtraction for each (Q^2, x_B) and $0. < \Phi(\text{deg}) < 72.0$

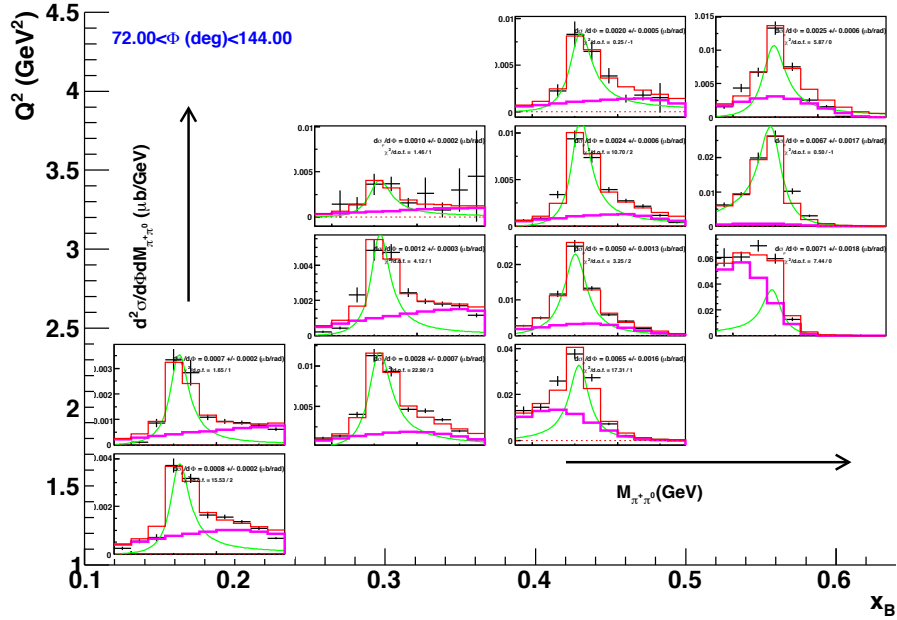


Figure F.2: $M_{\pi^+\pi^0}$ acceptance-corrected distributions, showing fits for the background subtraction for each (Q^2, x_B) and $72 < \Phi(\text{deg}) < 144$.

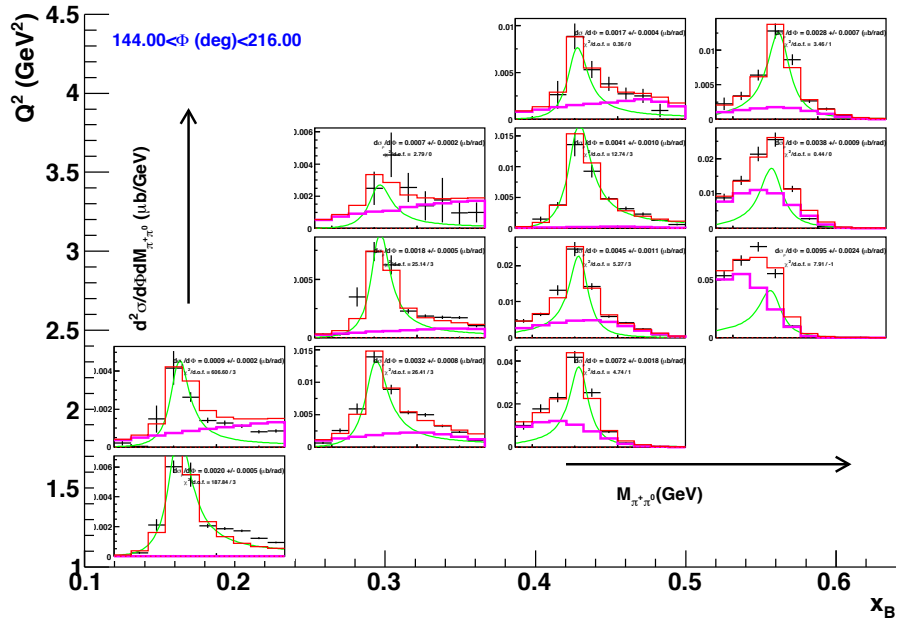


Figure F.3: $M_{\pi^+\pi^0}$ acceptance-corrected distributions, showing fits for the background subtraction for each (Q^2, x_B) and $144. < \Phi(\text{deg}) < 216$.

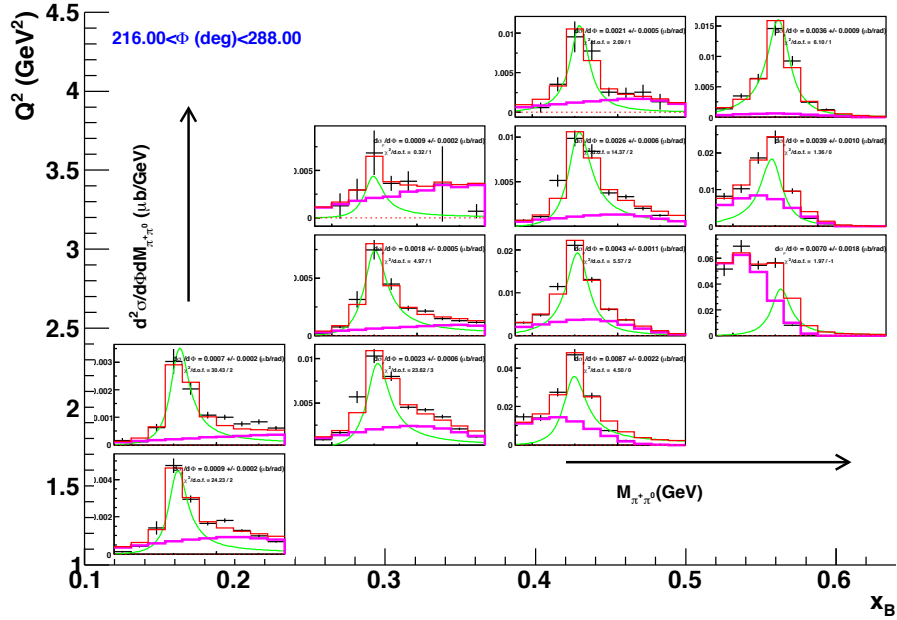


Figure F.4: $M_{\pi^+\pi^0}$ acceptance-corrected distributions, showing fits for the background subtraction for each (Q^2, x_B) and $216. < \Phi(\text{deg}) < 288.$

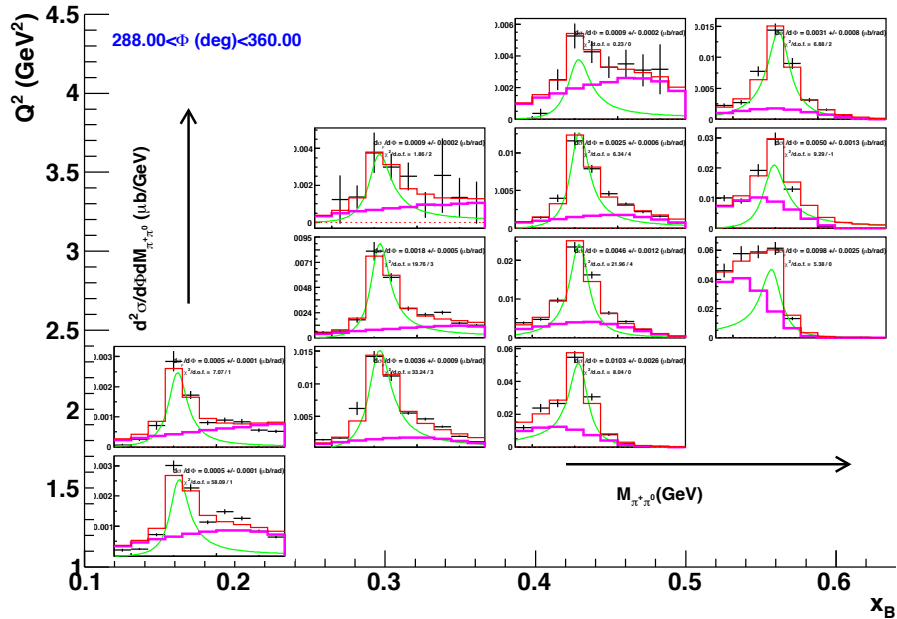


Figure F.5: $M_{\pi^+\pi^0}$ acceptance-corrected distributions, showing fits for the background subtraction for each (Q^2, x_B) and $288. < \Phi(\text{deg}) < 360.$

Appendix G

Background subtraction for each (Q^2, x_B, ϕ_{HS}) bin

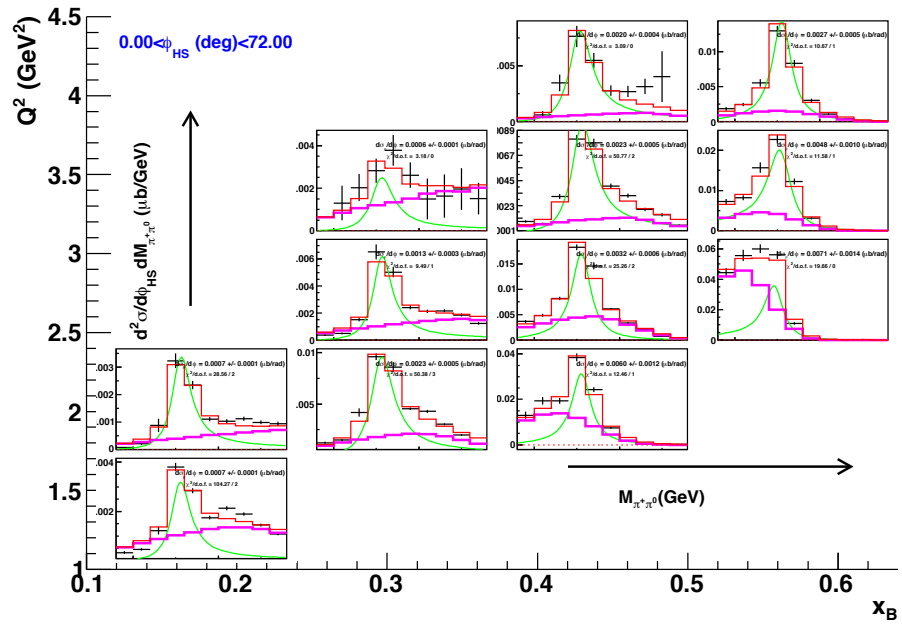


Figure G.1: $M_{\pi^+\pi^0}$ acceptance-corrected distributions, showing fits for the background subtraction for each (Q^2, x_B) and $0. < \phi_{HS}(\text{deg}) < 72$.

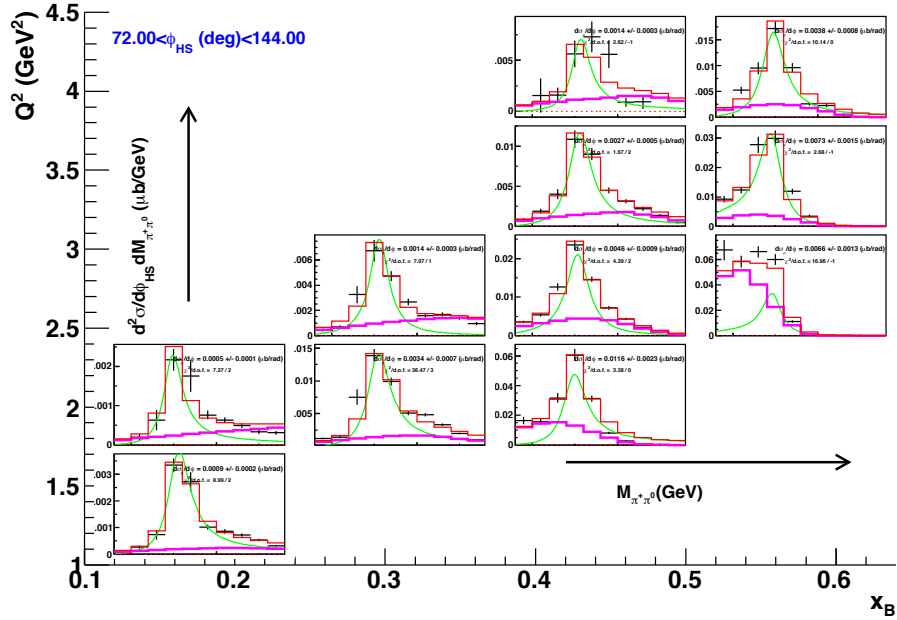


Figure G.2: $M_{\pi^+\pi^0}$ acceptance-corrected distributions, showing fits for the background subtraction for each (Q^2, x_B) and $72. < \phi_{HS}(\text{deg}) < 144.$

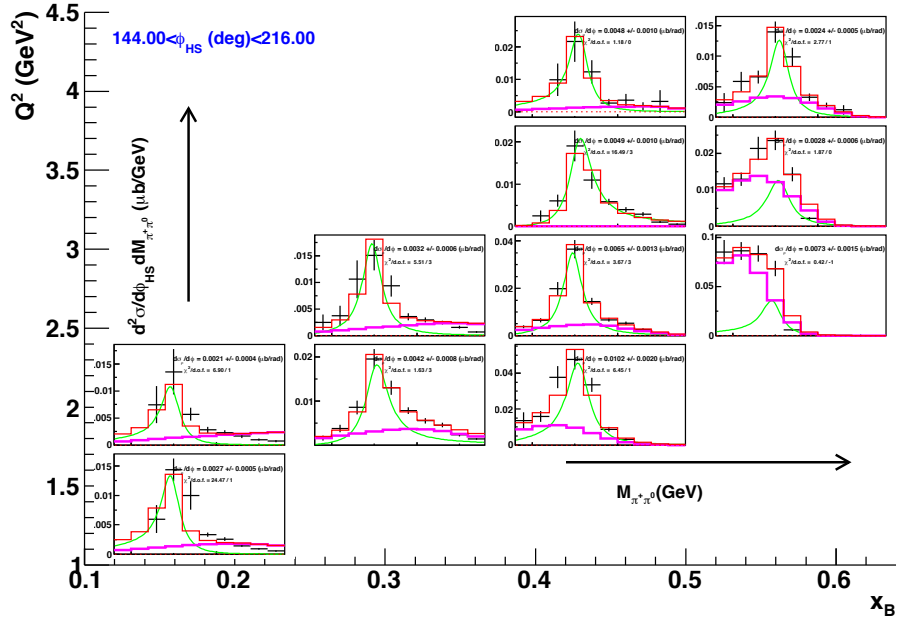


Figure G.3: $M_{\pi^+\pi^0}$ acceptance-corrected distributions, showing fits for the background subtraction for each (Q^2, x_B) and $144. < \phi_{HS}(\text{deg}) < 216.$

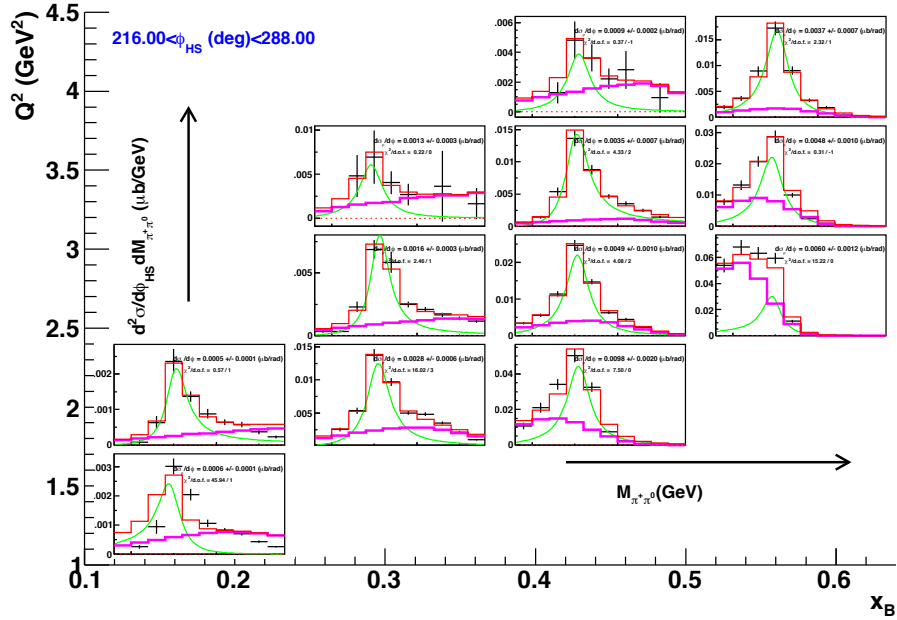


Figure G.4: $M_{\pi^+\pi^0}$ acceptance-corrected distributions, showing fits for the background subtraction for each (Q^2, x_B) and $216. < \phi_{HS}(\text{deg}) < 288.$

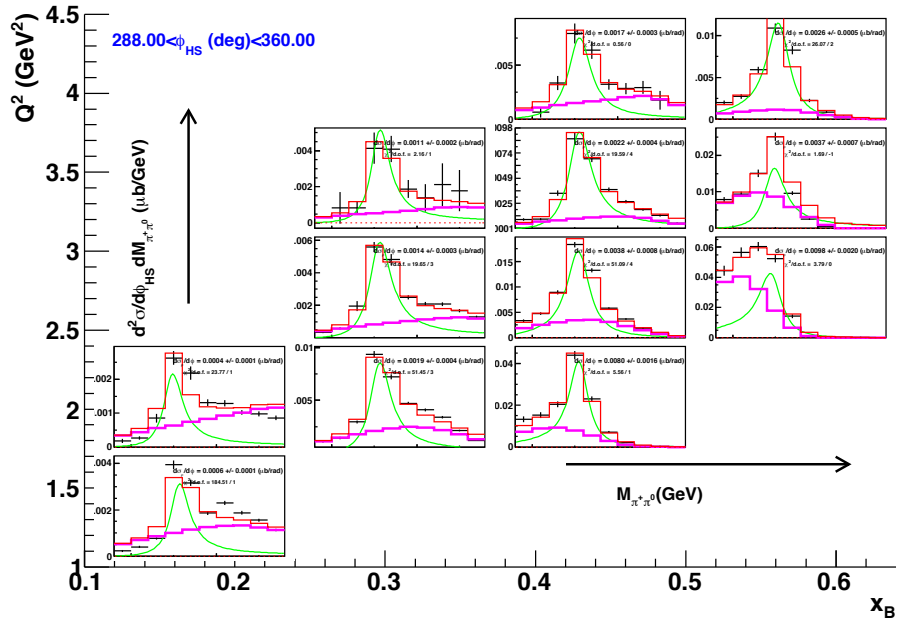


Figure G.5: $M_{\pi^+\pi^0}$ acceptance-corrected distributions, showing fits for the background subtraction for each (Q^2, x_B) and $288. < \phi_{HS}(\text{deg}) < 360.$

Appendix H

Background subtraction for each $(Q^2, x_B, \cos \theta_{HS})$ bin

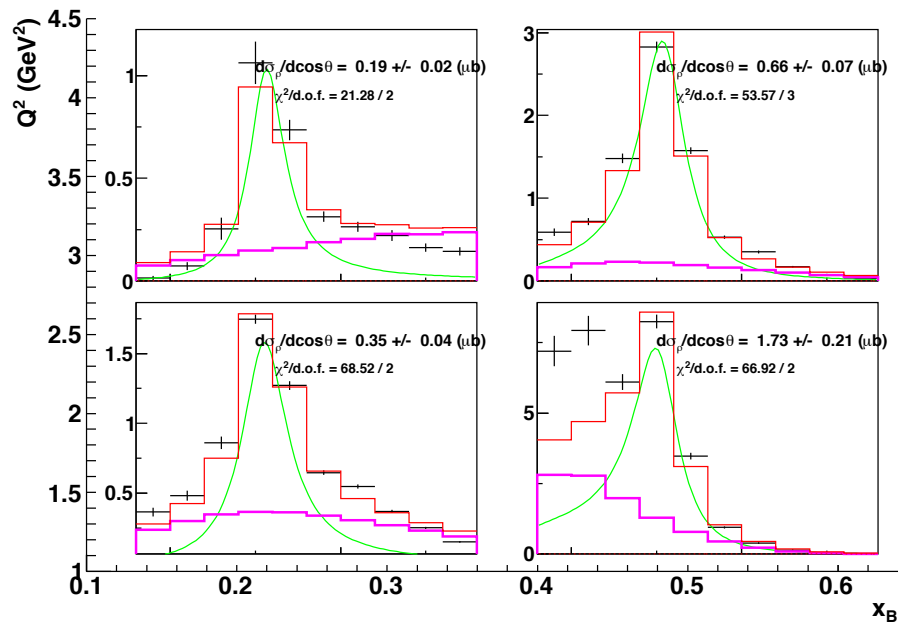


Figure H.1: $M_{\pi^+\pi^0}$ acceptance-corrected distributions, showing fits for the background subtraction for each (Q^2, x_B) and $-1. < \cos \theta_{HS} < -0.6$.

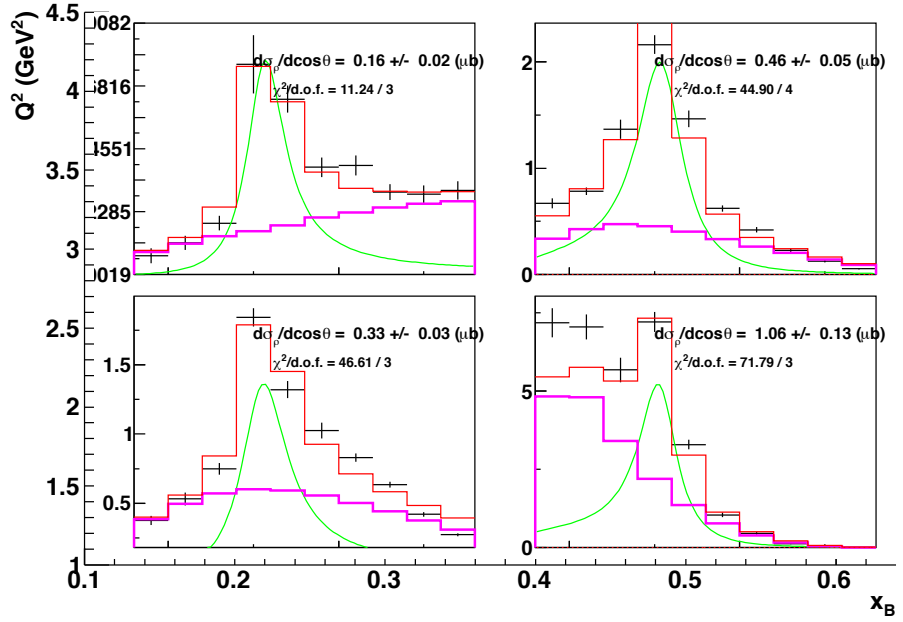


Figure H.2: $M_{\pi^+\pi^0}$ acceptance-corrected distributions, showing fits for the background subtraction for each (Q^2, x_B) and $-0.6 < \cos \theta_{HS} < -0.2$.

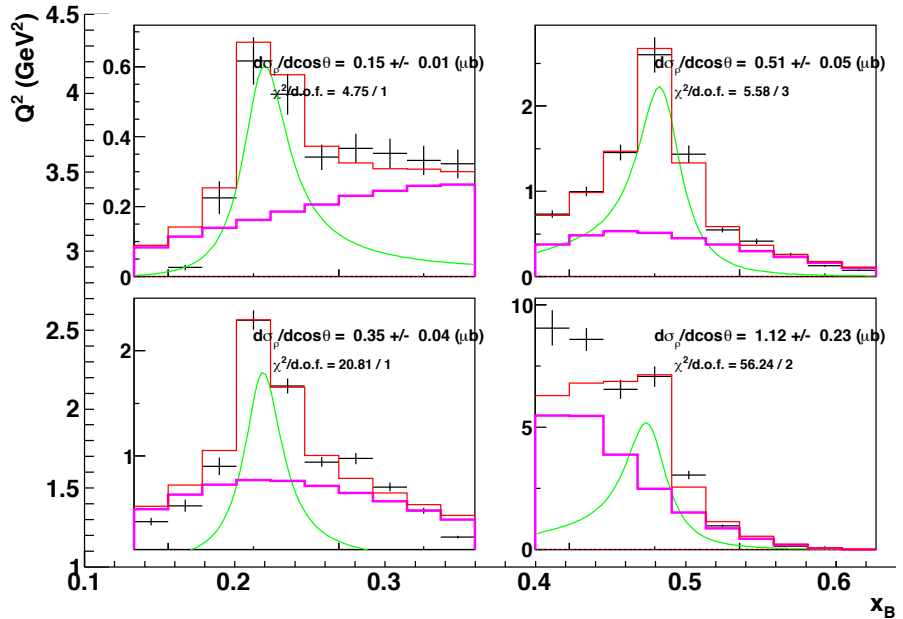


Figure H.3: $M_{\pi^+\pi^0}$ acceptance-corrected distributions, showing fits for the background subtraction for each (Q^2, x_B) and $-0.2 < \cos \theta_{HS} < 0.2$

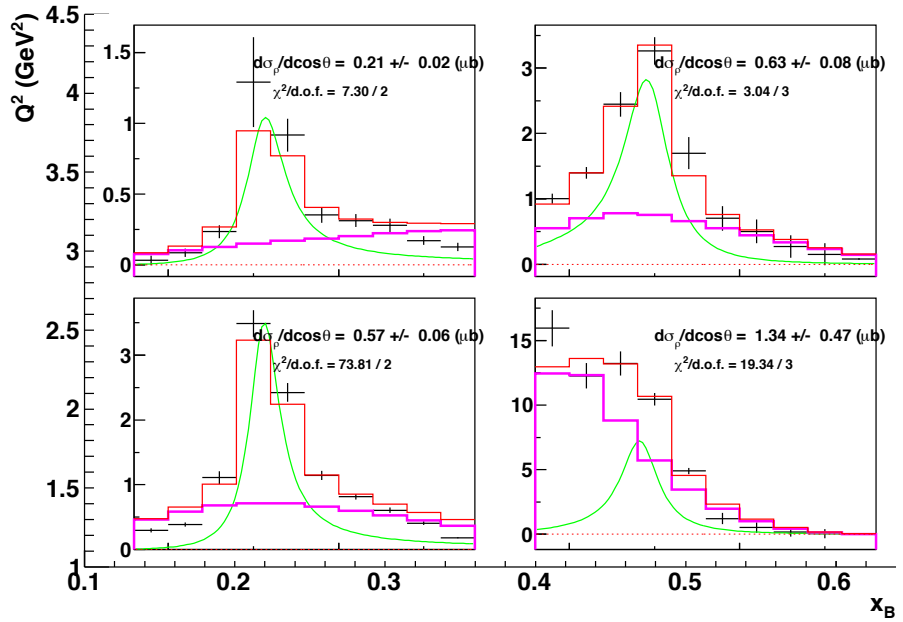


Figure H.4: $M_{\pi^+\pi^0}$ acceptance-corrected distributions, showing fits for the background subtraction for each (Q^2, x_B) and $0.2 < \cos \theta_{HS} < 0.6$.

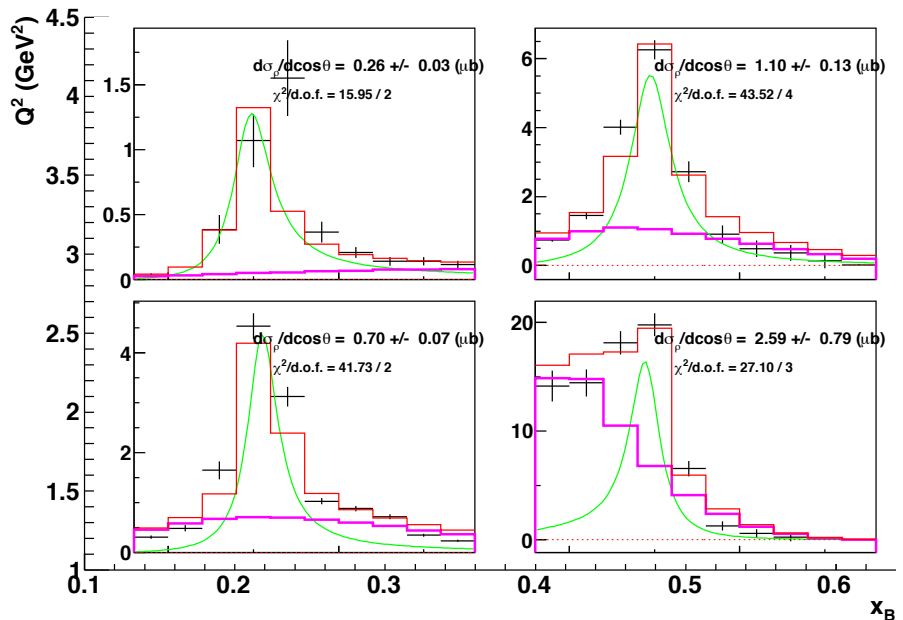


Figure H.5: $M_{\pi^+\pi^0}$ acceptance-corrected distributions, showing fits for the background subtraction for each (Q^2, x_B) and $0.6 < \cos \theta_{HS} < 1$.

Appendix I

Background subtraction for each (Q^2, x_B) fixing the skewdness parameter

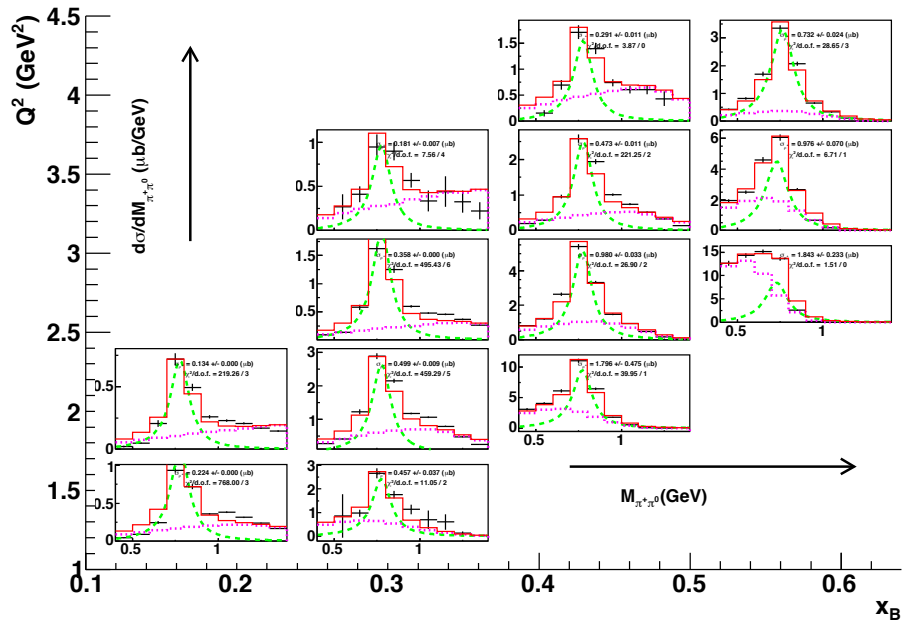


Figure I.1: $M_{\pi^+\pi^0}$ acceptance-corrected distributions, showing fits for the background subtraction. In black: experimental data; In green: Breit-Wigner of ρ^+ with $n_{skew} = 3$; in purple: $M_{\pi^+\pi^0}$ projection of the non-resonant continuum $\gamma^* p \rightarrow n\pi^+\pi^0$ reaction; in red: total fit result.

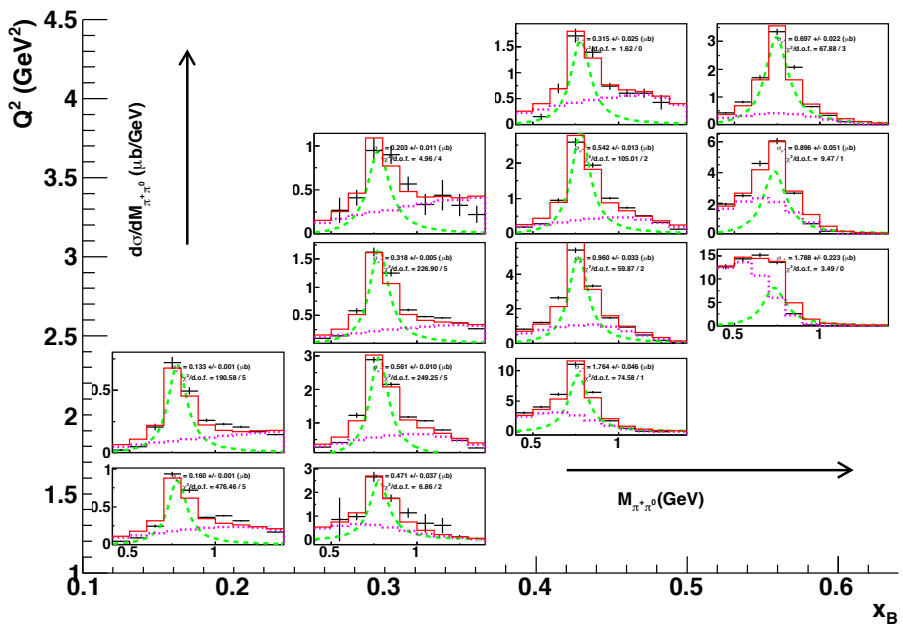


Figure I.2: $M_{\pi^+\pi^0}$ acceptance-corrected distributions, showing fits for the background subtraction. In black: experimental data; In green: Breit-Wigner of ρ^+ with $n_{skew} = 2$; in purple: $M_{\pi^+\pi^0}$ projection of the non-resonant continuum $\gamma^* p \rightarrow n\pi^+\pi^0$ reaction; in red: total fit result.

Appendix J

Background subtraction for each (Q^2, x_B) varing the exclusivity cuts

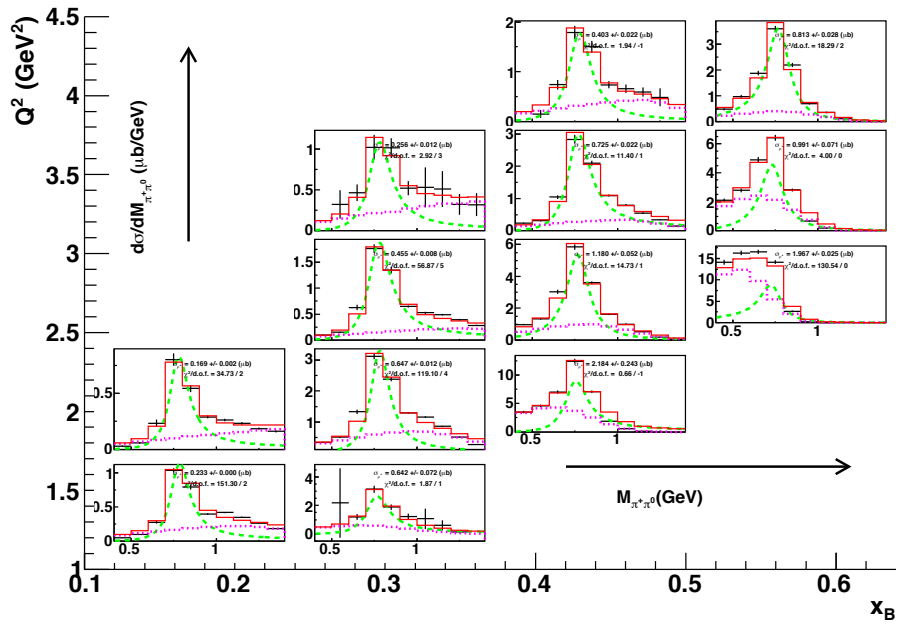


Figure J.1: $M_{\pi^+\pi^0}$ acceptance-corrected distributions, showing fits for the background subtraction for each (Q^2, x_B) with the following exclusivity cuts: 3 σ cut on $IM(\gamma\gamma)$ and 2 σ cut on $M_X(eX\pi^+\pi^0)$.

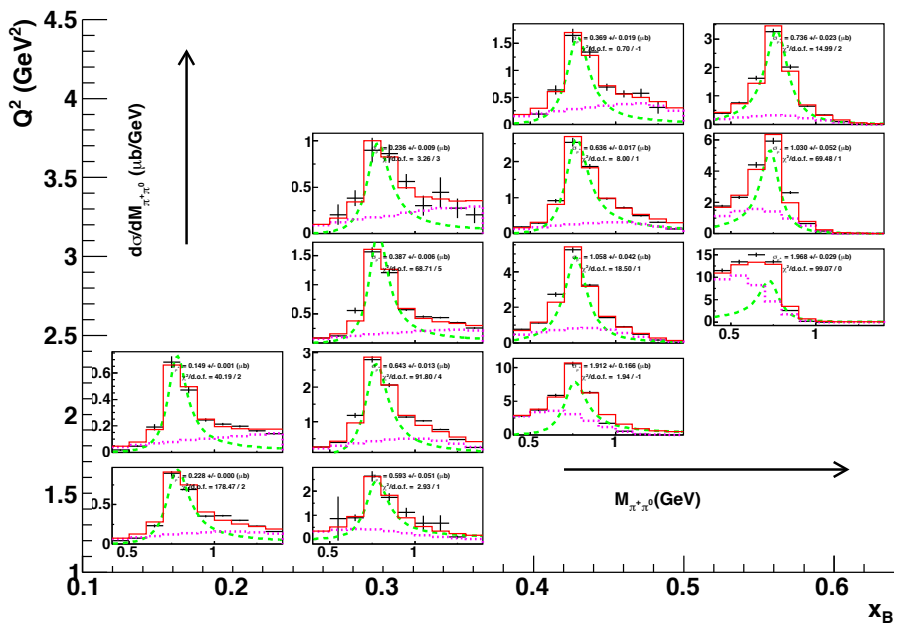


Figure J.2: $M_{\pi^+\pi^0}$ acceptance-corrected distributions, showing fits for the background subtraction for each (Q^2, x_B) with the following exclusivity cuts: 3 σ cut on $IM(\gamma\gamma)$ and 4 σ cut on $M_X(eX\pi^+\pi^0)$.

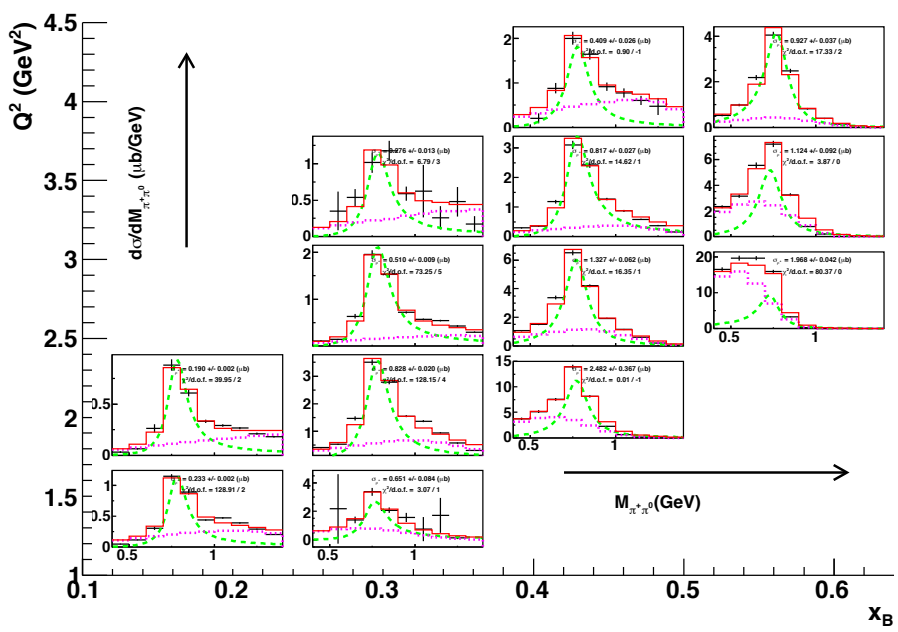


Figure J.3: $M_{\pi^+\pi^0}$ acceptance-corrected distributions, showing fits for the background subtraction for each (Q^2, x_B) with the following exclusivity cuts: 2 σ cut on $IM(\gamma\gamma)$ and 2 σ cut on $M_X(eX\pi^+\pi^0)$.

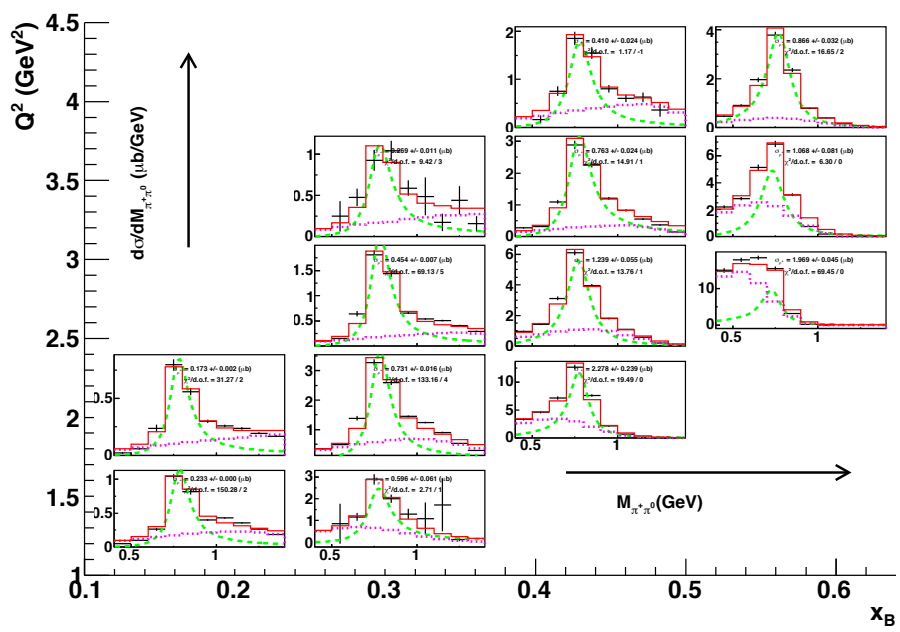


Figure J.4: $M_{\pi^+\pi^0}$ acceptance-corrected distributions, showing fits for the background subtraction for each (Q^2, x_B) with the following exclusivity cuts: 2 σ cut on $IM(\gamma\gamma)$ and 3 σ cut on $M_X(eX\pi^+\pi^0)$.

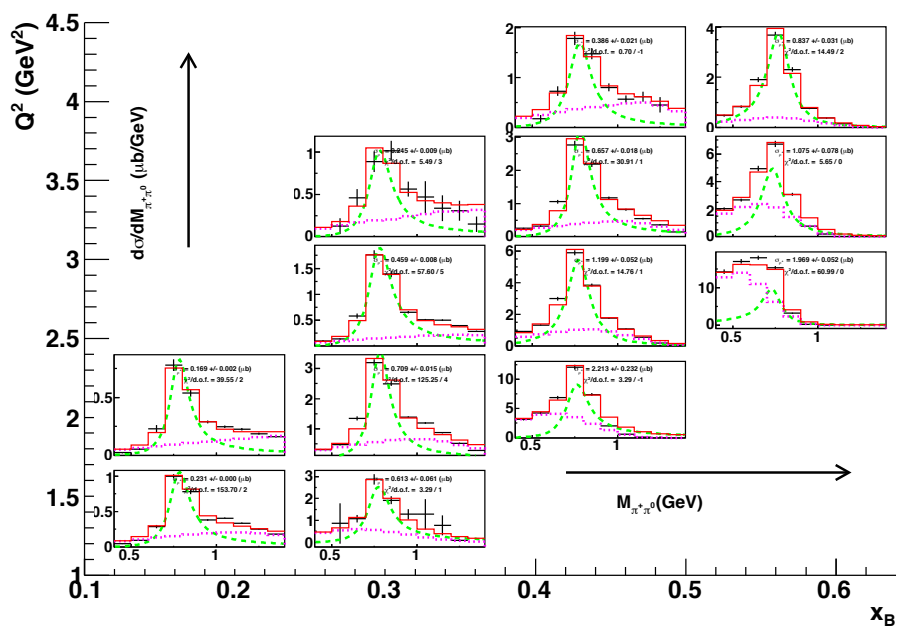


Figure J.5: $M_{\pi^+\pi^0}$ acceptance-corrected distributions, showing fits for the background subtraction for each (Q^2, x_B) with the following exclusivity cuts: 2 σ cut on $IM(\gamma\gamma)$ and 4 σ cut on $M_X(eX\pi^+\pi^0)$.

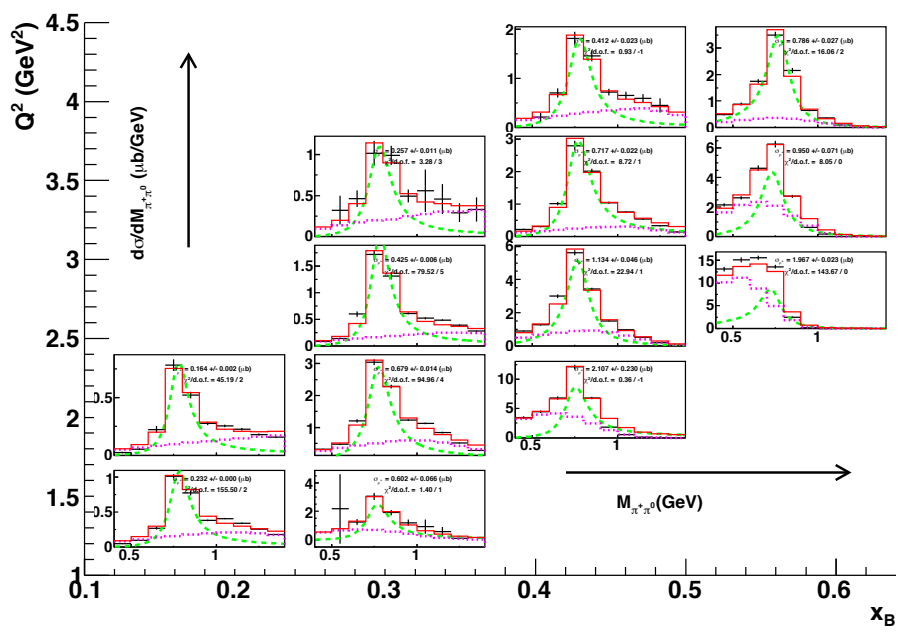


Figure J.6: $M_{\pi^+\pi^0}$ acceptance-corrected distributions, showing fits for the background subtraction for each (Q^2, x_B) with the following exclusivity cuts: 4 σ cut on $IM(\gamma\gamma)$ and 2 σ cut on $M_X(eX\pi^+\pi^0)$.

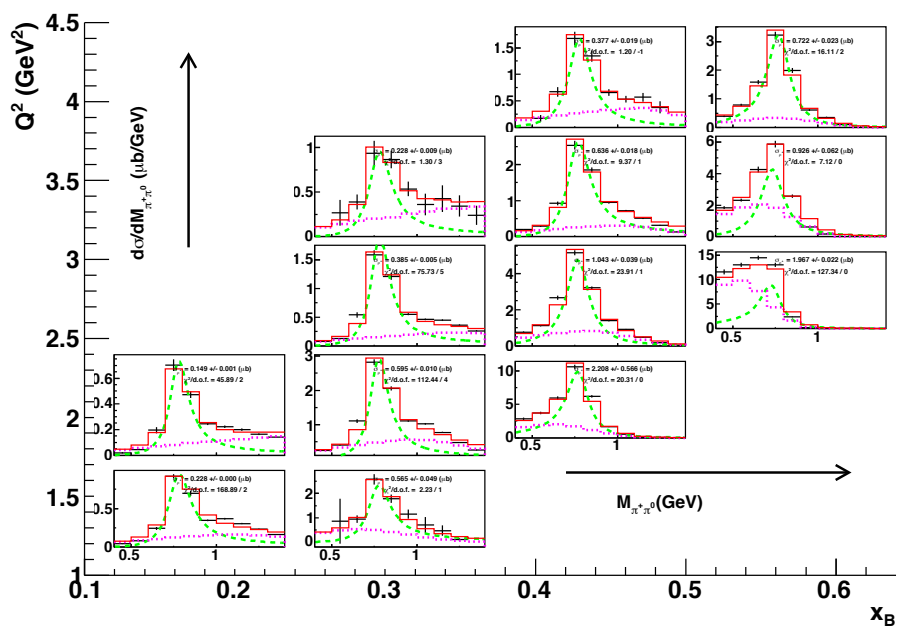


Figure J.7: $M_{\pi^+\pi^0}$ acceptance-corrected distributions, showing fits for the background subtraction for each (Q^2, x_B) with the following exclusivity cuts: 4 σ cut on $IM(\gamma\gamma)$ and 3 σ cut on $M_X(eX\pi^+\pi^0)$.

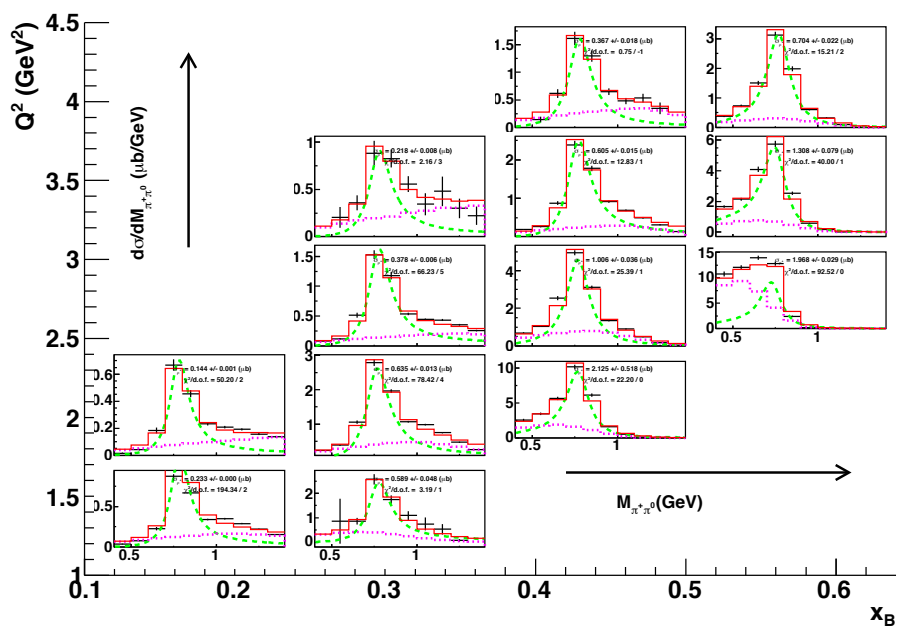


Figure J.8: $M_{\pi^+\pi^0}$ acceptance-corrected distributions, showing fits for the background subtraction for each (Q^2, x_B) with the following exclusivity cuts: 4 σ cut on $IM(\gamma\gamma)$ and 4 σ cut on $M_X(eX\pi^+\pi^0)$.

Bibliography

- [1] M. Guidal, J.-M. Laget and M. Vanderhaeghen, Phys. Lett. B **400**, 6. (1997) ;
M. Guidal, J.-M. Laget and M. Vanderhaeghen, Nucl. Phys. A **627**, 645 (1997) ;
M. Vanderhaeghen, M. Guidal and J.-M. Laget, Phys. Rev. C **57**, 1454 (1998).
- [2] J.-M. Laget, Phys. Lett. B **489**, 313 (2000);
F. Cano and J.-M. Laget, Phys. Rev. D **65**, 074022 (2002) ;
J. M. Laget, Phys. Rev. D **70**, 054023 (2004);
F. Cano and J. M. Laget, Phys. Lett. B **551**, 317 (2003).
- [3] T. Regge, Introduction to complex orbital momenta, Nuovo Cimento **14**, 951 (1959);
Bound states, shadow states and Mandelstam representation, Nuovo Cimento **18**, 947 (1960).
- [4] P. D. B. Collins,"An introduction to Regge theory and high energy physics", Cambridge University Press, Cambridge, 1977.
- [5] X. Ji, Phys.Rev.Lett. **78**, 610 (1997); Phys.Rev.D **55**, 7114 (1997).
- [6] A.V. Radyushkin, Phys.Lett.B **380**, 417 (1996); Phys.Rev.D **56**, 5524 (1997).
- [7] J.C. Collins, L. Frankfurt and M. Strikman, Phys.Rev.D **56**, 2982 (1997).
- [8] M. Burkardt, Phys. Rev. D **62**, 071503 (2000) [Erratum-ibid. C **66**, 119903 (2002)];
Int. J. Mod. Phys. A **18**, 173 (2003).
- [9] M. Diehl, Eur. Phys. J. C **25**, 223 (2002) [Erratum-ibid. C **31**, 277 (2003)].
- [10] J. P. Ralston and B. Pire, Phys. Rev. D **66**, 111501 (2002).
- [11] M. Vanderhaeghen, P.A.M. Guichon, and M. Guidal, Phys. Rev. Lett. **80**, 5064 (1998).
- [12] V.N. Gribov, L.N. Lipatov, Sov. J. Nucl. Phys. **15**, 438 (1972);
V.N. Gribov, L.N. Lipatov, Sov. J. Nucl. Phys. **15**, 675 (1972);
L.N. Lipatov, Sov. J. Nucl. Phys. **20**, 94 (1975);
Y.L. Dokshitser, JETP **46**, 641 (1977);
G. Altarelli, G. Parisi, Nucl. Phys. B **126**, 298 (1977).

- [13] S.J. Brodsky, G.P. Lepage, Phys. Lett. B **87**, 359 (1979) ;
 S.J. Brodsky, G.P. Lepage, Phys. Rev. D **22**, 2157 (1980);
 A.V. Efremov, A.V. Radyushkin, Phys. Lett. B **94**, 245 (1980);
 A.V. Efremov, A.V. Radyushkin, Theor. Math. Phys. **42**, 97 (1980).
- [14] M. Stratmann and W. Vogelsang, J. Phys. Conf. Ser. 69, 012035 (2007) and references therein.
- [15] M. Diehl, Phys. Rept. **338**, 41 (2003).
- [16] M. Vanderhaeghen, P.A.M. Guichon, and M. Guidal, Phys. Rev. D **60**, 094017 (1999).
- [17] M. Guidal, Habilitation à Diriger des Recherches, Université Paris-Sud 11 Orsay (2007).
- [18] HERMES, A. Airapetian et al., Phys. Rev. Lett. **84**, 2584 (2000).
- [19] PLB 633 (2006) 25-32 et PLB 676 31-38 (2009).
- [20] 2005: PRD 76, 051106 et 2006: arXiv: 0810.0694.
- [21] arXiv: 0812.0539 [hep-ph] (To appear in the proceedings of HERA and the LHC: 4th Workshop on the Implications of HERA for LHC Physics, Geneva, Switzerland, 26-30 May 2008).
- [22] L. Frankfurt, W. Koepf and M. Stikman, Phys. Rev. D **54**, 3194 (1996).
- [23] S. Stepanyan et al., Phys. Rev. Lett. **87**, 182002 (2001) ;
 S. Chen et al., Phys. Rev. Lett. **97**, 072002 (2006) ;
 C. Muñoz Camacho et al., Phys. Rev. Lett. **97**, 262002 (2006);
 M. Mazouz et al., Phys. Rev. Lett. **99**, 242501 (2007) ;
 F.-X. Girod et al., Phys. Rev. Lett. **100**, 162002 (2008).
- [24] S. Morrow et al., Eur. Phys. J. A **39**, 5 (2009).
- [25] C. Hadjidakis *et al.*, Phys. Lett. B **605**, 256 (2005).
- [26] L. Morand et al., Eur. Phys. J. A **24**, 445 (2005).
- [27] J. P. Santoro *et al.*, Phys. Rev. C **78**, 025210 (2008).
- [28] J. Botts and G. Sterman, Nucl. Phys. B **325**, 62 (1989).
- [29] B.A. Mecking *et al.*, Nucl. Instr. Meth. A **503**, 513 (2003).
- [30] M.D. Mestayer *et al.*, Nucl. Instr. Meth. A **449**, 81 (2000).
- [31] E.S. Smith *et al.*, Nucl. Instr. Meth. A **432**, 265 (1999).

- [32] G. Adams *et al.*, Nucl. Instr. Meth. A **465**, 414 (2001).
- [33] M. Amarian *et al.*, Nucl. Instr. Meth. A **460**, 239 (2001).
- [34] L. Morand, Thèse de Doctorat, Université Paris 7 - Denis Diderot (2003).
- [35] C. Hadjidakis, Thèse de Doctorat, Université Paris 7 - Denis Diderot (2002).
- [36] Hyon-Suk Jo, Thèse de Doctorat, Université Paris-Sud 11 Orsay (2007).
- [37] F.-X. Girod, Thèse de Doctorat, Université Louis Pasteur Strasbourg 1 (2006).
- [38] D. Cords *et al.*, CLAS Event Format with *BOS*, CLAS-NOTE 1994-012 (1994).
- [39] W.-M. Yao *et al.*, J. Phys. Lett. G **33**, 1 (2006).
- [40] R. De Masi, Accès restreint :
<http://www.jlab.org/Hall-B/secure/e1-dvcs/rita/corrections/corrections.html>
- [41] F.-X. Girod et M. Garçon, *Simulation of CLAS/DVCS Inner Calorimeter: optimization of position resolution, edge effects and fiducial cuts, photon energy reconstruction, neutral pion events*, CLAS-Note 2005-001.
- [42] R. Niyazov et S. Stepanyan, *DVCS Calorimeter Prototype Reconstruction and calibration procedures*, CLAS-Note 2005-007.
- [43] R. De Masi *et al.*, *Photon energy corrections in EC (from data)*, CLAS-Note 2006-015.
- [44] L. N. Hand, Phys. Rev. **129**, 1834 (1963).
- [45] M. Ripani, INFN Gênes, communication privée.
- [46] D. P. Barber *et al.* Z. PHYS.C **2**, 1 (1979).
- [47] L.W. Mo, Y.S. Tsai, Rev. Mod. Phys. **41**, 205 (1969).
- [48] E. Wolin, GSIM User's Guide Version 1.1, (1996).
- [49] GEANT, Detector Description and Simulation Tool
<http://wwwinfo.cern.ch/asd/geant/index.html>.
- [50] MINUIT, fonction de la librairie du CERN
<http://wwwasdoc.web.cern.ch/wwwasdoc/cernlib.html>.
- [51] J.D. Jackson, Nuovo Cimento **34**, 1644 (1964).
- [52] M. Ross and L. Stodolsky, Phys. Rev. **149**, 1172 (1966).
- [53] P. Soding, Phys. Lett. **19**, 702 (1966).

- [54] F.-X. Girod, P. Stoler,... communication privée.
- [55] K. Schilling and G. Wolf, Nucl. Phys. B **61**, 381 (1973).
- [56] M. Tytgat, phD Thesis, Diffractive production of ρ^0 and ω vector mesons at HERMES, April (2001).
- [57] P. Benz et al., Nucl.Phys. B **79**, 10 (1974).
- [58] J.-M. Laget, communication privée.
- [59] J.-M. Laget, proceedings du workshop "Physics and instrumentations with 6-12 GeV beams", Juin 1998, Newport-News (USA). Editeurs: S. Dytman, H. Fenker et P. Roos.
- [60] A.V. Radyushkin, Phys. Rev. D **59**, 014030 (1999); Phys. Lett. B **449**, 81 (1999).
- [61] D. Muller, D. Robaschik, B. Geyer, F. M. Dittes and J. Horejsi, Fortsch. Phys. **42**, 101 (1994).
- [62] J. Gronberg et al. (CLEO Collaboration), Phys. Rev. D **57**, 33 (1998).
- [63] M. Polyakov and C. Weiss, Phys. Rev. D **60**, 114017 (1999).
- [64] K. Goeke, M. V. Polyakov and M. Vanderhaegen, Prog. Part. Nucl. Phys. **47**, 401 (2001).
- [65] M.Gidal, M. V. Polyakov, A. V. Radyushkin and M. Vanderhaeghen, Phys. Rev. D **72**, 054013 (2005).
- [66] K. Goeke, M.V. Polyakov and M. Vanderhaeghen, Prog. Part. Nucl. Phys. **47**, 401 (2001).
- [67] M.Battaglieri et al., Phys. Rev. Lett. **87**, 172002-1 (2001).
- [68] M.Battaglieri et al., Phys. Rev. Lett. **90**, 022002-1 (2003).
- [69] E. Anciant et al., Phys. Rev. Lett. **85**, 4682 (2000).
- [70] I. Bedlinskiy, Analysis-note CLAS-Analysis 2012-101.
- [71] Hyon-Suk Jo, Analysis-note CLAS-Analysis 2014.